Novel Embolic Particles for Cancer Therapy

Rachel Anne Morrison

A thesis submitted for the degree of

DPhil in Healthcare Innovation

The University of Oxford

Department of Engineering Science

January 2016

Abstract

The aim of this thesis was to develop novel embolic particles for cancer therapy using a combination of nano and microparticles. The particles have been designed and synthesised to have a polystyrene core, be radiopaque, act as a radiosensitiser and have a high capacity for loading of chemotherapy drugs.

The polystyrene core has been designed so it effectively blocks the tumour vascualture thereby limiting oxygen and nutrient delivery to the tumour thus causing tumour necrosis. The core of the polystyrene particle incorporates tantalum oxide nanoparticles to provide X-ray contrast to the embolic microparticles.

The surface of the polystyrene particle has been coated with rare earth doped titanium dioxide (TiO_2) nanoparticles which produce reactive oxygen species upon X-ray activation. This allows the embolic particle to act as a radiosensitising agent and has been shown to reduce cell proliferation in the presence of X-rays.

The surface of the polystyrene particles has also been coated with mesoporous SiO_2 nanoparticles which allow for the high loading capacity of chemotherapeutic drugs. This permits chemotherapy to be delivered directly to the tumour location, thereby reducing the toxic side effects of systemic treatment. As a proof of concept, the chemoembolization particles have been loaded with a novel fungal derived chemotherapeutic Ophiobolin A and the controlled release has been demonstrated. The OphA chemoembolization particles reduced cell viability by approximately 70% compared to the blank chemoembolization particles.

The mechanism of cell death of OphA on eight cancer cell lines and one control cell line has also been studied and its effect on cellular organelles elucidated. OphA shows great promise as a novel chemotherapeutic which could be taken forward to animal trials.

Contents

6 Development of Chemoembolization Particles Incorporating Ophiobolin A 139

List of Figures

List of Tables

Nomenclature

Abbreviations

$\Delta\Psi_m$	Mitochondrial membrane potential
ddH_2O	Double distilled water
EDX	Energy dispersive X-ray spectroscopy
Em.	Emission
ER	Endoplasmic reticulum
Ex.	Excitation
GBM	Glioblastoma multiforme
HMSNP	Hexagonal mesoporous SiO_2 nanoparticle
IC_{50}	Half maximal inhibitory concentration
LD_{50}	The individual dose required to kill 50 percent of a population of test animals
MDR	Multi drug resistant
NCI	National Cancer Institute
NP	Nanoparticle
NS	Not significant
P-gp	P-Glycoprotein
PM	Plasma membrane
PS-HMSNP	Polystyrene-(hexagonal mesoporous SiO_2 nanoparticle) embolic particle
PS	Polystyrene
ROS	Reactive oxygen species
SD	Standard deviation
SEM	Scanning electron microscopy
SE	Standard error
TEM	Transmission electron microscopy
TGA	Thermogravimetric analysis
UV	Ultra violet
v	Volume
wt	Weight
XRD	X-ray diffraction

Chemicals

$CM\text{-}H_2DCFDA$	2',7'-dichlorodihydrofluorescein diacetate

CytoD	Cytochalasin D
DCM	Dichloromethane
FITC	Fluorescein isothiocyanate
OphA	Ophiobolin A
PBS	Phosphate buffered saline
PI	Propidium iodide
PS-TaOx	Polystyrene-tantalum oxide embolic particles
TaOx	Tantalum oxide
TMRM	Tetramethylrhodamine, methyl ester
TRITC	Tetramethylrhodamine

Equations

$< x, y >^2$	Mean squared displacement
δ	Compton scattering
ϵ	Interfacial tension between the two immiscible phases
ϵ	packing density of the particles
η	Viscosity
μ	linear attenuation coefficient
μ_d	Viscosity of suspension medium
μ_d	Viscosity of the droplet phase
ω	Coherent scattering
ρ	Density
ρ_p	Density of the particles
τ	Photoelectric effect
%TaOx$_s$	% of TaOx in the PS-TaOx microsparticles
A_m	Area of a mitochondrion
A_w	Area of the well
C_s	Stabiliser concentration
C	Contrast
C	initial concentration
d_h	Hydrodynamic diameter
D_s	Stirrer diameter
D_v	Vessel diameter
d	Diameter
E	Photon energy
f_{circ}	Circularity of a mitochondrion
I_0	Incident X-ray beam intensity
I_1	Transmittance X-ray beam intensity
K_B	Boltzmann constant
k	An empirical factor representing the reactor design, type of stirrer and self stabilisation, etc.
m_p	Mass of particles in the well
m_s	% mass remaining in the PS sample

m_s	% mass remaining in the TaOX sample
m_s	% mass remaining in the sample
N	Stirring speed
P_m	Perimeter of a mitochondrion
R	Ratio of droplet phase to suspension media
T	Temperature
V	Volume
w_i	mass proportion
X_p	Thickness of particles in the well
x	thickness of the material

Acknowledgements

I would like to thank my supervisor, Dr Helen Townley, for giving me the opportunity to carry out the work contained within this thesis. Her continued interest in the project and advice in carrying out the experimental work has made me the researcher that I am today. I would not have been able to complete this research without her continuous help. I would also like to thank my second supervisor, Prof. Peter Dobson, for all his help, support and constant encouragement, especially when I began this work. I am also grateful to Prof. Alison Noble for maintaining an interest in my work and for her support whilst allowing me to change the direction of my research.

I would like to thank the Digital Economy Centre for Doctoral Training in Healthcare Innovation and the Williams fund for funding this research.

I am very grateful to all of the many collaborators with whom I have worked over the course of my DPhil. Without their help it would not have been possible: Dr Mark Hill, Dr James Thompson and Mr Luke Bird, thank you for help with setting up and conducting the X-ray contrast experiments; Prof. Robert Kiss and Prof. Antonio Evidente, thank you for supplying Ophiobolin A and for your helpful discussions regarding its effect on cells. Dr Chris Gardner, thank you for the help with conducting the NanoSight experiments. Mrs Tiffany Lodge and Dr Alan Diot, thank you for conducting the IN Cell experiments. Dr Neil Young, thank you for the TEM training.

I would also like to thank all the students and post docs that I have had the opportunity to work with whether in the office, laboratory or within the centre of doctoral training program. There are too many people to individually name here, but without each and every one of you, this DPhil would not have been as enjoyable or as much fun as it has.

And finally, I would personally like to thank Ian for continually believing in me and in particular for keeping me calm when things became challenging.

Publications and Patents

The work contained within chapter 3 and chapter 4 is published as:

> R. Morrison, J. Thompson, L. Bird, M. Hill and H. Townley. Synthesis and characterization of polystyrene embolization particles doped with tantalum oxide nanoparticles for X-ray contrast. *Journal of Materials Science: Materials in Medicine* 2015 26 (218).

The work contained within chapter 5 has been filed for a patent with a publication to follow:

> R. Morrison, and H. Townley. Radio-activatable embolic particles. 2015.

The work contained within chapter 6 is published as:

> R. Morrison, C. Gardiner, A. Evidente, R. Kiss and H. Townley. Incorporation of Ophiobolin A into novel chemoembolization particles for cancer cell treatment. *Pharmaceutical Research.* 2014 10 pp 2904-17.

The work contained within chapter 7 is currently under preparation for publication:

> R. Morrison, T. Lodge, A. Diot, A. Evidente, R. Kiss and H. Townley. Investigating the mechanisms of cell death induced by Ophiobolin A on eight cancer cell lines.

The author assisted with particle characterization, similar to that described in chapter 2, of SiO_2 nanoparticles which resulted in the following publication.

> N. Barkalina, C. Jones, J. Kashir, S. Coote, X. Huang, R. Morrison, H. Townley and K. Coward. Effects of mesoporous silica nanoparticles upon the function of mammalian sperm *in vitro* . Nanomedicine. 2014 10 (4) pp 859-70.

Chapter 1

Introduction

1.1 Cancer

Cancer is the uncontrolled growth of tissues which arises after damage to genetic material which controls the cell cycle in healthy cells [1]. The damage can occur from a range of factors such as environmental carcinogens, an unhealthy lifestyle and/or genetic predisposition. Normally healthy cells would be able to repair the damage or trigger cell death, however cancerous cells are unable to do this [1]. Several 'hallmarks' of cancer have been defined and these include growth signal autonomy, resistance to anti-growth signals, the ability to invade and metastasize, an unlimited replication potential, sustained angiogenesis and the escape of apoptosis [2]. Since cancer cells have rapid cell division they require high metabolic rates which results in increased respiration and production of lactic and carbonic acid [3]. This causes a drop in pH in the tissue surrounding the tumour which promotes local invasive growth and metastasis [4].

Over the past several decades, remarkable breakthroughs have been made in advancing our understanding of cancer biology, how it originates and how it develops [5]. This has led to more effective methods for the diagnosis and treatment of cancer, however it still remains a major global health problem accounting for approximately 8 million deaths per year worldwide or 20% of all deaths [6]. The major reason for the high mortality rate lies in our inability to deliver treatment only to the cancerous cell without inducing severe side effects to healthy tissues and organs. Therefore the development of therapeutics which can effectively target the tumour cells while sparing the healthy tissue is highly desirable.

1.2 Current cancer diagnosis and treatment

Currently cancer is diagnosed through a range of tests and scans. The tests include blood tests and biopsies while the scans include computerised tomography (CT) imaging, positron emission tomography (PET) imaging, magnetic resonance imaging (MRI) and ultrasound imaging. These are used to determine the size and location of the tumour and for subsequent planning and monitoring of the treatment given. After cancer has been diagnosed it will normally be treated with surgery, radiotherapy, chemotherapy or some combination of these. Other treatment modalities which are less common include embolization treatment, hyperthermia treatment, gene therapy and immunotherapy.

1.2.1 Surgery

Surgery is often used in the treatment of cancer when an early diagnosis has been made and therefore the tumour is localised and has not had sufficient time to spread. The tumour and some healthy tissue surrounding the tumour are excised to ensure all the cancerous tissue is removed. The main disadvantages of surgery are that it can only be performed before the tumour has spread and cannot be performed if the tumour is close to other important organs or blood vessels. Often radiotherapy and/or chemotherapy is administered before surgery to induce a reduction in the tumour volume and/or after surgery to ensure that any remaining cancerous cells are killed.

1.2.2 Radiotherapy

Radiotherapy has been used in the treatment of cancer since the 1900s and still remains one of the most common forms of treatment. Approximately 50% of cancer patients will receive at least one cycle of radiotherapy during the course of their treatment [7]. Radiotherapy is an extremely cost effective treatment and in 2000 it was estimated to represent only 5% of Sweden's total cost of oncology care [8] Radiotherapy uses ionising radiation, most often X-rays but can include gamma rays or other particle beam radiations, to induce both direct and indirect DNA damage in the cancerous cells. Indirect DNA damage arises from the generation of reactive oxygen species (ROS) such as hydroxyl $OH^{\bullet}$, superoxide O_2^-, and water ions H_2O^+, H_3O^+ which can subsequently induce DNA damage [9].

The major limitation of radiotherapy is that in order to treat the cancerous cells, radiation is also delivered to the healthy cells causing them damage. Often this means that a lower magnitude dose of radiotherapy than necessary to kill all the cancerous cells is given to reduce the damage to the surrounding healthy tissue [10]. Healthy cells have a greater propensity to repair their damaged DNA compared to cancerous cells, however secondary malignancies are still common. Several methods such as intensity modulated radiotherapy (IMRT), brachytherapy and the application of contrast enhanced radiotherapy (CERT), have been developed to reduce the radiation dose received by the healthy tissue and therefore increase its effectiveness.

In IMRT CT and/or MRI images of the tumour and surrounding tissues are used to carefully plan the treatment area so that a high radiation dose is delivered to the tumour while protecting vital organs such as the spinal cord and the brain [11]. X-ray beams are controlled by complex computer algorithms so that their intensity is modulated and therefore the exact tumour morphology can be matched [12]. Thus IMRT requires a team of specialists to ensure the cancerous tissue is treated through the careful planning and delivery of the radiation[12].

In brachytherapy, a capsule or wire containing a radiation source is used to deliver radiotherapy directly at the tumour location [13]. This allows a highly localised dose of radiation to be delivered to the cancerous cells while reducing the probability of damaging the surrounding healthy cells. Furthermore radiolabelled antibodies, targeted to cancerous cells, have also been used to deliver radiation directly at the tumour location after systemic administration [14].

In CERT, radiotherapy is combined with the administration of high atomic number (Z) contrast agents [15]. These increase the local radiation dose due to the differing absorption properties of the element and the surrounding soft tissue. This effect is most pronounced at kilovoltage energies and thus kilovoltage X-rays are generally considered to be optimum for CERT.

1.2.3 Chemotherapy

Chemotherapy is a systemic treatment whereby cytotoxic drugs are introduced into the blood stream to kill the cancerous cells. The major challenge with using chemotherapy for cancer treatment is that it also kills the healthy cells leading to off-target effects resulting in severe side effects (nausea, vomiting and hair loss). Furthermore the emergence of multidrug resistance by cancer cells is reducing the efficacy of current anticancer drugs [16]. Natural products have been shown to be effective at treating cancer for more than 40 years and the search for novel drugs remains a priority due the rapid development of cancer cells to drug resistance and current undesirable side effects of chemotherapy [17].

The first chemotherapy agent discovered in the 1940's was Nitrogen Mustard and this led to the rapid development of other alkylating cytotoxic agents such as cisplatin [18]. Alkalating agents work by directly damaging the cells DNA and therefore they stop the cells from reproducing. The second group of chemotherapeutics to be discovered was the antimetabolites which work by interfering with both DNA and RNA growth during S phase of the cell cycle and therefore inhibit cell division. Common antimetabolites include methotrexate and 5-fluorouracil. Chemotherapy drugs are often given in combination with the aim of increasing their effectiveness by inducing a synergistic effect.

1.2.3.1 Natural products for cancer therapy

Natural products represent a rich source of biologically active compounds and therefore approximately 50% of the best selling pharmaceuticals are either natural products or natural product derivatives (Fig 1.1) [19]. Natural products used in chemotherapy are often small molecule secondary metabolites which the organism has evolved to ensure its survival in response to its own needs and by challenges presented in its environment [20]. Natural products statistically tend to have a higher molecular weight, more chiral centres, more oxygen atoms but fewer nitrogen atoms and more varied ring structures compared to fully synthetic drugs [21]. Complex natural products often only have one group of target molecules (although there are some exceptions to this) [22].

In 1964 Actinomycin D (Act D), derived from soil bacteria, was the first natural product to be approved for clinical use in the treatment of cancer [22]. The mode of action of Act D works by intercalating DNA thereby inhibiting mRNA and protein expression [23]. Its clinical use however has been limited by its extreme cytotoxicity and therefore it requires careful dose calculations before administration to patients [24]. Act D is often used for the treatment of patients with rhabdomyosarcoma and Wilms' tumour. Other

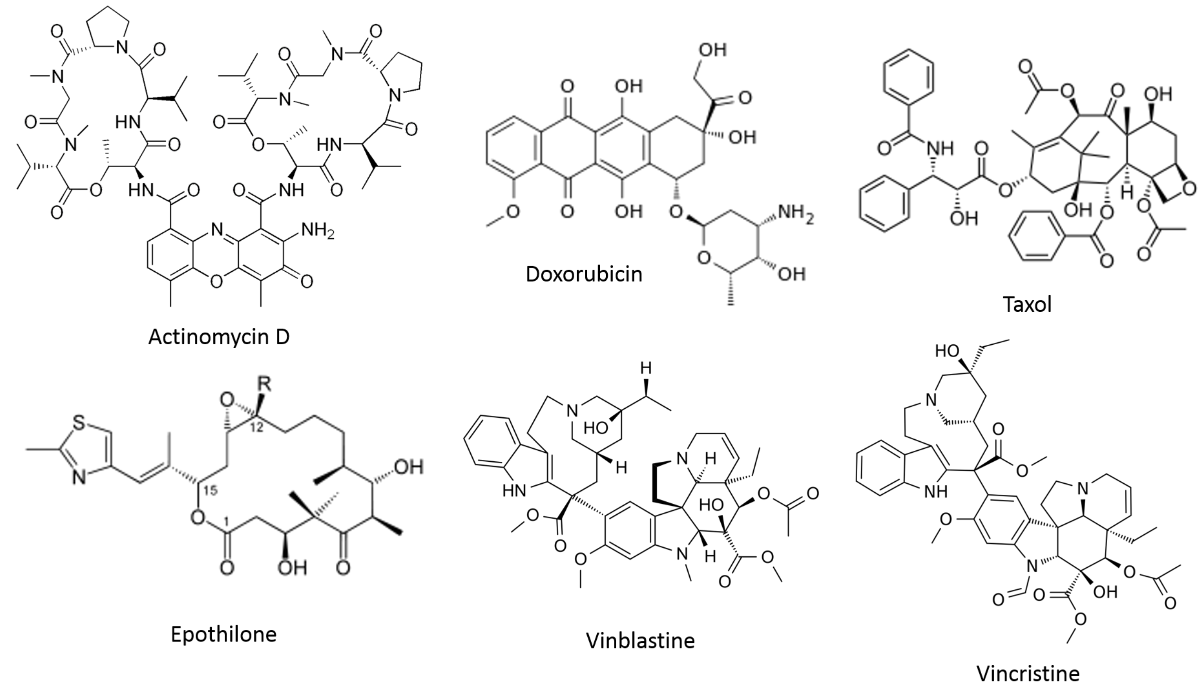

Figure 1.1: Chemical structures of some natural products used for cancer therapy.

microorganism derived natural products include the anthracyclines, Daunorubicin and Doxorubicin (Adriamycin), which are also DNA intercalating agents.

In 1960 the Natural Cancer Institute (NCI) set up a large screening programme of plant derived products active against two mouse leukaemia cell lines [25]. The most significant discovery from this screen was paclitaxel (Taxol®) which was obtained from the bark of the the Pacific yew tree *Taxus brevifolia*. More recently, Taxol was also found to be a fungal secondary metabolite [26]. The mode of action of Taxol works by stabilising the cells microtubules through β-tubulin which interferes with the normal breakdown of the microtubules during cell division [27]. Taxols have also been shown to block the anti-apototic activity of Bcl-2 [28].

The vinca alkaloids, such as vinblastine and vincristine, are another group of plant derived natural products which are isolated from the Madagascar periwinkle plant *Catharanthus roseus* [29]. The effectiveness of vinblastine as an anticancer agent was discovered by chance in the 1960s by a group researching it as a novel diabetes drug [30]. They found that high concentrations of vinblastine reduced the white blood cell count and caused the destruction of bone marrow in rats. The mode of action of the vinca alkoloids works by blocking the polymerisation of tubulin molecules in the microtubules which prevents the formation of the mitotic spindle [27]. Although, both Taxol and the vinca alkoloids interfere with the the microtubules, they work through different mechanisms.

In 1985 the NCI started a new screening programme which included extracts from plants, animals and microorganisms [25]. They screened the extracts against a panel of 60 cancer cell lines derived from lung, colon, skin, kidney, ovary, brain, breast, brain, prostate tumours and leukaemia (NCI 60 cell lines). In the 1980s and 1990s approximately 10,000 natural products per year were tested on the 60 cell lines in triplicate and at five concentrations [31]. From 1985-2007 this screening produced 21 (12 small molecule and nine biologics) potential hits which went into clinical trials [32]. The NCI screening programme was widely perceived as the single most effective mechanism for identifying novel chemotherapeutics and developing them for clinical use, however its cessation has limited new developments [32].

From 1997-2007, pharmaceutical companies focused their research on targeted therapies and therefore there were no new natural product derived chemotherapeutics approved for clinical use during this period [22]. Recently, natural products for cancer therapy have re-emerged with 12 novel natural product derivatives being approved for cancer treatment from 2007-2014 [22]. Marine organisms in particular show great potential for developing novel cancer treatments. Natural products from marine sources have not been widely researched due to limitations in collecting the material which is often present in a hostile environment and at low concentrations within the organism. Natural products could be derived from a range of marine sources such as marine microorganisms, seaweeds, sponges, soft corals, marine invertebrates, marine fungi and cyanobacteria.

Secondary metabolites derived from terrestrial fungi have been intensively studied and these produce a range of compounds such as polyketides, terpenes, steroids and peptides [33]. Fungal derived chemotherapeutics include taxol, camptothecin and fumagillin. Camptothecin is a modified monoterpene indole alkaloid produced by the endophytic fungus *Entrophospora infrequens* and is is a type 1 DNA topoisomerase [34]. Fumagillin is a secondary metabolite of *Aspergillus fumigatus* which acts a an anti-angiogenesis compound thereby stopping the recruitment of new blood vessels starving the tumour of oxygen and nutrients. Fungal metabolites are easy to culture and therefore easy to scale up for large scale manufacturing.

1.2.3.2 Ophiobolins

Ophiobolins are a group of naturally occurring sesterterpene compounds which all possess an unusual tricyclic or tetracyclic skeleton (Fig 1.2A). Historically, much of the research on ophiobolins focused on their effects on plants showing that they reduce seed germination, the growth of roots and the celeoptiles of wheat seedlings [35]. At the cellular level they cause rapid disorganisation of the plant cell membrane resulting in electrolyte and sugar leakage, [36], respiratory changes and inhibition of calmodulin-activated cyclic nucleotide phosphodiesterase [37]. They have been shown to induce a broad spectrum of inhibitory activity against nematodes, fungi and bacteria [38].

Ophiobolin A (OphA) was the first member of the group to be isolated and characterised in the mid 1960s (Fig 1.2A). OphA is a secondary metabolite produced by the pathogenic

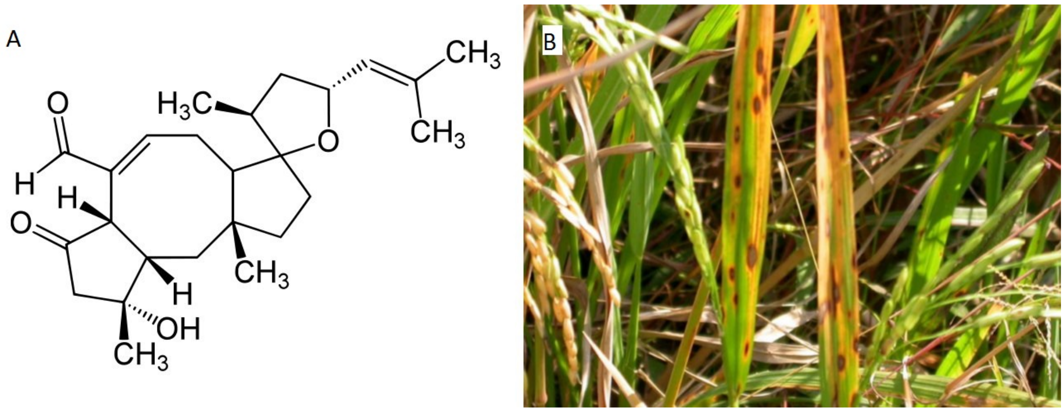

Figure 1.2: Ophiobolins are a fungal metabolites produced by the *Bipolaris* species. A) Chemical structure of Ophiobolin A (OphA) showing the tricyclic skeleton characteristic of the Ophiobolins. B) Photograph of a plant with brown spot disease which is caused by Ophiobolins.

fungi *Bipolaris* species which is known to attack rice, maize and sorghum to produce brown spot lesions (Fig 1.2B) [38]. OphA has been shown to exhibit a broad spectrum of inhibitory activity *in vitro* on various cancer cell lines including A549 (lung cancer), SKMEL28 (melanoma), Hs683 (brain cancer), and OVCAR3 (ovarian cancer) [39, 40]. Half maximal inhibitory concentrations (IC_{50}) were found to vary between 0.28 to 0.62 µM after three days treatment. More recently, OphA has also been shown to induce paraptosis in U373-MG, T98G and GL19 (Glioblastoma multiforme (GBM)) cell lines [41]. Paraptosis is a type of programmed cell death which is morphologically and biochemically distinct from apoptosis [42]. OphA induced cytoplasmic vacuolization and the swelling and fusion of the mitochondria and endoplasmic reticulum (ER) characteristic of paraptosis [41]. Furthermore they showed that OphA could inhibit big conductance Ca^{2+}-activated K^{+} channels (BKCa) which causes an imbalance in the calcium and potassium ion homeostasis. Moreover, OphA has also been shown to be effective at treating MDR cells with the same IC_{50} value as the parent cell line [39].

OphA has also been shown to reduce viability, inhibit motility and reduce the mitochondrial membrane potential of boar spermatozoa [43]. Boar spermatozoa can be used as a model target for monitoring mitochondrial toxins because they are insensitive to substances affecting the synthesis or regulation of proteins and nucleic acids in the cytoplasm [44]. Furthermore, all the signalling pathways known to operate in somatic cells are also found in spermatozoa.

Other ophiobolins which have shown promising results in cancer therapy include Ophiobolin O and 3-anhydro-6-hydroxy-ophiobolin (X15-2). Ophiobolin O has been shown to induce growth inhibition though G_0/G_1 cell cycle arrest in MCF7 (breast) cells [45, 46]. Furthermore, low concentrations (0.1 µM) were shown to down regulate the expression of the drug resistant protein P-Glycoprotein (P-gp) which reversed Adriamycin resistance in the Adriamycin-resistant MCF7/ADR cell line [47]. X15-2 has been shown to induce apoptosis in the K652 cell line with a IC_{50} value of 4.06 µM [17]. Furthermore, X15-2 has been shown to induce autophagic cell death through the degradation of α-synuclein in PC12 cells [48]. This was accompanied by an increase in cellular and mitochondrial ROS and a reduction in mitochondrial membrane potential.

1.3 Embolization therapy

Embolization is a non-surgical, minimally invasive procedure in which blood vessels are selectively occluded by introducing emboli. This technique can be used to treat a number of different conditions such as aneurisms, uterine fibroids, and cancer [49]. It is often used in cancer treatment as a form of palliative care for patients with unresectable tumours. Embolic particles can be introduced in to the blood stream close to the target using a catheter where they lodge in the small vessels which feed the tumour (Fig 1.3). This restricts the blood flow which limits oxygen and nutrient supply to the tumour causing tumour necrosis [50].

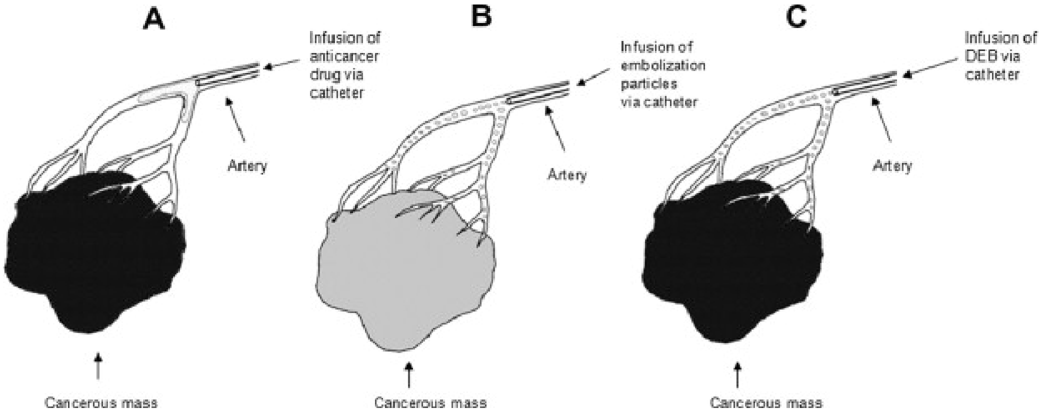

Figure 1.3: Schematic of embolic particles combined with chemotherapy for cancer treatment. (Image taken from [51]). A) Injection of chemotherapy by a catheter to induce cell death at the tumour location with B) the subsequent addition of embolization particles to induce tumour necrosis by blocking blood supply. C) Injection of drug eluting beads (DEB) which combine chemotherapy and embolization therapy into the same particle thus increasing efficacy.

Embolization has been used to treat liver tumours since the late 1970s since the liver has two blood supplies, an arterial source and the portal vein [52]. Blood is often supplied to the noncancerous liver tissue through the portal vein while the cancerous tissue is often supplied by the arterial source [53]. This means the cancerous tissue can be selectively targeted by blocking the arterial source while maintaining blood flow to the liver. Chemotherapy is often administered during the embolization procedure as this delivers the chemotherapy to tumour tissue thereby increasing the local concentration of the drug, prolonging the tumour contact time due to reduced chemotherapy washout and reducing the toxic systemic effects [51].

Several materials have been developed for use in embolization procedures including gelatin sponge, polyvinyl alcohol (PVA) particles, coils, polymeric particles, and degradable starch particles [54, 55]. The usefulness of embolic particles can be increased by combining them with either chemotherapy or a radioactive material to deliver localised radiotherapy. Furthermore, radiopaque embolic particles have been previously prepared using iodine [56, 57] tantalum [58] and barium [59] to provide X-ray contrast of the embolic particle. There are several suppliers of embolic particles for the treatment of hypervascularized tumours in clinical use and these are reviewed in Table 1.1

One of the limitations of embolization therapy is postembolization syndrome (PES) which can cause severe pain and fever [60] . PES is likely to be caused by an inflammatory response of the necrotic tissue after embolization. Patients can be treated with steroids after an embolization procedure to reduce the likelihood of PES [61].

1.3.1 Chemoembolic particles

Combining embolic particles with chemotherapy drugs to create with drug-eluting beads represents a relatively new mechanism of enhancing the delivery of potent anticancer agents to the tumour site. Embolic particles can be loaded with chemotherapy drugs which allows for the controlled and sustained release of the drug while reducing the toxic side effects. Examples of drug eluting beads include DC bead® and HepaSphere^{TM} which have can both be loaded with doxorubicin (Table 1.1).

There have been several clinical trials showing that chemoembolization particles are safe and effective for the treatment of tumours [52]. For example, a trial with 27 patients with hepatocellular carcinoma (HCC) treated with drug eluting beads had a response rate of 75% [66]. Furthermore they showed that the peak plasma concentration of doxorubicin was (78.97 ± 38.3) $\mathrm{ng\,mL^{-1}}$ after release from the drug eluting beads compared to (895.66 ± 653.1) $\mathrm{ng\,mL^{-1}}$ for doxorubicin administered at the same time as blank embolic beads were administered. This indicates that the use of drug eluting beads can reduce off target effects and systemic toxicity.

Table 1.1: Summary of the manufacturers, the size and material of commercially available embolic particles used for embolization procedures. (Y= yes is radioapaque or chemoembolic, N= no is not radioapaque or chemoembolic)

Manufacturer	Name	Size range	Material	Radio-paque	Chemo-embolic	Radio-embolic	Ref
Boston Scientific	Contour® PVA Embolization Particles	45 µm–1180 µm	PVA	N	N	N	[62]
Biocompatabilies	DC Bead®	100 µm–900 µm	PVA	N	Y (doxorubicin	N	[63]
	LC Bead^{TM}	100 µm–700 µm	modified, N-Fil hydrogel	N	N	N	
	DC Bead M1^{TM}	70 µm–150 µm	PVA	N	Y (irinitecan)	N	
	LC Bead M1^{TM}	70 µm–150 µm	modified, N-Fil hydrogel	Y	N	N	
Merit Medical	Embosphere®	40 µm–900 µm	trisacryl cross linked with gelatin	N	N	N	[64]
	EmboGold®	900 µm–1200 µm	trisacryl cross linked with gelatin	Y (2% gold)	N	N	
	HepaSphere^{TM}	120 µm–600 µm	sodium acrylate alcohol copolymer	N	Y (doxorubicin	N	
	QuadraSphere®	600 µm–800 µm	sodium acrylate alcohol copolymer	N	N	N	
SIRTeX	SIR-Spheres	20 µm–60 µm	Polymer resin	N	N	Y (yttrium-90)	[65]

Another trial comparing the effectiveness of doxorubicin-eluting beads and blank embolization particles showed that while the embolization particles induced ischemia resulting in tumour necrosis there was a clear additional benefit from the addition of doxorubicin [67]. The study showed that after six months the original tumour could no longer be measured in 26.8% of the patients treated with the drug eluting beads compared to 14% of patients treated with only the embolic particles. Furthermore, the time to progression was significantly ($p=0.008$) increased to (42.4 ± 9.5) weeks for the patients receiving the drug eluting beads compared to (36.2 ± 9.0) weeks for the patients receiving embolization treatment alone.

1.3.2 Radioactive embolic particles

Radioembolic particles allow radiotherapy to be administered internally by injecting resin or glass microspheres containing a radioisotope such as Yttrium (^{90}Y) into the arterial supply of a tumour [68]. ^{90}Y emits β radiation with a maximum energy of 2.3 MeV (average 0.94 MeV) via a half-life of 64 hours to form the stable Zirconium atom (^{90}Zr) [69]. Radioembolization can deliver radiation doses of up to 150 Gy without the complications observed in traditional external beam radiotherapy [52].

There are two types of commercially available radioembolic particles, TheraSpheres® which are glass microspheres and SIR-Spheres® which are resin microspheres (Table 1.1). These have both been shown to produce a high dose of radiation selectively to human liver tumours but not surrounding healthy tissue [69] due to the low penetration range of β-radiation (mean 2.5 mm and maximum 11 mm) [52, 70]. Additionally, combining radioembolisation with chemotherapy has been shown to have a synergistic effect [68]. Recent research has investigated using phosphorus-32 (^{32}P) because it has a much longer half-life (14.3 days) than ^{90}Y. This means that treatment can be given over a much longer time frame as the microspheres will have decayed less between manufacture and administration and once inserted they will remain radioactive for longer [70, 71].

Similarly to chemoembolization, radioembolization has also been shown to be safe and effective. Sangro *et al.* showed a tumour volume reduction of at least 30% in 19/21 patients treated with ^{90}Y SIR-Spheres® [72].

1.4 Nanoparticles for cancer diagnostics and therapy

Nanoparticles are technically defined as small particles which have at least one dimension in the range of 1 to 100 nm [73] however the prefix "nano"' is commonly used in drug delivery for particles up to several hundred nanometers in size [74]. These sizes are similar to biological molecules and therefore nanoparticles are able to be taken up into the cells through endocytosis. Nanoparticles generally possess dramatically different physical properties compared to bulk particles of the same composition [75]. Due to their small size they have a large surface area and therefore a larger proportion of atoms are on the particle surface leading to changes in surface properties including energy level, electronic structure and reactivity. Furthermore, their physicochemical properties such as their size, shape, structure, morphology and surface properties, can be finely tuned for the appropriate application (Fig 1.4). Nanoparticles show great promise for the diagnosis and treatment of cancer. The following nanoparticles have been studied for their use in cancer therapy: quantum dots (QD), metal oxides, superparamagnetic iron oxides (SPIONs), gold nanopartilces (AuNPs), carbon nanotubes (CNTs) and liposomes.

Nanoparticles can be targeted to tumour cells through passive or active mechanisms

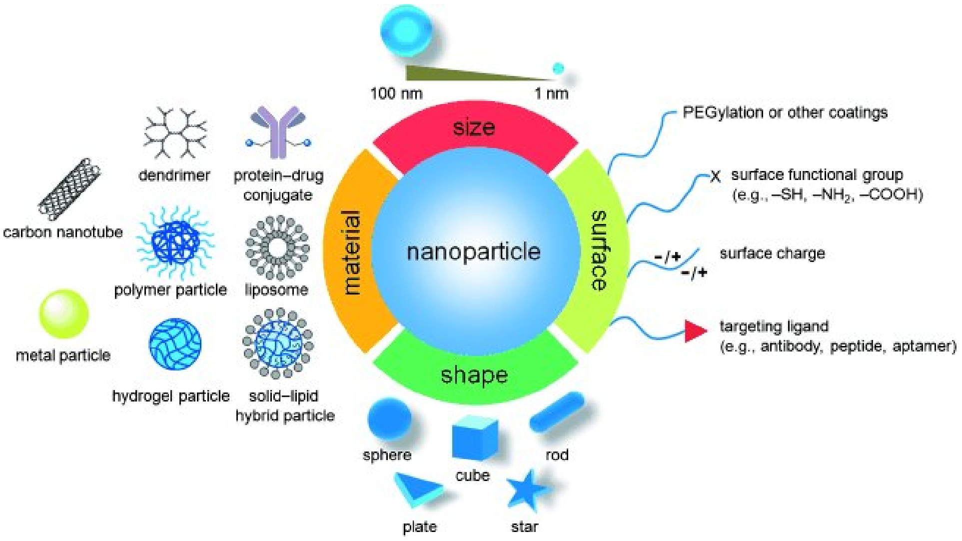

Figure 1.4: Schematic showing the different nanoparticle properties which can be controlled during the production of nanoparticle based drug delivery systems(Image taken from [6]).

and once they are present at the tumour location they are likely to be taken up by the cancerous cells because they are a similar size to biological molecules [76]. Passive targeting of nanoparticles occurs through the enhanced permeability and retention (EPR) effect. The EPR effect allows the preferential uptake and accumulation of molecules of a certain size such as liposomes, nanoparticles, and macromolecular drugs, into tumour tissue compared to normal tissue [77]. Since cancer cells have increased proliferation they must stimulate the production of new blood vessels (angiogenesis). Due to the rapid formation of these blood vessels they are abnormal in form and architecture and therefore they have wide fenestration and lack a smooth muscle [78]. Furthermore, tumour tissue often lacks effective lymphatic drainage. These two mechanisms cause an increase in drug concentration of 10-100 fold in the tumour from drug loaded particles compared to free drug administration[79]. In the 1980s the first passively targeted nanocarriers reached clinical trials while in the mid 1990s the first products based on lipsosomes and polymer-protein conjugates were approved for clinical use [80].

Active targeting involves the use of ligands conjugated onto the surface of nanoparticles which specifically increase the retention and uptake of the nanoparticles at the tumour location [81]. Ligands are selected to bind to the molecules or proteins overexpressed on the surface of the cancerous cells. Typical ligands include antibodies, proteins, aptamers, saccharides and small molecules such as vitamins (Fig 1.5) [81]. Nanoparticles tend to circulate within the body for longer than small drug molecules when administered intravenously (IV) provided that they are large enough not to be excreted by the kidneys or too large to be trapped by the reticuloendothelial system (RES) [82]. The most common method of reducing RES uptake is PEGylation which creates a hydrated barrier which stops the attachment of phagocytes by steric hindrance and increases the nanoparticle circulation time [83].

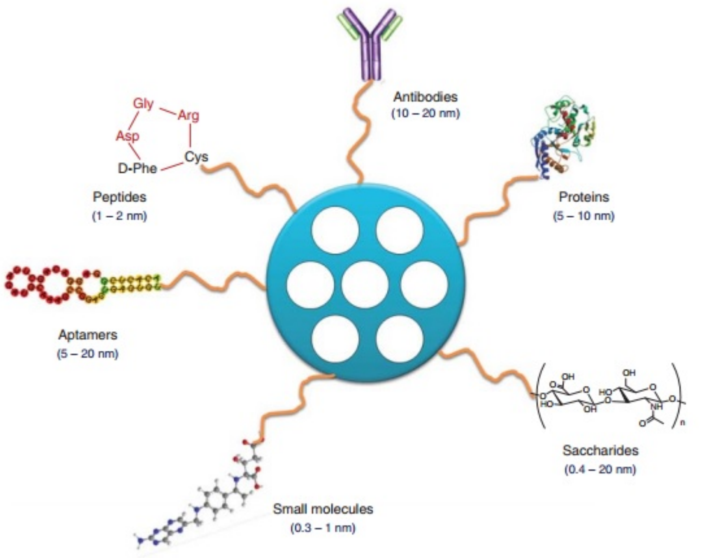

Figure 1.5: Schematic of the types of different types of molecules which can be used to actively target nanoparticles to tumour cells. [Image taken from [81]]

1.4.1 Nanoparticles as X-ray contrast agents

Nanoparticles have been developed for use as tracers or contrast agents for a wide variety of medical imaging modalities such as CT, MRI, and ultrsound imaging. The most common nanoparticles used for MRI contrast enhancement are superparamagnetic iron oxide (SPIO) nanoparticles [84] while microbubbles are often used as ultrasound contrast agents [85]. Combining magnetic nanoparticles with microbubbles creates dual modality MRI and ultrasound contrast agents [86].

Nanoparticles were first proposed for use as an X-ray contrast agent in the 1980s but due to their non-tolerable side effects they did not become commercially successful [87]. However in the last five years there has been a rapid growth in research into nanoparticle based contrast agents. Nanoparticles are able to provide excellent contrast compared to single molecule based contrast agents [88]. The most commonly studied nanomaterials for X-ray contrast are gold (Au) and bismuth (III) sulfide (Bi_2S_3) [89]. The cost of gold as an X-ray contrast agent limits its clinical uptake while the intrinsic toxicity of Bi_2S_3 limits its use [90]. Other elements have also been studied for there use as contrast agents such as iodine, bromine, tantalum, platinum, ytterbium, yttrium, gadolinium and tungsten [87]. Tantalum was selected for use as an X-ray contrast agent in this thesis due to good radiopacity and biocompatibility [91].

1.4.2 Nanoparticles for radiotherapy

There is growing interest in using nanoparticles as radiosensitisers which are inert except in the presence of radiation therapy. The most common nanoparticle based radiosensitiser are gold (Au) nanoparticles however gadolinium, TiO_2, silver, hafnium oxide, quantum dots, superparamagnetic iron oxide nanoparticles have also been studied [9].

Hainfeld *et al.* [92] were the first to show the effectiveness of gold nanoparticles as a radiosensitiser. They found that mice treated in combination with gold nanoparticles and radiotherapy had an increased survival compared to mice treated with radiotherapy alone. Zheng *et al.* [93] showed the ability of gold nanoparticles to induce DNA damage in plasmid DNA. Gold nanoparticles induced an approximately 2.5 fold increase in the number of single and double stranded DNA breaks after radiation treatment with 60 keV X-rays compared to radiation treatment alone. Brun *et al.* [94] showed that larger nanoparticles (92 nm), high molar concentration and X-ray radiation using 50 keV provided the best dose enhancement of the gold nanoparticle samples tested. *In vitro* studies carried out by Joh *et al.* [95] with gold nanoparticles and ionizing radiation showed DNA damage and a reduced colongenic survival in brain cancer cells. Subsequent *in vivo* studies with the same gold nanoparticles and ionizing radiation showed an increase survival time for mice with brain tumours [95]. Bobyk *et al.* [96] observed similar results to Joh *et al.* for brain cancer cells *in vitro* and rats with brain tumours *in vivo*. Hafnium oxide nanoparticles have been shown to be taken up by cells *in vitro* through endocytosis and then when combined with radiotherapy cause a reduction in the number of cells remaining after a clonogenic assay compared to the control cells [97]. *In vivo* the hafnium nanoparticles caused a reduction in tumour volume and increased the survival time of the mice after treatment with radiotherapy compared to radiotherapy alone.

TiO_2 nanoparticles have also been studied as potential radiosensitiser. Titanate nanotubes have been shown to induce cell death in the presence of X-rays [98]. TiO_2 nanoparticles have been shown to reduce cell survival in MCF7 and MKN-45 cell lines in the presence of ^{60}Co γ-rays [99]. Furthermore, TiO_2 nanoparticles have been doped with rare earth elements to increase their effectiveness both *in vitro* and *in vivo* [100, 101].

These nanoparticles will be discussed in detail in chapter 5.

1.4.3 Nanoparticles for drug delivery

Nanoparticles have been loaded with a range of chemotherapy drugs such as Taxol, doxorubicin and vinblastine because they offer so many advantages compared to current systemic treatment. They can be loaded with a high concentration of chemotherapy drug due to their large surface area which through nanoparticle targeting can be delivered directly at the tumour location thereby reducing the toxic side effects [102]. Moreover the drugs can be released in a controlled manner or on demand using sophisticated, stimuli-responsive systems [29]. Furthermore, chemotherapy drugs which are poorly soluble in water can be delivered therefore increasing the potential of currently unused hydrophobic drugs. The nanoparticles can protect the drug from degradation in the harsh environments found in the body such as the highly acidic stomach or the cell lysosomes and by enzymes in the blood stream [103]. This increases the plasma half life of the drug and therefore more effective treatment can be provided. Finally nanoparticles can be used for the co-delivery of multiple types of drugs allowing for combination therapy or they can be combined with diagnostic agents such as contrast agents for real time readout of treatment efficacy [103].

1.5 Aims and Objectives

The aim of the work presented in this thesis was to develop novel embolic particles for use in cancer therapy using a combination of nanoparticles and polystyrene microparticles. A general methods chapter is provided in chapter 2. The aim of the work presented in chapter 3 was to optimise the synthesis of polystyrene microparticles to ensure that the correct size and distribution of microparticles was produced for effective occlusion of the the tumour vasculature. Chapter 4 outlines work to determine if the radioopaque embolic particles could be synthesised by doping with tantalum oxide. The aim of work presented in chapter 5 was to determine if a radiosensitizing embolic particle could be developed. This work investigated possible synthesis methods to combine the polystyrene microparticles and rare earth doped TiO_2 nanoparticles to create core shell particles which have previously been shown to produce reactive oxygen species upon X-ray irrdation. Chapter 6's work aimed to produce embolic particles which had a high capacity for drug loading using silicon dioxide (SiO_2 nanoparticles. The aim of the final chapter, chapter 7, was to investigate the types of cell death induced by a novel natural product with promising anticancer activity, Ophiobolin A.

Chapter 2

General methods

Several methods are used in multiple chapters of this thesis and therefore they have been outlined here with specific details provided later in the text. Methods which are only relevant to one chapter have been included within the appropriate chapter. A table providing all the materials used within this thesis, the supplier and a justification for using them is provided in appendix A.

2.1 Particle characterization

The nanoparticles and microparticles were characterised using a range of techniques as outlined below.

2.1.1 Electron microscopy

Electron microscopy allows particles in the micro and nanoscale to be imaged using an electron beam due to the small de Broglie wavelength of electrons. Two types of electron microscopy were used in this work, transmission electron microscopy (TEM) and scanning electron microscopy (SEM). In TEM, images are formed by the electron beam interacting with the specimen as it passes through the ultra-thin specimen. In

SEM, an tightly focused beam of electrons scans across the sample. The interaction of the beam with the sample produces signals which reflect the sample's surface topography and composition.

2.1.2 Transmission electron microscopy

The morphology and crystal structure (through observation of high-resolution lattice fringe data) of the TiO_2, SiO_2 or tantalum nanoparticles were characterised by transmission electron microscopy (TEM). A JEOL JEM-2010 TEM equipped with a LaB_6 thermionic electron gun and operating at a primary beam energy of 200 keV was used. TEM specimens were prepared by resuspending nanoparticles in absolute ethanol, sonicating and drop-casting onto holey carbon coated copper TEM grids (Agar Scientific).

2.1.3 Scanning electron microscopy

Scanning electron microscopy (SEM) was used to characterise the nanoparticles and the microparticles using a JEOL JSM-840F SEM and a JEOL JSM-840A SEM. The 840F SEM was operated at a primary beam energy of 3-5 keV and images were collected in the secondary electron (SE) imaging mode which investigates the surface topography. The 840F preformed well for high resolution images. The 840A SEM was operated at a primary beam energy of 10 keV and images were collected in both the secondary imaging mode and the backscattered electron imaging mode which investigates the materials composition. SEM specimens were prepared by dusting onto a carbon taped SEM stub (Agar Scientific) and then coating with a 3 nm layer of platinum. The platinum layer adds a conductive layer which reduces charging during operation.

2.1.4 Energy Dispersive X-ray Spectroscopy

The elemental composition of the nano and microparticles was determined by Energy Dispersive X-ray Spectroscopy (EDX). Both the JEOL-2010 and the 840A were equipped with an Oxford Instruments INCA X-ray analysis system for carrying out energy dispersive x-ray spectroscopy. By analysing the characteristic X-rays produced by the interaction of the primary electron beam with the sample, elements (>1 % by weight) present in the sample were determined.

2.1.5 Disc centrifuge

The hydrodynamic diameter of the nanoparticles was measured using a CPS disc centrifuge (DC 18000; CPS instruments Europe).The machine was operated at 24,000 rpm and sucrose density gradient ranging from 8% to 24% (w/v) was built up by injecting decreasing concentrations of sucrose into the centrifuge. This density gradient stabilizes the particle sedimentation within the centrifuge. The highest density layer must be lower magnitude than the density of the particles in the sample or the particles will not arrive at the detector. Samples (100 µl) were inserted into the centre of the disc and the time taken to reach the outside of the disc measured. The size distribution can then be calculated based on the density of the particles (assumed to be the bulk tabulated density) and the rotation speed. Samples were prepared by resuspending the nanoparticles in double distilled water (ddH$_2$O), sonicating with an ultrasonic probe (Sonic Vibra-Cell) for 5 minutes (104 W (80 %) 5 seconds on/5 seconds off) and filtering with a 0.2 µm filter (33 mm cellulose acetate syringe filter, Anachem) . Samples were calibrated against particles of a known diameter (Polyvinyl chloride, 0.377 µm, CPS Instruments Europe).

2.1.6 Zeta sizer

Zeta (ζ) potential, also known as electrokinetic potential, is a measure of the electric charge on the nanoparticle surface and quantifies the stability of a colloidal suspension (Fig 2.1). The magnitude of the zeta potential provides information on the nanoparticles stability since particles with a higher magnitude potential have increased electrostatic repulsion and therefore increased stability. The zeta potential of the nanoparticles was measured using a Malvern Zetasizer Nano. Samples were prepared at a concentration of 0.2 to 0.3 $\mathrm{mg\,ml^{-1}}$ in tris (hydroxymethyl) aminomethane (Tris) (0.001 mM) buffered to a range of pHs using HCL (Sigma) and NaOH (Sigma).

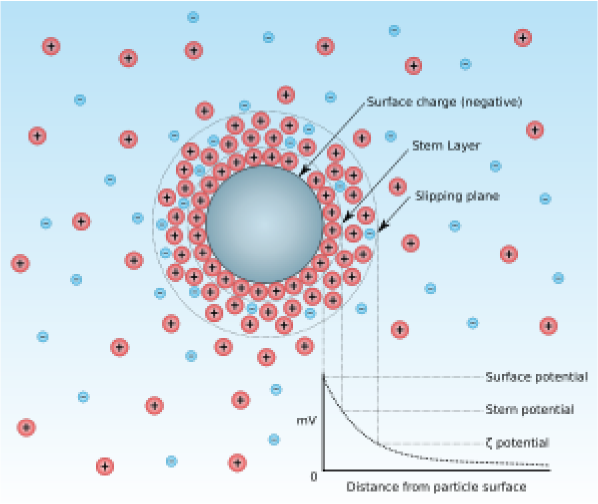

Figure 2.1: The zeta potential is used to quantify the charge on a particle. (Image taken from [104]) It originates from a net electrical charge on the nanoparticle contained within the region bound by the slipping plane. The surface charge on a nanoparticle is screened by ions of the opposing charge near the particle surface. The zeta potential is a measure of the difference in potential between the bulk fluid that the particle is dispersed in and the layer of fluid containing the oppositely charged ions that is associated with the nanoparticle surface.

2.1.7 X-ray diffraction

The crystal structure of the TiO_2 and TaOx nanoparticles was obtained by X-ray diffraction (XRD) using a fully automated Siemens D5000 powder diffractometer employing copper Kα radiation (λ=0.154 06 nm) and a secondary monochromator. The sample was supported on a single crystal of silicon and continuously spun during data collection. The sample was scanned using a step size of 0.05°2Θ, between the range of 10°-90°2Θ, and a count time of 12 seconds per step (where Θ is the angle between the incident rays and the sample). The crystal phases were determined by comparing the diffraction pattern obtained with standard data from the International Centre of Diffraction Data (ICDD).

2.2 Ophiobolin A

Ophiobolin A (OphA) was prepared by Prof Antonio Evidente lab (Department of Chemical Sciences, University of Naples Federico II, Italy) and obtained as white crystals from *Drechslera gigantea* culture filtrates according the procedure previously reported [36]. The purity of OphA was determined by RP-HPLC-UV to be $\geq$95 %. Stock OphA solutions were prepared by dissolving OphA in ethanol (Aldrich) at a concentration of 2500 µM and further dilutions were carried out in phosphate buffered saline (PBS; Aldrich). PBS was used as a no drug control for all samples.

2.3 Cell culture

Eight human tumour cell lines (RD, RH30, MCF7, MDA-MBA-231, HeLa, KB-31, U-87 MG and U2OS) and one control cell line (Fibroblasts) were used to investigate the effectiveness of the nanoparticles, their toxicity and the cell death induced by Ophiobolin A. Information regarding the cell line, its American Type Tissue Culture (ATCC) number, the tissue they originate from and the type of cancer they originate from can be found in Table 2.1. Additionally, RD cells expressing green fluorescent protein (GFP) were prepared by Miss Xinyue Huang (Department of Engineering Science, University of

Oxford) using a lentiviral vector to transfect RD cells with GFP following the modified method presented by Kafri *et al.* [105] for use in some of the flow cytometry experiments. The vinblastine resistant KB-VI cells [106] which are a derivative of the parental KB-31 cell line were used to test the effectiveness of OphA on a drug resistant cell line. One healthy control cell line derived from human fibroblasts was a gift from Mrs Tiffany Lodge (Nuffield Department of Obstetrics and Gynaecology, Oxford University).

Cells were grown in Dulbecco's Modified Eagle's Medium -high glucose (DMEM; Aldrich) supplemented with 10% Fetal calf serum (FCS;Aldrich), 2 mM L-Glutamine (Aldrich), 100 U/ml Penicillin (Aldrich) and $0.1\,\mathrm{mg\,ml^{-1}}$ Streptomycin (Aldrich). Cells were incubated at 37 °C in a 5% CO_2 atmosphere and passaged when confluent (approximately every four days).

Table 2.1: Summary of the cell lines used in this study indicating the tissue and disease of origin. (*American Type Tissue Culture Collection).

Cell line	ATCC* number	Tissue	Disease
RD	CCL-136	muscle	embryonal rhabdomysarcoma
RH30	CRL-7763	muscle	alveolar rhabdomysarcoma
MDA-MB-231	HTB-26	breast	adenocarcinoma
MCF7	HTB-22	breast	adenocarcinoma
HeLa	CCL-2	cervix	adenocarcinoma
KB-31	CCL-17	HeLa contaminant	carcinoma, papilloma
Fibroblast		connective	control cells
U2OS	HTB-96	bone	osteosarcoma
U-87 MG	HTB-14	brain	glioblastoma

2.3.1 Mycoplasma testing

Cells were tested for mycoplasma using the MycoAlert^{TM} mycoplasma detection kit (Lonza, UK) as per the manufacturers instructions. In brief, media supernatant from the cells prior to trypsinisation was collected and centrifuged at 1500 rpm for 5 minutes to remove any remaining cells. Cleared supernatant (100 µl) was then placed in an 1.5 ml micro-centrifuge tube and 100 µl of MycoAlert^{TM} reagent was added to lyse any viable mycoplasma. After 5 minutes the sample was measured in a luminometer with a 4 second integration time to give Reading A. Then a luciferin MycoAlert^{TM} substrate (100 mL which produces light in the presence of ATP. After 10 minutes a second reading (Reading B) was measured using the luminometer and the ratio of Reading B/Reading A was calculated. A ratio of Reading B to Reading A of ≤ 0.9 shows cells which are negative for mycoplasma, between 0.9-1.2 indicates cells which are borderline for mycoplasma and ≥ 1.2 indicate cells which are contaminated with mycoplasma.

2.3.2 Cell viability assays

There are many different methods for assessing cell viability and proliferation including cell counting and colorimetric techniques. Manual cell counting removes the need for external dyes however it is time consuming to perform and has large sample variation. Colorimetric techniques allow a rapid screening method to be carried out using a plate reader based assay and by flow cytometry. Many dyes exist including, MTT, reaszurin, crystal violet and BrdU however they often interact with nanoparticles and therefore can provide misleading results. For example, the MTT (3-(4,5-dimethyl-2-thiazol)-2,5-diphenyl-2H-tetrazolium bromide) assay works by the conversion of MTT to an insoluble purple formazan product by mitochondrial enzymes [107]. There was a major problem with using these colorimetric dyes for testing the viability of cells after nanoparticle treatment because the nanoparticles were often also dyed by the colorimetric dye. For example, SiO_2 nanoparticles were dyed with crystal violet in a concentration dependent manner which could lead to misleading results (Fig 2.2). Additionally, reactive oxygen species produced by nanoparticles have been shown to convert MTT to the purple formazan product thus overestimating viability. Therefore either manual cell counting or flow cytometry was used to assess the cell death after nanoparticle treatment to remove any misleading results.

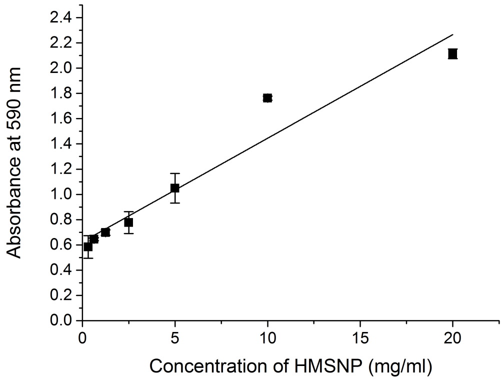

Figure 2.2: Ability of crystal violet to dye nanoparticles and therefore provide misleading results. SiO_2 nanoparticles were stained with crystal violet for one hour, washed and then resuspended in ddH_2O and the absorbance was measured in a method similar to that described in section 2.3.2.1 for staining cells with crystal violet. Data is presented as mean ± SD of triplicate samples and a linear fit has been applied to the data (R^2=0.97)

2.3.2.1 Crystal violet assay

The crystal violet assay was used to asses the cell viability of the cells after treatment with microparticles or Ophiobolin A. Cells were seeded in 96 well plates at 1x10^4 cells per well in 150 µl growth media and left overnight in the incubator for the cells to adhere. after the appropriate treatment was applied, the media on the cells was removed and the cells were washed in PBS twice. Cells were fixed in 100 µl of 1% (v/v) glutaraldehyde (aq; Sigma Aldrich) for 30 minutes and stained with 100 µl of 0.5% (w/v) crystal violet solution (aq; Sigma Aldrich) for at least one hour. Crystal violet stains the nucleus of the cell and therefore can be used to determine the number of cells. The plate was washed with water, dried overnight and cells were solubilised using 150 µl of solubilising solution (1% (w/v) sodium dodecyl sulphate (SDS; Fisher Scientific) and 10% (v/v) acetic acid (Sigma Aldrich)). The absorbance of the solution was measured at 590 nm using a Tecan Infinite f200 plate reader. Samples were blank corrected and expressed as a percentage of the control cells viability. Experiments were performed in at least triplicate and repeated on three separate occasions.

2.3.2.2 Manual cell proliferation assay

Cell proliferation was determined by manual counting of the cells using a hemocytometer. After the appropriate treatment was applied the growth media was removed and the cells were washed with PBS twice. Adherent cells were removed from the plate using 30 µl of Tryspsin-EDTA. Both the adherent cells and the cells removed in the growth media were counted separately. Trypan blue was initially used to stain the dead cells from the adherent cells however this was deemed unnecessary as the majority of cells were viable. Experiments were performed in at least triplicate and repeated on three separate occasions.

2.3.3 Flow cytometer

Flow cytometry can be used to measure the physical and chemical properties of cells which are fluorescently labelled with a range of dyes. Thousands of particles per second can be analysed by the flow cytometer as they pass a laser in single file. Two flow cytometers were used in this work due to availability of the equipment. The work presented in chapter 6 was carried out using an Accuri C6 Flow Cytometer (BD) while the work presented in chapter 7 was carried out FACS Calibur flow cytometer (BD). Both cytometers have a blue 488 nm and a red diode 635 nm laser and filters for forward scatter and side scatter, and green, orange, red and far red fluorescence.

2.3.3.1 Sample preparation

For all flow cytometry experiments, cells were seeded in either 12 or 24 well plates at 15x10^4 or 8x10^4 cells per well, respectively, in growth media and left overnight in the incubator for the cells to adhere. Cells were treated with OphA (See later in the text for the different treatments applied) and samples were prepared by collecting the supernatant containing the non-adherent cells while the adherent cells were washed and trypsinized (Trypsin-EDTA; Aldrich) and then combined with the first supernatant. For unfixed cell analysis the combined cells were then centrifuged and washed in the appropriate buffer twice before resuspended in 50 µl buffer. PBS was used as the buffer for every sample except those dyed with Annexin V where Binding buffer (BioLegend) was used. For fixed cell analysis cell the combined cells were then centrifuged and washed in the appropriate buffer twice before being resuspended in 1 ml of 70% methanol (Fisher) under gentle vortexing. Fixed cells were stored at 4 °C until the day of analysis where they were were washed in cold PBS twice , suspended in 200 µl PBS and incubated at 37 °C with 50 µg ml^{-1} RNase for one hour.

Cells were stained with dyes of interest (See later in the text for dyes used and the appropriate incubation times). Subsequently, 200 µl of buffer was added to the cells and then at least 10,000 cells from the samples were analysed using the flow cytometers described above. Flowing Software version 2 (www.flowingsoftware.com) was used to visualize the cell data and the debris was excluded from further analysis by gating the area containing the cells (Fig 2.3). Subsequently the florescence intensity of the dyes of interest were determined. Experiments were performed in triplicate and repeated on at least two separate occasions.

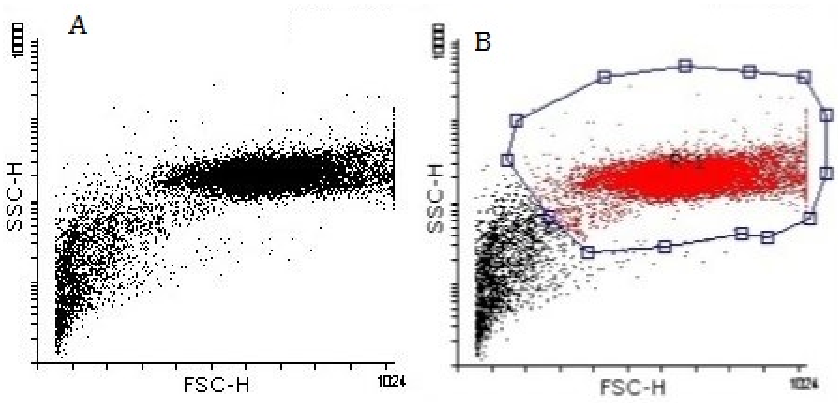

Figure 2.3: Representative flow cytometry data indicating the gating of the cells for further analysis. The cells are in region 1 in red while the debris is black (FSC= forward scatter and is related to cell size, SSC= side scatter and is related to cell integrity.)

2.3.4 Statistical analysis

The data is presented as mean ± standard deviation (SD) of triplicate samples throughout the text unless specified in the figure legend. Statistical analysis was performed by a one or two tailed students t-test in excel as appropriate. $p \leq 0.05$ was taken as the criteria for statistical significance.

Chapter 3

Polystyrene Embolic Particles

3.1 INTRODUCTION

Embolization is a non-surgical, minimally invasive procedure in which blood vessels are selectively occluded by introducing emboli. This technique can be used to treat a number of different conditions such as aneurisms, uterine fibroids, and cancer [49]. In cancer treatments, embolic particles can be introduced into the blood stream close to the target and lodge in the small vessels which feed the tumour thus restricting blood flow. As such, oxygen and nutrient supplies to the tumour are reduced which causes tumour necrosis [50]. This thesis focuses on the development of novel multimodal embolic particles for cancer therapy which have a polystyrene microparticle at its core.

3.1.1 Current embolic agents

There are many different types of embolic agent currently used in clinical practice such as microparticles, coils and liquid agents. Balloons were historically used for embolization procedures but these have been taken off the market due to the high risk of movement within the body after administration [108]. The choice of embolic agent depends on its desired clinical outcome, its material properties and if temporary or permanent occlusion is required.

3.1.1.1 Gelatin foam

Gelatin foam is made from purified skin gelatin and has been used as an embolic agent for more than 30 years [54]. It is available as either thin sheets or as 40 µm to 60 µm powdered microparticles [54]. Gelatin foam microparticles swell on hydration into larger particles to provide temporary vessel occlusion which is not ideal for cancer treatment. Gelatin foam is cheap and has clinical precedent for embolization treatment however the particles often aggregate within the body trapping air bubbles within the vasculature system and inducing infection.

3.1.1.2 Polyvinyl alcohol particles

Polyvinyl alcohol (PVA) particles have also been used as embolic agents for more than 30 years [54]. The particles are made from PVA foam sheets which are vacuum dried, rasped and then sieved into different size bands. The prepared particles are irregular in shape and present as oblong, oval, sharp and angulated particle fragments. This promotes particle aggregation and therefore they tend to occlude vessels which larger than their specified diameter and which are further from the tumour [109]. PVA particles provide a permanent occlusion which is ideal for tumours, they are biocompatible and have clinical precedent. The major disadvantage of using PVA particles for embolization treatment is their tendency to aggregate which can cause occlusion of vessels which are more proximal to the tumour and cause blockage of the catheter during the administration procedure [110].

3.1.1.3 Tris-acryl getalin microspheres

Tris-acry gelatin microspheres (TAGM) have been used as embolic agents since 2000 and are made from an acrylic polymer matrix which is embedded with porcine gelatin. Unlike

PVA particles, TAGM microparticles are precisely calibrated, smooth and spherical particles [108]. They do not have the problems associated with aggregation that occurs in PVA particles and therefore tend to penetrate smaller vessels than PVA particles. Furthermore, they rarely cause catheter blockage [111]. The main disadvantage of TAGM microparticles is that they are likely to sediment and therefore require frequent agitation to maintain the suspension.

3.1.1.4 Coils

Coils are permanent embolic agents which come in a variety of shapes and sizes and are usually made of steel or platinum [54]. They are often used for the occlusion of larger vessels by inducing thrombosis on the surface of the coil. Therefore the effectiveness of the treatment is dependant on the patients ability to form clots [55]. Complications arising from coils include the occlusion of non-target vessels, coil migration resulting in pulmonary embolization, stroke or myocardial infarction and vessel dissection, perforation or rupture [54].

3.1.1.5 Liquid embolic agents

Liquid embolic agents are made from cyanoacrylates (glue) which rapidly polymerize once exposed to an ionic environment such as saline or blood forming a blockage inside the vessel [108]. The polymerization reaction often induces an inflammatory reaction within the occluded vessel. The major disadvantage of liquid embolic agents is that expert knowledge of the vascular anatomy is needed to prevent embolization of non-target vessels.

3.1.2 Polystyrene microparticles

Polystyrene microparticles were selected for the core of the embolic particle because they are non-biodegradable and therefore able to provide a permanent occlusion of the blood vessels. The polystyrene particles were synthesised by suspension co-polymerization which is a technique that is relatively simple to perform and therefore easy to manufacture. Suspension polymerisation produces particles which are between 40 µm–1000 µm [112] which are ideal for embolization particles. Furthermore, it produces high yields of microparticles and therefore has the potential for producing embolic particles at a commercial scale.

Polystyrene particles have previously been shown to be non-toxic in both *in vitro* and *in vivo* studies. They are often used as a negative control for comparing the toxicity of other elastometers [113] demonstrating that they are non toxic.

3.2 Efficacy testing of embolic particles

The effectiveness of the embolic particles would ideally be tested using an animal model; however, as this was not possible, alternative methods were sought for initial proof of concept studies. Embolic particles have been used for the treatment of tumours since the 1970s [52] which demonstrates the concept is possible. Moreover, in line with the Three Rs (3Rs), the use of animals in scientific research should be limited.

The 3Rs, replacement, reduction and refinement, were first proposed in 1959 by Russell and Burch [114] as the guiding principles for the more ethical use of animals in scientific testing. Replacement involves the use of non-animal methods such as tissue culture, perfused organs tissue slices, cellular and/or subcellular fractions rather than animal methods whenever possible to test new scientific ideas [115]. Reduction minimises the number of animals required to provide sufficient scientific information on the tested system or by using the same number of animals but gaining increased information about the tested system. Refinement involves using methods which alleviate or minimize the potential pain, suffering and/or distress to the animals used in the study. Therefore alternative methods were sought for testing in this work.

3.2.1 Aims and Objectives

The aim of the work presented in this chapter was to synthesise and characterise the polystyrene particles which form the core of the multimodal embolic particles. A literature study was carried out to determine the size of vasculature surrounding tumours and therefore determine the optimum diameter of embolization particles required for effective occlusion. Furthermore, effective occlusion with the polystyrene particles was investigated using a synthetic microvessel and by the modification of a perfusion cell culture kit to match the size of tumour vasculature found in the literature.

3.3 MATERIALS AND METHODS

3.3.1 Polystyrene microparticles

The polystyrene microparticles were prepared by the method presented by Ihara *et al.* [116, 117]. Firstly, 2.5 ml of styrene (Aldrich), 2.5 ml of ethylene glycol dimethacrylate EGDMA (Aldrich) and 2.5 mg of azobisisobutyronitrile (AIBN; Aldrich) were mixed to create an oil phase. The oil phase was added to the 30 ml of an aqueous phase containing 4 wt % poly (vinyl alcohol) (PVA) (87–90% hydrolyzed, average molecular weight (30.000–70.000 Aldrich) in a round-bottomed flask. The mixture was stirred for one hour at room temperature and then left to stand for 24 hours at 60 °C. The stirring speed affected the resultant distribution of particle sizes. The particles were collected by centrifugation, washed twice in ddH_2O, then re-suspended in 30 ml ddH_2O and refluxed overnight to remove any remaining PVA. The particles were finally collected by centrifugation, washed twice with methanol (Rathburn) and dried under vacuum. A reaction scheme is provided in Fig 3.1.

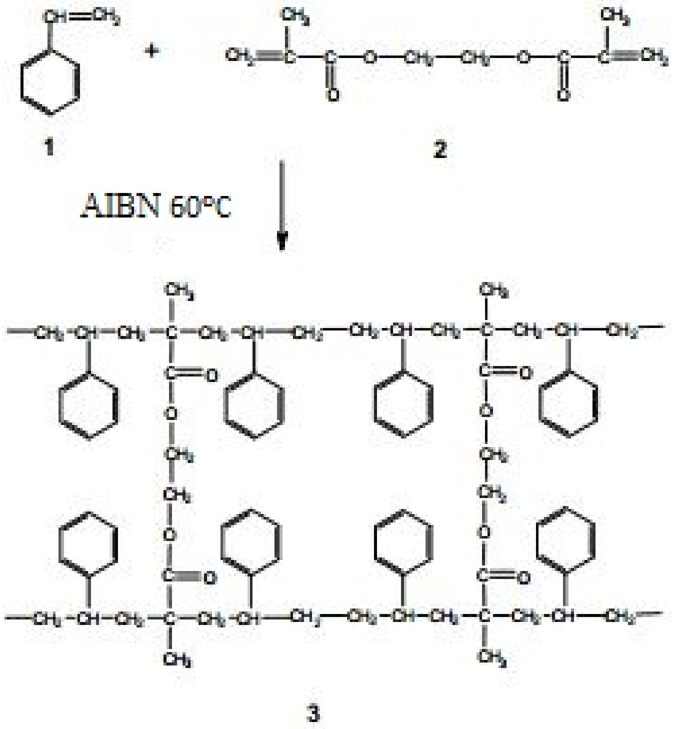

Figure 3.1: Reaction scheme for the synthesis of polystyrene cross-linked with ethylene glycol dimethacrylate. (1-styrene, 2-EGDMA, 3-polystyrene cross-linked with EDGMA.) Reaction scheme adapted from Ajikumar *et al.* [118] .

3.3.2 Fluorescent dyed polystyrene embolic particles

The polystyrene particles were dyed with Rhodamine B and fluorescein isothiocyanate (FITC) to create red and green fluorescent particles. Polystyrene microparticles (50 mg) were resuspended in a mixture of 2.5 ml dichloromethane (Aldrich), 2.5 ml of isopropanol and 25 mg of tween 80 (Aldrich). Subsequently either 2.5 mg of Rhodamine B (Aldrich), or 2.5 mg of FITC (Aldrich), was added and the mixture was stirred in the dark at 500 rpm for three days. The dyed polystyrene microparticles were collected by centrifugation and washed in isopropanol (Fisher) until the supernatant was colourless. The particles were imaged with a Motic AE31 microscope equipped with a mercury lamp and filters for TRIC (Ex. 547 nm, Em. 572 nm) and FITC (Ex. 495 nm, Em. 519 nm).

3.3.3 Particle characterization

The size and surface morphology of the polystyrene particles was investigated by SEM, as described in section 2.1.3, and by bright field microscopy using a Motic AE31 microscope. The diameter of the particles was assessed ($n \geq 200$) using the Motic AE31 microscope software. The change in zeta potential with pH of the polystyrene particles was determined using a Malvern Zetasizer as described in section 2.1.6.

3.3.4 Cell viability assay

Cell viability of the RD cell line after $0.04\,\mathrm{mg\,ml^{-1}}$ to $10\,\mathrm{mg\,ml^{-1}}$ PS treatment was assessed by crystal violet staining as described in section 2.3.2.1. Experiments were performed in triplicate and repeated three times.

3.3.5 Microvessel models

Linear and branched synthetic microvessel models were custom made by SynDaver^{TM} Labs (USA) for use in this project. SynDaver^{TM} Labs have developed synthetic arteries and veins which are designed to ensure that their material properties, such as tensile modulus, abrasion resistance, penetration force, coefficient of friction, thermal conductivity and dielectric constant, are similar to human tissue [119].

The custom made linear microvessels were specified to have internal diameters of 100 µm and 200 µm and the custom made branched microvessel was specified to have branches with the following internal diameters 100 µm, 200 µm and 500 µm (Fig 3.2). Attempts were made at blocking the microvessel with the PS particles by injecting the polystyrene particles into the microvessels using a Hamilton syringe.

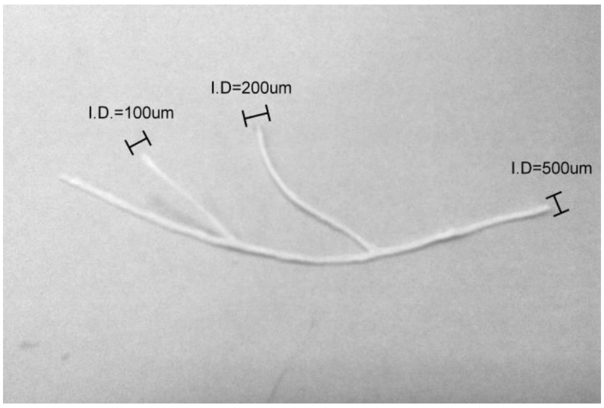

Figure 3.2: Syndaver^{TM} Labs microvessel models. Photograph of a branched microvessel with specified branches of 100 µm, 200 µm and 500 µm internal diameter.

3.4 RESULTS AND DISCUSSION

3.4.1 Literature review of the diameter of tumour vasculature

Before polystyrene microparticle synthesis was carried out, a review of the literature was performed to ensure that the embolic particles were designed for the most effective occlusion of tumour blood vessels (Table 3.1). In normal tissue, vasculature is very organised and has a regular branching network beginning with arteries, continuing down to arterioles and ending with capillaries. In contrast tumour vasculature is disorganized due to rapid angiogenesis and therefore lacks the conventional hierarchy of blood vessels [120]. Tumour vessels are also often dilated and contain bidirectional shunts [82]. Data mining of a large number of studies in the literature showed that vessel diameter ranges from 1 µm–225 µm depending on the tumour type and the species of origin (Table 3.1). In all the reports which discussed size distribution, most of the vasculature was smaller than 50 µm with only a few vessels larger than 50 µm (Table 3.1).

Historically, most of the embolic particles developed have been large ($\geq$ 100 µm up to 1 mm) however recent research has suggested that using smaller microspheres (1 µm–225 µm) could provide better treatment outcomes as the particles are able to penetrate to more distal locations within the tumour thus providing more homogeneous blocking [121]. This is supported by data from the literature review; there are only very few large vessels that would become blocked by large particles and those are the vessels furthest from the tumour.

3.4.2 Design and synthesis of polystyrene microparticles

In order to achieve good embolization along the tumour vasculature tree, embolic agents were prepared as polydispersed polystyrene spheres (PS) ranging from 10 µm–250 µm (Fig 3.3A). The polystyrene particles were synthesised by suspension co-polymerization using a free radical initiator as described by Ihara *et al.* [116, 117]. An oil phase was created by mixing styrene monomers with a cross linker ethylene glycol (EDGMA). The monomer solution was then mixed with aqueous polyvinyl alcohol (PVA) which acts as a stabilizer for the monomer mixture [116, 117]. The resultant oil-in-water (O/W) suspension was subsequently heated to induce activation of the initiator ABIN which starts the radical polymerisation reaction [112]. Based on the reactivity ratios for styrene and ethylene glycol dimethacrylate [132], the copolymer is calculated to contain 55% styrene monomers and 45% ethylene glycol dimethacrylate monomers.

Suspension polymerisation is normally used to produce larger polymer particles (10 µm–1000 µm) [88]. The size distribution of the prepared polystyrene spheres could be tuned by changing the rotation speed from 200 rpm to 300 rpm during synthesis (Fig 3.3B). The diameter of the particles produced (d) is dependent on the diameter of the vessel (D_v) and

Table 3.1: Review of vasculature diameters found in literature.

Human or animal	Tumour type	Study size	Diameter and range of vasculature measured	Size distribution information	Ref
Human	Prostate	572 patients	Mean= 25.2 µm, Range= 12.9 µm–55.6 µm	Not reported	[122]
Human	Prostate	62 patients	Mean=24.4 µm	Not reported	[123]
Human	Laryngeal	16 patients	Range=5->60 µm	75% were 5 µm–20 µm, 1% was >60 µm	[124]
Mouse	Colorectal	15 tumours	Range=2 µm–55 µm	Majority of the vessels were <10 µm	[125]
Mouse	Colon	1500 vessels	Range= 4 µm–29 µm	Not reported	[126]
Mouse	Mammary carcinomas	6 tumours	Mean= 39 µm, Range= 0 µm–225 µm	Majority of the vessels were 0 µm–55 µm	[127]
Mouse	Human cervical epithelial adenocarcinoma	25 vessels	Range= 5 µm–60 µm	Not reported	[128]
Rat	Mammary adenocarcinoma	4 tumours	Range= 5 µm–225 µm	Majority of the vessels were small	[129]
Rat	Colon	22 tumours	Range= 5 µm–10 µm	Majority of the vessels were 5 µm–50 µm	[130]
Rat	Glioma	3138 vessels	Mean= 16.8 µm, Range= 1 µm–55 µm	Peak vessel size was 10 µm	[131]

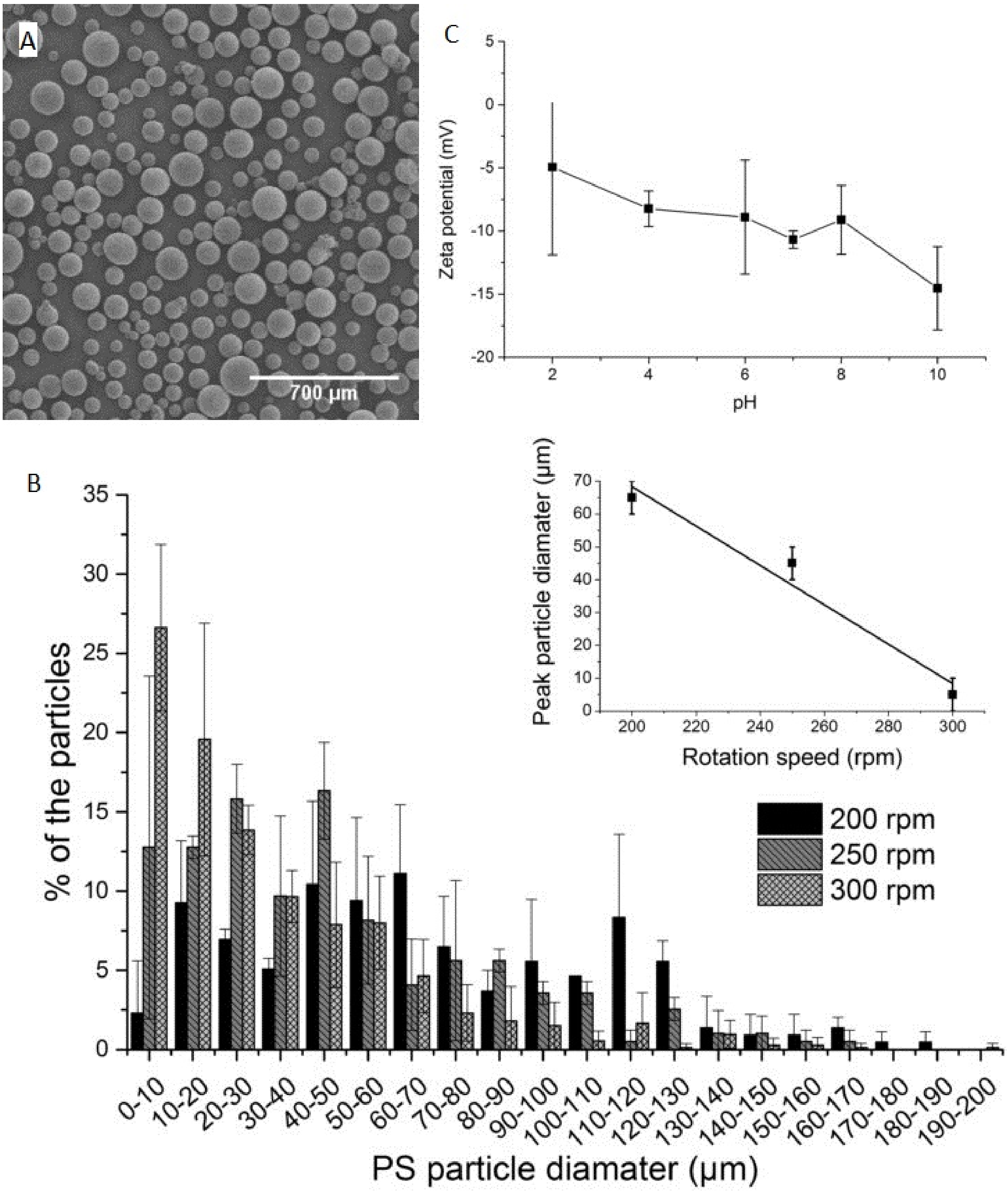

Figure 3.3: Characterisation of the polystyrene embolic particles for effective embolization of branched tumour vasculature. A) Representative SEM image of the polystyrene microspheres showing the size distributions. B) Results from an independent experiment (n=3) showing the change in size distributions with rotation speed during synthesis. Data is presented as mean ± SD of triplicate samples. Insert in B) shows the change in peak particle size with rotation speed. C) Results from an independent experiment (n=3) showing the change in zeta potential of the PS particles with pH. Data is presented as mean ± SD of triplicate samples.

the stirrer (D_s), the ratio of droplet phase to suspension medium (R), the stirring speed (N), the viscosity of the droplet phase (μ_d) and suspension medium (μ_m), the interfacial tension between the two immiscible phases (ϵ) and the stabiliser concentration (C_s) and an empirical factor (k) representing the reactor design, type of stirrer, self-stabilisation, e.t.c as shown in equation (3.1) [133]

$$d = k\frac{D_v R \mu_d \epsilon}{D_s N \mu_m C_s} \tag{3.1}$$

As expected the peak particle size was found to be linear with respect to the rotation speed during synthesis (Fig 3.3B insert). Subsequently, PS particles were prepared at 250 rpm as this would create particles with a peak size of 50 µm ideal for embolization procedures. The PS particles are negatively charged with a zeta potential of $\leq -30\,\text{mV}$ at pH2-10 (Fig 3.3C). As the zeta potential is less negative than $-30\,\text{mV}$ the PS particles do not form a stable suspension and the particles settle quickly.

3.4.3 Polystyrene embolic particle cytotoxicity test

The toxicity of the polystyrene particles was determined using by a crystal violet assay which showed that the polystyrene particles were not toxic to RD cells within the range ($0.04\,\text{mg}\,\text{ml}^{-1}$ to $10\,\text{mg}\,\text{ml}^{-1}$) tested (Fig 3.4). Unlike the SiO_2 nanoparticles shown in Fig 2.2, the PS particles were not dyed with the crystal violet at any of the concentrations tested and therefore the crystal violet assay could be used to determine cell viability. Polystyrene particles have previously been shown to be non-toxic in both *in vitro* and *in vivo* studies. For example, Hafeli *et al.* [134] showed that there was no significant difference in cell viability between microspheres made from materials which are commonly considered to be biocompatible, e.g. poly (lactic acid) and polystyrene latex microspheres. Furthermore, Menei *et al.* [135] showed that polystyrene microspheres (20 µm–30 µm) implanted into rat brains were still intact and had not induced neuronal toxicity after 9 months.

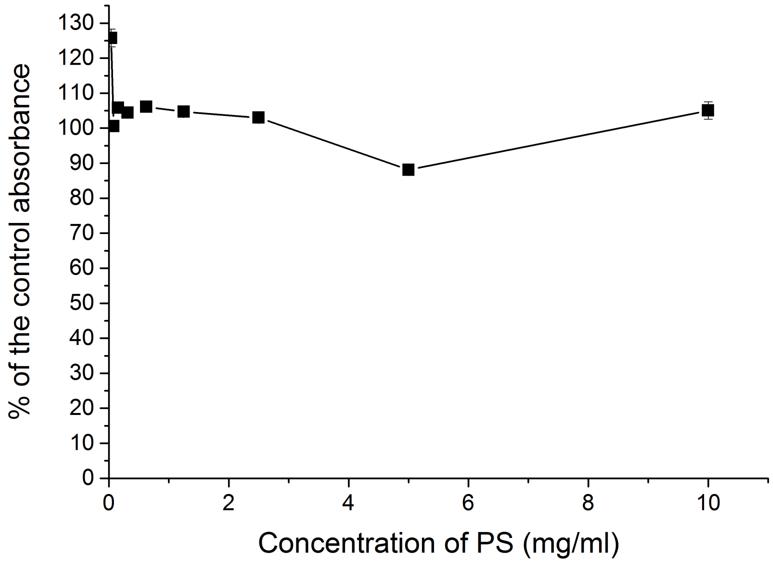

Figure 3.4: Polystyrene embolic particles are not toxic to RD cells. Results from an independent experiment (n=3) showing that there is no difference in cell number after RD cells are treated with PS microparticles measured using a crystal violet assay. Data is presented as mean ± SD of triplicate samples (where error bars are not visible they are smaller than the point size.)

3.4.4 Visualization of fluorescent PS particles within microvessels

The prepared embolization particles were labelled with the fluorescent dyes Rhodamine B (Ex.480 nm, Em. 535 nm; Fig 3.5A) or FITC (Ex. 350 nm, Em. 460 nm; Fig 3.5B) to allow for visualisation of embolic particles within the microvessels models.

To assess the ability of the particles to occlude vessels, bespoke microvessels were purchased from SynDaver^{TM} Labs. After injection of the FITC and Rhodamine B polystyrene particles into the SynDaver^{TM} Labs microvessel the particles could be visualised using brightfield and fluorescent imaging (Fig 3.6). However, examination of the vessels cross section showed that the vessels were not of the specified diameter.

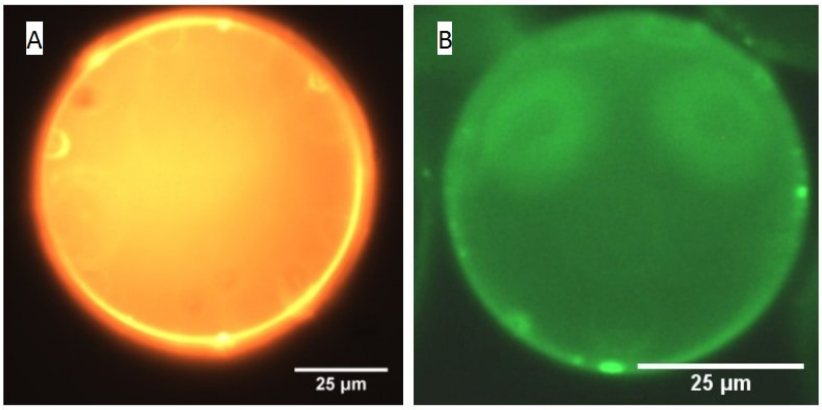

Figure 3.5: Representative fluorescence images of a polystyrene particles dyed with A) Rhodamine B to provide red fluorescence and B) FITC to provide green fluorescence.

The internal diameter of the vessels was between 370 µm and 690 µm) (Fig 3.2) rather than the specified 200 µm. The particles could clearly be seen within the vessel, although no occlusion could occur because of the incorrect vessel size. Unfortunately it was not economically viable to purchase further synthetic vessels for subsequent testing.

3.4.5 Occlusion of a perfusion 3D cell culture kit

Due to the cost of the synthetic SynDaver^{TM} Labs microvessel, it was decided to investigate blockage of PEEKsil® polymer-sheathed fused SiO_2 microtubing. CN Bio (previously Zyoxel) manufacture a perfusion 3D cell culture kit designed for testing the behaviour and function of cells in response to drug treatment. The kit is designed to be a more representative of an *in vivo* response (Fig 3.7). The Zyoxel kit was modified with 25 µm and 50 µm internal diameter PEEKsil® tubing to represent the diameter of tumour vasculature found in literature. While initial experiments planned to look at the effect on the cells growing in the wells after introduction of the the particles in the modified Zyoxel kit, the blockage was so effective that no liquid was able to pass through the tubes. In fact, introduction of the particles resulted in such a large pressure build up that eventually the joints in the system broke to relieve the pressure which led to leaks

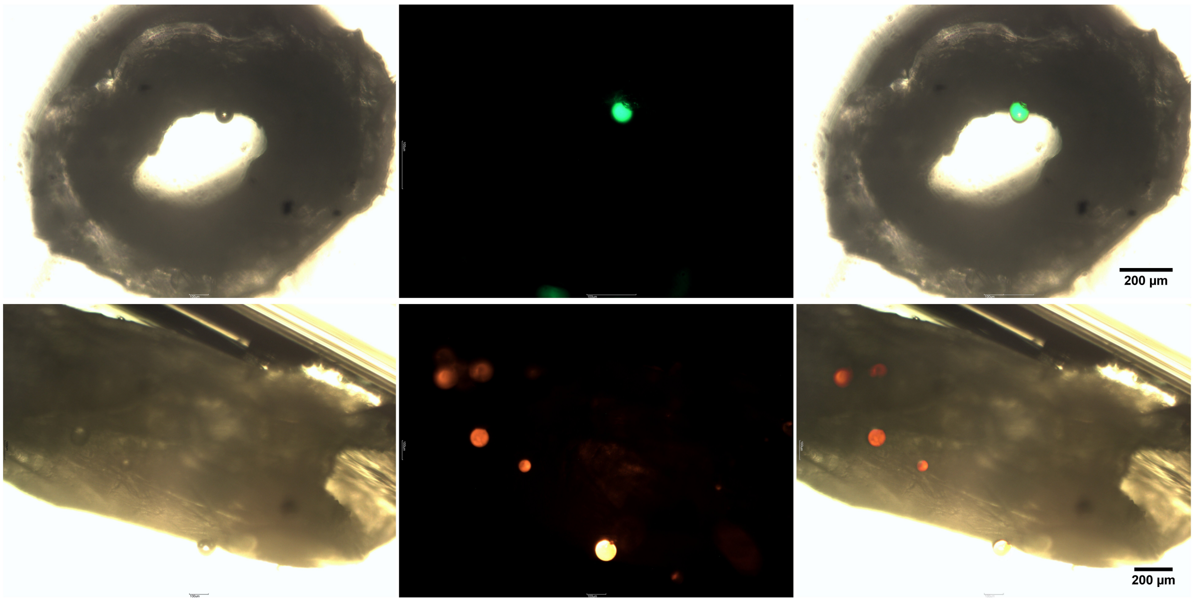

Figure 3.6: Fluorescent embolic particles could be visualised within the SynDaver^{TM} Labs microvessels A) Representative brightfield and fluorescence images of a cross section of the custom made SynDaver^{TM} Labs microvessel showing a FITC dyed polystyrene particle within the microvessel. The internal diameter was designed to be 200 µm however from the image the internal diameter is between 370 µm to 690 µm. B) Representative brightfield and fluorescence images of a lengthwise section of the SynDaver^{TM} Labs microvessel containing several Rhodamine B dyed polystyrene particles.

in the system. It was therefore not possible to investigate the effect of the particles on the cells after occlusion however it does demonstrate the embolic particles would stop the tumour receiving the required nutrients for growth providing effective embolization had occurred.

3.5 CONCLUSIONS

The synthesis of the polystyrene microparticles was optimized to prepare microparticles which were 50 µm and therefore they would effectively occlude the vasculature surrounding tumours. The resultant polystyrene microparticle diameter was finely tuned by changing the rotation speed during synthesis and it was found that 250 rpm was optimal

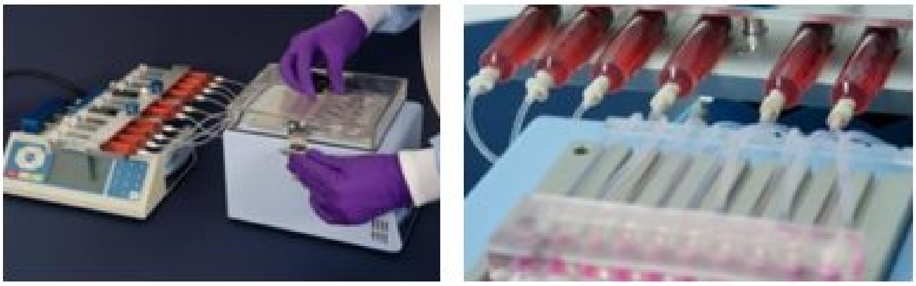

Figure 3.7: Zyoxel kit for the continuous perfusion of cells. The kit was modified to allow for perfusion through 25 µm and 50 µm PEEKsil® tubing as a model of tumour vasculature.

to produce 50 µm particles. The polystyrene particles were not toxic to RD cells at any of the concentrations tested showing that the particles are biocompatible. The polystyrene particles were successfully dyed with Rhodamine B and FITC to allow for visualisation within the synthetic branched microvessel. Effective occlusion of the modified Zyoxel kit with the embolic particles was observed. These polystyrene particles form the basis of the multimodal embolic particles which are presented later in chapter 4, chapter 5 and chapter 6 of this thesis.

Chapter 4

Development of a radiopaque embolic particle

4.1 INTRODUCTION

The usefulness of embolic particles can be increased by formulating them so that they are radiopaque. This allows the particle placement to be monitored during the procedure and for post treatment monitoring. This chapter focuses on the theoretical and experimental aspects of the development of a radiopaque embolic particle. The embolic particles have been designed to include tantalum oxide (TaOx) nanoparticles which act as an X-ray contrast agent inside the polystyrene microparticles (PS-TaOx).

4.1.1 X-ray attenuation

X-ray attenuation is key to understanding how changes in matter affect X-ray image production. The image contrast on an X-ray film is dependent on the difference in intensity of an X-ray beam hitting a film at neighbouring locations. When an X-ray beam interacts with matter it causes photons to be absorbed or deflected. This attenuation causes a reduction in the beam intensity which is dependent on the incident beam intensity (I_0), the thickness of the material (x) and its linear attenuation coefficient (μ)

$$I = I_0 e^{(-\mu x)}. \tag{4.1}$$

The linear attenuation coefficient is dependent on the density of the material and therefore the mass attenuation (μ/ρ) of a material is often reported in the literature [136]. Equation (4.2) can be used to convert between the mass attenuation coefficient and the linear attenuation coefficient using the material's density (ρ)

$$\mu = (\mu/\rho)\rho. \tag{4.2}$$

The mass attenuation coefficient, in the energy range used for diagnostic imaging, is a combination of three interactions between X-ray photons and matter. These are: coherent scattering (ω), the photoelectric effect (τ) and Compton scattering (δ). These interactions sum together to give the mass attenuation coefficient

$$\mu = \omega + \tau + \delta. \tag{4.3}$$

A schematic of these different interactions between X-rays and matter is shown in Fig 4.1. Where these interactions originate from is explained further below. Coherent scattering contributes to the noise on X-ray films, however it is a minor component in comparison to the photoelectric effect and Compton scattering; and therefore is excluded from further consideration.

The photoelectric effect is due to the interaction of X-ray photons and inner-shell electrons. An electron can be ejected from its orbit when an incident photon impacts on an electron with energy greater than its binding energy. The ejected electron is absorbed almost instantly and the vacancy left in the inner shell is immediately filled by an outer shell electron producing lower magnitude energy radiation. The probability of the photoelectric effect occurring is more likely when the photon energy is high. This means that at high photon energy there is less X-ray attenuation and therefore τ is inversely proportional to the photon energy (E) to the third power

$$\tau \propto 1/E^3. \tag{4.4}$$

However, when K shell electrons have high binding energies, such as those absorbers with high atomic number (Z), they are more likely to be involved in the photoelectric

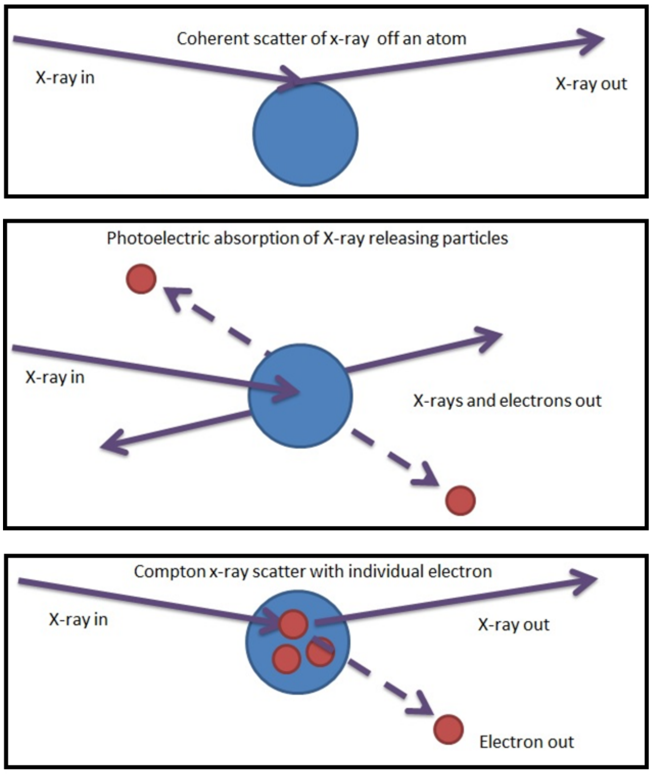

Figure 4.1: Diagram showing the three types of interactions which occur when an X-ray beam interacts with matter, at the energy used for diagnostic X-ray imaging, causing the beam to attenuate. These are: coherent scattering (ω), the photoelectric effect (τ) and Compton scattering (δ).

effect and τ is proportional to the third power of Z

$$\tau \propto Z^3. \tag{4.5}$$

To summarize, the contribution of the photoelectric effect to X-ray attenuation is high under low energy radiation and in the presence of high Z absorbers.

Compton scattering (δ) arises from the interaction of an X-ray photon with an outer shell electron causing it to be ejected from its orbit. The photon is deflected as scattered radiation with lower magnitude energy and a different direction. The probability of Compton scattering occurring, depends on the number of electrons present in the absorber and is independent of atomic number. Compton scattering dominates X-ray attenuation for low Z matter, while at high Z, the photoelectric effect dominates. Compton scattering is responsible for most scattered radiation which increases noise and decreases the contrast on an X-ray image. The quantity of Compton scattering diminishes as the X-ray photon energy increases, so that high energy photons are more likely to pass through the body than low energy photons. This means the magnitude of the radiation dose received by patients is lower with high energy X-rays compared to low energy X-rays. However, a compromise is required to ensure that good image contrast is obtained, whilst at the same time minimizing the radiation dose the patient receives.

4.1.2 X-ray contrast agents

X-ray contrast agents are used in medicine to increase the image contrast whilst minimizing the radiation dose received by the patient. All contrast agents contain a high atomic number element which means they have high X-ray attenuation due to the photoelectric effect described in equation (4.5). Common X-ray contrast agents contain iodine or barium with Z numbers of 53 and 56 respectively. Iodine is cheap and safe to use however it is not an optimal X-ray attenuator [137]. Most diagnostic X-ray machines use a tungsten tube to produce the X-rays. The attenuation characteristics of iodine are mismatched to the X-ray photon energy provided by the tungsten tube and therefore non-optimal contrast is obtained. By appropriately matching the mass attenuation of a heavy element to the X-ray photons produced by the tungsten tube better contrast can be achieved. Additionally, by selecting a heavy metal with greater magnitude intrinsic contrast then a lower magnitude of radiation exposure or a smaller volume of contrast material can be used for effective imaging.

Recently, interest in nanoparticles as X-ray contrast agents has grown in interest due to their favourable properties allowing for increased *in vivo* detection [138]. The most studied nanomaterials for X-ray contrast are gold (Au) and bismuth (III) sulfide (Bi_2S_3) [89]. The use of Bi_2S_3 is limited by the intrinsic toxicity of bismuth and while the synthesis of gold nanoparticles is straight forward, the cost of gold as an X-ray contrast agent is an obstacle to clinical uptake [90].

4.1.3 Tantalum oxide

Tantalum oxide is chemically stable and is resistant to corrosion [139]. Tantalum has a Z number of 73 and hence it is highly radiopaque with an attenuation of 1.08 times iodine at 60 keV and 3.3 times iodine at 80 keV [140]. Tantalum has been historically used as an X-ray contrast agent since the late 1960's for imaging the lungs [141, 142, 143, 144], sinuses [145], larynx [146, 147] and the brain [148]. In the majority of these applications it showed rapid clearance from the body [139]. Additionally, tantalum oxide is non-magnetic which means the patient can still undergo magnetic resonance imaging (MRI) postoperatively; a technique often used to track tumour progression postoperatively.

Recently, various groups have investigated using tantalum oxide nanoparticles as X-ray contrast agents. In 2009, Colborn *et al.*[149] patented a technique for preparing tantalum oxide nanoparticles coated with a material containing a zwitterionic functional group for use as an X-ray contrast agent. Their first publication showed that 6 nm tantalum oxide nanoparticles provided greater contrast enhancement than iodine, at equimolar concentrations, from 80 to 140 kVp [150]. Subsequently, they published work using diethylphosphatethyl-derivatized siloxane coated tantalum oxide nanoparticles. These showed no physiological effects in rats at $400\,\mathrm{mg\,kg^{-1}}$ body weight and only minimal effects at $1500\,\mathrm{mg\,kg^{-1}}$ body weight [151]. However, they identified some problems which would stop the diethylphosphatethyl-derivatized siloxane coated tantalum oxide nanoparticles being used in clinical practice and hence suspended their future development. For example, the tantalum nanoparticle formulation had a high viscosity, the nanoparticles had a long tissue retention time and the nanoparticles induced a pathological response in the kidneys. Instead, they investigated coating the tantalum oxide nanoparticles with a zwitterionic siloxane polymer which reduced the viscosity of the tantalum oxide nanoparticle solution by a factor of 5, decreased the tissue retention time of the tantalum oxide nanoparticles by a factor of 10 and reduced the build up of tantalum oxide nanoparticles within the kidneys [152].

Oh *et al.* [153] synthesized bioinert tantalum oxide nanoparticles which showed *in vitro* and *in vivo* X-ray contrast enhancement which was linear in relation to tantalum oxide concentration. There were no histological changes in the liver, spleen, heart, kidney and lung after 2 weeks when rats were injected with $840\,\mathrm{mg\,kg^{-1}}$ body weight. They also prepared core-shell iron oxide, tantalum oxide nanoparticles which can be used as both X-ray and MRI contrast agents [154].

Herein the tantalum oxide nanoparticles will be embedded into PS-TaOx microparticles and so the tantalum oxide will not be in direct contact with the body and therefore there is less concern regarding the toxicity of the tantalum oxide nanoparticles and the possibility of them causing a pathological response in untreated areas of the body.

4.1.4 Aims and Objectives

The aim of the work in this chapter was to prepare embolic particles which provide X-ray contrast. Doping of the polystyrene particles with tantalum oxide nanoparticles was investigated to determine if sufficient X-ray contrast could be obtained. This was supplemented by calculations being performed to determine the number of particles required for the particles to be seen within the body. Furthermore, characterisation of the tantalum nanoparticles was carried out to determine their material properties.

4.2 MATERIALS AND METHODS

4.2.1 Tantalum oxide nanoparticle synthesis

Tantalum oxide nanoparticles were prepared according to the method presented by Oh *et al.* [153]. An oil phase was created by mixing 2.3 g of the non-ionic surfactant Igepal Co-520 (Aldrich), 0.75 ml of ethanol (Fisher) and 20 ml of cyclohexane (Aldrich) by stirring. A microemulsion was then created by adding 250 µl of 2 mM NaOH (aq; Aldrich). Finally, 50 µl of tantalum(V) ethoxide (Aldrich) was added to the microemulsion at room temperature and incubated for 5 minutes. Ethanol was then added to the mixture to allow the particles to sediment. Particles were collected by centrifugation, washed in ethanol three times and dried in a desiccator overnight.

4.2.2 PS-TaOx microparticle synthesis

The PS-TaOx microparticles were prepared by a modification of the method previously described in section 3.3.1 for the synthesis of polystyrene microparticles. Different masses of TaOx nanoparticles were mixed into the oil phase to create PS-TaOx microparticles containing theoretically 0 wt %, 5 wt %, 10 wt %, 20 wt % and 50 wt % TaOx nanoparticles (Samples A —E, respectively). The oil phase was then sonicated using an ultrasonic probe (Sonic Vibra-Cell) for one minute (104 W (80 %) five seconds on/ five seconds off) to increase the dispersion of the nanoparticles throughout the oil phase. The oil phase was then added to the standard aqueous phase and synthesis carried out as described in section 3.3.1.

4.2.3 Oleic acid coating

In one iteration, TaOx nanoparticles were coated with oleic acid to increase the hydrophobicity of the nanoparticles and therefore increase their dispersion in the oil phase during polymer synthesis [155]. The majority of methods in the literature for coating nanoparticles with oleic acid relate to iron oxide nanoparticles and the coating often takes place during the synthesis of the nanoparticles rather than post-synthesis [156, 157, 158]. The coating method was modified from the method presented by Majewski and Krysinki [159] for the surface modification of ferrite nanoparticles with oleic acid.

Pre-prepared tantalum oxide nanoparticles (200 mg) were resuspended in 20 ml of ddH_2O and the pH of the mixture was then adjusted to 2 using 2 M nitric acid (Aldrich). The TaOx nanoparticles were subsequently flocculated by the addition of 0.5 M ammonium hydroxide (Aldrich) until the solution reached pH 6.5. The nanoparticles were collected by centrifugation and washed in ddH_2O twice. The particles were once again resuspended in 20 ml of ddH_2O and then 2 ml of oleic acid (Aldrich) was added. The mixture was shaken vigorously for 5 minutes on a vortex mixer and then the oil and water phases were left to settle. The oil phase was then extracted, centrifuged and washed in 10 ml of a 3:1 (v/v) methanol (Rathburn) /water mixture twice. Finally, the unbound oleic acid was reacted with 10 ml of 0.1 M ammonium hydroxide to form the ammonium salt and again this was washed with a 3:1 (v/v) methanol/water mixture twice.

PS-TaOx microparticles were also synthesised using oleic acid coated tantalum oxide nanoparticles. The method was exactly the same as that described in section 4.2.2. Samples with 10 wt % maximum possible concentration of oleic acid coated tantalum oxide nanoparticles (Sample C@OA) and 20 wt % maximum possible concentration of oleic acid coated tantalum oxide nanoparticles (Sample D@OA) were synthesised.

4.2.4 Particle characterization

The size of the tantalum oxide nanoparticles was measured by both TEM and centrifugal sedimentation as described in section 2.1.2 and section 2.1.5 respectively. The change in zeta potential of the tantalum oxide nanoparticles before and after coating with oleic acid was monitored using the Malvern Zetasizer as described in section 2.1.6. The crystal structure of the TaOx nanoparticles was obtained by XRD using a fully automated Siemens D500 powder diffractometer as described in section 2.1.7.

The dispersion of tantalum oxide within the PS-TaOx microparticles was investigated by sectioning the microparticles and then imaging using TEM, and also by fracturing the microparticles with liquid nitrogen and then imaging using SEM. For the sectioning, the composite particles were embedded into epoxy resin using the Agar 100 Resin Kit as per the manufacturer's instructions. In brief, 10 ml of Agar 100 epoxy resin, 4.5 ml of dodecenyl succinic anhydride (DDSA) and 6 ml methyl nadic anhydride (MNA) were prewarmed to 60 °C and then mixed together at 60 °C by gentle hand rotation for a few minutes. Once fully mixed, 0.6 ml of benzyl dimethylamine (BDMA) was added and the mixture was shaken for a further two minutes. The epoxy resin mixture was then poured onto the PS-TaOx microparticles inside a resin holder (Gilder Grids, EM 5 Embedding Mould). The resins were left to set for at least 36 hours at 60 °C. Sections were cut using an Ultratome Nova microtome and placed on copper mesh TEM grid. The grids were imaged using a JEOL-2010 TEM.

The PS-TaOx microparticles were fractured in a small volume of liquid nitrogen using a precooled mortar and pestle. The fractured pieces were then dusted onto a standard SEM stub (further details can be found in section 2.1.3). The surface morphology and changes in elemental composition of the fractured surface was examined using a JEOL JSM-840A SEM. The 840A SEM was operated at a primary beam energy of 10 keV and images were collected in both the secondary imaging mode and the backscattered electron imaging mode. EDX was also performed to determine the elements present in the sample.

The mass concentration of tantalum oxide nanoparticles within the different PS-TaOx microparticle samples was interpolated from thermogravimetric analysis (TGA). A TG DTA 6300 (PerkinElmer) was used to measure the change in mass of each sample when heated from 30 °C to 650 °C at a rate of $10\,^{\circ}\mathrm{C\,min^{-1}}$. The percentage change in mass of TaOx nanoparticles and polystyrene microspheres was then used to interpolate the concentration of TaOx within the PS-TaOx microparticles ($\%TaOx_s$)

$$\%TaOx_s = \frac{(m_s - m_{ps})}{m_{TaOx}} \times 100\%. \tag{4.6}$$

where m_s is the percentage mass remaining in the tested sample, m_{ps} is the percentage mass remaining in the polystyrene sample and m_{TaOx} is the percentage mass remaining in the TaOx nanoparticle sample after heating to 650 °C.

4.2.5 X-ray contrast experiments

To determine the contrast enhancement of the PS-TaOx microparticles compared to the polystyrene spheres, the PS-TaOx microparticles (Samples B-E) were irradiated with superficial X-rays using a tungsten anode Comet MXR-321 tube and an X-ray transmission image was obtained. Additionally, the polystyrene microparticles (Sample A) and the TaOx nanoparticles (Sample F) were also tested. The nanoparticles and microparticles were resuspended in ddH$_2$O at 50 mg mL^{-1} and 100 mg mL^{-1} respectively and 200 µL of each sample was placed into 96 microwell plate sparsely to ensure no scatter from neighbouring wells. The surface area of the base of the well was 0.32 cm^2. The plate was placed on a 1.5 mm thick Perspex (PMMA) shelf which sat on top of an applicator and a sheet of Gafchromic EBT3 film (Vertec Scientific) film was subsequently placed on the lid of the plate. The films were exposed to bremsstrahlung X-rays with a peak energy of 50 keV, a tube current of 20 mA and with no additional filtration other than the 1.5 mm Perspex shelf and the beryllium window of the X-ray tube to obtain a transmission image. Three films of each plate was taken and the experiment was repeated three times.

The films were scanned in transmission mode using a flatbed scanner [Epson Expression 10000XL] with the optional transparency unit [Epson B12B813363] and a calibration curve was used to convert the optical density of the X-ray film to the dose of radiation received in each well location. The calibration curve had previously been prepared by Dr James Thompson (Gray Institute for Radiation Oncology and Biology, Oxford

University). Local background subtraction was performed to reduce errors arising from the uneven change in optical density across the X-ray film. The contrast of the PS-TaOx microspheres was compared to the undoped PS microspheres.

4.2.6 CT scan of the PS-TaOx microparticles

A CT image of the TaOx nanoparticles, the PS-TaOx microparticles and the undoped PS microparticles was obtained using a small animal radiation research platform (SARRP) (Xstrahl Ltd, Camberley, UK) to show that the particles are able to show contrast using a pre-clinical setup. A sample holder was prepared by cutting holes in the top of a T25 tissue culture flask and inserting thin walled PCR tubes to hold the samples. Powder samples of the TaOx nanoparticles, PS-TaOx microparticles and undoped PS microparticles were placed into the PCR tube and were exposed to X-rays with a peak voltage of 50 keV filtered with 0.22 mm of copper to obtain the CT image.

4.2.7 X-ray contrast calculations used to ascertain the level of TaOx doping required for sufficient PS-TaOx X-ray contrast

Calculations were used to ascertain the concentration of TaOx required within PS-TaOx microparticles to ensure sufficient X-ray contrast within a tumour volume. A schematic to aid understanding of the calculations is shown in Fig 4.2. The patient thickness was set as a constant. The region of interest was calculated as a one dimensional line of between zero and one hundred 50 µm PS-TaOx microparticles containing 0 wt%, 5 wt%, 10 wt%, 20 wt%, 50 wt% and 100 wt% TaOx which is equivalent to the transmission of the X-ray beam through 0 to 5 mm of PS-TaOx material.

The change in intensity of the X-ray beam through the patient (I_1 on Fig 4.2) was

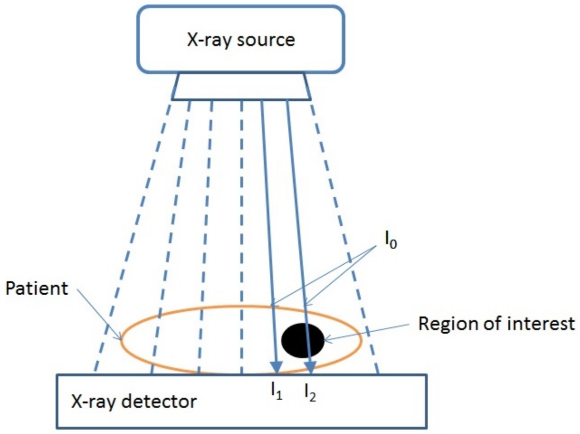

Figure 4.2: Diagram showing the % change intensity of an X-ray beam as it attenuates from interactions from a patients body or region of interest containing the PS-TaOx microparticles. This is used to help understand the x-ray contrast calculations.

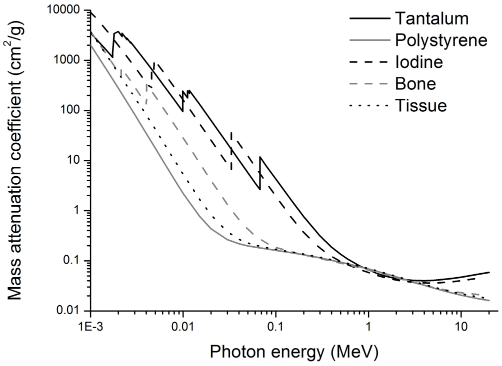

Figure 4.3: Change in mass attenuation coefficients with photon energy for tantalum, polystyrene, iodine, bone and tissue. Data taken from NIST [160]

calculated from equation (4.7) which combines equation (4.1) and equation (4.2) to give

$$I_1 = I_0 e^{-(\mu/\rho)_t \rho_t x_t}, \tag{4.7}$$

where I_0 is the initial intensity of the X-ray beam, $(\mu/\rho)_t$ is the mass attenuation coefficient of the tissue, ρ_t is the density of the tissue and x_t is the thickness of the patient. The change in mass attenuation with photon energy is provided by NIST [136] and relevant plots for tantalum, polystyrene, iodine, bone and tissue, soft (ICRU-44) are shown in Fig 4.3. The peak energy of the X-ray beam used was 50 keV and SpekCalc was used to generate the spectrum of energy from of the X-rays with the following settings: Energy range = 5 to 50 keV, Theta = 30 Degree, 1000 mm of air and 3 mm of beryllium [161]. Furthermore the mass attenuation coefficient and density of Polymethyl Methacrylate, taken from the NIST database [136], were used to include the 1.5 mm Perspex shelf.

The change in intensity of the X-ray beam through the patient and the region of interest (I_2 on Fig 4.2) was calculated from a modified version of equation (4.7)

$$I_2 = I_0 e^{-(\mu/\rho)_t \rho_t (x_t - x_p) - (\mu/\rho)_p \rho_p x_p}, \tag{4.8}$$

where the suffix p refers to particle.

The mass attenuation coefficient of the particles was estimated using the mixture rule [136]

$$(\mu/\rho)_p = \Sigma_i w_i (\mu/\rho)_i, \tag{4.9}$$

where w_i is the mass proportion of the i^{th} element in the compound and a similar expression was used to estimate the density of the particles,

$$\rho_p = \Sigma_i w_i (\rho)_i. \tag{4.10}$$

The TaOx was assumed to be TaOx which is the chemical formula determined by the paper that the TaOx synthesis was taken from [153].

Finally the contrast enhancement (C) of the particles can be calculated from

$$C = \frac{I_1 - I_2}{I_1} = 1 - \frac{I_2}{I_1}. \tag{4.11}$$

Assuming a perfect detector with a response independent of photon energy and ignoring photon scatter.

4.2.8 Further development of the calculations for comparison with experimental results

The calculations were further developed to estimate the contrast enhancement expected from the X-ray contrast experiments described previously in section 4.2.5. The particles were irradiated in 96 well plates and an X-ray transmission image of the plate was obtained. The thickness of particles within each well (X_p) was estimated based on the mass of particles within the well (m_p), the density of particles (ρ_p), the area of each well (A_w) and an estimate of the packing density of the particles (ϵ)

$$X_p = \frac{\epsilon m_p}{\rho_p A_w}. \tag{4.12}$$

The packing density was assumed to be 0.95 and the area of each well in the 96 well plate was 0.32 cm. The change in intensity of the beam was then calculated using equation (4.11). Finally the change in contrast for the PS-TaOx microparticles compared to polystyrene microparticles was estimated based on,

$$\%C = \frac{I_{polystyrene - I_{PS-TaOx}}}{I_{\text{polystyrene}}} = 1 - \frac{I_{PS-TaOx}}{I_{\text{polystyrene}}} \tag{4.13}$$

4.3 RESULTS

4.3.1 Synthesis of 5-8 nm amorphous TaOx nanoparticles

Tantalum oxide nanoparticles were synthesised to act as X-ray contrast agents. TEM images of the synthesised TaOx nanoparticles show monodispersed 5 to 8 nm nanoparticles (Fig 4.4A). The nanoparticles were shown to be amorphous TaOx by both the Fast Fourier transform of the TEM image of the TaOx nanoparticles (Fig 4.4B) and from XRD (Fig 4.4C). The composition of the nanoparticles was confirmed to be tantalum oxide by EDX (Fig 4.4D). In one iteration of the method, TaOx nanoparticles were coated with oleic acid to increase the uptake and dispersion of the nanoparticles within the polystyrene matrix. The presence of the coating on the nanoparticles was confirmed by measuring the change in zeta potential pre- and post- coating across a wide range of pH values. The data shows that the zeta potential of the TaOx nanoparticles becomes more negative across the pH range 2-9 after coating with oleic acid, compared to the uncoated TaOx nanoparticles (Fig 4.4E). The zeta potential of the oleic acid coated TaOx nanoparticles is less than $-30\,\mathrm{mV}$ across the pH range 2-9 and therefore the nanoparticles can be deemed to be stable.

4.3.2 TaOx nanoparticles were successfully incorporated into the polystyrene matrix of the embolic particles

Radiopaque polystyrene microspheres were prepared by incorporating the tantalum oxide nanoparticles into the polystyrene microspheres during the synthesis. The incorporation of TaOx nanoparticles into the polystyrene matrix of the embolic particles was confirmed by (i) sectioning the microparticles and imaging with TEM, and (ii) fracturing the microparticles with liquid nitrogen and imaging using SEM. A representative section of a PS-TaOx microparticle shows areas of high contrast which are due to TaOx nanoparticles

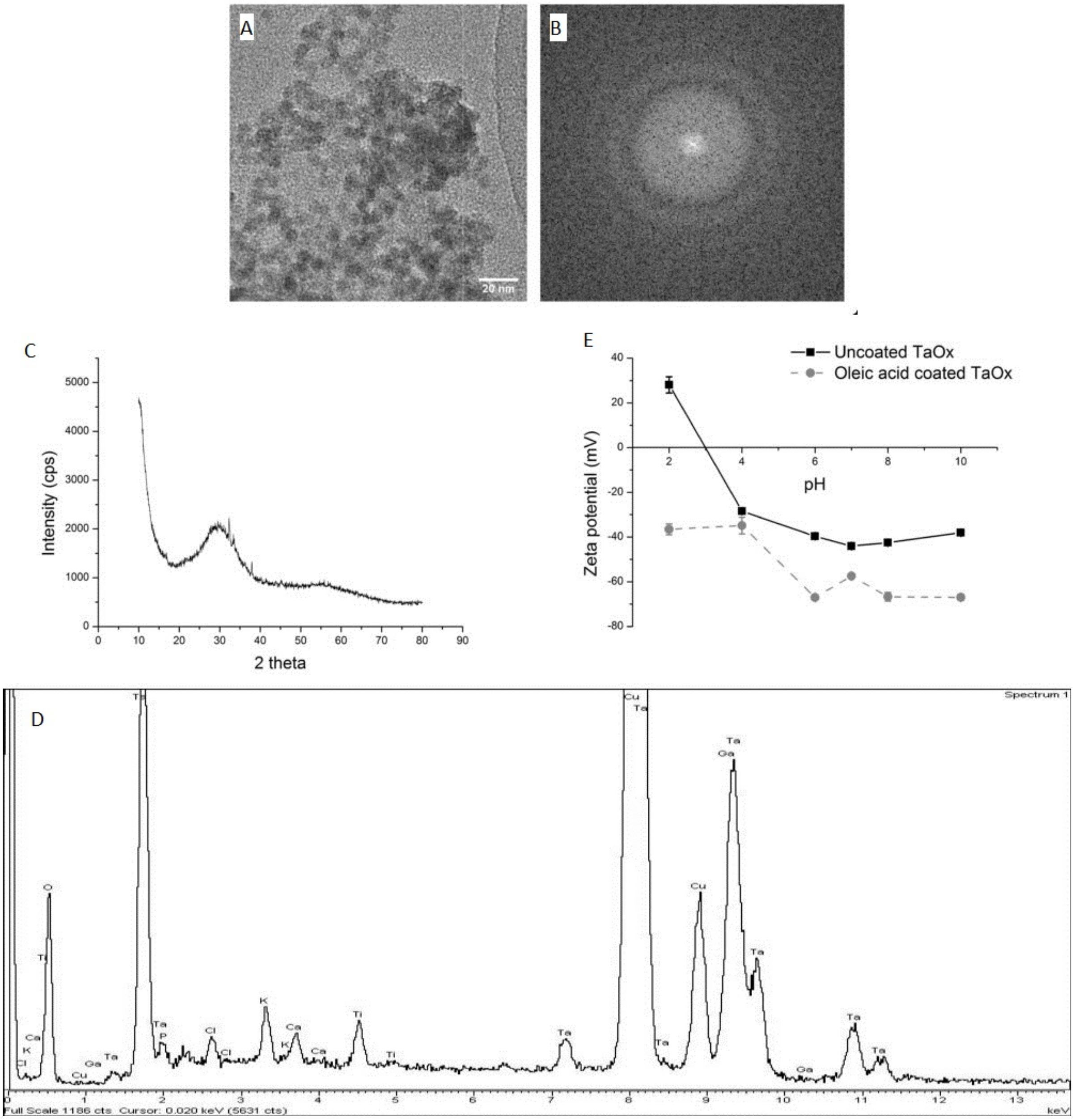

Figure 4.4: Characterisation of the tantalum oxide (TaOx) nanoparticles to act as X-ray contrast agents. A) Representative transmission electron microscope (TEM) image of the TaOx nanoparticles with an external diameter of approximately 5 to 8 nm (scale bar 20 nm). B) Fast Fourier Transform of the TaOx nanoparticles in A) showing amorphous rings. C) Representative X-ray diffraction trace showing that the TaOx nanoparticles are amorphous. D) Representative energy dispersive X-ray spectroscopy (EDX) confirming the presence of tantalum within the nanoparticles. E) Results from an independent experiment (n=3) showing the change in zeta potential of the TaOx nanoparticles before and after coating with oleic acid resuspended in ddH$_2$O across a range of pH values. Data is presented as mean ± SD of triplicate samples.

and the outline of the polystyrene curvature (Fig 4.5A,B). The liquid nitrogen fractured PS-TaOx microparticles were imaged by SEM using both secondary electron (SE) and backscatter (BS) electron mode. SE imaging mode is most suitable for investigating the surface topology of a sample, and the surface fracture lines can be seen (Fig 4.5C). BS imaging mode is used to assess changes in elements within the sample since high atomic mass (high Z number) elements cause greater backscatter of electrons than low Z elements; therefore areas of high Z show up more brightly on the image than low Z. Since tantalum has an atomic mass of 73, compared with an atomic mass of 12 for the carbon found in the polystyrene, the tantalum shows up as bright areas on the image. Therefore the especially bright areas seen in the BS image are likely to be aggregates of TaOx nanoparticles (Fig 4.5D) and the presence of tantalum in these areas was confirmed by EDX. Since the nanoparticles are 5 to 8 nm (Fig 4.4A) individual nanoparticles are too small to be resolved by SEM and therefore it is likely that the particles are distributed throughout the sample.

The percentage (w/w) of TaOx nanoparticles incorporated into the polystyrene matrix was quantified using TGA. Polystyrene microparticles (Sample A; 100% PS) started to decompose above 300 °C and were completely burnt off after heating to 550 °C (Fig 4.5E,F). Over this temperature range the TaOx nanoparticles (Sample F; 100% TaOx) show a reduction in mass of 14%. The mass lost for the PS-TaOx microparticles (Samples B-E; 0.8-9.7% TaOx in PS-TaOx) is less than the loss in mass seen from the polystyrene-only microparticle (Sample A). The percentage of TaOx within each PS-TaOx microparticle was interpolated using equation (4.6) to produce the results shown in Table 4.1. The overall trend of TaOx incorporated into the PS-TaOx microparticle sample was as expected but the extent of incorporation is low compared to the maximum possible TaOx nanoparticle loading for each sample. Coating the nanoparticles with oleic

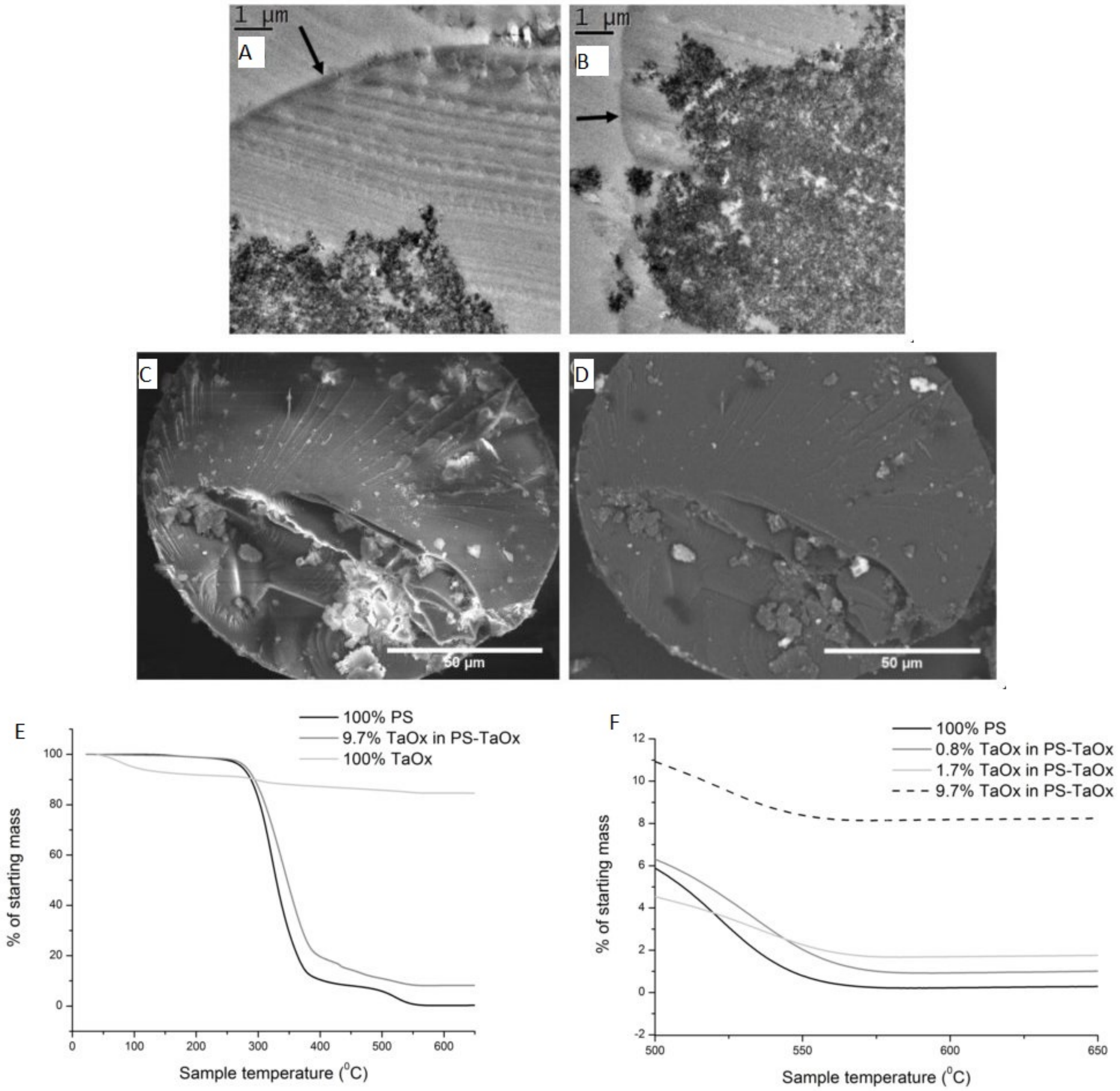

Figure 4.5: Characterisation of the PS-TaOx microparticles to act as radiopaque embolization agents. A,B) Representative transmission electron microscope (TEM) images of a section of the synthesised PS-TaOx microparticles showing the tantalum oxide (TaOx) nanoparticles as areas of high contrast and the outline of the microparticle disc (Black arrows; Scale bar 1 µm). Representative scanning electron microscopy (SEM) images of a synthesised PS-TaOx microparticle which has been fractured using liquid nitrogen. C) Secondary electron image to show topographical features. D) Backscatter electron image to show changes in elements in the sample. Bright areas are due to greater backscatter of electrons from greater magnitude atomic number (Z number) elements. Energy-dispersive X-ray (EDX) confirmed the presence of tantalum within the bright areas on D (Scale bars 50 µm).

Figure 4.5: (Cont.). Results from an independent experiment showing thermogravimetric analysis traces when PS-TaOx microparticles were heated from 30 °C to 650 °C at a rate of 10 °C min^{-1}. E) The percentage change in mass of polystyrene microparticle (Sample A), a PS-TaOx microparticle sample (Sample E) and TaOx nanoparticles (Sample F). F) Expanded section from E) showing the end point percentage mass change from 500 °C to 650 °C for polystyrene (Sample A) and 3 PS-TaOx microparticle samples (Samples C-E).

acid resulted in an increased incorporation of TaOx into the polystyrene matrix; 1.4% compared to 0.8% for samples C, and 1.9% compared to 1.7% for samples D (Table 4.1).

Table 4.1: Showing the percentage of tantalum oxide (TaOx) which is incorporated into the PS-TaOx microparticles based on thermogravimetric analysis. The percentage of TaOx within the PS-TaOx microparticles (Sample B-E) can be interpolated from the percentage mass remaining, after heating to 650 °C for the polystyrene microparticles (Sample A), the TaOx nanoparticles (Sample F) and the measured sample.

Sample ID	Maximum possible % of TaOx within the sample	Interpolated concentration of TaOx within the sample based on the TGA results (%)
A	0	0
B	5	0
C	10	0.8
C@OA	10	1.4
D	20	1.7
D@OA	20	1.9
E	50	9.4
F	100 (TaOx nanoparticles)	99.7

4.3.3 Results from the x-ray contrast calculations.

X-ray contrast calculations were generated to determine the number of PS-TaOx embolic particles required to obtain a certain level of contrast assuming the beam goes through the centre of the spheres (Fig 4.6). To allow for easy comparison with a clinically relevant example, the contrast expected to be seen for 1 cm, 2.5 cm and 5 cm thickness of bone has been included. As expected, the 100% TaOx sample provides the highest contrast and only 150 µm TaOx microparticle material, which is equivalent to the beam traversing the centre of three 50 µm TaOx microparticles, would be required to get the same contrast as 5 cm of bone. However, as polystyrene has a lower magnitude mass attenuation coefficient than tissue (Fig 4.3), 100% polystyrene shows negative contrast (Fig 4.6A). The number of particles required to obtain the same contrast as 1 cm, 2.5 cm and 5 cm of bone is shown in Fig 4.6B. This shows that at above 10% TaOx doping within the PS-TaOx microparticles only 3.7 mm of TaOx microparticle material, which is equivalent to the beam traversing the centre of seventy five microparticles, is required to get contrast equivalent to 5 cm of bone therefore 9.4% doping should easily allow particles to be seen within a tumour. For comparison, clinical embolization treatment in current clinical use delivers between 1x10^4 and 1.3x10^6 particles [162].

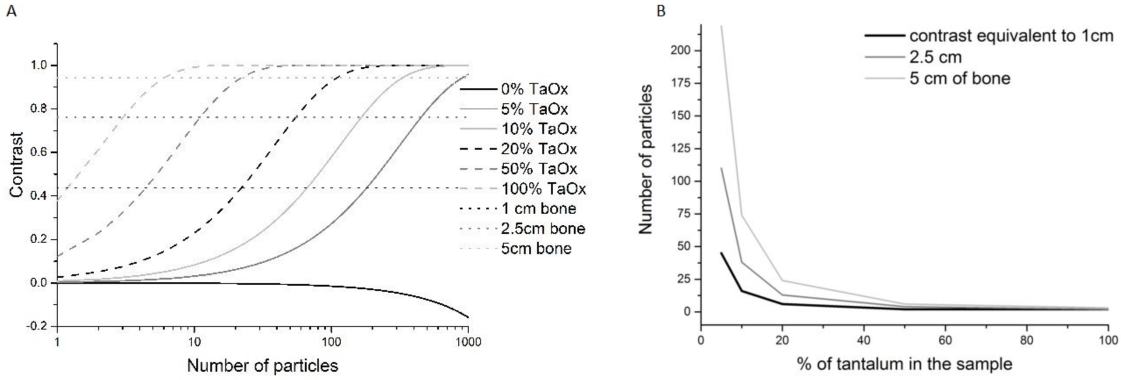

Figure 4.6: Calculation results showing the expected contrast obtained by the radiopaque embolization particles. A) Results from the calculations showing the expected contrast enhancement relative to the number of 50 µm PS-TaOx microparticles, for different concentrations of tantalum oxide doping. The contrast for 1 cm, 2.5 cm and 5 cm of bone within the same patient thickness has been provided for reference. B) Calculation results showing the number of particles needed to get the same contrast as 1 cm, 2.5 cm and 5 cm of bone.

4.3.4 Embolic microparticles show X-ray contrast proportional to the concentration of embedded TaOx nanoparticles

The X-ray film produced by the X-ray contrast experiments is shown in Fig 4.7A. The samples containing the tantalum oxide nanoparticles (Sample F) show up the brightest on the X-ray film (Fig 4.7B). The X-ray film was digitized and plotting this as a colour map confirms that the tantalum oxide nanoparticles (Sample F) produce the highest contrast (Fig 4.7C). The radiation dose received on the X-ray film was determined using a calibration curve. The radiation dose received was related to the intensity of the X-ray beam hitting the film having passed through the samples. The samples will attenuate the X-ray beam reducing its intensity.

Initially, the TaOx nanoparticles were tested and the results show a linear agreement (R^2=0.97) between the tantalum concentration and the X-ray contrast obtained (Fig 4.7D). Subsequently, the PS-TaOx microparticles were tested and these show an increase in contrast compared to the polystyrene microparticles (Fig 4.7E). There is also good linear agreement between the concentration of TaOx incorporated within the PS-TaOx microparticles and the contrast for the PS microparticles with a R^2 value of 0.9. Additionally, the calculations predicts that the contrast enhancement obtained is linear with respect to the concentration of TaOx within the PS-TaOx microparticles (Fig 4.7D). The calculations showed a strong correlation (R^2 value = 0.86) with the experimental data. Additionally the CT scans of the PS-TaOx microparticles doped with 9.4% TaOx (Sample E) would provide sufficient contrast for the samples to be observed in a pre-clinical model of an X-ray contrast setup (Fig 4.8).

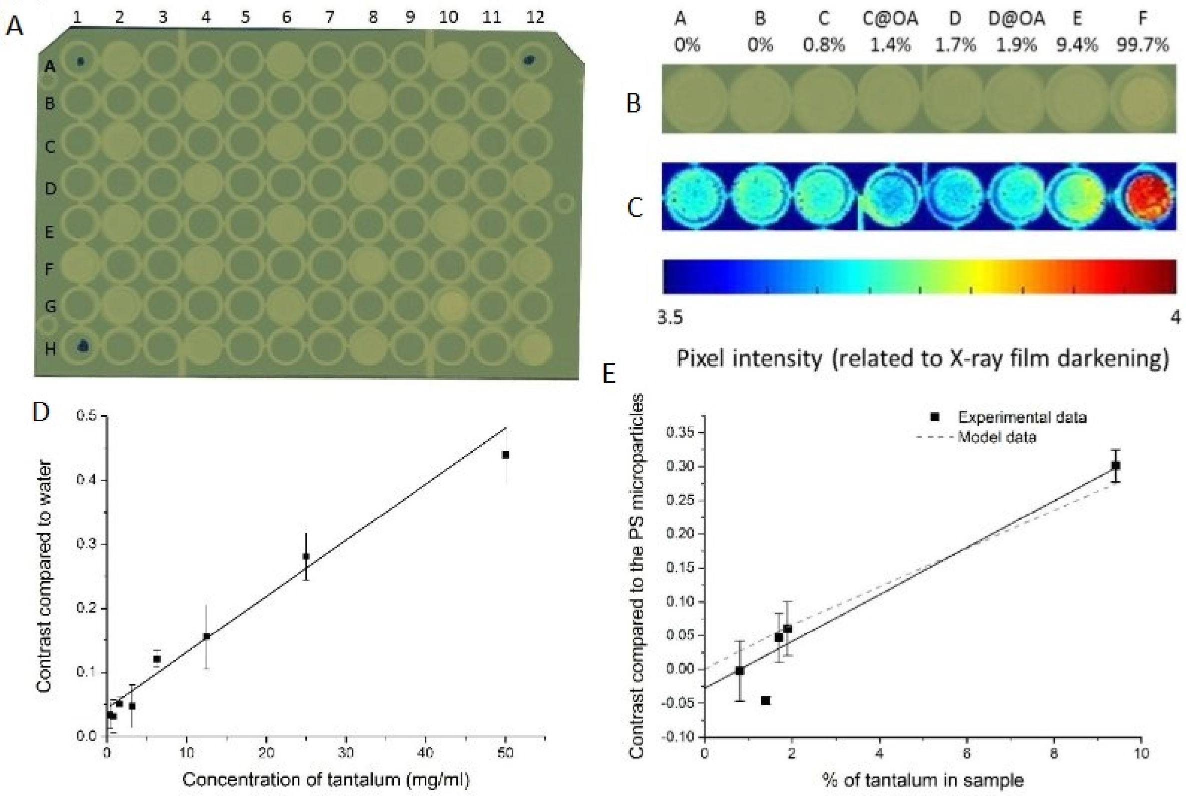

Figure 4.7: Experimental results showing that the TaOx nanoparticles and the PS-TaOx embolic particles provide X-ray contrast. A) Example X-ray film produced by irradiating a mixture of Samples A-F to indicate the sparsely populated film. B) X-ray film showing wells containing 100 mg mL^{-1} polystyrene microparticles (Sample A), 100 mg mL^{-1} of PS-TaOx microparticles (Samples B-E) and 50 mg mL^{-1} of tantalum oxide nanoparticles (Sample F). The samples cause the X-ray beam to be attenuated to different degrees which causes darkening of the film which, using a calibration curve, can be converted to a radiation dose received on the X-ray film. C) A colourmap of the X-ray film shown in A which visualizes the difference in X-ray film darkening. D) Results from an independent experiment (n=3) showing the difference in contrast of the TaOx nanoparticles compared to the water. A linear fit (solid line) has been applied to the experimental data with an R^2 value of 0.97. Data is presented as mean ± SD of triplicate samples. E) Results from an independent experiment (n=3) showing the difference in contrast of the PS-TaOx microparticles compared to the PS microparticles. A linear fit (solid line) has been applied to the experimental data with an R^2 value of 0.9. Data is presented as mean ± SD of triplicate samples. Results from the calculations (dashed line) have also been added which show a strong correlation (R^2= 0.86) with the experimental data.

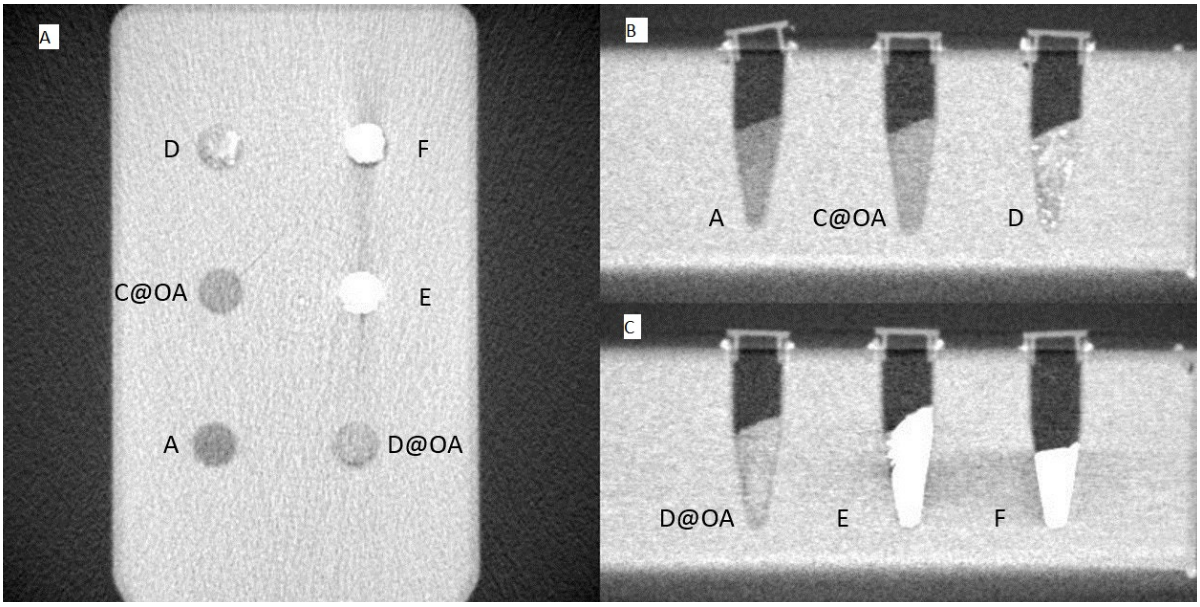

Figure 4.8: Representative CT images of the TaOx nanoparticles, PS-TaOx microparticles and PS microparticles. A) The cross section and B,C) side views of the samples (Sample A=polystyrene microparticles, Sample C@OA= 1.4% TaOx doped PS-TaOx, Sample D=1.7% TaOx doped PS-TaOx, Sample D@OA= 1.9% TaOx doped PS-TaOx, Sample E= 9.4% doped TaOx doped PS-TaOx, and Sample F= TaOx nanoparticles. Additionally water can be seen surrounding the samples and air at the top of the PCR tubes.

4.4 DISCUSSION

Tantalum oxide nanoparticles have been successfully synthesised which are between 5 nm and 8 nm in diameter. Subsequently, these nanoparticles have been incorporated into the polystyrene matrix to produce PS-TaOx microparticles. Both the TEM images of the sections of the PS-TaOx microparticles (Fig 4.5A,B) and the SEM images of the liquid nitrogen fractured PS-TaOx microparticles (Fig 4.5C,D) show that tantalum oxide has been successfully incorporated into the polystyrene matrix. The TGA results show that the mass of tantalum oxide incorporated was lower in magnitude than the theoretical maximum for total inclusion in the PS-TaOx microparticles. The TGA shows that the maximum incorporation of tantalum oxide into the PS-TaOx microparticles is 9.4% for Sample E. This compares favourably with Puig *et al.* [155] who achieved a maximum of 8% incorporation of 9.5 nm oleic acid coated magnetite nanoparticles into a diglycidylether of bisphenol A (DGEBA) epoxy matrix.

The presence of TaOx nanoparticle aggregates within the PS-TaOx microparticles will cause an increase in the local contrast enhancement of the particles. However, by increasing the dispersion of TaOx nanoparticles through the PS-TaOx microparticles it is likely that the percentage incorporation will also increase. Increasing the dispersion of nanoparticles through a polymer matrix has been widely studied in the literature as it is often a challenge. Some of the methods used to increase the dispersion include chemical modification of the nanoparticles, *in situ* polymerization, high shear mixing or sonication [163]. The nanoparticles can be coated with a hydrophobic layer which encourages the nanoparticles into the oil phase during synthesis and therefore into the final polymer matrix [155]. The work presented in this chapter shows the successful coating of the tantalum oxide nanoparticles with oleic acid which increased their stability across pH values of 2 to 9 (Fig 4.4D). Coating the tantalum oxide nanoparticles showed a notable increase, of up to 75%, in the incorporation of tantalum oxide into the PS-TaOx microparticles compared to the uncoated tantalum oxide nanoparticles. Sonication was also used to increase the dispersion of the tantalum oxide nanoparticles in the oil phase. High shear mixing could not be used for producing the PS-TaOx microparticles as this would change the size of the final microparticles (Fig 3.3). As previously discussed in section 3.4, the speed of mixing is proportional to the size of microparticles produced and therefore high shear mixing would produce microspheres too small for embolization procedures.

The obtained X-ray films show that the PS-TaOx microparticles can provide X-ray contrast. The colourmap of the films is pixelated and since the spatial resolution of the Gafchromic EBT3 X-ray film is $\geq$ 5000 dots per inch, which is equivalent to a 5 µm dot size, this could suggest that there is not a even distribution of the PS-TaOx microparticles across the well. The contrast enhancement which is obtained between the PS-TaOx microparticles and the polystyrene microparticles was shown to be dependent upon the concentration of TaOx within the microparticle sample. The contrast change of the PS-TaOx microparticle samples compared to the polystyrene microparticles was linear with respect to the tantalum concentration within the sample (R^2 values= 0.9). The theoretical calculations predicted that the contrast enhancement between the PS-TaOx microparticles and the polystyrene microparticles would be linear with respect to TaOx concentration. This is consistent with the experimental data and there was a strong correlation with the calculated data and the experimental data (R^2 value= 0.86). Oh *et al.* [153] also showed that the contrast obtained is linear with respect to the TaOx nanoparticle concentration. Furthermore, the PS-TaOx microparticles could be observed in the pre-clinical animal CT scan indicating that they are a promising option for animal trials. The transmission images were obtained with no additional filtration except the Perspex shelf and the beryllium window. In clinical practice, filtration would be used to reduce the radiation dose received by the patient by reducing the Compton scattering as described in section 4.1.1.

The calculations predict that at low, $\leq$10 wt%, TaOx doping of the PS-TaOx microparticles the X-ray beam would need to traverse the centre of seventy five microparticles, for the same contrast enhancement equivalent to 5 cm of bone at an average X-ray energy of 25 keV. Although this seems like a significant number of particles this is equivalent to a thickness of 3.75 mm of PS-TaOx microparticles. Xu *et al.* [164] measured the volume of 37 liver tumours, these ranged from 2 to 700 ml (average 153.3 ml). Based on the average tumour volume of 153.3 mL and assuming a cube tumour this results in 0.02% of the tumour volume containing PS-TaOx microspheres. Additionally, current clinical embolization treatment delivers between 1x10^4 and 1.3x10^6 microparticles to the treatment site [162]. Therefore the location of the PS-TaOx microspheres is likely to be seen within a tumour volume.

4.5 CONCLUSIONS

In conclusion, radiopaque embolic particles have been successfully designed and synthesised containing TaOx nanoparticles. Theoretical calculations were used to ascertain an appropriate doping level of TaOx within the PS-TaOx microparticles for achievable X-ray contrast. The calculations showed that at 10% TaOx doping the PS-TaOx microparticles should be able to be seen within a tumour volume. Radiopaque embolic particles were successfully synthesised to contain up to 9.4% TaOx nanoparticles. The TaOx nanoparticles appear to be in an aggregated form within the PS-TaOx microparticles. The PS-TaOx microparticles showed significant contrast enhancement experimentally when compared to the polystyrene only microparticles. Additionally, effective contrast was observed with the 9.4 wt % doped PS-TaOx using a small animal CT scanner indicating they could be used for pre-clinical animal studies.

Chapter 5

Development of a radiosensitising embolic particle

5.1 INTRODUCTION

Radioactive embolic particles have previously been developed to combine an embolic agent with a radioactive element such as yttrium-90 to provide localized radiotherapy [68]. There are several difficulties involved in using radioactive elements such as their storage, handling, use and disposal [165]. For example, specialist facilities are required to ensure the safe storage of the embolic particles in lead pots, safe preparation areas for specific patient radiation doses and for the safe disposal of any radioactive material. Furthermore, care must be taken by medical staff to ensure they are not exposed to the radiation both during and after the implantation procedure.

A more useful approach would be to combine an embolic particle with a radiosensitiser which would be inert until activation by X-rays. Townley *et al.* [100, 101] have previously developed TiO_2 nanoparticles doped with rare earth elements which produce reactive oxygen species upon X-ray irradiation. In this study, the doped TiO_2 nanoparticles were bound onto the surface of the polystyrene embolic particles to create a PS-TiO_2 embolic particle which could be activated by X-rays.

5.1.1 Radiosensitisers

One of the major limitations of radiotherapy is that both healthy tissue and cancerous tissue can be affected by the ionizing radiation. Radiosensitisers have been used to make cancerous cells more susceptible to radiation thereby increasing the effectiveness of radiotherapy [166]. Radiosensitisers are composed of high atomic number (Z) elements which have a greater magnitude photoelectric photon absorption compared to soft tissue. This means that if a high Z material is present at high concentrations within the tumour then a greater magnitude dose will be delivered to the tumour than the surrounding healthy tissue [167]. The first radiosensitisers used contained iodine (Z=53) which has been shown to incorporate into cellular DNA and subsequently induce a radiation enhancement of approximately 3 fold [168]. More recently, nanoparticles such as gold [166], silver [169], TiO_2 [100, 101], and hafnium oxide have been investigated for their radiosensiting properties. For example, Hainfeld *et al.* [92] showed that mice treated in combination with gold nanoparticles and radiotherapy has an 86% one year survival while mice treated with radiotherapy alone had a 20% survival rate.

5.1.2 TiO_2

Titanium dioxide (TiO_2) is a wide band gap ($EG = 3.2\,eV$) semiconductor photoactive agent which has strong oxidization powers, is chemically inert, and has a low toxicity [170]. TiO_2 has been successfully used for environmental clean-up and solar energy conversion due to its high yield of reactive oxygen species (ROS) when illuminated by ultra violet (UV) light [171]. The most common types of TiO_2 induced ROS are hydroxyl ($OH^\bullet$) and peroxy (HO_2) radicals and singlet oxygen ($^1O_2$). More recently

TiO_2 has been shown to have photo-killing ability in a variety of cancer cells both *in vitro* [84, 172, 173] and *in vivo* [84, 174]. ROS have been shown to cause irreversible damage to tumour cells through the oxidation of various cellular components including the plasma, mitochondria, and nuclear membranes [175]. Additionally, ROS generation may aid treatment by causing vasculature damage and the indirect stimulation of inflammatory mediators [176]. Therefore the use of TiO_2 nanoparticles in cancer treatment has been widely studied for use in photodynamic therapy and radiotherapy.

Photodynamic therapy (PDT) is a minimally invasive treatment modality which works by combining a photosensitiser and light energy to convert molecular oxygen to reactive oxygen species [176]. The effectiveness of PDT is mainly dependent on the efficiency of singlet oxygen production [177]. PDT can only be used to treat cancers near the surface of the skin due to the limited penetration depth (up to 20 µm) of UV light in tissue and therefore its usefulness is limited [178].

Previous work by Townley *et al.* developed TiO_2 nanoparticles doped with rare earth elements (gadolinium (Gd), erbium (Er) and europium (Eu)) which have been shown to generate ROS specifically upon X-ray irradiation. X-rays have a much greater penetration depth of up to 14 cm compared to UV light [179] and hence they can be used to treat deeper tumours. *In vitro* studies using RH30 cells showed a 67% reduction in cell proliferation using TiO_2: 10%Gd@SiO_2 (3 Gy radiation treatment) and 66% reduction in cell proliferation with TiO_2: 10%Gd, 1%Er, 1%Eu@SiO_2 (3 Gy radiation treatment) nanoparticle treatment compared to the unirradiated nanoparticle control [101]. This means the nanoparticles could be selectively activated by the radiation. *In vivo* studies using TiO_2: 5%Gd, 1%Eu, 1%Er@SiO_2 (10 fractions of 2.5 Gy followed by 3 fractions of 2 Gy radiation treatment) injected intratumorally to mice xenografts showed a dramatic decrease in tumour size to approximately half the size of those treated solely with radiation [100].

More recently, titanate nanotubes have been investigated as a radiosensitizer on two brain cancer cell lines (U87-MG and SNB-19) showing that the nanotubes were internalised into the cells by endocytosis [98]. The nanotubes were not cytotoxic but could induce cell death in the presence of X-rays accompanied by an increase in reactive oxygen species. Furthermore, Rezaei-Tavirani *et al.* showed that there was a decrease in cell survival for both MCF7 and MKN-45 cells treated in combination with TiO_2 nanoparticles and ^{60}Co γ-rays [99] .

5.1.3 Aims and Objectives

The aim of work presented in this chapter was to develop a radio-sensitising embolic particle using doped TiO_2 nanoparticles, which had previously been shown to have radiosensitising properties. The first objective was to find a suitable method for synthesising the PS-TiO_2 embolic particles. Further objectives were to demonstrate the ability of PS-TiO_2 nanoparticles to produce reactive oxygen species *in chemico* and to determine their effects on cell proliferation after X-ray irradiation.

5.2 MATERIALS AND METHODS

5.2.1 Doped TiO_2 NP Synthesis

Doped TiO_2 nanoparticles were prepared by the sol gel method. Rare earth metals (gadolinium (III) nitrate hexahydrate (Aldrich), europium (III) nitrate hydrate (Aldrich), erbium (III) nitrate pentahydrate (Aldrich) and terbium (III) nitrate pentahydrate (Aldrich)) were dissolved at the molar % indicated in the text in 30 ml of anhydrous isopropanol (Aldrich). Subsequently, 10 ml of titanium (IV) isopropoxide (Aldrich) was added and this was dropped into a 500 ml solution of isopropanol (Fisher) and ddH_2O (50:50 by volume) under vigorous stirring. The solution was stirred for a further 10 minutes and then the particles were left to settle. The supernatant was removed; the particles were resuspended in isopropanol (200 ml), stirred for 10 minutes and again left to settle. The particles were then filtered using a Büchner funnel under vacuum, resuspended in ddH_2O and autoclaved. Finally the particles were fired (Carbolite RWF 1200 furnace) at 300 °C, 500 °C and 700 °C in air for 3 hours.

5.2.2 SiO_2 coating of doped TiO_2 NP

A SiO_2 coating was added to the TiO_2 nanoparticles (TiO_2@Si) to limit aggregation and increase biocompatibility of the particles. Previously prepared TiO_2 nanoparticles (2 g) were resuspended in 100 ml ddH_2O [solution 1]. Simultaneously, 1.89 ml 3-Mercaptopropyl trimethoxysilane (Aldrich) was dissolved in 50 ml of ddH_2O [solution 2]. Solution 2 (10 ml) was added to solution 1 and this was left stirring for one hour [Solution 3]. Sodium silicate (20 ml) was then added to solution 3, the solution was centrifuged and washed in ddH_2O twice before drying under vacuum. The optimum incubation time for the SiO_2 coating was determined by taking samples at set time points after addition of the sodium silicate and subsequently measuring the zeta potential.

5.2.3 PS-TiO_2 embolic particle sysnthesis

Three methods were used to create the PS-TiO_2 embolic particles, i) a one pot method using a cross linking agent, ii) a polyelectrolyte method and iii) a sintering method (Fig 5.1). PS-TiO_2 embolic particles were synthesised using TiO_2@Si, TiO_2: 1%Gd, 1%Eu@Si, TiO_2: 1%Gd, 1%Tb@Si, TiO_2: 5%Gd, 1%Eu, 1%Er@Si nanoparticles by the methods described in sections 5.2.3.1 to 5.2.3.3 below.

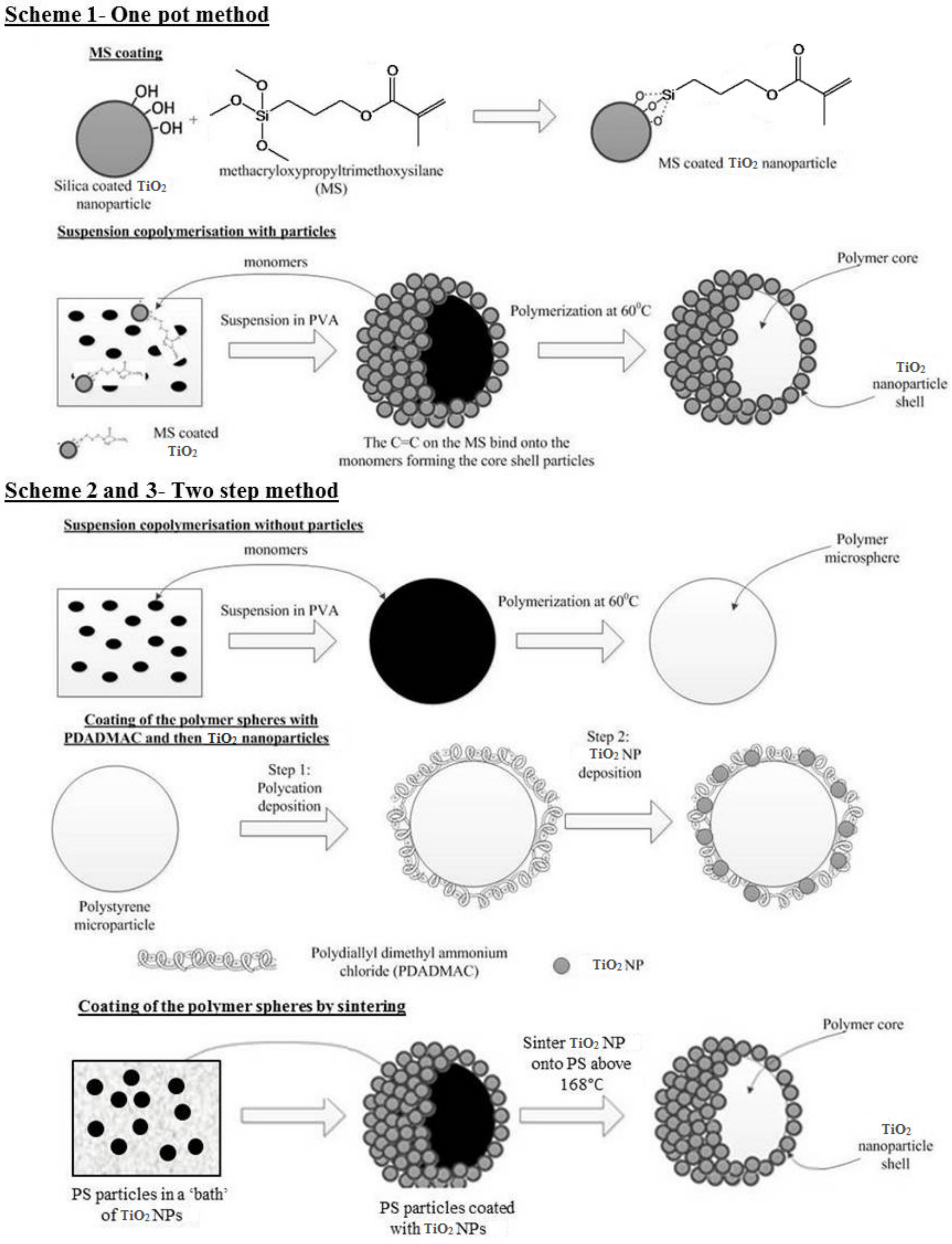

Figure 5.1: Schematic of the three synthesis methods investigated for creating the PS-TiO$_2$ embolic particles. Scheme 1) A one pot method which coats the TiO$_2$ nanoparticles with a cross linking agent Methacryloxypropyl trimethoxysilane (MS). The MS binds onto the surface of the polystyrene during the polymerization reaction to form the PS-TiO$_2$ embolic particles. Scheme 2) Polystyrene particles are initially prepared by suspension polymerization and then the positively charged PDADMAC is used to electrostatically bind the negatively charged TiO$_2$ onto the surface of the polystyrene to create the PS-TiO$_2$ embolic particles. Scheme 3) As for Scheme 2, polystyrene particles are prepared by suspension polymerization and then the TiO$_2$ nanoparticles are sintered onto the surface of the polystyrene at a temperature above the glass transition temperature of polystyrene.

5.2.3.1 One pot method

The one pot method is based on the method presented by Ihara *et al.* [116] for preparing 50 µm SiO_2 polystyrene core shell particles. In the original method the SiO_2 microparticles were coated with a cross linking agent, Methacryloxypropyl trimethoxysilane (MS) which allows the SiO_2 to be suspended on the outside of the monomer droplet. During the polymerization reaction the carbon-carbon double bond is able to bind into the monomer therefore anchoring the SiO_2 microparticles onto the surface of the polystyrene particle to create the polystyrene-silicon dioxide core shell particle. A reaction scheme for the polymerisation reaction of styrene and EDGMA is provided in Fig 3.1.

The steps for preparing the PS-TiO_2 embolic particles are outlined below. SiO_2 coated TiO_2 nanoparticles (1.5 g) were resuspended in 30 ml of toluene. MS (1.5 ml) was added and the mixture was stirred for one hour. The temperature was then increased to 110 °C and left stirring for 72 hours. The particles were then washed with toluene (Sigma) and methanol (Rathburn) and dried under vacuum. MS coated TiO_2 nanoparticles (1 g) were them mixed with styrene, EDGMA and AIBN and then the steps outlined in section 3.3.1 were followed to create the PS-TiO_2 embolic particles.

5.2.3.2 Polyelectrolyte method

The polyelectrolyte method is based on the method presented by Radice *et al.* [180] for the synthesis of polystyrene-TiO_2 core shell particles. The positively charged PDADMAC (Poly(diallyldimethylammonium chloride) solution) is used to electrostatically bind the negatively charged TiO_2 nanoparticles onto the surface of the polystyrene particles to create the PS-TiO_2 embolic particles. In brief, polystyrene spheres were prepared by the method described in section 3.3.1. The polystyrene spheres (0.1 g) were resuspended in ddH$_2$O (25 ml). Ammonium hydroxide (500 µl; Sigma) was added and the mixture stirred for 15 minutes [sol 3]. Potassium chloride (0.44 g, Sigma) was dissolved in ddH$_2$O and then 5.77 ml of PDADMAC (20% in water, average molecular weight 100,000-200,000, Sigma) was added [sol 4]. Solution 4 (5 ml) was added to solution 3 and this was stirred for one hour. The polystyrene spheres were then centrifuged and washed in 3 ml of ddH$_2$O to remove any excess PDADMAC. The spheres were then resuspended in ddH$_2$O and 150 µl of ammonium hydroxide was added. TiO$_2$ nanoparticles (0.06 g) were added and this was stirred for one hour. The particles were then centrifuged, washed in isopropanol (Fisher) and dried under vacuum.

5.2.3.3 Sintering method

The final method used to create the PS-TiO$_2$ embolic particles was based on the method presented by Fabiyi *et al.* [181] for the synthesis of polystyrene-TiO$_2$ microparticles by sintering the P25 (commercially available TiO$_2$ nanoparticles, Degussa) onto the surface of the polystyrene. The manufacturer states the P25 nanoparticles are 21 nm however they do not comment on the presence of any coating [182]. In brief PS microparticles, prepared by the method described in section 3.3.1, were mixed (1:9 v/v) with SiO$_2$ coated TiO$_2$ nanoparticles. The TiO$_2$ nanoparticles were sintered onto the surface of the polystyrene spheres by heating the mixture to at least 168 °C at a ramping rates of seven degrees per minute and then holding at that temperature for fifteen minutes in a Carbolite RWF 1200 furnace. The PS-TiO$_2$ embolic particles were separated from the excess TiO$_2$ nanoparticles using a sucrose density gradient containing 60% and 15% sucrose. The gradient was prepared by layering 15 ml of a 15% sucrose solution on top of 15 ml of a 60% sucrose solution in a 50 ml centrifuge tube. The tube was then placed on its side for at least 30 minutes to allow the gradient to form. The particles were then added to the top of the gradient and the tube was centrifuged at 8600 g for one hour. A visible band of PS-TiO$_2$ particles formed which was extracted, centrifuged at 8600 g and washed in ddH_2O three times to remove sucrose (Fig 5.2). Finally the prepared PS-TiO_2 particles were dried overnight under vacuum.

In the final iteration, PS-TiO_2 microparticles were prepared using commercial 39 µm polystyrene divinlybenzene (DVB) microparticles (Duke scientific) and TiO_2 nanoparticles (TiO_2 (JM) and TiO_2: 5%Gd (JM)) provided by Johnson Matthey synthesised by flame spray pyrolysis. Johnson Matthey has a Flame Spray Pyrolysis facility with the capability to produce up to $100\,g\,h^{-1}$ of nanopowder product and therefore it is a possible method for the scaling up the production of nanoparticles for commercial applications [183]. Flame spray pyrolysis works by spraying a liquid phase containing the metal precursor(s) dissolved in a solvent into a flame zone where it combusts producing nanosized metal or metal oxide nanoparticles. The PS-TiO_2 particles were prepared by sintering as described above.

5.2.4 Particle characterization

The size of the TiO_2 and doped TiO_2 nanoparticles was measured by both TEM and centrifugal sedimentation as described in section 2.1.2 and section 2.1.5 respectively. TEM was also used to characterise the morphology and crystal structure of the TiO_2 and doped nanoparticles. The surface morphology and nanoparticle coverage of the PS-TiO_2 was examined by SEM as described in section 2.1.3. The change in zeta potential before and after firing, SiO_2 coating and MS coating the TiO_2 and doped TiO_2 nanoparticles was measured as described in section 2.1.6. The crystal structure of the TiO_2 and doped TiO_2 nanoparticles was assessed by XRD as described in section 2.1.7. The introduction of the rare earth elements into the TiO_2 nanoparticles was confirmed by both EDX as described in section 2.1.4 and by their phosphorescence signal. The phosphorescence signal of a powder sample was measured using a Cary Eclipse Fluorescence Spectrophotometer

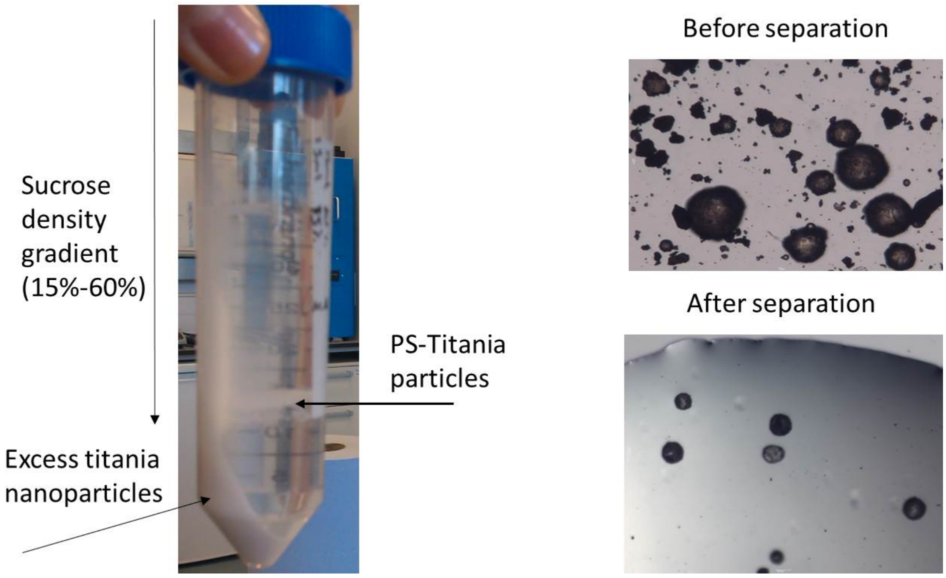

Figure 5.2: Separation of PS-TiO_2 core shell particles from excess TiO_2 nanoparticles using a sucrose density gradient. A) Representative photograph of the centrifuge tube showing the excess TiO_2 nanoparticles and the band containing the PS-TiO_2 embolic particles which could be extracted. Representative brightfield microscopic images of the TiO_2: PS-TiO_2 mixture B) before and C) after separation indicating that the sucrose density gradient was an efficient way to separate out the PS-TiO_2 embolic particles.

(Agilent Technologies) at the appropriate excitation wavelength as provided in the text.

5.2.5 Coumarin assay

The ROS generation from the particles was measured *in chemico.* Coumarin reacts with reactive oxygen species to produce 7-hydroxycoumarin which is a highly fluorescent and stable compound [184].

5.2.5.1 UV irradiation

For the UV irradiation experiments, previously prepared TiO_2 and doped samples were resuspended in ddH_2O at $0.03\,\mathrm{mg\,mL^{-1}}$. Resuspended samples (100 µl) were added to 5 ml of $2\,\mathrm{mg\,ml^{-1}}$ coumarin (aq; Sigma) in triplicate. Samples were irradiated in a UVA cube 400 (Honle, Munich Germany) and 500 µl samples were removed at set time points up to two hours during the experiment. Samples were centrifuged at 2300g to remove any particulate TiO_2 and 200 µl of the supernatant was diluted in 1.8 ml of ddH_2O. Initially the fluorescence was measured using a Cary Eclipse Fluorescence Spectrophotometer (Agilent Technologies; Excitation 345 nm, Emission 450 nm). To increase sample throughput, later experiments used a Tecan Infinite f200 plate reader to measure the fluorescence of the supernatant using Ex. 340 nm and Em. 465 nm filters. To ensure that the results obtained from both the spectrophotometer and the plate reader were equivalent an initial test was carried out to measure the fluorescence of the samples by both techniques. No significant difference ($p \geq 0.05$) between any of the samples tested was observed and therefore it was assumed that the results were comparable between the different methods. Commercially available 21 nm TiO_2 nanoparticles (Degussa P25; Sigma), were used as an internal control for all experiments. The activity of P25 was set to 100% and the activity of the prepared TiO_2 samples was expressed as a percentage of this so that samples could be compared across experiments.

5.2.5.2 X-ray irradiation

For the X-ray irradiation experiments nano and microparticle samples were resuspended in 150 µL of 2 mg ml^{-1} coumarin (aq) on three separate 96 well plates. The following samples were used i) 25 µg PS, ii) 15 µg TiO_2: 5%Gd, 1%Er 1%Eu@Si, iii) 25 mg PS-TiO_2: 5%Gd, 1%Er 1%Eu@Si, iv) 15 mg P25 and v) coumarin alone. The 96 well plates were exposed to a broad spectrum of X-ray energies up to 250 keV with and average energy of approximately 80 keV–90 keV and a radiation dose of 3 Gy, 5 Gy or 10 Gy was given. After irradiations, the samples were centrifuged to pellet any particles and the fluorescence of the supernatant (100 µL) was measured by Tecan Infinite f200 plate reader using Ex. 340 nm and Em. 465 nm filters.

5.2.6 Cell death experiments

The effectiveness of the nanoparticles and the nanoparticle coated microparticles was determined *in vitro* using the RD cell line. RD cells were seeded on three separate 96 well plates at 1x10^4 cells per well in 150 µl of fresh cell culture media and incubated overnight to allow the cells to adhere to the plate. After 24 hours both plates of cells were treated, in four or six replicates, with either i) 15 µg of TiO_2 nanoparticles, ii) 150 µg of PS-TiO_2 microparticles or v) phosphate buffered saline (PBS) as a control. The TiO_2 nanoparticles were either TiO_2 (JM), TiO_2: 5%Gd (JM) or P25. After another 24 hours, each plate of particle-treated cells was exposed to a broad spectrum of X-ray energies up to 250 keV with and average energy from 80 keV–90 keV and a dose of either 0 Gy, 3 Gy or 5 Gy. The exact exposure time was not measured since it is related to the radiation dose received by the cells but it was a maximum of 15 minutes. On the final day of the experiment, another 24 hours later, cell proliferation was determined by manual cell counting using a hemocytometer as described in section 2.3.2.2.

5.3 RESULTS AND DISCUSSION

5.3.1 Synthesis of 65 nm doped TiO_2 nanoparticles

TiO_2 nanoparticles and TiO_2 nanoparticles doped with gadolinium, europium, erbium and terbium were successfully synthesized and characterised using several methods. TEM and disc centrifugation was used to measure the physical and hydrodynamic diameter of the TiO_2 and doped TiO_2 nanoparticles as approximately 65 nm particles and 75 nm respectively (Fig 5.3A,B,D). The Fourier transform of the TiO_2 nanoparticle in Fig 5.3B shows a series of dots indicating that the nanoparticle is crystalline (Fig 5.3 C). The introduction of the rare earth dopants into the TiO_2 nanoparticles was confirmed using phosphorescence spectra and EDX. The fluorescence spectrum of the TiO_2:

1%Gd, 1%Eu and TiO_2: 1%Gd, 1%Tb confirms the presence of europium and terbium within each sample receptively (Fig 5.3E). The EDX spectrum confirms the presence of gadolinium, europium and erbium within the TiO_2: 5%Gd, 1%Eu, 1%Er nanoparticles at approximately the level of doping expected (Fig 5.3F).

5.3.2 TiO_2 and doped TiO_2 nanoparticles produce reactive oxygen species under UV irradiation

The ability of the TiO_2 and doped TiO_2 nanoparticles to produce reactive oxygen species under UV irradiation was used as a proof of concept system for the X-ray activation experiments. The photoactivity of P25 was used as an internal control across all experiments and data is expressed as a percentage of P25 activity. The optimum firing temperature was determined by measuring the photoactivity of the particles after firing at 300 °C, 500 °C and 700 °C. There was an increase in activity for the TiO_2 sample from (34.8% ± 0.5) to (47.0% ± 0.1) after firing at 300 °C and (38.5% ± 0.4) after firing at 500 °C. However when the sample was fired at 700 °C the activity dropped to (11% ± 0.1) which is less than the unfired sample (Fig 5.4A). TiO_2 is found in one of three crystal phases, rutile, anatase or brookite with anatase generally considered as most active photocatalytic form [185, 186, 187]. The crystal phase of the unfired TiO_2 sample is anatase the most active form, however when the TiO_2 sample is fired at 700 °C the crystal phase changes to mainly rutile which is significantly less active and this is explains the drop in activity after firing at 700 °C (Fig 5.4B,C).

For both the doped TiO_2 samples the photoactivity increased with increasing firing temperature from (42% ± 1.5) (unfired) to (64.4% ± 2.2) (fired at 700 °C) for the TiO_2: 1%Gd, 1%Eu nanoparticles and from (8.2% ± 0.1) (unfired) to (21.9% ± 3.4) (fired

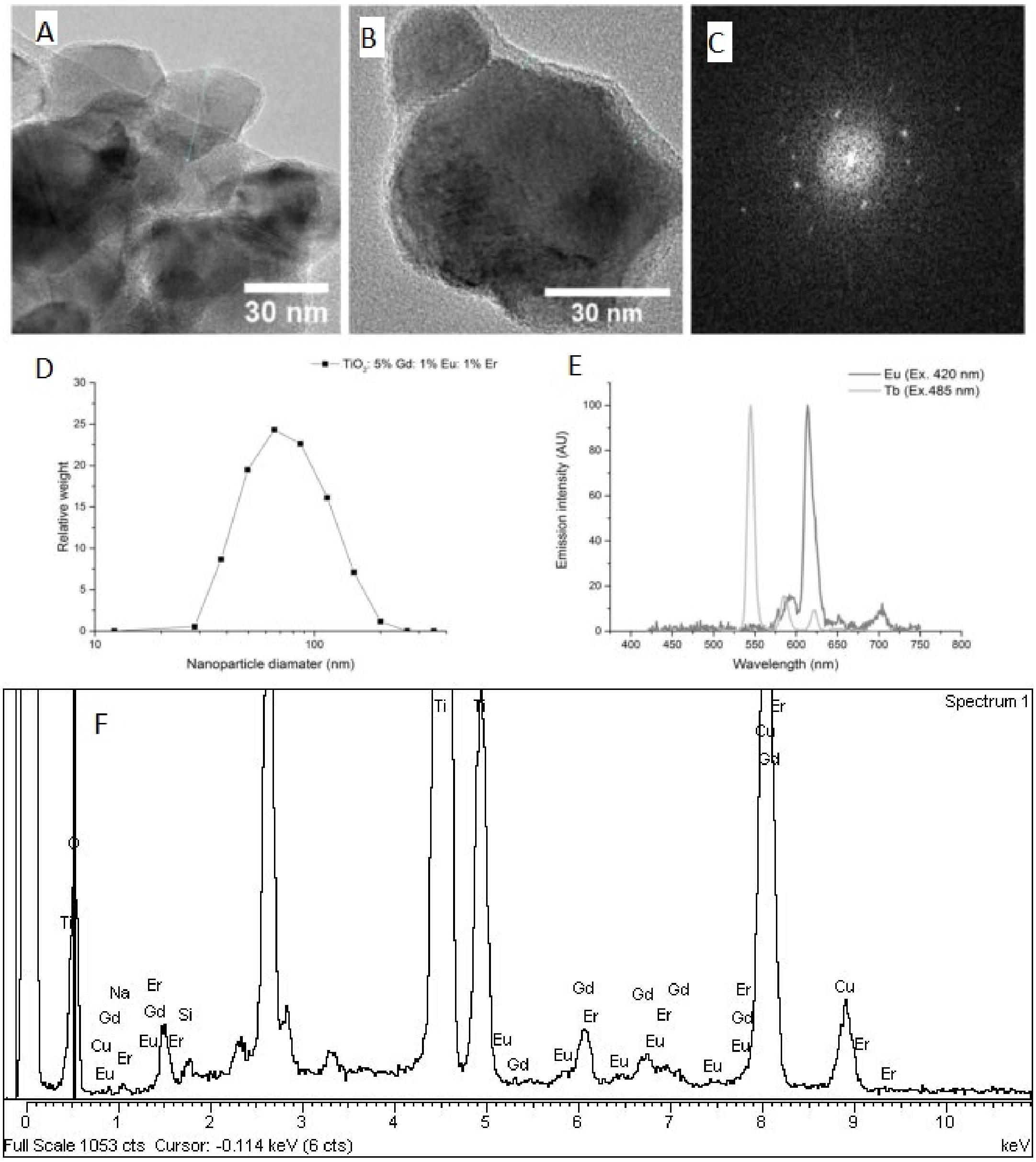

Figure 5.3: TiO_2 nanoparticle synthesis. Representative TEM images of A) fired and B) SiO_2 coated TiO_2 nanoparticles showing approximately 65 nm particles. B) shows a single crystalline nanoparticle with a 2 nm amorphous SiO_2 layer. C) Fast Fourier Transform of the TiO_2 nanoparticle in B) with single dots indicating that it is crystalline. D) Representative disc centrifuge trace for TiO_2: 5%Gd, 1%Eu: 1%Er showing nanoparticles with a peak diameter of 70 nm. E) Representative phosphorescence signal from the TiO_2 nanoparticles confirming the presence of europium and terbium within the TiO_2: 1%Eu and TiO_2: 1%Tb nanoparticles receptively. F) Representative EDX trace confirming the presence of gadolinium, europium and erbium within the TiO_2: 5%Gd, 1%Eu, 1%Er nanoparticles.

at 700 °C) for the TiO_2: 1%Gd, 1%Tb nanoparticles (Fig 5.4A). The europium doped sample showed significantly greater magnitude photoactivty than the terbium doped sample at all firing temperatures measured. After firing at 700 °C the TiO_2: 5%Gd, 1%Eu crystal phase of the TiO_2 was still antatase indicating that it was still in its most active phase and therefore the highest activity was observed (Fig 5.4D). Xu *et al.* [188] investigated the effects of europium doping on the structure, luminescence properties and photocatalytic activity of TiO_2. They found that the transformation of anatase to rutile for undoped TiO_2 occurred between 300 to 500 °C compared with 500 to 700 °C for the europium doped TiO_2. Additionally, Zhang *et al.* [189] found that doping at 1% europium maintained that anatase crystal phase when firing at 900 °C for one hour. This suggests that the europium stabilizes the crystal phase and therefore increases the temperature at which rutile forms. Therefore, a firing temperature of 700 °C was used for all further experiments using doped TiO_2 nanoparticles.

5.3.3 SiO_2 coating increases TiO_2 nanoparticle stability and photoactivity

Nanoparticles which have a zeta potential of $\leq \pm 30\,\mathrm{mV}$ can be deemed unstable and therefore they are likely to aggregate. The zeta potential of the unfired and fired TiO_2 nanoparticles is between 30 mV and −30 mV across a range of pH values from pH2-10 thus the nanoparticles have a tendency to aggregate (Fig 5.5A). Therefore a thin SiO_2 layer was used to coat the nanoparticles which can be observed as an approximately 2 nm amorphous layer surrounding the crystalline TiO_2 on the TEM image (Fig 5.3B). The optimum incubation time for the SiO_2 coating was determined by taking samples at set time points after addition of the sodium silicate and subsequently measuring the zeta potential. After 6 minutes SiO_2 incubation time the zeta potential was $\geq -30\,\mathrm{mV}$ at pH7 and therefore the suspension could be deemed stable (Fig 5.5B). To ensure effective

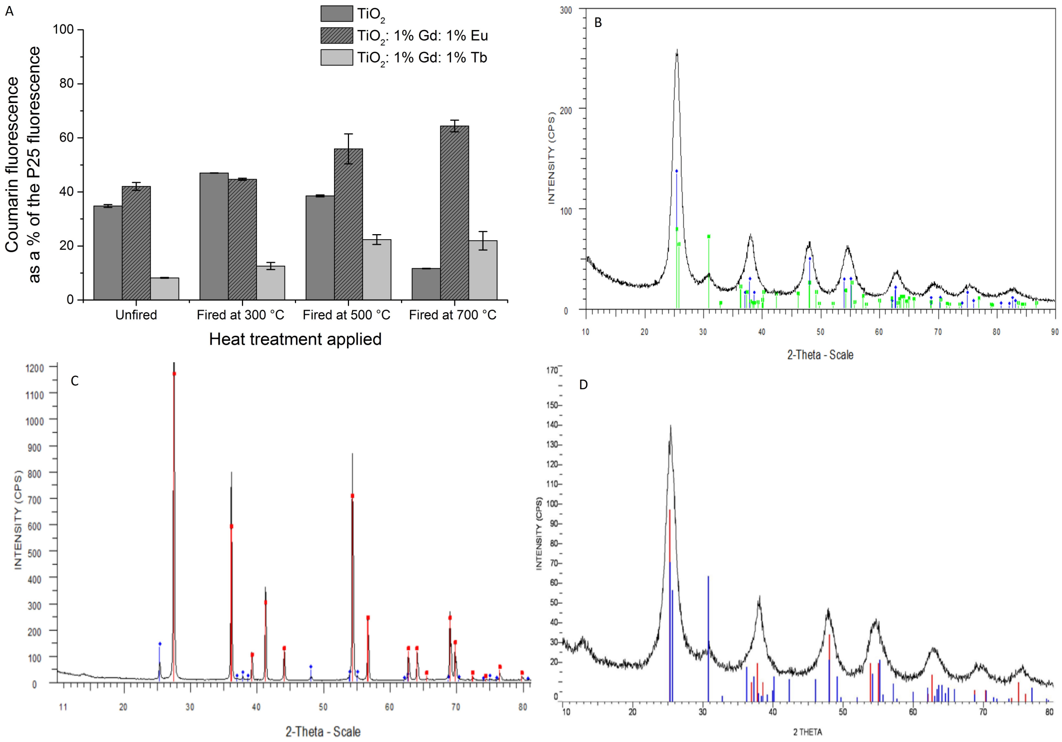

Figure 5.4: Effect of TiO_2 nanoparticle firing temperature on photoactivity. A) Results from independent experiments (n=3) showing the change in photoactivity with firing temperature for TiO_2, TiO_2: 1%Eu and TiO_2: 1%Tb after two hours UV irradiation. Data is presented as mean ± SD of triplicate samples and expressed as a % of the P25 photoactivity. P25 was used as an internal control for all experiments. B-D) Representative XRD traces for B) unfired TiO_2 nanoparticles, C) TiO_2 nanoparticles fired at 700 °C and D) TiO_2: 5%Gd, 1%Eu, 1%Er nanoparticles fired at 700 °C. B and D) show that the most abundant crystal phase of the TiO_2 nanoparticle is antase while C) shows the crystal phase is rutile

coating of all the particles an optimum incubation time of 10 minutes was selected for all subsequent experiments to minimise the thickness of the SiO_2 coating while ensuring that aggregation was limited. Applying the SiO_2 layer resulted in an increase in the zeta potential to $\geq -30\,\mathrm{mV}$ at pH values ≥ 4 which would increase the stability of the suspension and limit aggregation (Fig 5.5A). As healthy tissue is at pH 7.4 and the tumour microenvironment is slightly acidic [190] this means that the SiO_2 coated particles are unlikely to aggregate within the body.

Furthermore, the SiO_2 coating significantly ($p \leq 0.05$) increased the photoactivity of the TiO_2: 1% Eu and TiO_2:1% Tb by approximately 30% because the SiO_2 layer increased the surface area of the particles and therefore more was able to react to produce reactive oxygen species (Fig 5.5C). Egerton *et al.* [191] showed that SiO_2 coatings below 3% have an photoactivity greater than uncoated TiO_2 but as you increase the % of SiO_2 coating the photoactivity decreases. This is because a patchy coating increases the surface area of the particles and hence an increased exposed surface area leading to an increase in photoactivity. However a complete coating limits the contact of the TiO_2 with the water molecules and therefore reduces the generation of reactive oxygen species.

5.3.4 Synthesis of PS-TiO_2 embolic particles

Three methods were investigated for preparing the PS-TiO_2 embolic particles: i) the one pot method; ii) the PDADMAC polyelectrolyte method and iii) the sintering method.

5.3.4.1 One pot method

The one pot method coats the TiO_2 nanoparticles with Methacryloxypropyl trimethoxysilane (MS) which then allows the TiO_2 to be anchored onto the the surface of the polystyrene spheres during the polymerization reaction by cross-linnking with the

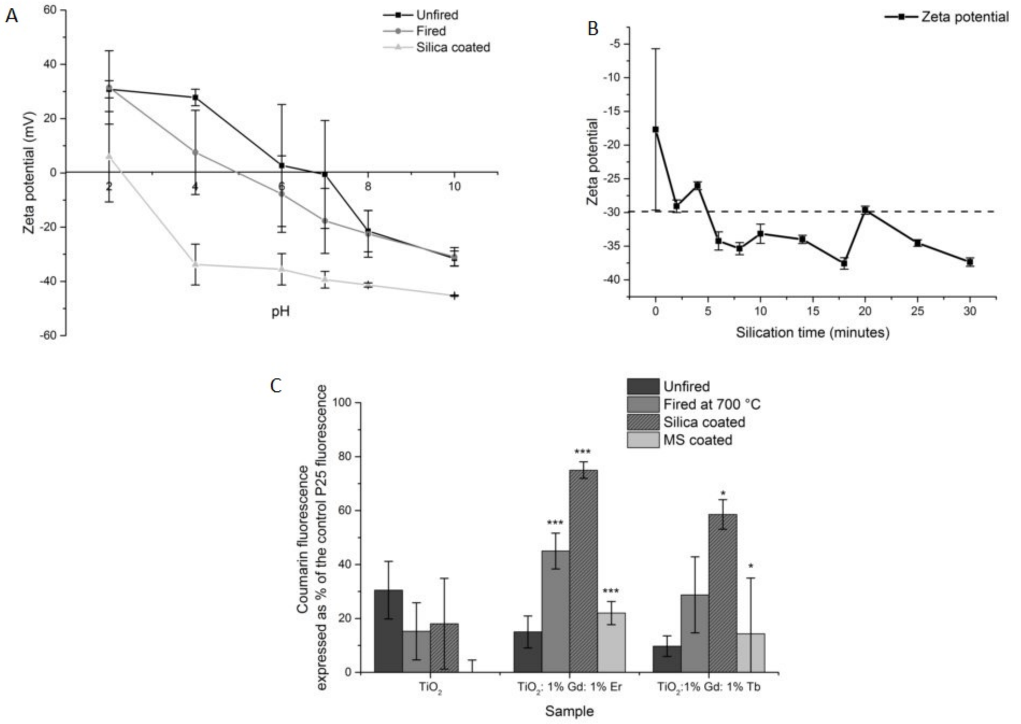

Figure 5.5: Effect of SiO_2 and Metharcyrloxypropyl trimethoxisilane (MS) coating of the TiO_2 nanoparticles on nanoparticle zeta potential and photoactivity. A) Results from independent experiments (n=3) showing the change in zeta potential across a range of pH values from pH2-10 for TiO_2 nanoparticles which are unfired, fired and SiO_2 coated. Data is presented as mean ± of triplicate samples. B) Trace showing the change in zeta potential with silication time for optimization of the synthesis. Data is presented as mean ± SD of triplicate samples. C) Results from independent experiments (n=3) showing the change in photoactivity of TiO_2, TiO_2: 1%Gd, 1%Eu and TiO_2: 1%Gd, 1%Tb nanoparticles which are unfired, fired, SiO_2 coated and MS coated. Data is presented as mean ± SD of triplicate samples and significance was tested using a two tailed t-test (*$p \leq 0.05$, ***$p \leq 0.005$).

polymer core. The one pot method produced polystyrene spheres ranging from 30 to 150 µm in diameter however they had variable and patchy coverage with the TiO_2 nanoparticles which presented as aggregates (Fig 5.6A,B). It is feasible that the coverage of the embolic particles could have been increased by increasing the mass of TiO_2 used within the synthesis. The mass of TiO_2 used was the same as that described in the original paper for SiO_2, however SiO_2 is less dense than TiO_2 and therefore an increased mass should have been used to allow for complete coverage. This was not attempted because it was found that the MS coating inhibited the photoactivity of the TiO_2 nanoparticles reducing the activity to (0% ± 4.6), (22% ± 4.3) and (14.3% ± 20.6) for the TiO_2, TiO_2: 1%Eu and TiO_2: 1%Tb respectively (Fig 5.5B). This is likely to be due to the MS coating limiting the contact of the TiO_2 with the surrounding water which limits the potential for ROS to form and thus no photoactivity is observed. Similarly, Gilles *et al.* showed that coating gold nanoparticles with a range of coatings, such as polyethylene glycol (PEG) or human serum albumin, dramatically reduced $OH^{\bullet}$ radical production by up to 92% and the reduction correlated well with the amount of DNA damage observed [192].

5.3.4.2 Polyelectrolyte method

The second method used a positively charged polyelectrolyte PDADMAC to electrostatically bind the TiO_2 nanoparticles onto the surface of the pre-prepared polystyrene spheres. The PS particles have a zeta potential of (+17.9 ± 9.8) mV therefore they are positively charged in ddH_2O (pH∼7) (Table 5.1). To coat the PS particles with the positively charged PDADMAC, the PS particles were first incubated in ammonium hydroxide to induce a negative surface charge (zeta potential of (-10.7 ± 7.8) mV) on the PS particles. Successful coating of the PS particles with the PDADMAC was confirmed by the increased positive charge of the PS particles in both ddH_2O and ammonium hydroxide. Finally the negatively charged TiO_2 nanoparticles (zeta potential $\geq -30\,\mathrm{mV}$

(Fig 5.3G)) were able to bind onto the positively charged PS@PDADMAC.

This method showed improved coverage with approximately 50% of the polystyrene spheres covered with TiO_2 nanoparticles (Fig 5.6C,D). The TiO_2 nanoparticles are present as individual unaggregated particles of approximately 70 nm. However, this method was not investigated further due to the sub-optimal coverage of the polystyrene spheres and the risk that the TiO_2 nanoparticles could detach from the polystyrene spheres and be released within the body. For example, the enzymatic degradation of a PGEDMC/Hb polyelectrolyte film has been shown to release 80% of the encapsulated FITC while no release was observed in the absence of enzyme [193]. Therefore it is possible that enzymes in the blood stream could cause the degradation of the PDADMAC and release the TiO_2 nanoparticles from the embolic particles reducing their effectiveness.

Table 5.1: Zeta potential of the PS particles at various stages during the synthesis of the PS-TiO_2 embolic particles prepared by the polyelectrolyte method.

	Zeta potential
PS particles	+17.9 ± 9.8
After the addition of ammonium hydroxide	-10.7 ± 7.8
After the addition of PDADMAC	+15.2 ± 3.3
After washing the particles in ddH$_2$O	+36.3 ± 2.0
After the second addition of ammonium hydroxide	+21.7 ± 10.7
After the addition of the TiO_2 nanoparticles	+31.1 ± 0.3

5.3.4.3 Sintering method

The final and most successful method for producing the PS-TiO_2 particles used a sintering method. The pre-prepared polystyrene spheres were suspended in a bath of TiO_2 and then heated until the surface of the polystyrene melted allowing the

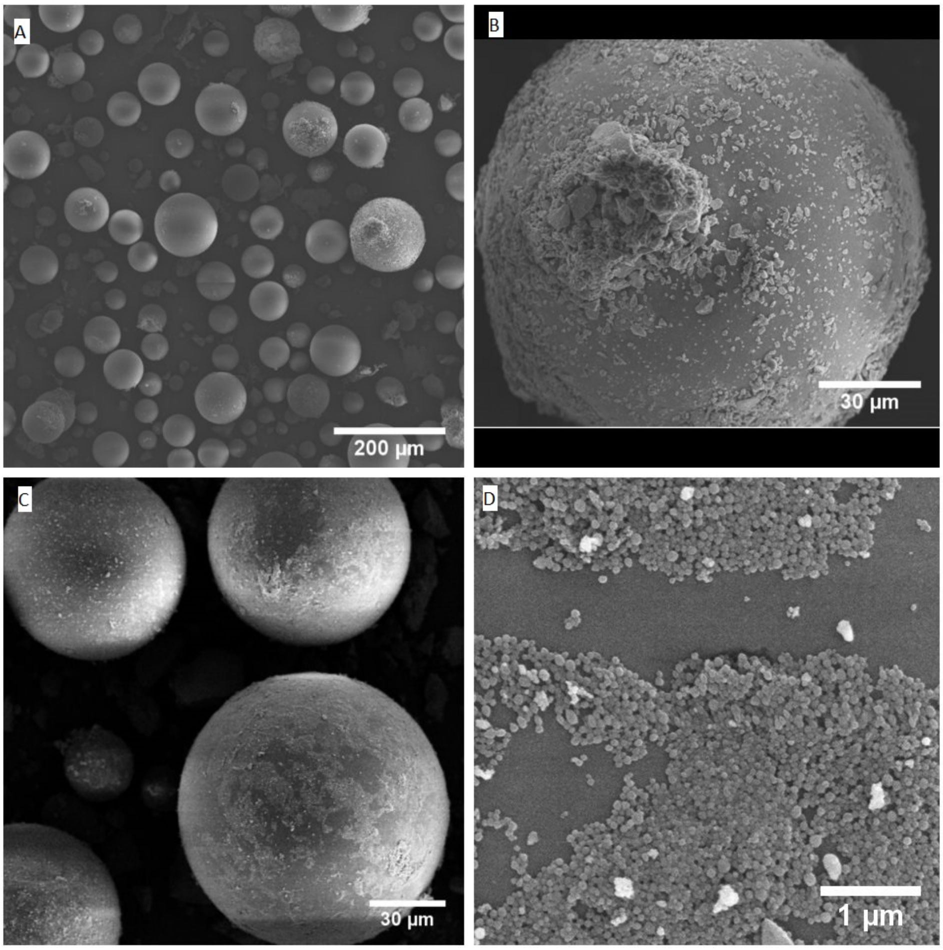

Figure 5.6: PS-TiO$_2$ core shell particle synthesis. A and B) Representative SEM images of PS-TiO$_2$ core shell particles synthesised using the one pot method and showing poor coverage of the the polystyrene with the TiO$_2$ nanoparticles. C and D) Representative SEM images of the PS-TiO$_2$ core shell particles synthesised using the PDADMAC polyelectrolyte method showing improved albeit suboptimal coverage.

TiO_2 to bind onto the polystyrene core. The mixture was heated to $\geq$ 165 °C as this is the glass transition temperature of the polystyrene spheres (Fig 5.7). Sintering the polystyrene TiO_2 mixture at 165 °C showed approximately 70% coverage with the TiO_2 nanoparticle while increasing the sintering temperature to both 200 °C and 230 °C increased the coverage to almost 100% (Fig 5.7B-D). It is important that the sintering temperature is not increased past 260 °C where the polystyrene starts to burn and the mass decreases (Fig 5.7A). Furthermore, as previously discussed in section 5.3.2, firing the TiO_2 nanoparticles can change their crystal structure to a less active form therefore the sintering time and temperature was kept to minimum and the activity of the unbound TiO_2 nanoparticles was tested after sintering to ensure there was no significant difference ($p \geq 0.05$) in activity before and after sintering (data not shown).

5.3.5 Doped TiO_2 nanoparticles and PS-TiO_2 embolic particles produce reactive oxygen species upon X-ray radiation

To confirm X-ray activation of the TiO_2 nanoparticles *in chemico*, ROS generation was assessed using the coumarin assay. The doped TiO_2 nanoparticles (TiO_2:5% Gd: 1% Eu: 1% Er@Si) showed a significant ($p \leq 0.05$) increase in the coumarin fluorescence of (3.5% ± 1.2), (7.8% ± 0.3) and (7.5% ± 2.5) for nanoparticles treated with 3 Gy, 5 Gy and 10 Gy doses of X-ray radiation respectively (Fig 5.8). This shows that the X-rays are able to induce the photocatalyic response to produce reactive oxygen species of the doped TiO_2 nanoparticles. The commercial P25 nanoparticles did not show any significant change in ROS after X-ray treatment. Both the TiO_2: 5%Gd, 1%Eu, 1% Er@Si and the P25 behave similarly to the data presented by Townley *et al.* [101].

The PS microparticles showed no significant increase in ROS indicating that the core of the embolic particles is inert (Fig 5.8). However when the particles have been coated

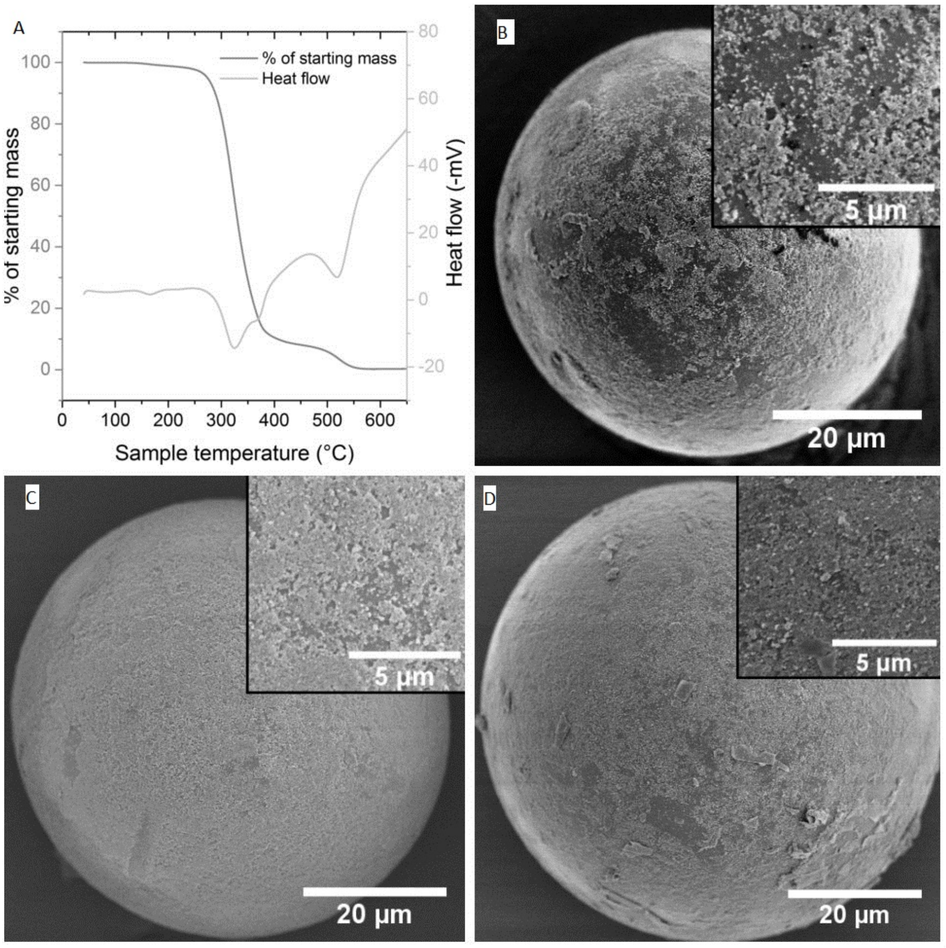

Figure 5.7: Optimization of the PS-TiO$_2$ synthesis using the sintering method. A) Representative thermal gravimetric analysis of the polystyrene spheres showing the % of the starting mass and the heat flow traces. A glass transition temperature of 165 °C is observed. Representative SEM images of the PS-TiO$_2$ core shell particles after sintering at B) 168 °C, C) 200 °C and D) 230 °C.

with the TiO_2: 5%Gd, 1%Eu, 1%Er@Si nanoparticles there was a significant ($p \leq 0.05$) increase in coumarin fluorescence of (3.5% ± 2.0) for the samples treated with 3 Gy showing that the embolic particle could be effective in generating ROS.

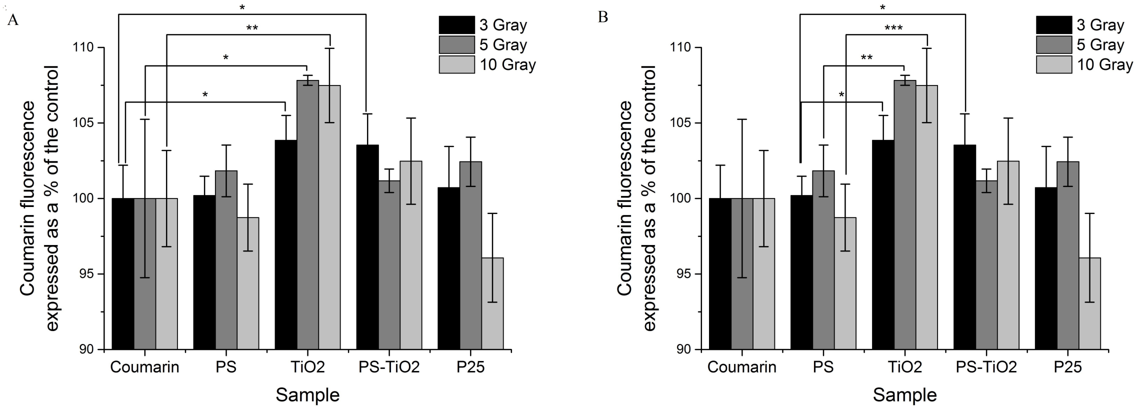

Figure 5.8: X-ray activation of PS, TiO_2: 5%Gd, 1%Eu, 1% Er@Si nanoparticles, and PS-TiO_2: 5%Gd, 1%Eu, 1%Er@Si embolic particles to produce reactive oxygen species. Results from independent experiments (n=3) showing the change in coumarin fluorescence for each of the samples after 3 Gy, 5 Gy and 10 Gy doses of X-ray radiation. Similarly to the UV experiments, P25 was used as a control. Data is presented as mean ± SD of triplicate samples and expressed as a percentage of the coumarin fluorescence with no particle treatment. Significance was tested using a two tailed t-test (*$p \leq 0.05$, **$p \leq 0.01$, ***$p \leq 0.01$) and A) shows significance w.r.t no particle coumarin fluorescence and B) shows significance w.r.t PS particle coumarin fluorescence.

5.3.6 Flame spray pyrolysis TiO_2 nanoparticles obtained from Johnson Matthey

Johnson Matthey supplied the group with both TiO_2 and 5% gadolinium doped TiO_2 nanoparticles synthesised by flame spray pyrolysis (FSP). These particles were supplied as part of another project within the lab to investigate the potential of using FSP for the production of doped TiO_2 nanoparticles. FSP is a possible method of producing nanoparticles on a commercial scale due to its high throughput of up to 100 g h^{-1} of nanopowder product [183]. Therefore, much larger batches of the nanoparticles could be obtained compared to the sol gel method synthesised in the lab and presented in section 5.3.1. This was ideal for use in the sintering method as it required a large excess of the TiO_2 nanoparticles.

The doped TiO_2 nanoparticles synthesised by Johnson Matthey range from 10 to 50 nm in diameter (Fig 5.9A,B) which is characteristic of nanoparticles prepared by FSP. Additionally the doped TiO_2 nanoparticles synthesised by FSP are less dense (or more 'fluffy') than the nanoparticles made in the lab using the sol gel method. This means they coat the polystyrene more evenly when used as part of the sintering method for preparing the polystyrene-TiO_2 core shell particles and hence good coverage was obtained (Fig 5.9 C,D).

5.3.7 Doped TiO_2 nanoparticles and radio-sensitising embolic particles inhibit cell proliferation after X-ray treatment

The ability of the doped TiO_2 nanoparticles and PS-TiO_2 embolic particles to inhibit cell proliferation was tested *in vitro* on the RD cell line. Cells were treated with the nano or microparticle sample prepared using commercial PS-DVB beads and TiO_2 (JM) or TiO_2: 5%Gd (JM) for 24 hours. Cells were irradiated with X-rays providing a dose of 0 Gy, 3 Gy or 5 Gy and cell proliferation was assessed after a further 24 hours by manual cell counting. Both the undoped and the doped TiO_2 nanoparticles did not show any significant difference in the number of live cells after no radiation treatment (0 Gy) was administered indicating that the TiO_2 nanoparticles in the absence of radiation are not toxic. The undoped TiO_2 nanoparticles showed a small decrease in the number of live cells by (20.1% ± 4.8) with cells treated with a radiation dose of 3 Gy but there was no difference for cells treated with a radiation dose of 5 Gy. There was a very significant decrease ($p \leq 0.005$) in the number of live cells by (56.9% ± 11.4) and (28.7% ± 11.9)

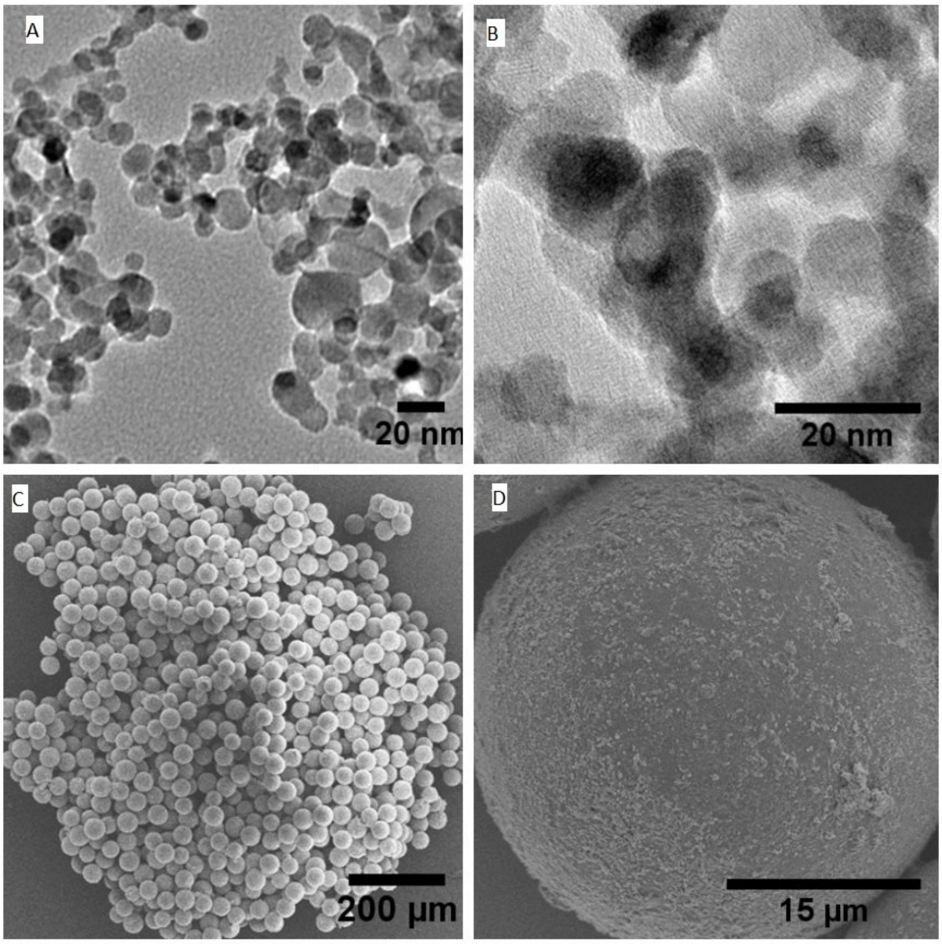

Figure 5.9: PS-TiO$_2$ core shell particles synthesised with TiO$_2$: 5%Gd nanoparticles obtained from Johnson Matthey. A and B) Representative TEM images of the Johnson Matthey's TiO$_2$: 5% Gd nanoparticles showing approximately 20 nm particles. C and D) Representative SEM images of PS-TiO$_2$ core shell particles showing good coverage of the polystyrene with the doped TiO$_2$ nanoparticles.

for cells treated with the TiO_2: 5%Gd nanoparticles at radiation doses of 3 Gy and 5 Gy respectively. This shows that the cell killing can be specifically induced by radiation and hence it can be used to target the cancerous cells. This means that either i) a lower magnitude radiation dose could be administered to obtain the same therapeutic effect while reducing the radiation dose administered to the healthy tissue or ii) the same radiation dose could be used but achieve a larger therapeutic response and therefore improve patient outcomes.

Similarly, the PS-TiO_2 and PS-TiO_2: 5%Gd were not toxic to the RD cells when no radiation was administered confirming that the PS-TiO_2 particle are not toxic. Similar to the TiO_2: 5%Gd nanoparticles there was a very significant ($p \leq 0.005$) decrease in the number of live cells by (60.6% ± 18.9) and (36.1% ± 15.3) treated with a combination of PS-TiO_2: 5% Gd embolic particles and 3 Gy or 5 Gy radiation dose respectively. This is the first time a radiosensitising embolic particle has been demonstrated which is inert without radiation but then can be activated using X-rays to produce reactive oxygen species and inhibit cell proliferation.

5.4 CONCLUSIONS

PS-TiO_2 embolic particles have been successfully synthesised to produce reactive oxygen species and inhibit cell proliferation upon X-ray activation. TiO_2 nanoparticles have been doped with rare earth elements to increase their effectiveness. Three methods were investigated for preparing the PS-TiO_2 using i) a one pot method, ii) a polyelectrolyte method and iii) a sintering method. PS-TiO_2 embolic particles synthesised by the sintering method had good, approximately 100%, coverage of the PS with TiO_2 nanoparticles. The PS-TiO_2: 5%Gd, 1%Er, 1%Eu@Si produced ROS when irradiated with a 3 Gy dose of irradiation. Similarly, the PS-TiO_2: 5%Gd (JM) showed a decrease

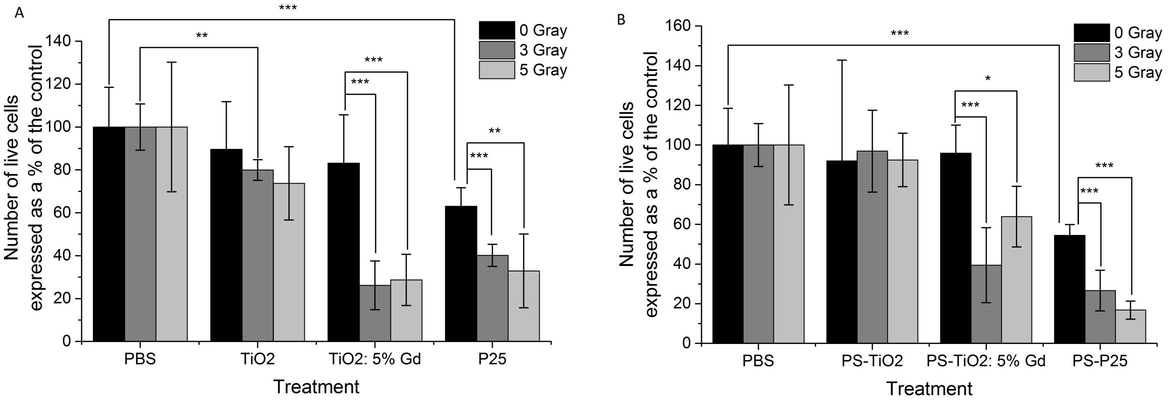

Figure 5.10: Doped TiO_2 nanoparticles and radio-sensitising embolic particles inhibit cell proliferation after X-ray treatment. Results from an independent experiment (n=2) showing the number of live RD cells after a combination of particles and X-ray radiation (0 Gy, 3 Gy and 5 Gy dose). RD cells were incubated with A) 15 µg of TiO_2 (JM), TiO_2: 5%Gd (JM) and P25 or B) 150 µg of PS-TiO_2 (JM), PS-TiO_2: 5%Gd (JM) and PS-P25 for 24 hours before irradiation. The number of live cells was evaluated by manual cell counting after a further 24 hours. Data is presented as mean ± SD of A) six or B) four replicate samples and expressed as a percentage of the PBS control. Significance was tested using a two tailed t-test (*$p \leq 0.05$, **$p \leq 0.01$, ***$p \leq 0.005$).

in the number of live cells after both a 3 Gy and a 5 Gy dose of irradiation. This is the first time a radio-sensitising embolic particle has been shown.

Chapter 6

Development of Chemoembolization Particles Incorporating Ophiobolin A

6.1 Introduction

Combining chemotherapy drugs with embolic particles has been shown to have a synergistic effect on the reduction of tumour size [194]. Incorporation of chemotherapeutic drugs into an embolization particle (chemoembolization) also allows a drug to be delivered directly to cancerous cells. Whereas systemic chemotherapy delivers a drug into the bloodstream and exposes the whole body to the toxic effects of the compound, chemoembolization particles allow the chemotherapy to be delivered around the site of the cancerous cells through passive targeting. Therefore, embolic microparticles were coated with mesoporous SiO_2 nanoparticles which have a high surface area and a nanoporous structure for a high loading capacity. The agent chosen for investigation and incorporation into the chemoembolic particles was a fungal phytotoxic derived compound, Ophiobolin A (OphA).

6.1.1 SiO_2 nanoparticles

Multifunctional mesoporous SiO_2 nanoparticles (MSNPs) have been widely studied for use in cancer therapy because they are highly robust and tuneable delivery platforms for the controlled release of therapeutics [195]. MSNPs are known to have good biocompatibility, a large surface area and are chemically stable [196]. The pores are also tunable to the size of the particular drug to be delivered for maximum loading and release [197, 198]. Furthermore, the SiO_2 surface has a high density of silanol groups which can be functionalized with a range of organic functional groups including peptides, antibodies or siRNA to allow for tumour targeting or gene therapy [199]. The SiO_2 particles can be modified so that they release cargo in response to physico-chemical stimuli such as light, heat, ultrasound and changes in pH [200, 201, 202]. One such example, showed that MSNPs loaded with a drug and capped with pH responsive polyelectrolyte layers, could selectively release their cargo at a reduced pH. This demonstrates that the nanoparticles could be used to deliver a drug selectively to the tumour microenvironment which has a lower magnitude pH (pH 6.5-6.9) than the surrounding healthy tissue (pH 7.2-7.5) [190, 203]. Another study showed that hyperthermia treatment using thermally responsive PLGA-b-(PEGMEMA-co-PPGMA) nanoparticles loaded with Paclitaxel could be used to increase the cellular uptake of the nanoparticles and reduce the metabolic activity of MCF7 cells when the temperature was raised above the thermal transition temperature of the nanoparticles [201]. Furthermore, MSNPs have been used to deliver weakly basic drugs, for example doxorubicin, which have a poor uptake in the acidic tumour microenvironment [204]. Therefore MSNPs are effective at increasing the bioavailability of drugs and selectively treating cancerous cells.

There are a range of synthesis methods resulting in SiO_2 nanoparticles with different morphologies, dimensions and porosities including hexagonal-symmetry, 'blackberrylike'and 'chrysanthemum like' nanoparticles [205]. In this work, SiO_2 nanoparticles with the hexagonal symmetry of the pore (HMSNP) were used because of their uniform and regular physical properties and reproducibility of the synthesis method [206]. The nanoparticles were prepared by the base catalysed sol-gel reaction using a surfactant, the amphiphilic molecule cetyl trimethylammonium bromide (CTAB) as a template for the mesopores (Fig 6.1). The SiO_2 precursor tetraethyl orthosilicate (TEOS) is then hydrolysed and condensed around the surfactant template at high temperature and under vigorous stirring to form the HMSNP. The SiO_2 surface was subsequently modified with a phosphonate group, 3-(trihydroxysilyl) propyl methylphosphonate (THMP), to reduce aggregation and increase the stability of the HMSNP [207]. Finally the organic template was removed by refluxing in acidic methanol.

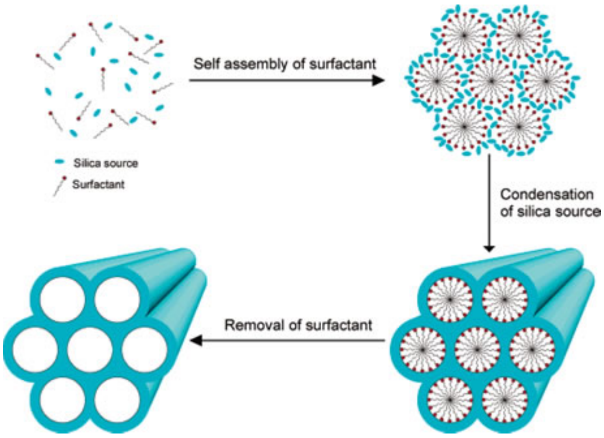

Figure 6.1: Schematic showing the synthesis of mesoporous SiO_2 nanoparticles with hexagonal arrangement of the the pores. (Image taken from [208]).

6.1.2 Drug resistant cells

Nanopartilces have been shown to be effective at delivering chemotherapy drugs to multi drug resistant (MDR) cells. Cancer cells can acquire resistance to chemotherapy drugs through two main mechanisms: i) the over-expression of multidrug transporters and ii) altered apoptosis pathways [209]. In transporter-dependent MDR, transmembrane drug efflux pumps are overexpressed and therefore they actively export the drugs to reduce the intracellular drug concentration and thus reduce its effectiveness. A common pump is the P-glycoprotein (P-gp) which is overexpressed in liver, ovarian, pancreatic, kidney and breast cancers [210] and has been shown to readily export doxorubicin, vinblastine and Paclitaxel. Furthermore, mutations in the apoptotic pathway can reduce the effectiveness of a drug to induce cell death and thus contribute to the MDR (Further details regarding the apoptotic pathway can be found in section 7.1.1.1). Nanoparticles have been developed to combine MDR modulators and cytotoxic drugs to increase the effectiveness of the drug. Moreover, it has been suggested that nanoparticles can overcome P-gp transport by a range of mechanisms including enhancement of cellular drug uptake by endocytosis, ATP depletion and change of downstream P-gp signalling pathways [211].

6.1.3 Microvesicles

OphA has been shown to induce vacuolization and subsequent expulsion of the vacuoles from the surface of the cells in the U373-MG (brain cancer) cell line [41]. Microvesicles are secreted by various cell types as a form of cell to cell communication. Microvesicles include (i) exosomes (40 nm–100 nm) which are constitutively released by the exocytosis of multivesicular bodies (ii) shedding microvesicles (50 nm–1000 nm) which arise due to the direct budding of the plasma membrane and (iii) apoptotic bodies (50 nm–5000 nm) which are produced during apoptosis and contain cellular content and organelles [212] (Fig 6.2).

6.1.3.1 Exosomes

Exosomes consist of a lipid bilayer membrane surrounding a small cytosol and do not contain cell organelles [214]. Cells can release exosome via two different mechanisms:

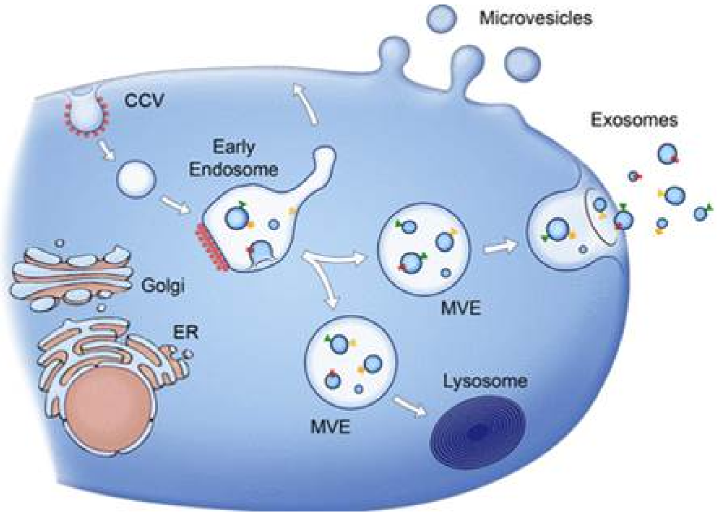

Figure 6.2: Schematic showing the difference between microvesicles and exosomes. (Image taken from [213]). Microvesicles bud directly from the plasma membrane while exosomes are released when multivesicular endosomes (MVE) fuse with the plasma membrane resulting in the release of exosomes.

the classical pathway and the direct pathway. In the classical pathway intracellular vesicles appear from the inward budding of the plasma membrane (PM) which form early endosomes. The endosomes then convert to form multivesicular endosomes (MVE's) which can then fuse with the PM and are released in the the extracellular space [213]. In the direct pathway, vesicles are released directly from the plasma membrane without the involvement of MVB. Common exosomal markers include Alix, CD9 and CD63 [215].

6.1.3.2 Microvesicles

Microvesicle formation is distinct from exosome formation and results in the outward budding of the plasma membrane [216]. Microvesicles are formed in response to stimulation which cause phosphatidylserine (PS) to be translocated from the inner membrane leaflet to the outer membrane. The resultant cytoskeleton rearrangement causes an outward blebbing of the PM and the release of microvesicles into the extracellular space. The budding process is completed through the contraction of cytoskeletal structures by actin-myosin interactions [217].

6.1.3.3 Apoptotic bodies

Apoptotic bodies are released in the later stages of apoptosis after the cell has reduced in size and breaks up into smaller pieces called apoptotic bodies [218]. Similarly to microvesicles, apoptotic bodies have PS on their surface and can contain parts of the mother cells organelles including PM markers, proteins, RNA and microRNA.

6.1.4 Aims and Objectives

The aim of this chapter was to develop a chemoembolic particle loaded with a model drug, Ophiobolin A. The initial objective was to synthesise chemoembolic particles which had a high capacity for loading the selected drug and its subsequent slow release. Once successful particles were synthesised their effect *in vitro* was determined using the RD cell line, the vinblastine resistant KB-VI and its parent KB-31 cell line. Furthermore the effect of OphA on the expulsion of vesicles from RD cells after treatment was sought to be established.

6.2 MATERIALS AND METHODS

6.2.1 Synthesis of mesoporous SiO_2 with hexagonal-symmetry (HMSNP)

Synthesis of mesoporous SiO_2 nanoparticles with hexagonal symmetry of the pores (HMSNP) was performed by a surfactant-templated base catalysed sol-gel reaction, as previously described by Hom *et al.* [207]. Briefly, 100 mg of CTAB (Aldrich; 99%) was dissolved in 48 ml of ddH_2O and 350 µl of 2 M NaOH (Aldrich) and stirred at 500 rpm in a round bottomed flask. The mixture was heated to 80 °C and once the temperature was stable, 0.5 ml of TEOS (Aldrich) was added. After 15 minutes incubation, 127 µl of THMP was added. After, a further two hours incubation the nanoparticles were collected by centrifugation and washed twice in methanol (Rathburn). The nanoparticles were resuspended in 20 ml of methanol and 1 ml of 37% hydrochloric acid (Aldrich) and then refluxed overnight at 80 °C to remove the CTAB. The nanoparticles were collected by centrifugation and washed in ethanol (Fisher) twice before drying under vacuum.

6.2.2 Synthesis of polystyrene spheres (PS)

Synthesis of polystyrene spheres (PS), for the core of the embolic particle, was performed as previously described in section 3.3.1.

6.2.3 Coating of the embolic particle with HMSNP

The coating of the PS with HMSNP to create PS-HMSNP embolic particles was similar to the method presented in section 5.2.3.3. The HMSNP were mixed with the PS (1:9 v/v) and the HMSNP was then sintered onto the surface of the polystyrene spheres by heating the mixture to 230 °C at a ramping rate of seven degrees per minute and then holding at 230 °C for two hours in a Carbolite RWF 1200 furnace. The hold time was increased to two hours, compared to the 15 minutes described in section 5.2.3.3, because SiO_2 has a thermal conductivity of (1.3 to 1.5 $\mathrm{W\,m^{-1}\,K}$) [219] compared to (4.8 to 11.8 $\mathrm{W\,m^{-1}\,K}$) for TiO_2 [220]. This means it will take longer for the heat to transfer through the SiO_2 before melting the surface of the polystyrene and hence an increased hold time was used. Additionally, heating will not cause detrimental effects to the SiO_2 whereas it had the possibility of changing the crystal structure of the TiO_2 and therefore a longer time was allowed to increase the coverage. The prepared PS-HMSNP were separated and dried as described in section 5.2.3.3.

6.2.4 Particle characterisation

HMSNP and PS-HMSNP were characterised using transmission and scanning electron microscopy (TEM and SEM), disc centrifugation and electokinetic (ζ) potential. TEM was used to measure the size, surface morphology and nanopores of the HMSNP as described in section 2.1.2. SEM was used to evaluate the size and surface morphology of the HMSNP and the size distribution and surface coverage of the PS-HMSNP using a JEOL JSM-840F microscope as described in section 2.1.3. The hydrodynamic size distribution was measured using a Disc Centrifuge as described in section 2.1.5. The zeta potential was measured by electrophoretic light scattering as described in section 2.1.6.

6.2.5 Loading of OphA into the HMSNP and PS-HMSNP

HMSNP (10 mg) were incubated in 2 ml of 0.5 mg ml^{-1} OphA in either dicloromethane (DCM; Aldrich), ethanol (Fisher) or toluene (Aldrich). Samples were agitated using a magnetic stirrer at 500 rpm for three days at room temperature. Three days was selected after preliminary experiments, loading 0.1 mg ml^{-1}, indicated that an equilibrium was achieved after three days (Fig 6.3A) The samples were centrifuged at 12,000 rpm for five minutes to pellet the nanoparticles and the supernatant was removed. Finally the loaded HMSNP@OphA were dried overnight at 18 °C under vacuum. A similar procedure was used for loading the PS-HMSNP with OphA.

The concentration of OphA remaining in the supernatant after loading was measured by liquid chromatography (LC). An Agilent LC 1120 Compact equipped with an Agilent Eclipse Plus C18, 4.6 X 150 mm I.D., 5 µm particle size column was used for the analysis. OphA samples (20 µl) were injected into a water-acetonitrile (Aldrich) gradient with a flow rate of 0.5 ml min^{-1}. The gradient started with water-acetonitrile (85:15) mix, changed to water-acetonitrile (10:90) mix over ten minutes, held the water-acetonitrile

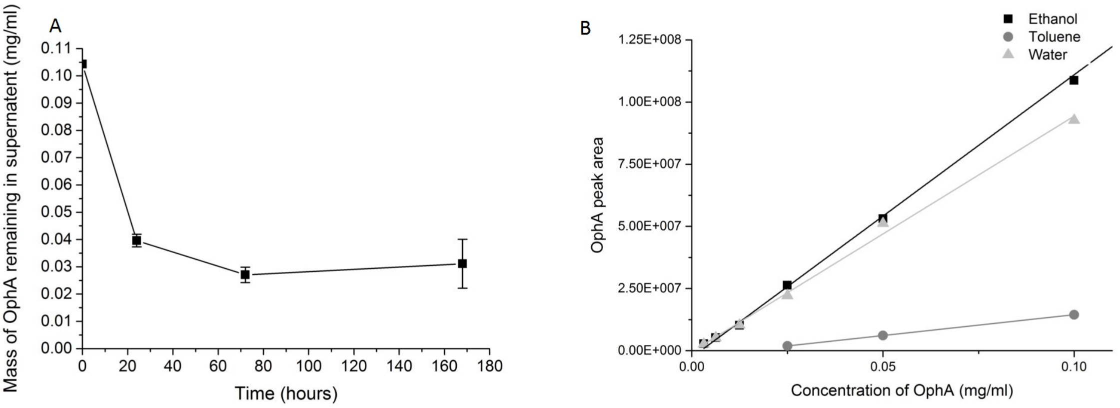

Figure 6.3: Optimisation of the method for loading of HMSNP with OphA. A) Preliminary results showing the concentration of OphA in the supernatant after loading HMSNP for 0, 24, 72 and 168 hours with 0.1 $\mathrm{mg\,mL^{-1}}$. B) Representative calibration curves for OphA in ethanol, toluene and water showing the change in OphA peak area with OphA concentration. Linear fits have been applied to the data with R^2 values $\geq$ 0.99.

mix constant for seven minutes, returned to the start conditions over three minutes and then equilibrated for five minutes prior to the next sample. The UV detector voltage was set to 236 nm. Under these settings OphA had a retention time of 14.7 minutes. A calibration curve for OphA concentration against peak area was prepared for each solvent used (DCM, ethanol, toluene) and R^2 values of 0.99 were obtained (Fig 6.3B). The change in concentration of OphA from before loading to after loading within the particles was used to infer the loading of OphA by the particles (equation (6.1) and equation (6.2))

$$\%\,\text{uptake} = \frac{\text{area of OphA peak after loading}}{\text{area of OphA peak initially, prior to loading}} \tag{6.1}$$

$$\text{moles of OphA uptaken} = \%\ \text{uptake} * c * V \tag{6.2}$$

where c is the initial concentration of OphA prior to loading and V is the volume of loading solvent.

6.2.6 Release of OphA from HMSNP and PS-HMSNP

The release of OphA from the HMSNP@OphA and PS-HMSNP@OphA was monitored *in chemico* over 24 hours. HMSNP@OphA loaded in DCM, ethanol or toluene (2.5 mg) or PS-HMSNP@OphA loaded in DCM (2.5 mg) were resuspended in 0.5 ml of PBS and placed on a rocking table at room temperature. HMSNP@OphA and PS-HMSNP@OphA samples were centrifuged at 12,000 rpm for five minutes to pellet the particles and then 20 µl of the supernatant was removed for further analysis. An equal volume of PBS was added to the HMSNP@OphA and PS-HMSNP@OphA samples to maintain a constant volume of PBS throughout the experiment. Sampling occurred after one, four, eight and 24 hour incubation times. The removed supernatant was diluted in 180 µl of PBS and then the concentration of OphA within the sample was determined by LC using the same setup as described in section 6.2.5. Experiments were performed in triplicate on three separate occasions.

6.2.7 Degradation of OphA

The degradation of free OphA was monitored *in chemico* over 72 hours. OphA was resuspended in 2 ml of PBS at a concentration of 0.1 mg ml^{-1}. Samples (250 ml) were taken after 0, 24, 48 and 72 hours and analysed by LC (as described in section 6.2.5). Chromotography peaks relating to OphA degradation products were observed at R_t=13.3, 14.5, 15.5 and 15.9 minutes.

6.2.8 Cell viability assays

Cell viability of RD cells after a range of treatments was assessed using Annexin V and PI staining and flow cytometry. Further details regarding the applied treatments can be found in Table 6.1. RD cells expressing GFP were used and samples were dyed with 2.5 µl PI and 2.5 µl APC-Annexin V in 50 µl of annexin V binding buffer for 15 minutes at room temperature. Subsequently 200 µl of binding buffer was added and samples were analysed using a Accuri C6 Flow Cytometer (BD) as described in section 2.3.3. Fluorescence intensity of both the PI and the APC channels was used to determine the cells which were live, undergoing early apoptosis or were dead due to either apoptosis or necrosis. Quantitative analysis was conducted by determining the percentage of stained cells compared to the total number of cells. Experiments were performed in triplicate using PBS as a control and repeated on three separate occasions.

Cell viability of the vinblastine resistant KB-VI and its parent KB-31 cell line after a range of treatments was assessed by crystal violet staining and manual cell counting as described in section 2.3.2.1 and section 2.3.2.2, respectively. Treatments included i) 0 to 100 µM OphA, ii) 0 to 4 $\mu g\,ml^{-1}$, iii) 0 to 400 ng per well blank HMSNP and iv) 0 to 50 ng per well HMSNP@OphA. Experiments were performed in triplicate and on at least two separate occasions.

Table 6.1: Selection of treatments assessed by flow cytometery after annexin V and PI staining.

	Treatment	Concentration
i	Free OphA	0 mg–0.02 mg per well (0 µM–100 µM)
ii	Free CytoD	0 mg–0.01 mg per well (0 µM–10 µM)
iii	Free OphA in combination with free cytoD	0 mg–0.002 mg per well (0 µM–10 µM) OphA+ 0.005 mg per well (5 µM) CytoD
iv	blank HMSNP and PS-HMSNP	3.5 mg per well
v	HMSNP@OphA and PS-HMSNP@OphA	3.5 mg per well
vi	PBS as a control	N/A

6.2.9 Nanoparticle tracking analysis

Nanoparticle tracking analysis (NTA), using a NanoSight NS500 (Nanosight, Amesbury, UK) was used to monitor the release of microvesicles from the RD cells after treatment.

6.2.9.1 NanoSight

NTA uses a finely focused laser beam which illuminates the particles within the sample. The particles resident within the beam can be visualised using a conventional optical microscope, fitted with a video camera, which can detect the light scattered from the particles within the field of view. Five separate videos of 30 seconds were recorded at camera level 12 and then the particle movement due to Brownian motion was analysed using NTA 2.3 software (NanoSight). The velocity of the particle movement is used to calculate the particle size by applying the two-dimensional Stokes-Einstein equation

$$< x, y >^2 = \frac{K_B T t_s}{3\pi\eta d_h} \tag{6.3}$$

where $< x, y >^2$ is the mean squared displacement, K_B is Boltzmanns constant, T is the temperature of the solvent in Kelvin, t_s is the sampling time, η is the viscosity and d_h is the hydrodynamic diameter.

6.2.9.2 NanoSight sample preparation

RD cells were plated at a density of 75x10^4 cells per flask (T25 flask) in 3 ml of OPTIMEM (Gibco) and allowed to attach to the flask for 24 hours. OPTIMEM was used as it is a low serum media and therefore the background level of microvesicles was low and because the phenol red within DMEM is known to cause interference with the NTA. Subsequently cells were treated with 200 µl of (i) PBS only as a control, (ii) 1 µM OphA, (iii) 10 µM OphA, (iv) 1 µM OphA + 5 µM CytochalasinD (CytoD; Aldrich), (v) 10 µM + 5 µM CytoD, (vi)5 µM CytoD. The cells were incubated for a further 24 hours.

The size and concentration of the microvesicles released from the cells into the supernatant was measured using a NanoSight NS500. The microvesicles were diluted in PBS to ensure the concentration of particles was within the optimum range of 2-10x10^8 particles per ml for NanoSight measurement and then each sample was measured in light scatter mode. Experiments were repeated on three separate occasions.

6.2.9.3 Fluorescent labelling of microvesicles

The microvesicles were labelled with SYBR® green (Ex. 497 nm, Em. 520 nm; Life technologies) as a marker for DNA, and CellMask^{TM} orange (Ex. 554 nm, Em. 567 nm ; Life technologies) as a marker for plasma membrane. Microvesicles from the supernatant (250 µl) were incubated with either 10 µl of SYBR® green (x1000 stock solution) or 0.5 µl of 5 µg ml^{-1} CellMask^{TM} orange for 30 minutes at 37 °C, protected from light. The microvesicles were pelleted by centrifugation at 30,000 rpm for one hour and washed in PBS to remove any residual dye. Finally the cells were resuspended in 0.5 ml of PBS, centrifuged at 10,000 rpm for 10 minutes to pellet any cell debris whilst keeping the microvesicles in suspension before analysis by NTA.

The NanoSight NS500 equipped with a 488 nm laser has been adapted to allow for the detection of microvesicles labelled with fluorescent dyes. A 500 nm long pass filter is used so that only fluorescent emitted light can be measured. The fluorescent microvesicles are tracked in real time, as with conventional NTA analysis, and the microvesicle size, concentration and fluorescence intensity can be determined. Under conventional light scatter mode the total number of particles can be determined and subsequently compared to the number of dyed microvesicles. Experiments were repeated on three separate occasions.

6.3 RESULTS AND DISCUSSION

6.3.1 Chemoembolic particles for targeted drug delivery

OphA has been shown to be an effective chemotherapeutic both later within this thesis and in previous studies; however, to avoid off-target effects it is optimal to deliver the therapeutic at the site of action. Novel composite embolic particles (PS-HMSNP) have been designed comprising a polystyrene microsphere (PS) at the core, covered with mesoporous SiO_2 nanoparticles (HMSNP) to create a shell layer (Fig 6.4A). The PS core has been designed to effectively obstruct the tumour vasculature, while the HMSNP shell can be loaded with drug. The chemoembolization particles allow the drug to be delivered directly at the tumour location.

The synthesised mesoporous SiO_2 particles were examined by TEM (Fig 6.4B) and SEM (Fig 6.4C) and shown to have a hexagonal arrangement of the pores channels, and the overall shape to be roughly spherical with a slight elongation of the nanoparticles in the direction of the channels. The HMSNPs were determined by these methods to be approximately 120 nm in diameter, with a pore diameter of approximately 2 nm. Another study from our group measured a large sample of these HMSNPs and the nanoparticles were shown to be (106 ± 23) nm (n= 431) in diameter and to have a pore diameter of (2.1 ± 0.2) nm (n=544) [205]. The mean hydrodynamic diameter of the HMSNP was determined to be 120 nm by disc centrifugation; which is similar to the diameter measured by TEM. The zeta potential of the HMSNP was (-39 ± 1) mV at pH7, and therefore at physiologically relevant pH values the nanoparticles are stable (zeta potential $\leq -30\,\text{mV}$), and will form a stable suspension without aggregation. As a basis for the embolic particles, polystyrene spheres were synthesised and used as a carrier for the HMSNP. The coverage of the PS with HMSNP was optimised by changes in both the duration and temperature of sintering. Samples were assessed using SEM and good

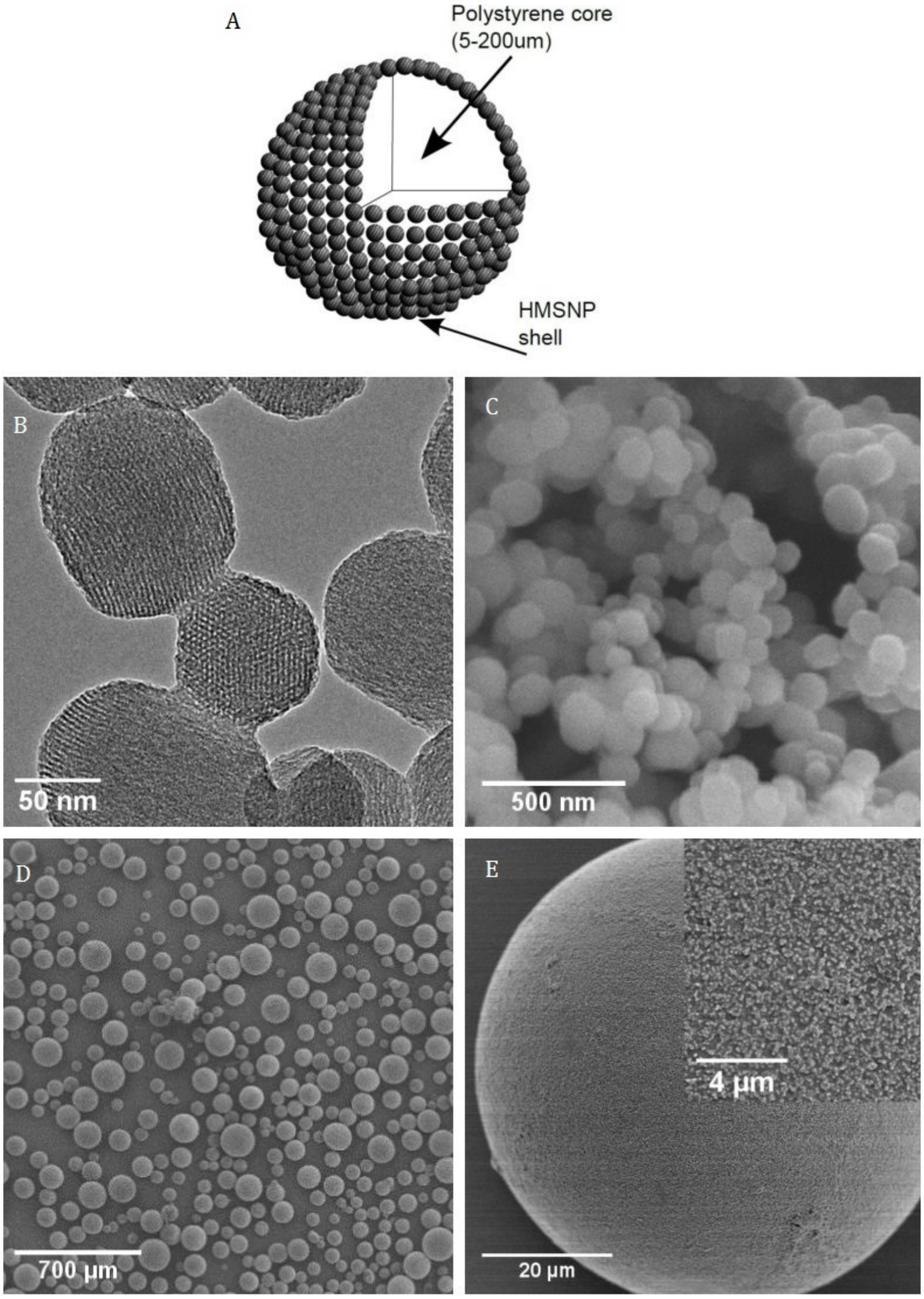

Figure 6.4: Representative electron microscopy images of the as synthesised HMSNP and PS-HMSNP. A) Schematic of the prepared PS-HMSNP chemoembolization particles. The polystyrene core acts an embolic agent obstructing the tumour vasculature and the HMSNP shell can be loaded with a chemotherapy drug (Image not to scale) B) Representative TEM image of the HMSNP showing the size and hexagonal orientation of the pores (scale bar: 50 nm). C) Representative SEM image of the HMSNP (3 kV, scale bar: 500 nm). D) Representative SEM image of the PS-HMSNP and insert showing the size dispersion of the PS particles (3 kV, scale bar: 300 µm). E) Representative SEM image of the PS-HMSNP microparticle (3 kV, scale bar: 20 µm) and insert showing the HMSNP on the surface of the polystyrene microparticle (3 kV, scale bar: 4 µm).

coverage of the PS-HMSNP was observed in samples sintered at 230 °C for two hours (Fig 6.4E).

6.3.2 High loading of OphA into the pores of HMSNP and PS-HMSNP

Successful loading of OphA into the pores of the mesoporous SiO_2 is required for the drug to be carried by the embolic particles. Liquid chromatography was used to monitor the loading of OphA into the pores of both HMSNP and PS-HMSNP. A number of solvents were trialled for drug loading; the highest loading of OphA was found in dichloromethane (DCM) (95%) and toluene (95%) whereas ethanol (38%) showed poor loading (Table 6.2). This is due to the solubility of OphA in each solvent and their respective solubility parameters (Table 6.2). The proton acceptor solubility parameter indicates the degree of dissolving of alcohol, phenol and carboxylic acid functional groups. OphA has both hydroxyl groups and carbonyl groups which allow for hydrogen bonding, hence it has a good affinity for solvents with high solubility parameters of proton acceptors like ethanol (5). DCM and toluene have low solubility parameters of proton acceptors (0.5), therefore the OphA had a greater interaction with the silanol groups in the mesoporous SiO_2 than the solvent and hence the OphA was adsorbed into the pores of the SiO_2 [221]. Although loading HMSNP with OphA in toluene was successful, this could not be used for loading of OphA into PS-HMSNP since it causes the polystyrene to swell and degrade [222] and therefore the integrity of the PS-HMSNP would not be maintained.

6.3.3 Successful release of OphA from HMSNP and PS-HMSNP *in chemico*

Good temporal release of OphA from the pores of the mesoporous SiO_2 is required to ensure that sustained drug delivery will be achieved. OphA has been successfully

Table 6.2: Loading and release of OphA into PBS from HMSNP and PS-HMSNP. The table details the percentage loading OphA into the particles depending on the solvent it was loaded in, the absolute number of moles of OphA per mg of HMSNP and the maximum moles of OphA released from the particles after 24 hours in PBS.

	HMSNP in DCM	**HMSNP in Ethanol**	**HMSNP in toluene**	**PS-HMSNP in DCM**
Proton acceptor solubility parameter of the solvent	0.5	5	0.5	0.5
% loaded based change in area of the OphA peak measured using liquid chromatography	94.6±5.1	38.1±4.2	95±1.4	95.4±6.2
Moles of OphA loaded per mg of HMSNP (nmoles)	237±13	95±11	238±04	238±16
Moles of OphA released after 24 hours per mg of HMSNP (nmoles)	92±23	6±03	116±02	39±9
% moles released after 24 hours	38.8	6.3	48.7	16.4

released from the pores of HMSNP both *in chemico* into PBS. Release was shown in all the samples with the full cargo being released after approximately 24 hours (Fig 6.5). The highest release was observed for the samples loaded in toluene and DCM both in terms of absolute moles released and as a percentage of the total number of moles adsorbed into the SiO_2 pores (Table 6.2). Samples loaded in toluene released (116 ± 02) nmoles of OphA per mg of HMSNP over 24 hours, while samples loaded in DCM released (92 ± 2.3) nmoles of OphA per mg of HMSNP (Fig 6.5). This equates to 49% and 39% release of the total encapsulated OphA for samples loaded in toluene and DCM respectively over the duration of the experiment. Poor release was observed in the HMSNP loaded in ethanol, with only (0.6 ± 0.3) nmoles OphA per mg of HMSNP, which is only 6.3% of the total encapsulated cargo.

The relative size of the drug compared to the pore size of the SiO_2 will also affect its loading and unloading profile. A large ratio of pore size to drug molecule size results in a high release rate whereas a small ratio will result in a sustained release due to the confinement effect of the pore [223].

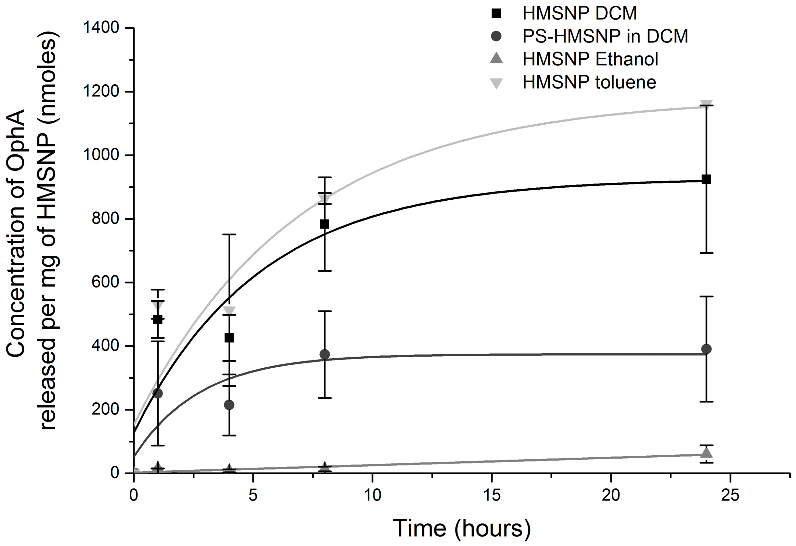

Figure 6.5: Release profiles of OphA into PBS from the HMSNP and PS-HMSNP from independent experiments (n=3). Data is presented as mean ± SD of triplicate samples.

6.3.4 HMSNP protects OphA from degradation

One of the limiting factors in the clinical development of OphA is its poor chemical stability. The stability of the free drug in PBS was monitored by liquid chromatography over a period of 72 hours (Fig 6.6A,B). During this time the OphA peak area reduced by 75% and OphA had a half life of approximately 24 hours. There were four main degradation peaks visible on the LC trace and these occurred at retention times of 13.3, 14.5, 15.5 and 15.9 minutes (Fig 6.6C). Unfortunately, mass spectrometry (MS) was not available on the LC used to identify the degradation products. However, the products have been previously identified by Bury *et al.* [39], and the main OphA degradation product was shown to be 3-anhydro-6-epi-Ophiobolin A, which was significantly less potent (approximately 30 times) than OphA itself.

Interestingly, the OphA released from the HMSNPs underwent significantly less degradation compared to free OphA. After 24 hour release from the HMSNP@OphA and PS-HMSNP@OphA the largest degradation product for all samples occurred at R_t=15.9 minutes (Fig 6.6D). Quantifying the ratio of this peak area to that of the OphA peak area (R_t=14.7 minutes) showed a very significant ($p \leq 0.005$) reduction in degradation of OphA for the HMSNP@OphA (16% ± 1, 21% ± 5 and 28% ± 3 for samples loaded in DCM, ethanol or toluene respectively) and PS-HMSNP (14% ± 11 for sample loaded in DCM) compared to the free drug (78% ± 8). Therefore, we have shown that nanoparticles can be used to successfully protect a fragile chemical molecule and therefore increase its half-life within the body. Other studies, such as those of Karve *et al.* [224], where wortmannin was loaded into lipid polymer nanoparticles, show an increase in the stability of the molecules upon encapsulation.

6.3.5 OphA induces apoptosis in RD cells

Ophiobolin A was assessed in terms of its ability to effect cell death in Rhabdomyosarcoma (RD) cells. Morphologically RD cells in culture present as a spindle shape with large multinucleated cells (Fig 6.7A). Incubation of the cells with 10 µM OphA for 24 hours caused cells to round up and become more spherical. Cytoplasmic shrinkage could also be seen, along with membrane blebbing (Fig 6.7B). To further interrogate the mechanism of action of OphA on RD cells, an inhibitor of actin polymerisation, Cytochalasin D (CytoD) was employed [225, 226]. Incubation of RD cells with CytoD alone was shown to induce microfilament formation (Fig 6.7C). Combination of OphA and CytoD, however, resulted in RD cells which still exhibited the characteristic spherical shape, membrane blebbing and cytoplasm shrinkage seen in cells treated only with OphA

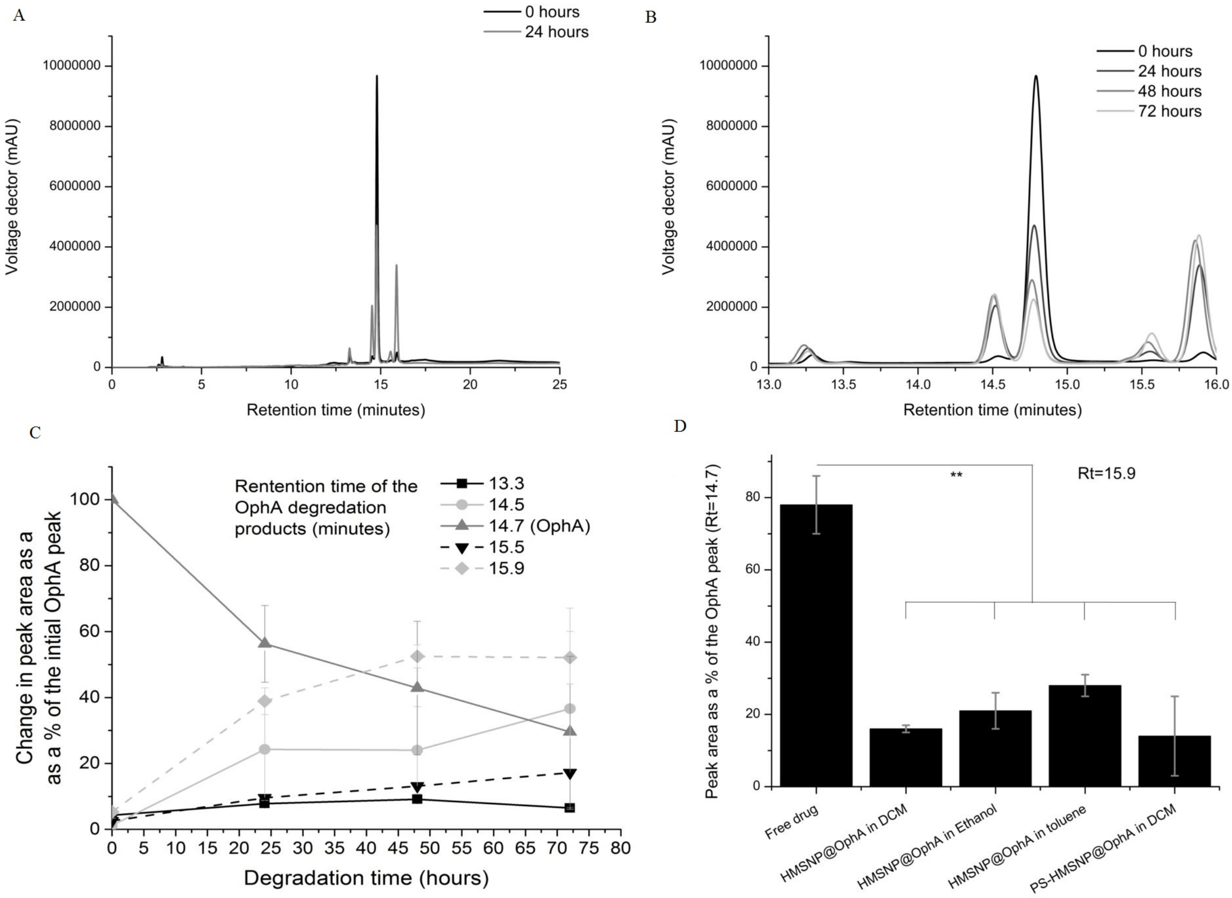

Figure 6.6: Degradation of OphA. A,B) Representative liquid chromatography traces showing the degradation of $0.1\,\mathrm{mg\,ml^{-1}}$ OphA in PBS at 37 °C A) after 24 hours and A) Insert showing only the region between retention time 13-16 minutes after 24, 48 and 72 hours. C) Results from an independent experiment (n=3) showing the degradation of $0.1\,\mathrm{mg\,ml^{-1}}$ free OphA (R_t=14.7 minutes) to 4 main degradation products at R_t= 13.3, 14.5, 15.5 and 15.9 minutes. Data is presented as the mean change in peak area as a percentage of the OphA peak at the start of the experiment ± SD of triplicate samples. D) Results from an independent experiment (n=3) showing the degradation of OphA after 24 hours release from the HMSNP@OphA and PS-HMSNP@OphA. The largest degradation peak was observed at R_t=15.9 minutes. Data is presented as the mean ± SD of the ratio of the peak area for OphA to the peak area for R_t=15.9 minutes from triplicate samples and significance was tested using a one tailed t-test ($^{**}p \leq 0.005$).

(Fig 6.7D)

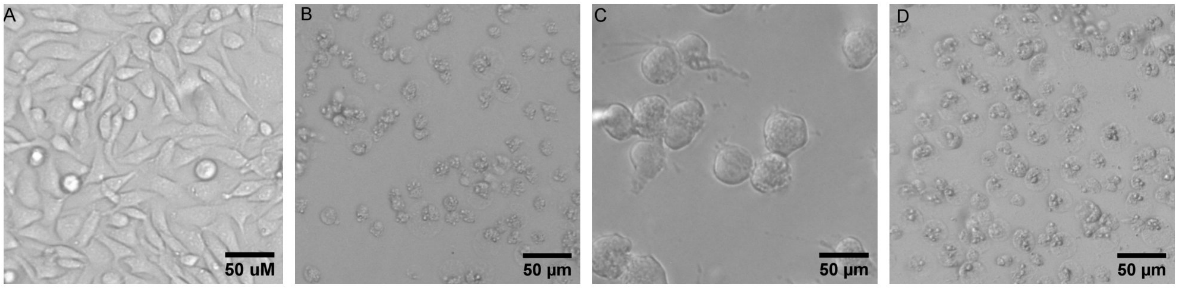

Figure 6.7: Representative bright field microscope images of RD cells with different treatments applied. A) RD cells treated with PBS as a control, B) RD cells treated with 10 µM OphA showing the cells rounding up and becoming more spherical. Blebbing at the membrane surface and cytoplasmic shrinkage can be seen due to the presence of OphA. C) RD cells treated with 5 µM Cytochalasin D (CytoD) showing microtubule formation due to the inhibition of actin polymerisation caused by CytoD. D) RD cells treated with 10 µM OphA plus 5 µM (CytoD) showing that the OphA still causes cells to round up and the membrane to bleb. Scale bars are all 50 µm.

To investigate the mechanism of cell death in RD cells exposed to OphA, cells were tagged with fluorescent markers and analysed by flow cytometry. The fluorophores used were propidium iodide (PI), a membrane impermanent dye that is generally excluded from viable cells, and APC-Annexin V. Annexin V binds to phosphatidylserine, a cell surface marker of apoptotic cells and therefore indicates cells undergoing early apoptosis, cells stained with PI were deemed to be dead and cells stained with neither fluoropore were deemed to be viable. Low concentrations of OphA (1 µM) induced early apoptosis in RD cells while treatment with 10 µM showed a peak in the percentage of apoptotic cells (Fig 6.8A). Additionally treatment with $\geq$ 10 µM caused 80% of cells to die. RD cells treated with 0 µM–10 µM CytoD showed no significant change ($p \geq 0.05$) in the percentage of live, dead or apoptotic cells compared to the untreated control cells. This indicates that the 5 µM CytoD used in subsequent experiments would not cause any adverse effects to the cells (Fig 6.8B).

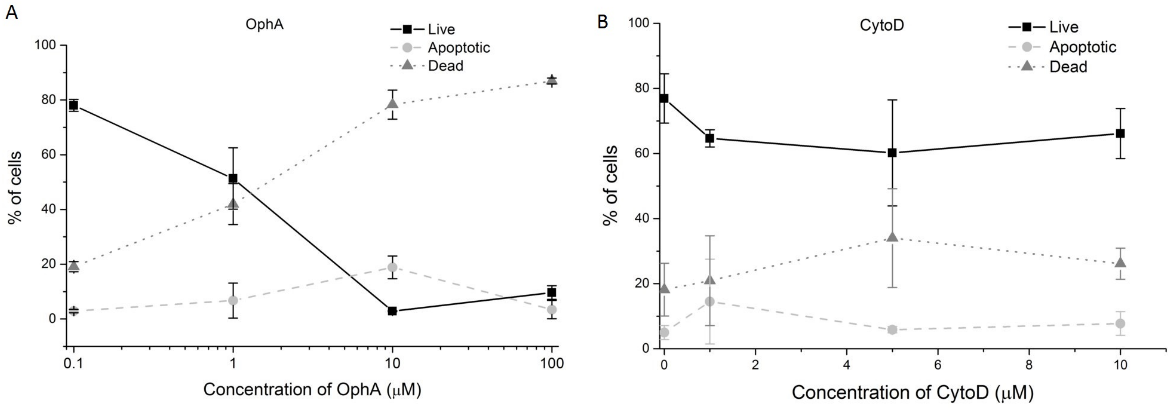

Figure 6.8: Effect of OphA and CytoD on cell viability measured by flow cytometry after staining with APC-Annexin V and PI. High PI fluorescence indicates dead cells while high APC-Annexin V fluorescence indicates early apoptotic cells, live cells show no fluorescence in these channels. A) Results from independent experiments (n=3) showing the percentage of live, apoptotic and dead RD cells after treatment with 0 µM–100 µM OphA. B) Results from independent experiments (n=3) showing the percentage of live, apoptotic and dead RD cells after treatment with 0 µM–10 µM CytoD. Data for all experiments is presented at mean ± SD of triplicate samples.

The IC_{50} of OphA on RD cells after 24 hours treatment is between 1 to 2 µM (Fig 6.8). This is greater magnitude, and thus less cytotoxic, than previously reported IC_{50} values for OphA on a number of different cell lines, [39, 40]. However these studies all applied the OphA treatment for three days rather than 24 hours which could explain the lower cytotoxicity observed in this study. It is likely that the drug would need an IC_{50} value in the nanomolar range to allow for effective exposure to cancerous cells. However if the drug is delivered at the tumour location, for example using nanoparticles, it is possible that a less cytotoxic drug be used whilst still producing desirable effects.

Previously, Bury *et al.* [41] found that GBM cells incubated with OphA did not show Annexin V binding and therefore cell death proceeded via paraptosis rather than apoptosis. This difference could be accounted for because GBM cells are known to have a defective apoptotic signalling pathway meaning they are resistant to apoptosis, [227] whereas there are many reports showing that apoptosis can be induced in RD cells [228, 229]. Another plant derived compound, honokiol, has been shown to induce paraptosis in NB4 and K562 leukaemia cell lines at low concentrations [17]. In those cells where vacuoles were observed in the cytoplasm, a hallmark of paraptosis, no annexin V binding was observed. However at greater magnitude concentrations, honokiol induced apoptosis and necrosis. Therefore, apoptosis could have been observed in this study because greater magnitude concentrations of OphA were used than by Bury *et al.* [41] or because RD cells have a greater propensity to die *via* apoptosis.

6.3.6 OphA increases microvesicle production and size

Nanoparticle tracking analysis (NTA) was used to further investigate membrane blebbing effects in terms of microvesicle production. A representative NTA trace of microvesicle concentration versus microvesicle size shows the increase in microvesicle production after treatment with 1 µM OphA for 24 hours (Fig 6.9A). There was a significant increase ($p \leq 0.05$) in the concentration of microvesicles produced from (72 ± 6) to (180 ± 31) x10^8 microvesicles/ml after treatment with 1 µM OphA compared to the control (Fig 6.9D). There was a very significant ($p \leq 0.005$) increase from (72 ± 6) to (170 ± 11) x10^8 microvesicles/ml in the concentration of microvesicles produced after treatment with 10 µM OphA (Fig 6.9D) compared to the PBS only treated control. Microvesicle release in response to drug has been observed previously, for example, Shedden *et al.* [230] observed that doxorubicin could be found in microvesicles after treatment and the rate of vesicle shedding was proportional to doxorubicin resistance across various cell lines.

There was a slight shift in the mode, mean and peak size of the microvesicles produced due to OphA treatment (Table 6.3). The mode microvesicle size increases from 117 nm (control) to 126 nm (1 µM OphA) or 121 nm (10 µM OphA), mean microvesicle size increases from 158 nm (control) to 160 nm (1 µM) or 189 nm(10 µM) and peak microvesicle size increases from 115 nm (control) to 122 nm (1 µM) or 121 nm (10 µM) (Table 6.3). Since OphA induces apoptosis in RD cells this could be due to apoptotic bodies forming as a result of the OphA treatment, and hence the increase in microvesicle size.

Table 6.3: Effect of OphA and CytoD on microvesicle size. Results from an independent experiment (n=3) showing the mode, mean and peak microvesicle size.

	Mode Microvesicle size (nm)	Mean Microvesicle size (nm)	Peak Microvesicle size (nm)
PBS only treated RD cells	117	157.92	115
1 µM OphA treated RD cells	125.8	160.15	122
10 µMOphA treated RD cells	121.2	180.22	121
1 µM OphA + 5 µM CytoD treated RD cells	127.2	170.06	115
10 µM OphA + 5 µM CytoD treated RD cells	111.6	142.48	97
5 µM CytoD treated RD cells	116.2	171.56	115

6.3.7 Cytochalasin D prevents the release of large microvesicles

CytoD is often used in combination with a drug to further probe its mechanism of action [231, 232]. In this study CytoD was used to investigate whether changes in the cytoskeleton affect microvesicle production. In the presence of CytoD only there is no significant increase in the number of microvesicles produced above the control, (72 ± 6) and (104 ± 30) x10^8 microvesicles/ml (Fig 6.9D). The mode and peak microvesicle size observed for CytoD treated cells are 116 nm and 115 nm respectively (Table 6.3). Thus there is no significant change from the mode (117 nm) and peak microvesicle size (115 nm) produced by the PBS control (Table 6.3). This indicates that CytoD does not have any significant effect on the production of microvesicles under normal culture

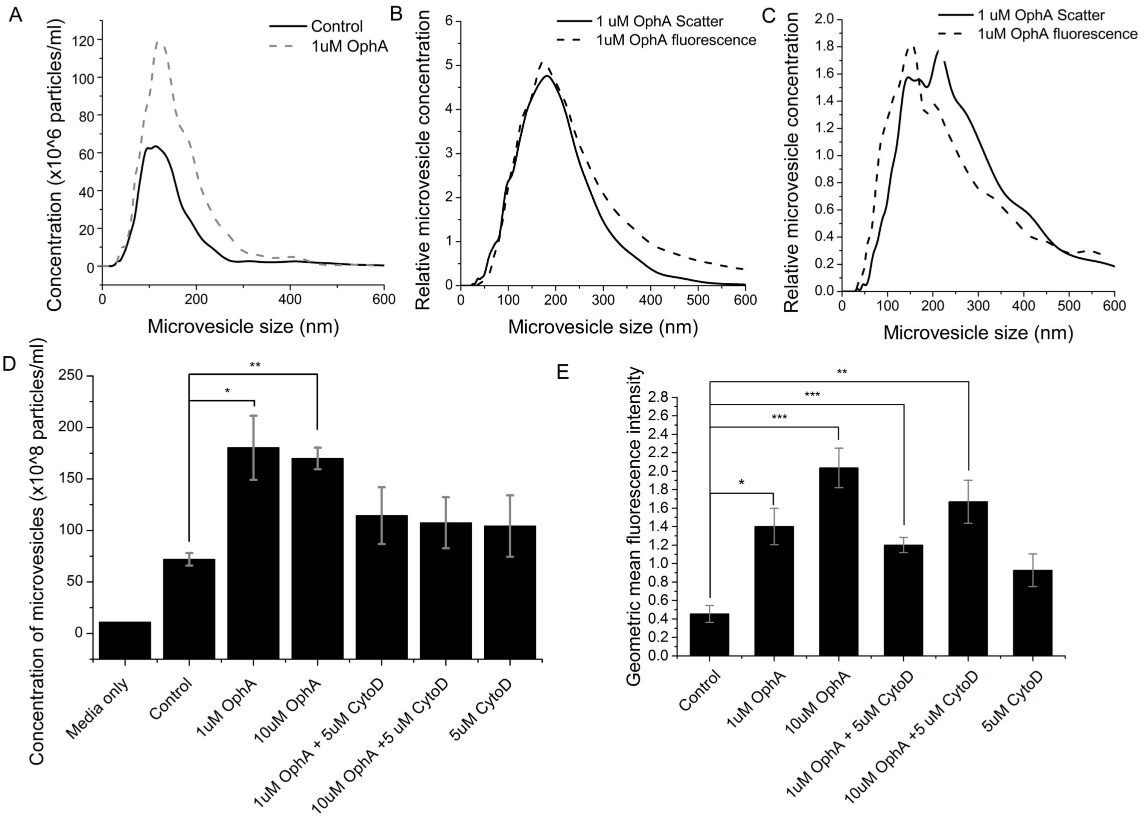

Figure 6.9: Effect of OphA and CytoD on microvesicle production. A) Representative nanoparticle tracking analysis trace showing the change in microvesicle concentration with microvesicle size for PBS control treated cells and cells treated with 1 µM OphA. B) Representative fluorescence nanoparticle trace (cells treated with 1 µM OphA) showing that microvesicles produced can be stained with CellMask^{TM} orange showing that the shed microvesicles originate from the plasma membrane. C) Representative fluorescence nanoparticle trace (cells treated with 1 µM OphA) showing that microvesicles produced can be stained with SYBR® green suggesting that they contain DNA. D) Results from an independent experiment (n=3) showing the change in microvesicle concentration after different treatments (PBS only, 1 and 10 µM OphA, 1 and 10 µM OphA plus 5 µM CytoD and 5 µM CytoD only). Data is presented as mean ± SD of triplicate samples and significance was tested using a two tailed t-test (*$p \leq 0.05$, ***$p \leq 0.005$). E) Results from an independent experiment (n=3) showing the fluorescence intensity of SYBR® green stained microvesicles indicating the presence of DNA in the microvesicles. Data is presented as the geometric mean fluorescence intensity ± SD of triplicate samples and significance was tested using a two tailed t-test (*$p \leq 0.05$,**$p \leq 0.05$, ***$p \leq 0.005$).

conditions. When cells are incubated in a combination of OphA and CytoD, both the number and size of the microvesicles produced is the same as that observed in the PBS only control (Fig 6.9d, Table 6.3). This indicates that the CytoD inhibits the formation of the larger apoptotic bodies but the smaller constitutively expressed exosomes, as seen in the control, are still produced. Thus our results are in line with the proposed mechanism whereby the actin-myosin system is the source of contractile force which drives both membrane blebbing and apoptotic body formation, [233] and this is prevented by the inhibition of actin polymerization with CytoD. Previous work has shown that CytoD (10 µM) inhibits microvesicle formation from activated platelets by 70% [234] and Cytochalasin B, which also inhibits actin polymerisation prevents the formation of 200 to 800 nm microvesicles from leukocytes [235].

6.3.8 Microvesicles originate from the plasma membrane

To determine the origin of the microvesicles, samples were stained with CellMask^{TM} orange; a fluorescent dye which stains the plasma membrane. Signals from both light scatter (showing the total number of microvesicles) and fluorescence (showing the number of fluorescently labelled microvesicles) were recorded by NTA. A representative NTA trace, showing the scatter and fluorescence signal for cells treated with 1 µM OphA has been provided (Fig 6.9B). This shows that there is a good agreement between the scatter and fluorescence signals indicating that the majority, $\geq$86%, of the microvesicles were stained with the CellMask^{TM} orange and hence they originated from the plasma membrane furthermore indicating that the actin-myosin system in responsible for OphA inducing microvesicle production.

6.3.9 Microvesicles contain DNA

Apoptotic bodies are known to contain DNA and therefore we used SYBR® green, a nucleic acid stain which preferentially stains double stranded DNA, to determine if the shed microvesicles contained DNA. This was done using fluorescence NTA using a similar method as for the CellMask^{TM} orange. There was good agreement between the scatter and fluorescence traces which suggests that the DNA is found within the shed microvesicles and not in larger cell debris (Fig 6.9C). However, not all the microvesicles were stained with SYBR®green which indicated that not all the microvesicles contained DNA (Fig 6.9E). There was an increase in the fluorescence intensity by 164% (1 µM OphA) and 258% (10 µM OphA) compared to the PBS only control treated cells (Fig 6.9E). A smaller increase of 147% was observed in the cells treated with CytoD only. This suggests that the cells are releasing more DNA under stress conditions [236] or during apoptosis. Guescini *et al.* [237] showed both glioblastoma cells and astrocytes constitutively release exosomes containing mitochondrial DNA (mtDNA) [237]. Additionally, Bergsmedh *et al.* [238] and Waldenstrm *et al.* [239] have both shown that DNA contained within either tumour apoptotic bodies or shedding microvesicles can be taken up by fibroblast cells. This suggests that cells may be releasing DNA within microvesicles as a means of cell-to-cell signalling. Here, the highest DNA release was seen in the cells which were treated with the highest concentration of OphA and would likely be under the most stress.

6.3.10 Successful release of OphA from HMSNP and PS-HMSNP *in vitro*

In addition to the successful release of OphA from the pores of HMSNP *in chemico*, successful release of OphA from the pores of the HMSNP *in vitro* was also demonstrated. Flow cytometry was used to determine the *in vitro* effect of cell death due to the release of OphA from the HMSNP and the PS-HMSNP on RD cells in growth media. There was a significant ($p \leq 0.05$) decrease in cell viability after treatment with HMSNP@OphA loaded in either ethanol or toluene compared with unloaded control HMSNP (Fig 6.10A). The number of live cells was reduced by 46% and 37% for cells treated with HMSNP@OphA loaded in either ethanol or toluene respectively. The *in vitro* results from the release of OphA from PS-HMSNP showed a very significant ($p \leq 0.0005$) reduction in cell viability, approximately 70%, compared to the blank PS (Fig 6.10B).

6.3.11 Delivery of OphA to drug resistant cells

Nanoparticle drug delivery systems have the potential to evade cell drug resistance mechanisms as the are transported into the cell via different mechanisms to drugs. The effectiveness of the HMSNP@OphA on the vinblastine resistant cell line (KB-VI) and its parent cell line (KB-31) was tested *in vitro*. Vinblastine induced cell death in the parent KB-31 cell line at all concentrations tested (minimum $0.25\,\mu g\,mL^{-1}$) while the vinblastine resistant cell line only showed toxicity above $2\,\mu g\,mL^{-1}$ (Fig 6.11A). In comparison, OphA induced cell death in both the parent KB-31 cell line and the vinblastine resistant cell line (Fig 6.11B). There was no significant difference ($p \geq 0.05$) in cell viability between the cell lines which suggests that OphA could be effective at treating this type of drug resistant cells. Similarly, Bury *et al* [39] showed that OphA could be used to treat a variety of multidrug resistant cell lines (cisplatin, adriamycin, vincristine and mitoxantrone) with no significant difference in LD_{50} value compared to the parent cell line. This suggests that OphA is not removed by the cell though a MDR-related efflux pump. Furthermore, another Ophiobolin, Ophiobolin O, has been shown to reverse adriamycin resistance in the MCF-7/ADR cell line hence increasing its effectiveness at treating drug resistant cells [47].

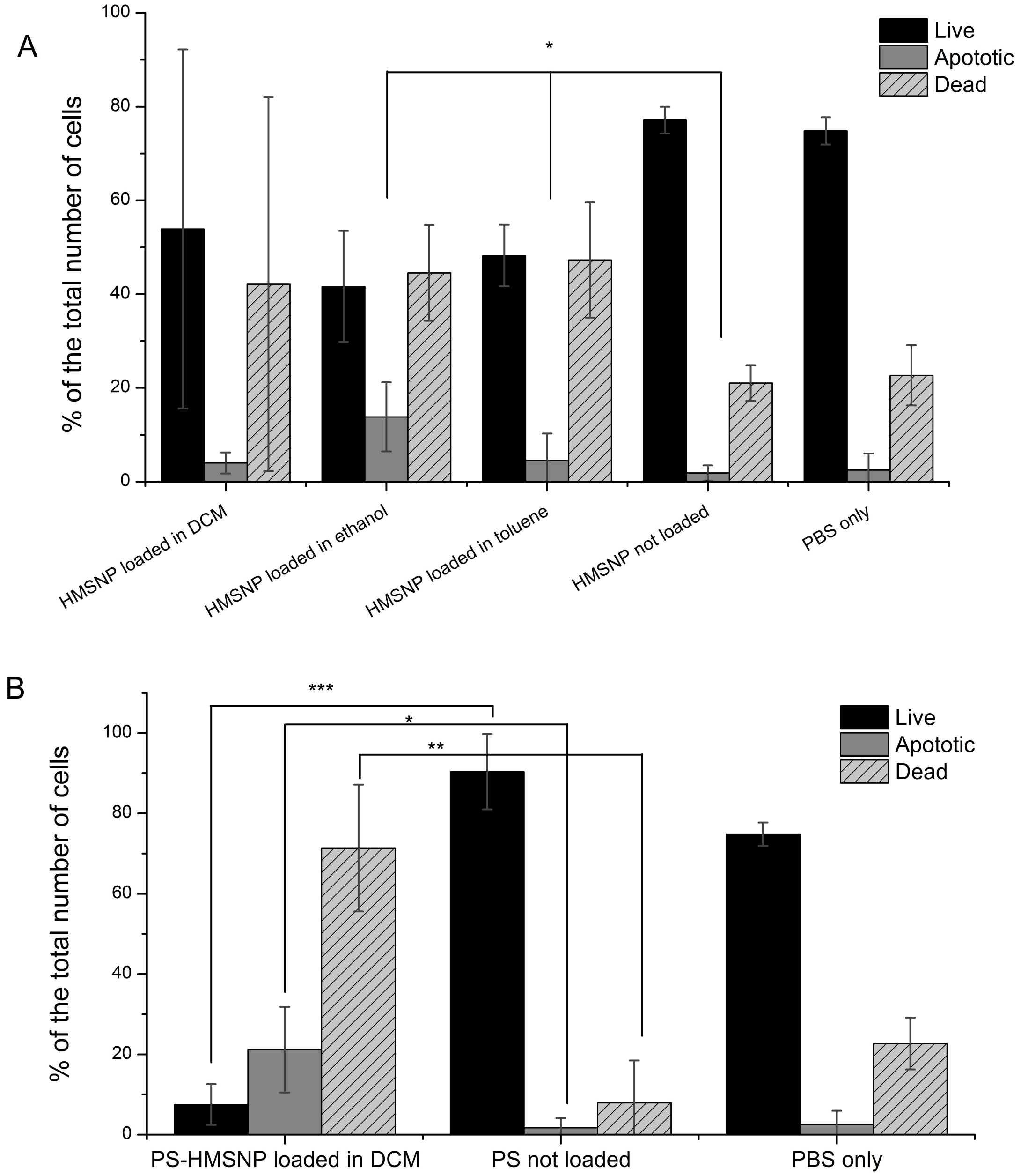

Figure 6.10: Showing the ratio of live, apoptotic and dead cells after the release of OphA from loaded HMSNP and PS-HMSNP into RD cells. A) Results from the mean ± SD of three experiments showing the ratio of live, apoptotic and dead cells after treatment with HMSNP loaded in DCM, ethanol and toluene. B) Results from an independent experiment (n=3) showing the ratio of live, apoptotic and dead cells after treatment with PS-HMSNP loaded with OphA. Data is presented as mean ± SD of triplicate samples and significance was tested using a two tailed t-test (*$p \leq 0.05$, **$p \leq 0.005$, ***$p \leq 0.0005$).

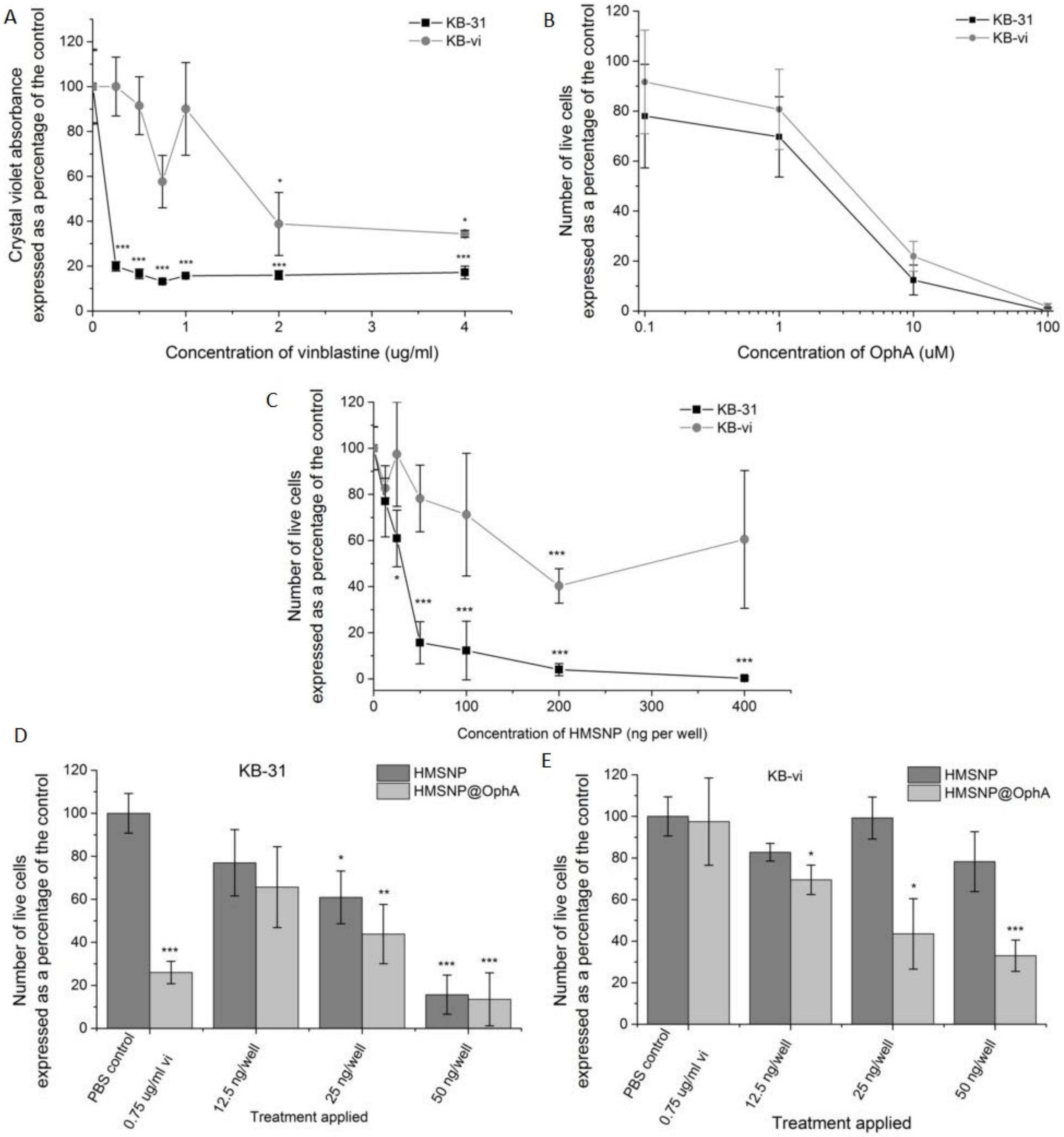

Figure 6.11: OphA and HMSNP@OphA can be used to treat the drug resistant cell line KB-VI. Results from an independent experiment (n=3) showing the effect of A) vinblastine and B) OphA concentration on the vinblastine resistance cell line (KB-VI) and its parent cell line (KB-31) measured by the crystal violet assay and manual cell counting respectively. C) Results from an independent experiment (n=3) showing the effect of HMSNP on the vinblastine resistance cell line (KB-VI) and its parent cell line (KB-31) measured by manual cell counting.

Figure 6.11: (Cont.). Results from an independent experiment (n=3) showing the effect of HMSNP and HMSNP@OphA on D) the vinblastine resistance cell line (KB-VI) and E) its parent cell line (KB-31) measured by manual cell counting (vinblastine ($0.75\,\mu g\,mL^{-1}$) was run as a control to ensure the KB-VI cells remained resistant to vinblastine throughout the experiments). Data for all graphs is presented as mean ± SD of triplicate samples and significance was tested using a two tailed t-test (*$p \leq 0.05$, **$p \leq 0.005$, ***$p \leq 0.0005$).

HMSNP alone were toxic to the KB-31 cell line at concentrations of $\geq$ 25 ng per well compared to the KB-VI cell line where toxicity was first observed at 200 ng per well which is an order of magnitude larger (Fig 6.11C). Hence, the HMSNP are less toxic to the drug resistant cells. Treatment with HMSNP@OphA showed a reduction in live cell number compared to the PBS control for both the KB-31 and KB-VI cell lines (Fig 6.11D,E). However, for the KB-31 cells there was no significant difference ($p \geq 0.05$) in KB-31 cells treated with HMSNP@OphA and blank HMSNP indicating that the majority of the toxicity is resulting from the HMSNP and not the OphA being released from the nanoparticles. In comparison, there was a significant difference ($p \leq 0.05$) in KB-VI cells treated with HMNSP compared to blank HMSNP further indicating that HMSNP@OphA could be an effective method for treating drug resistant cells. Several studies have shown that nanoparticles offer an effective solution to bypass the MDR transporters [80]. For example, Meng *et al.* [200] showed that the expression level of the drug efflux transporter in KB-VI cells was more than 1000 times the expression level in the parent KB-31 cell line. Furthermore, they delivered a multifunctional mesoporous SiO_2 nanoparticle loaded with doxorubicin and surface modified with siRNA to induce gene knockdown of P-gp to KB-VI cells and found that doxorubicin sensitivity could be restored but not to the same level observed in the parental KB-31 cell line.

6.4 CONCLUSIONS

In conclusion, a chemoembolic particle has been we have designed and synthesised which has a high surface area for loading with a novel chemotherapeutic drug OphA. OphA has been shown to be effective at inducing apoptosis in an rhabdomyosarcomaa cancer cell line causing the cells to round up, their membrane to bleb and the cytoplasm to shrink. Membrane blebbing caused an increase in the number microvesicles shed due to OphA treatment. The microvesicles were shown to originate from the plasma membrane and they contained DNA which may have implications in cell-to-cell signalling. Furthermore, OphA has been shown to be effective at treating the vinblastine resistant KB-VI cell line. Successful encapsulation of OphA into the designed drug delivery system was observed and good release in chemico was achieved. Furthermore, significant cell death was shown in RD cells exposed to the OphA loaded chemoembolic particles and KB-VI cell exposed to OphA loaded HMSNP.

Chapter 7

The mechanism of cell death induced by Ophiobolin A

7.1 INTRODUCTION

The evasion of apoptosis is considered a 'hallmark' of cancer cells and it is often is attributed to the resistance of cancer cells to chemotherapeutic agents [2]. All tumour cells have increased proliferation either through the overexpression of antiapoptotic proteins and/or the down-regulation of loss of function mutations in the pro-apoptotic proteins. Therefore the need to discover novel agents which induce other types of cell death are key to discovering effective treatments for cancer in the future. Ophiobolin A (OphA) has been shown to induce both an apoptotic like cell death in RD cells (presented earlier in chapter 6) [240] and a paraptotic like cell death in U373-MG, T98G and GL19 cells [41]. Since OphA can induce different types of cell death it could be effective at treating apoptosis resistant cells and therefore shows great promise as a novel chemotherapeutic. Before a new cancer agent can reach market its molecular target must be identified and its mode of action must be fully elucidated [241]. Therefore the mechanism of cell death induced by OphA on eight cancer cell lines and a control fibroblast cell line has been studied.

7.1.1 Classical types of cell death

Cell death can be triggered by a range of intracellular stresses such as DNA damage, oxidative stress, cystolic Ca^{2+} overload and the accumulation of misfolded proteins [242]. These activate a multitude of signalling pathways resulting in cell death. Traditionally cell death was classified as either 'Type 1 cell death' which is most commonly associated with apoptosis, 'Type 2 cell death' which is most commonly associated with autophagy and 'Type 3 cell death' most commonly associated with necrosis [243].

7.1.1.1 Apoptosis

The most common and well defined type of cell death is apoptosis. Apoptosis is characterised by a rounding up of the cell, a reduction in cellular volume, condensation of the chromatin, nuclear fragmentation (karyorrhexis) and membrane blebbing. Furthermore there is little or no modification to the cytoplasmic organelles and the plasma membrane is maintained until the final stages of cell death [244]. Apoptosis can be induced in cells by two main signalling pathways, the intrinsic or mitochondrial pathway and the extrinsic or death receptor pathway (Fig 7.1). Both the pathways result in the activation of caspase-3 which initiates the caspase cascade leading to the morphological changes associated with apoptosis [245].

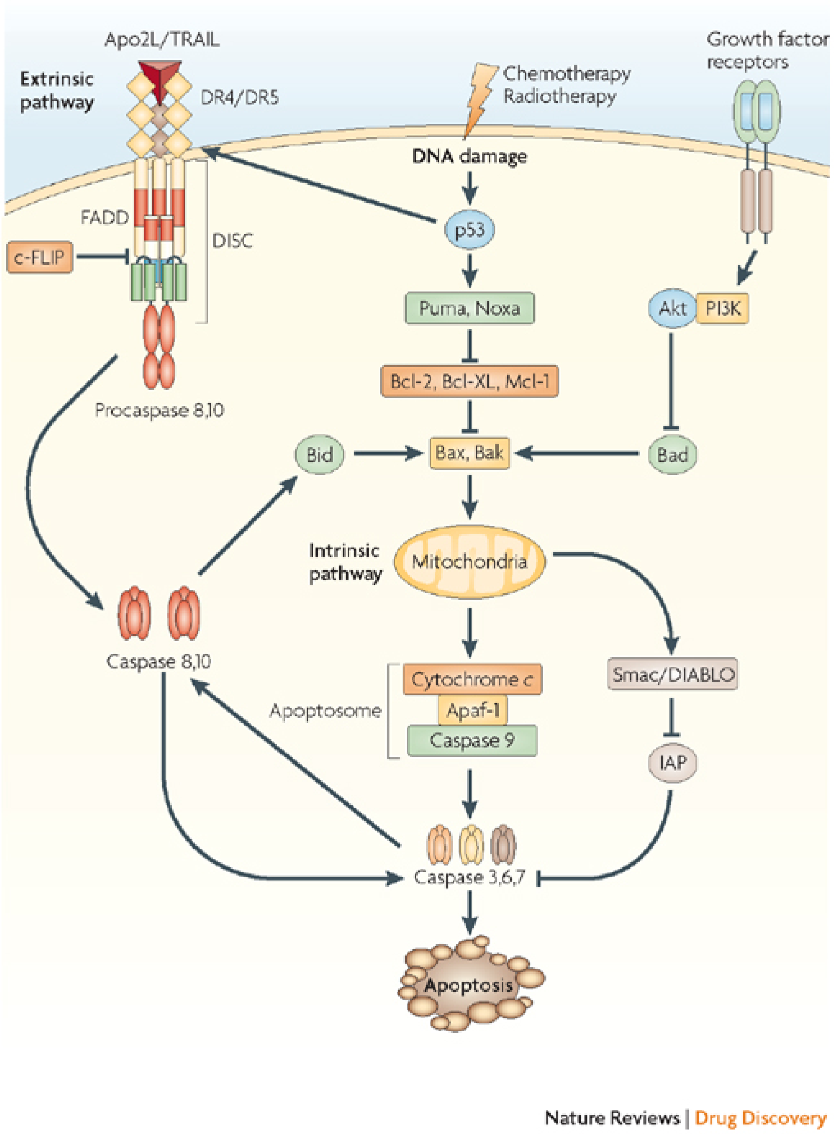

Figure 7.1: Schematic of the intrinsic and extrinsic apoptosis cascades. (Image taken from [246]) This intrinsic pathway is induced by DNA damage, hypoxia and growth factor deprivation which causes the tumour suppressor protein p53 to accumulate in the cell nucleus. This increases the expression of the pro-apoptotic proteins PUMA and NOXA which in turn activate Bcl-2-associated X protein (Bax) and Bcl-2 antagonist or killer protein (Bak) [247]. Upon activation by a pro-apoptotic stimuli Bak undergoes a conformational change on the mitochondrial outer membrane while Bax translocates from the cytosol to the mitochondrial outer membrane causing mitochondrial outer-membrane permeabilization (MOMP) [248]. MOMP causes the release of toxic proteins such as cytochrome c and apoptosis inducing factor (AIF) into the cytosol initiating the caspase cascade [249]. The extrinsic pathway is initiated by death receptors from the tumour necrosis factor (TNF) family which are found on the plasma membrane of the cell [250].

Figure 7.1: (Cont.). These death receptors, such as CD95 (APO-1/Fas) and TNF-related apoptosis inducing ligand (TRAIL), activate caspase-8 which initiates the caspase cascade through caspase-3 [251]. Furthermore the intrinsic and extrinsic pathways are linked, for example caspase-8 can cause cleavage of BH3 interacting-domain death agonist (Bid) initiating the intrinsic pathway and caspase-3 can activate caspase-8.

7.1.1.2 Autophagy

Autophagy is a pro-survival mechanism of the cell in response to stimulation such as nutrient deprivation, hypoxia and/or metabolic stress [252]. It involves the sequestration of damaged cytoplasmic organelles or cytosol into double membranes vacuoles called autophagosomes which are then degraded by the lysosomes. Sustained autophagy results in autophagic cell death either through self cannibalism or though the induction of apoptosis. Autophagic cell death occurs without chromatin condensation but with massive autophagic vacuolization of the cytoplasm [244].

7.1.1.3 Necrosis

Necrosis is a quick and violent form of cell death which is induced by extensive ROS and excess intracellular Ca^{2+} concentrations [253]. Necrotic cell death results from a quick depletion of ATP which causes failures in the ion pumps/channel and a loss of membrane potentials [254]. Therefore necrotic cell death can be characterised by a gain in cell volume (oncosis), swelling of cellular organelles, a pynotic (irreversible chromatin condensation) nucleus and rupture of the cellular membranes [255]. Furthermore necrotic cells can randomly degrade their DNA, mRNA and proteins, induce a massive Ca^{2+} ion influx and trigger an inflammatory response in surrounding cells. Traditionally necrosis was considered an accidental and uncontrolled form of cell death recently however regulated necrosis such as necroptosis, mitochondrial permeability transition (MPT)-dependent regulated necrosis, parthanatos, have been observed [256].

7.1.1.4 Non-classical types of cell death

Recent research has suggested numerous different ways in which a cell can die and this has led to great confusion in the area. Moreover this means it is difficult to review the cell death literature effectively since historic articles present the type of cell death as one of the three original types while more recent research regularly propose new types of cell death without comprehensive definitions. Some of these newly defined types of cell death include necroptosis, mitotic catastrophe, anoikis, excitotoxicity, paraptosis, pyroptosis, pyronecrosis and entosis [244].

7.1.2 Aims and Objectives

The aim of the work presented in this chapter was to determine the effects of OphA on eight cancer cell lines and one control fibroblast cell line. The objectives included determining how OphA effects the morphology of the cells and their nucleus, endoplasmic reticulum and mitochondria. Furthermore, the effects of OphA on intracellular calcium concentration, reactive oxygen species generation and mitochondrial function were sought to be established. The final objective was to determine possible modes of cell death, namely apotosis and cell cycle arrest, induced by OphA.

7.2 MATERIALS AND METHODS

7.2.1 Cell lines

The mechanism of cell death induced by OphA was investigated on the following cell lines: RD, RH30, MDA-MB-231, MCF7, HeLa, KB-31, Fibroblast, U2OS and U-87 MG. The mutations found in the cells lines are provided in Table 7.1. Further information regarding the cell lines used can be found in section 2.3.

Table 7.1: Summary of the mutations found in the cell lines used in this study. CDKN2A (cyclin-dependent kinase inhibitor 2A) is a tumour suppressor gene which encodes three proteins of which two variants are inhibitors of CDK4 kinase and therefore are capable of inducing G_1 cell cycle arrest. The PIK3CA (phosphatidylinositol-4, 5-bisphosphate 3-kinase, catalytic subunit alpha) gene encodes the p85α catalytic subunit of class 1 phosphatidylinositol 3-kinases (PI3K). PI3K operates as part of the PI3K/AKT/mTOR pathway which mediates cell proliferation, survival, migration and vesicular trafficking. PTEN (Phosphate and tensin homolog) is a tumour suppressor gene which down-regulates PI3K activity, inhibits AKT signaling pathway and affects cell cycle regulation. RAS (Rat sarcoma) encodes for proteins (KRAS, HRAS and NRAS) which belong to the small GTPase superfamily. RAS proteins recruit and activate downstream effector such as the AKT and ERK pathways which results in changes to cell growth, differentiation and survival. TP53 encodes the major tumour transcription factor p53 which plays a significant role in regulating cellular responses to DNA damage. p53 activation leads to cell cycle arrest and apoptosis [257] .

Cell line	**Tissue type**	**Mutation**	**Ref**
RD	muscle	NRAS, TP53	[257]
RH30	muscle	TP53	[258]
MDA-MB-231	breast	CDKN2A, KRAS, TP53	[257]
MCF7	breast	CDKN2A, PIK3CA, caspase 3	[257],[259]
HeLa	cervix	Mutations in cell cycle and DNA repair signaling pathways	[260]
KB-31	HeLa contaminant	Likely to be similar to HeLa	
Fibroblast	fibroblast	Healthy control cell line	
U2OS	bone	wildtype TP53A	[261]
U-87 MG	brain	CDKN2A,PTEN	[257]

7.2.2 Cell viability assay

Cell viability after 24 hours of 0 µM–100 µM OphA treatment was assessed using crystal violet staining as described in section 2.3.2.1.

7.2.3 Immunofluorescence staining

7.2.3.1 Staining of cell DNA using Hoechst

Cells were seeded in 96 well plates at 1x10^4 cells per well in growth media and left overnight in the incubator for the cells to adhere. The following day cells were treated for 24 hours with i) PBS as a control, ii) 1 µM OphA, iii) 10 µM OphA or iv) 100 µM OphA. After treatment the cell DNA was stained with 10 nM Hoechst for 30 minutes. The cells were imaged with a Motic AE31 microscope equipped with a mercury lamp and filters for DAPI (Ex. 345 nm, Ex. 455 nm). Experiments were performed in triplicate and repeated on at least two separate occasions.

7.2.3.2 Staining of cell mitochondria using Mitotracker® Green and TMRM

Cells were seeded in 24 well plates at 8x10^4 cells per well in growth media and left overnight in the incubator for the cells to adhere. The following day cells were pre-stained with 200 nM MitoTracker® green (Invitrogen), 50 nM Tetramethylrhodamine, methyl ester (TMRM; Invitrogen) and 10 nM Hoechst for 30 minutes. After staining was confirmed, cells were washed in fresh media and treated for one hour with either i) PBS, ii) 1 µM OphA or iii) 10 µM OphA in triplicate. The cells were imaged with a Motic AE31 microscope equipped with a mercury lamp and filters for DAPI, TRITC (Ex. 547 nm, Em. 572 nm) and FITC (Ex. 495 nm, Em. 519 nm). Experiments were performed in triplicate and repeated on at least two separate occasions.

7.2.3.3 Reactive oxygen species detection in cells using CM-H_2DCFDA

Cells were seeded in 24 well plates at 8x10^4 cells per well in growth media and left overnight in the incubator for the cells to adhere. The following day cells were pre-stained with 1 µM 2',7'-dichlorodihydrofluorescein diacetate (CM-H_2DCFDA; Invitrogen) for 45 minutes. After staining was confirmed, cells were washed in fresh media and treated for one hour with either i) PBS, ii) 1 µM OphA or iii) 10 µM OphA in triplicate. Cells were imaged using a Motic AE31 microscope with filters for FITC. Experiments were performed in triplicate and repeated on at least two separate occasions.

7.2.4 Intracellular calcium concentration

Cells were seeded in 96 well plates at 1x10^4 cells per well in growth media and left overnight in the incubator for the cells to adhere. The following day cells were washed in PBS and pre-stained with 2 µM Fluo4 AM (Invitrogen) in PBS for one hour. The acetoxymethyl (AM) ester is conjugated to the Fluo-4 dye which results in an uncharged molecule that can permeate cell membranes [262]. Once inside the cell the lipophilic blocking groups are cleaved by non specific esterases which significantly reduces leakage of the parent compound from the cell. After staining was confirmed, cells were washed in PBS twice and then the following treatments were applied i) PBS, ii) 1 µM OphA and iii) 10 µM OphA. The change in Fluo4 fluorescence over six hours, at five minute intervals, was measured using a Tecan Infinite f200 series plate reader equipped with filters for FITC (Ex. 495 nm, Em. 519 nm). Samples were blank corrected and the maximum slope of the linear region of each curve was calculated. Experiments were performed in triplicate on two separate occasions.

7.2.5 Flow cytometry

Flow cytometry was used to assess the effects of OphA on cell morphology, mitochondrial membrane potential, reactive oxygen species generation, Annexin V and cell cycle. Samples were prepared as previously described in section 2.3.3 and measured using a FACS Calibur flow cytometer (BD). The OphA treatments and dyes used for staining are provided in section 7.2.5.1 to section 7.2.5.5.

7.2.5.1 Cell size

Cells were treated for 24 hours with either i) PBS, ii) 1 µM OphA or iii) 10 µM OphA or iv) 100 µM in triplicate. The change in cell size was investigated by monitoring the change in median forward scatter (FSC) signal intensity (Fig 7.2).

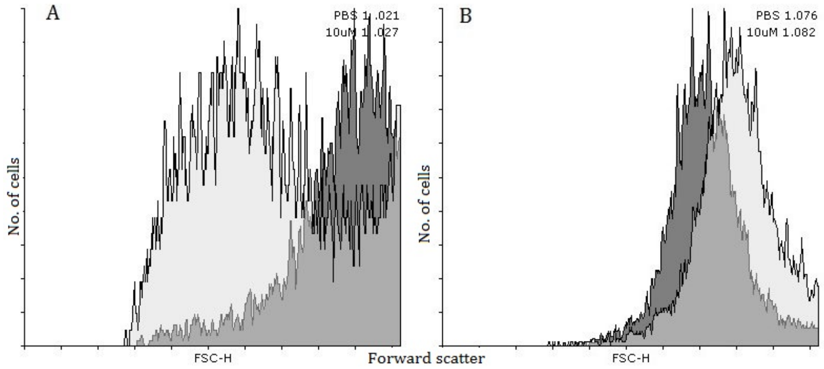

Figure 7.2: Representative flow cytometry data showing the change in cell size. A) RD cells showing cell shrinkage and B) U2OS cells showing cell swelling after treatment with 10 µM OphA (FSC=Forward scatter, Dark grey= PBS treated cells, Light grey=10 µM treated cells).

7.2.5.2 Quantification of mitochondrial membrane potential using TMRM

Cells were treated for one hour with either i) PBS, ii) 1 µM OphA or iii) 10 µM OphA in triplicate. Cells were stained with 500 nM MitoTracker® Green and 50 nM TMRM for

30 minutes at room temperature. The change in mitochondrial membrane potential was investigated by monitoring the change in median TMRM fluorescence intensity (Fig 7.3).

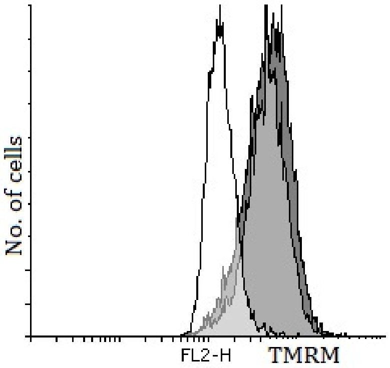

Figure 7.3: Representative flow cytometry data showing the change in mitochondrial membrane potential ($\Delta\psi_m$). RD cells show a decrease in 50 nM TMRM fluorescence after treatment with 10 µM OphA (FL2-H= TMRM fluorescence intensity, dark grey= PBS, light grey=1 µM OphA, white=10 µM OphA treated cells).

7.2.5.3 Quantification of reactive oxygen species in the cells using CM-H_2DCFDA

Cells were treated for one hour with either i) PBS, ii) 1 µM OphA or iii) 10 µM OphA in triplicate. Cell were stained with 1 µM CM-H_2DCFDA and 120 mM PI for 45 minutes at room temperature. PI stains cells with a permeable membrane, therefore dead cells. The reactive oxygen species production was investigated by monitoring the change in median CM-H_2DCFDA fluorescence intensity of the live cells (PI negative) (Fig 7.4).

7.2.5.4 Quantification of phosphatidylserine translocation to the outer membrane

Cells were treated for 24 hours with either i) PBS, ii) 1 µM OphA or iii) 10 µM OphA or iv) 100 µM in triplicate. Cells were dyed with 2.5 µl of APC-Annexin V (Biolegend) to probe phosphatidylserine translocation onto the outer membrane and 150 mM PI. The

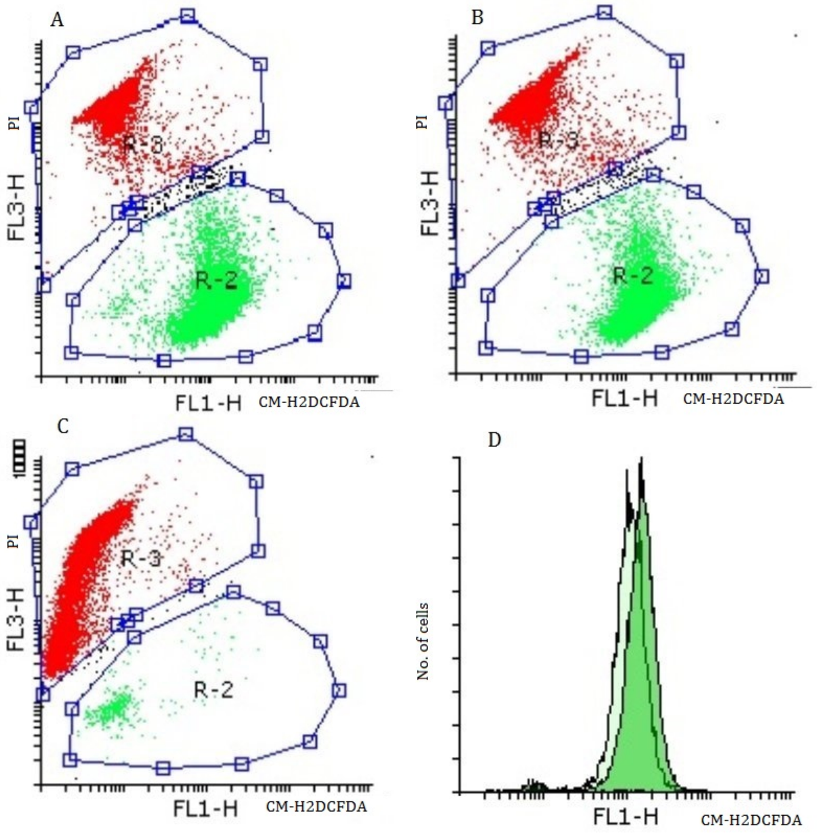

Figure 7.4: Representative flow cytometry data showing the change in reactive oxygen species. RD cells stained with 1 µM CM-H_2DCFDA (FL1) and 120 mM PI (FL3) after treatment with A) PBS, B) 1 µM OphA and C) 10 µM. The live cells (PI negative) are in region 2 and coloured green while the dead cells (PI positive) are in region 3 and coloured red. D) Histogram plot showing the change in median CM-H_2DCFDA (FL1) fluorescence of the live cells which was used to obtain the median fluorescence of each sample (light green= control, dark green=1 µM OphA, black=10 µM OphA). There were very few live cells after 10 µM OphA treatment. (FL1-H= CM-H_2DCFDA fluorescence intensity, FL3-H= PI fluorescence intensity)

number of cells which showed positive APC annexin V staining with negative PI staining were recorded (Fig 7.5).

7.2.5.5 Quantification of cell cycle using PI

Cells were treated for 24 and 48 hours with either i) PBS or ii) 1 µM OphA in triplicate. Fixed cells were stained with 66 mM Propidium iodide (PI; Aldrich) for 15 minutes. The cell cycle was analysed using a demo version of FCS express software to determine the

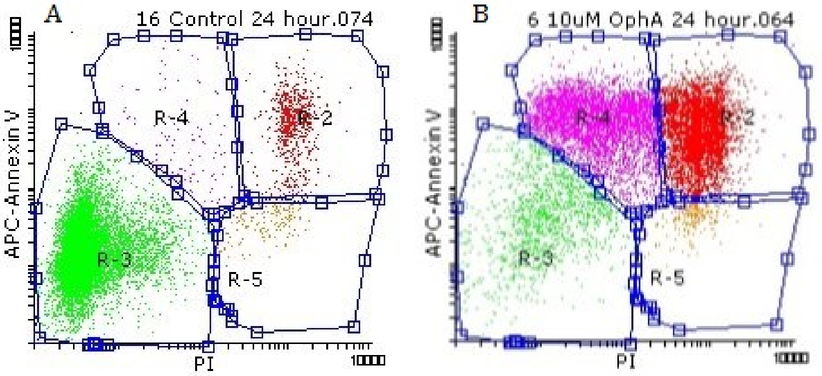

Figure 7.5: Representative flow cytometry traces for MDA-MB-231 cells treated for 24 hours with A) PBS as a control and B) 10 µM OphA and stained with annexin V and PI showing the gating applied to determine the levels of apoptosis. Region 3 (green) indicates unstained cells therefore live cells. Region 2 (red) indicates both annexin V and PI stained cells and therefore dead cells. Region 4 (pink) indicates annexing V positive, PI negative cells and therefore early apoptotic cells. Region 5 (orange) indicates annexin 5 negative and PI positive cells and therefore dead cells.

number of cells in each of the three cell cycle phases (G_0/G_1, S and G_2/M) Fig 7.6. Debris and doublets were excluded from the analysis and Model 2 (Sliced nucleus background modelling, clumping compensation with zero order S phase) was applied to fit the G_0/G_1, S and G_2/M peaks to the data [263].

7.2.6 Automated high throughput image acquisition and analysis

Cells were seeded in 96 well plates at 7.5x10^3 cells per well in growth media and left overnight in the incubator for the cells to adhere. The following day cells were treated for 24 hours with either i) PBS or ii) 1 µM OphA in triplicate. Cells were then washed in PBS, fixed in 4% paraformaldehyde (PFA; Sigma) for 15 minutes, washed twice again in PBS and left in PBS until staining. The endoplasmic reticulum (ER) was stained with calnexin (Santa Cruz), the mitochondria with TOM20 (Santa Cruz) and the nucleus with DAPI. Alexa-fluor secondary antibodies (Invitrogen) were used to stain the ER green

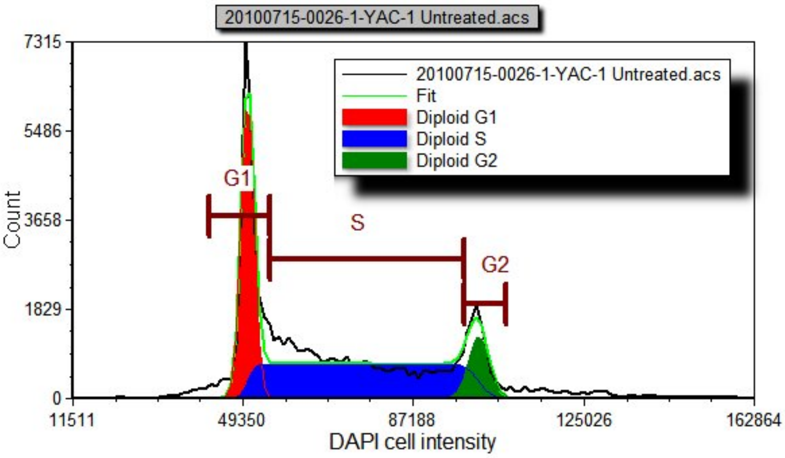

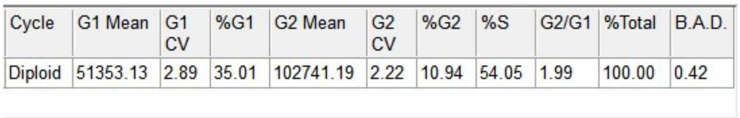

Cycle	G1 Mean	G1 CV	%G1	G2 Mean	G2 CV	%G2	%S	G2/G1	%Total	B.A.D.
Diploid	51353.13	2.89	35.01	102741.19	2.22	10.94	54.05	1.99	100.00	0.42

Figure 7.6: Representative flow cytometry trace showing the phases of the cell cycle. The intensity of the PI fluorescence is related to the amount of DNA in the cell and therefore can be used to determine which phase of the cell cycle the cells are in. The phases of the cell cycle were evaluated using FSC express software by fitting three curves to the data representing the G_0/G_1, S and G_2/M peaks.

and the mitochondria red. Staining was performed within seven days of fixing.

Image acquisition was performed using an automated imaging platform equipped with a Nikon Fluor ELWD 40 X 0.6 objective (IN Cell Analyser 1000). Six fields of view were taken from each well in all three fluorescence modes. Cells were automatically segmented using DAPI (cell nuclei) and the properties of the ER and mitochondria were obtained using the IN Cell Analyzer Workstation 3.4 software. The total area of the endoplasmic reticulum, the total area of the mitochondria, the mitochondrial size and the mitochondrial branching network were investigated. Experiments were performed in triplicate and repeated on at least two separate occasions. The staining, image acquisition and image segmentation were carried out by Mrs Tiffany Lodge and Dr Alan Diot (Nuffield Department of Obstetrics and Gynaecology, Oxford University).

7.2.7 Immunoblotting

Cells were seeded in T25 flasks at 75x10^4 cells per flask in growth media and cells were allowed to adhere to the flask overnight in the incubator. The following day cells were treated for 24 hours with either i) PBS or ii) 1 µM OphA. Cell lysates were prepared using 200 µl of Complete Lysis-M kit supplemented with protease and phosphatase inhibitors (Roche Diagnostics) and scraping the cells from the bottom of the flasks. Cell lysates were centrifuged to separate cell debris and the protein concentration of the supernatant was determined using the bicinchoninic acid assay (BCA assay; Pierce). Protein (10 µg per sample) was mixed with loading buffer, boiled for 4 minutes and subjected to SDS-PAGE at 120 V using Precise^{TM} Tris-HEPES 8%-16% Gels (Invitogen) and Tris-HEPES-SDS (Invitrogen) running buffer. Transfer to PVDF membrane (Amersham biosciences) for 50 minutes at 30 V in transfer buffer(25 mM tris base (Sigma), 190 mM glycine (Sigma), 20% methanol (Fisher) in ddH$_2$O). Membranes were blocked with 5% milk in TBST (Tris buffered saline + 1% Tween 20) for one hour at room temperature and subsequently probed with BIP (1:1000), PDI (1:1000), CHOP (1:1000), cleaved PARP (1:1000) or β-actin (1:100 000) in TBST supplemented with 5% milk as a primary antibody overnight at 4 °C. Horseradish peroxidase-conjugate secondary antibodies were used and blots were revealed by ECL (Clarity ECL Western Blot Substrate, Biorad). Experiments were performed on two separate occasions.

7.3 RESULTS

7.3.1 OphA causes changes in cell morphology and induced cell death

OphA was assessed in terms of its ability to effect cell death in nine cell lines. In all the cell lines tested, OphA caused the cells to round up and become more spherical.

Representative bright field images of RH30 cells treated with 0 µM–100 µM OphA are provided as an example. Control RH30 cells in culture present as spindle shaped large multinucleated cells (Fig 7.7A). Incubation of cells with 1 µM OphA for 24 hours show no significant difference in morphology compared to the control cells (Fig 7.7B). Incubation of cells with 10 and 100 µM OphA for 24 hours causes the cells to round up, their membrane blebs and their cytoplasm shrinks (Fig 7.7C,D).

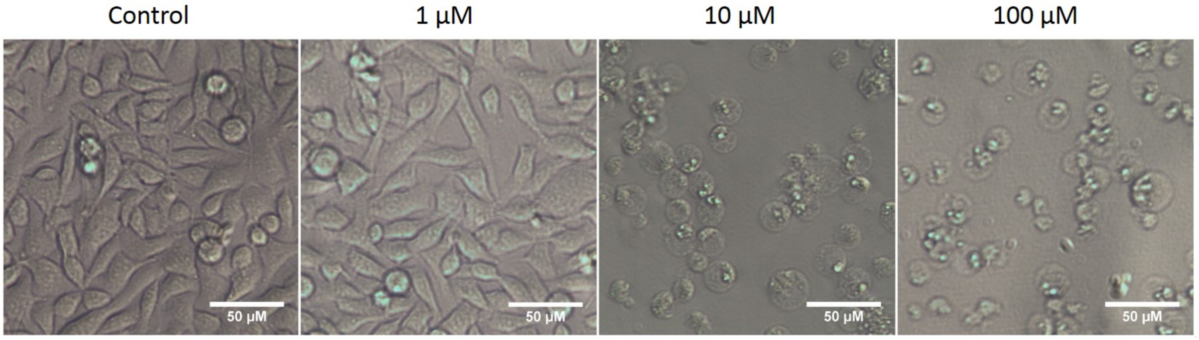

Figure 7.7: Representative bright field microscope images of RH30 cells treated with 0 µM–100 µM OphA. A) RH30 cells treated with PBS as a control, B) RH30 cells treated with 1 µM OphA showing no significant difference in morphology to the control. RH30 cells treated with C) 10 µM OphA and D) both showing the cells rounding up and becoming more spherical. All scale bars are 50 µm

Cell viability after 24 hour treatment with 0 µM–100 µM OphA was assessed using a crystal violet assay for all the cell lines (Fig 7.8). As expected, increasing the concentration of OphA reduced the cell viability in all the cell lines. The LD_{50} values ranged from 0.7 µM to 4.5 µM for MDA-MB-231 and HeLa cells respectively (Table 7.2).

Cells are known to change size during cell death: for example, cells are known to shrink during apoptosis while they are known to swell during necrosis [264]. Changes in cell size, after 24 hour treatment with OphA, was monitored using the FSC channel on the flow cytometer (Fig 7.9). After 24 hours of OphA treatment either cell shrinkage, cell swelling or no change in cell size was observed depending on the cell line treated. RD,

Table 7.2: OphA LD$_{50}$ values for each cell line taken from the data provided in Fig 7.8.

Cell line	LD$_{50}$ (μM)
RD	1.3
RH30	1.5
MDA-MB-231	0.7
MCF7	4
HeLa	4.5
KB-31	1.4
Fibroblast	1.4
U2OS	2.8
U-87 MG	3.8

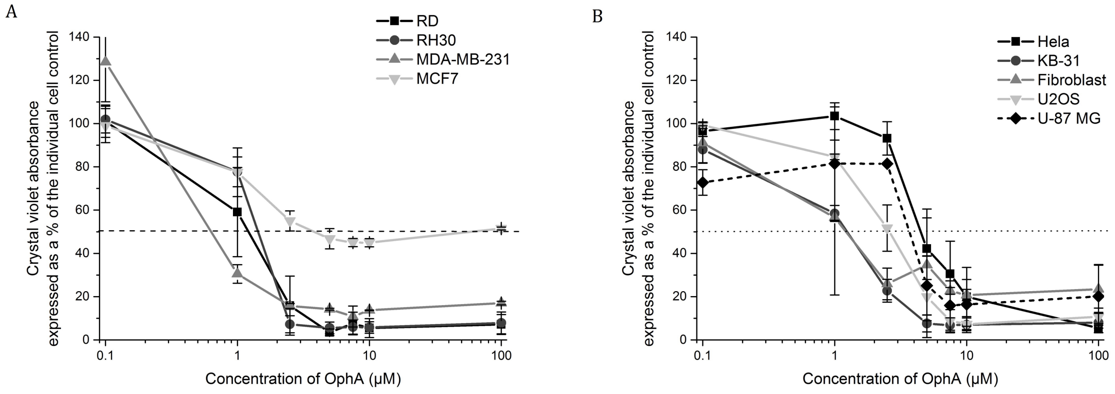

Figure 7.8: OphA induced cell death in all cell lines tested. Cell viability results from independent experiments (n=3) after treatment with 0 µM–100 µM OphA using crystal violet staining for all the cell lines used in the study. Data is presented as mean ± SD of triplicate samples expressed as a percentage of the control cells absorbance.

RH30, MDA-MB-231 and MCF7 cells showed very significant ($p \leq 0.005$) cell shrinkage of (32% ± 1), (32% ± 1), (40% ± 1) and (23% ± 4) respectively compared to the individual no drug cell control. HeLa, Fibroblast and U2OS cells showed significant ($p \leq 0.01$) cell swelling of (22% ± 1), (19% ± 1) and (23% ± 1) respectively compared to the individual cell control. There was no significant change in cell size of the KB-31 and U-87 MG cell lines. Treatment with the lower magnitude concentration of 1 µM OphA for 24 hours resulted in no significant change in cell size for any of the cell lines tested

(Fig 7.9).

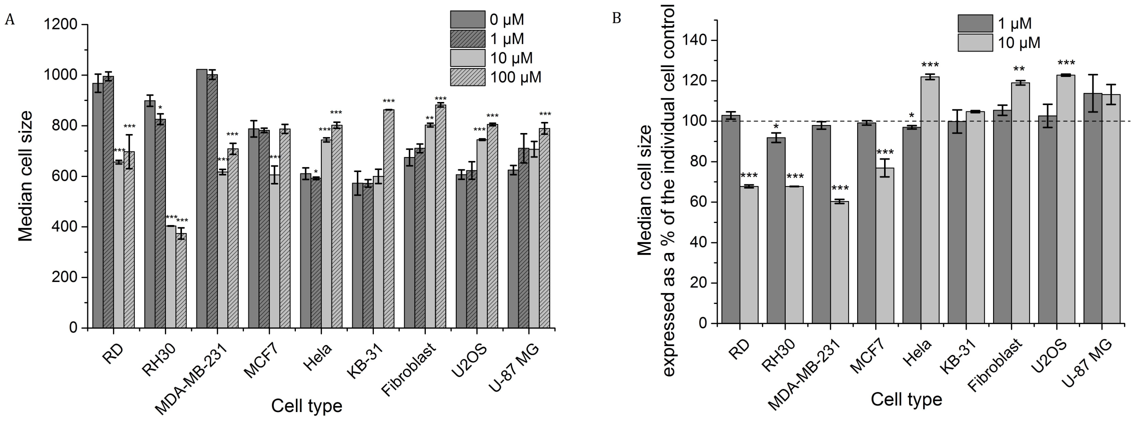

Figure 7.9: OphA causes both cell shrinkage and cell swelling depending on the cell line. Flow cytometry results for independent experiments (n=2-3) for each cell line showing the change in cell size after 24 hour treatment with 0 µM–100 µM OphA. Data is presented as mean ± SD of triplicate samples for each individual cell line expressed as A) the raw data and B) as the data as a percentage of the untreated cells. Significance was tested using a two tailed t-test compared to the untreated cells for each cell line (*$p \leq 0.05$, **$p \leq 0.01$, ***$p \leq 0.005$).

7.3.2 OphA causes nuclear destruction in all cell lines except U-87 MG cells

There are three forms of nuclear destruction which occur in dying cells: namely karyolysis, pynkosis and karyorrhexis (Fig 7.10). Staining of the DNA with Hoechst after 24 hours of treatment with 10 µM OphA showed nuclear destruction in all cell lines except U-87 MG cells (Fig 7.11). Karyorrhexis was observed in RD, RH30, MDA-MB-231, MCF7, HeLa, KB-31 and U2OS. Additionally, karyolysis was observed in RH30, MDA-MB-231, MCF7, HeLa and KB-31 cells and pynokis was observed in KB-31 and U2OS cells. Only pynkosis was observed in fibroblast cells. There was no change in nuclear morphology compared to the control for any of the cell lines after 1 µM OphA treatment. Furthermore, a time course experiment with RD cells showed no nuclear destruction with 0 µM–100 µM OphA when cells were prestained with Hoechst (data not shown).

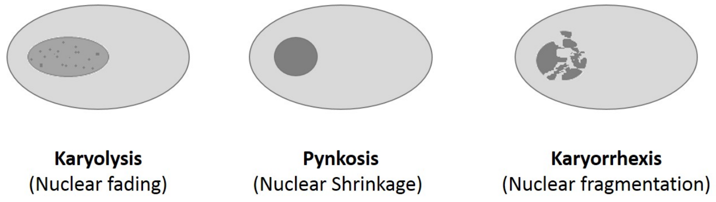

Figure 7.10: Schematic of three forms of nuclear destruction: karyolysis, pyknosis and karyorrhexis. Karyolysis or nuclear fading is the complete dissolution of chromatin in a dying cell due to the action of DNAases and RNAases. Pyknosis or nuclear shrinkage is the irreversible condensation of chromatin in the cell nucleus. Karyorrhexis or nuclear fragmentation is the destructive fragmentation of the nucleus of a dying cell which occurs after karyolysis or pyknosis.

7.3.3 OphA affects intracellular cell calcium concentration

OphA is known to inhibit the calcium binding protein calmodulin [265] and therefore we studied the change in calcium concentration after treatment with OphA. Cells were pre-stained with a calcium sensitive dye Fluo-4 AM, OphA treatment was applied and the change in Fluo-4 fluorescence was monitored over time. There was an increase in Flou-4 fluorescence with time for all samples measured however the increase in Fluo-4 fluorescence was inhibited by at least one hour in cells treated with 10 µM OphA (Fig 7.12). After six hours of 10 µM treatment all the cell lines showed either an increase, or no significant difference, from the control except the U2OS cells where the final florescence was significantly lower in magnitude than the untreated cells. The sample with the highest Fluo4 fluorescence after six hours and thus containing the maximum calcium concentration was the MDA-MB-231 cells treated with 10 µM OphA (Table 7.3). The maximum rate of change of the Fluo4 fluorescence was quantified from the data provided in Fig 7.12A and there was a significant increase from the untreated cells in all cell lines except HeLa and U2OS (Fig 7.12B). RH30 and MDA-MB-231 cells showed the highest rate increase of 18 and 20 times the control rate respectively (Fig 7.12B).

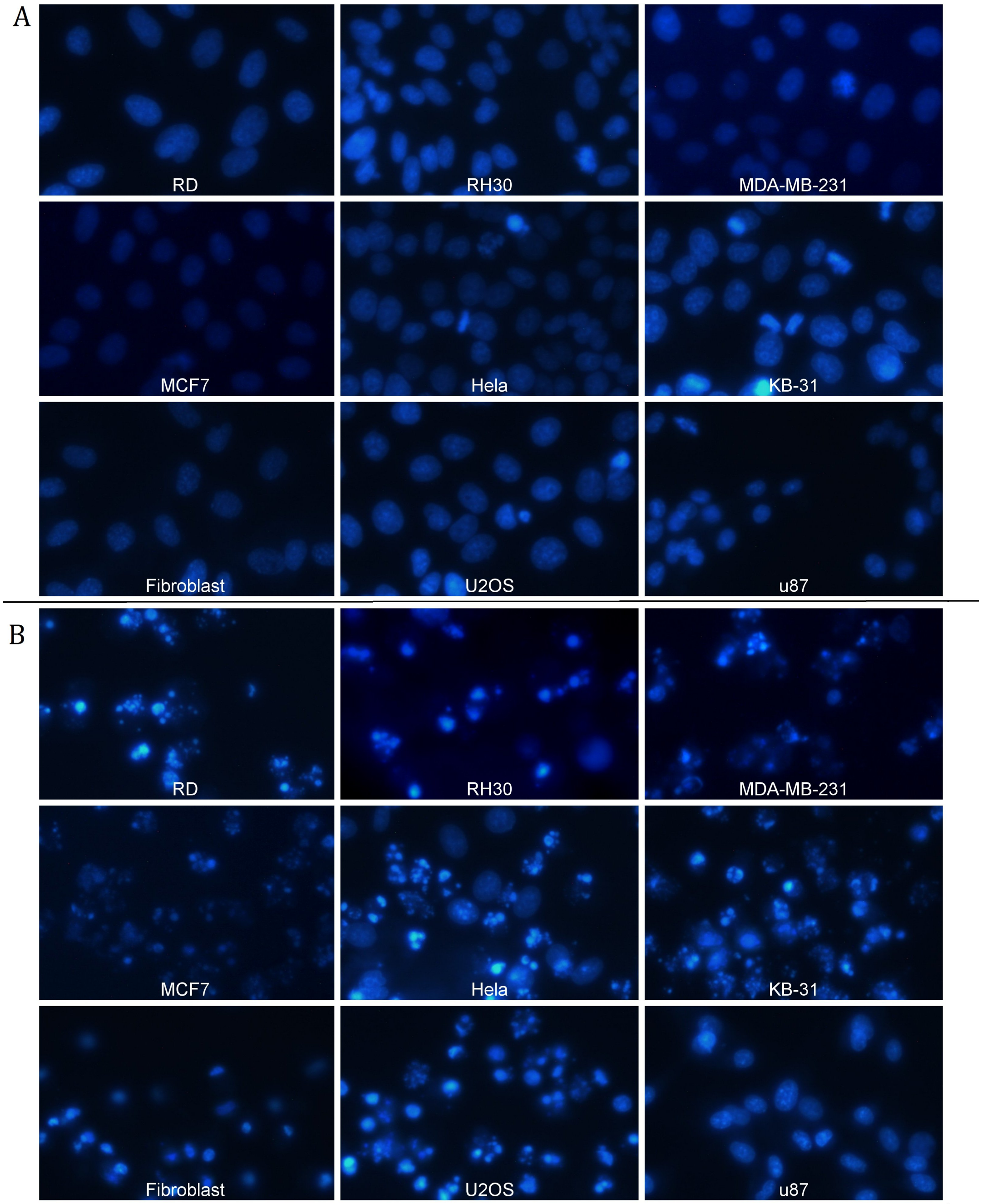

Figure 7.11: OphA induced nuclear destruction in all cell lines except U-87 MG cells. Representative fluorescence images of the cell DNA using Hoechst stain after 24 hour treatment with A) PBS as a control and B) 10 µM OphA for each cell line.

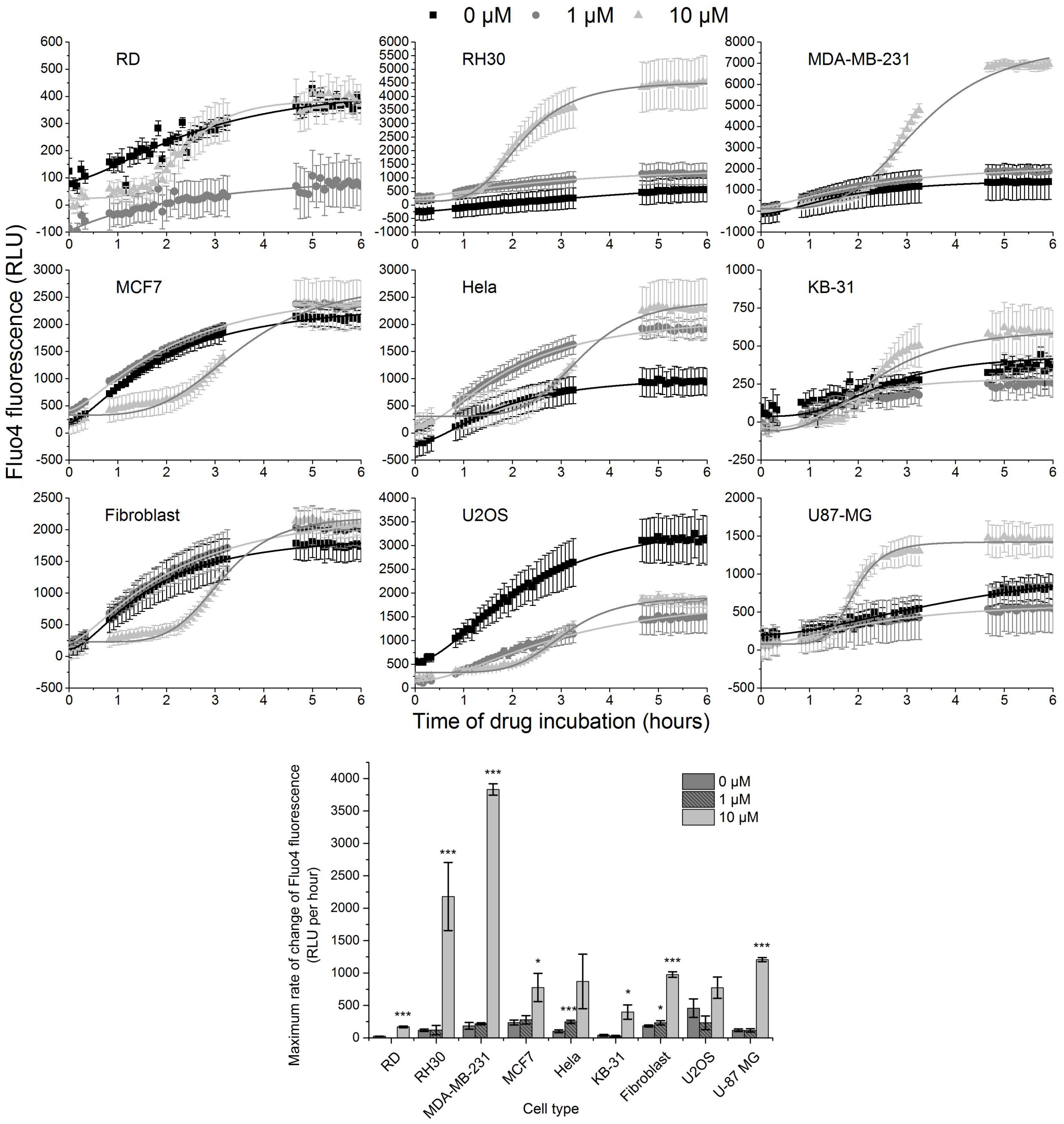

Figure 7.12: Effect of OphA on cell calcium concentration measured using Fluo4. A) Results from independent experiments (n=2) showing the change in Fluo4 fluorescence with time after treatment with either i) PBS (Black squares), ii) 1 µM OphA (Dark grey circles), iii) 10 µM OphA (Light grey triangles) for each cell type. The data is presented as mean ± SD of triplicate samples for each individual cell line. Logistic curves have been fitted to all the data with R^2 values ≥ 0.9 for all cell lines except KB-31 cells. B) Results from independent experiments (n=2) showing the maximum rate of change of Fluo4 fluorescence per hour after treatment with OphA. The data is presented as mean ± SD of triplicate samples each individual cell line. Significance was tested using a two tailed t-test compared to the untreated cells for each cell line (*$p \leq 0.05$, **$p \leq 0.01$, ***$p \leq 0.005$).

Table 7.3: Effect of OphA on calcium concentration measured using Fluo4 showing the maximum Fluo4 fluorescence value for cells treated with 10 µM OphA for six hours.

Cell type	**Maximum Fluo4 fluorescence value (RLU)**
RD	415 ± 75
RH30	4534 ± 980
MDA	6985 ± 221
MCF7	2400 ± 467
HeLa	2331 ± 484
KB-31	622 ± 167
Fibroblast	2176 ± 191
U2OS	1991 ± 121
U87	1493 ± 206

7.3.4 OphA induced endoplasmic reticulum stress

Similar to autophagy, the ER stress response is another adaptive mechanism to support cell survival in response to detrimental conditions such as low nutrient levels, hypoxia, calcium imbalance or the accumulation of misfolded proteins [266]. When the stress conditions become too long or too severe, the response activates a death pathway. There are three main pathways of the ER stress response which are initiated by three sensor proteins located on the ER membrane (Fig 7.13).

As it was shown that OphA causes changes to intracellular calcium concentration it was decided to study the effect of OphA on the ER. The change in ER total area was measured using an automated high throughput image acquisition and analysis system (IN Cell). The ER was stained with calnexin and the IN Cell Analyser software was used to determine the change in ER area after 24 hour treatment with 1 µM OphA (Fig 7.14).

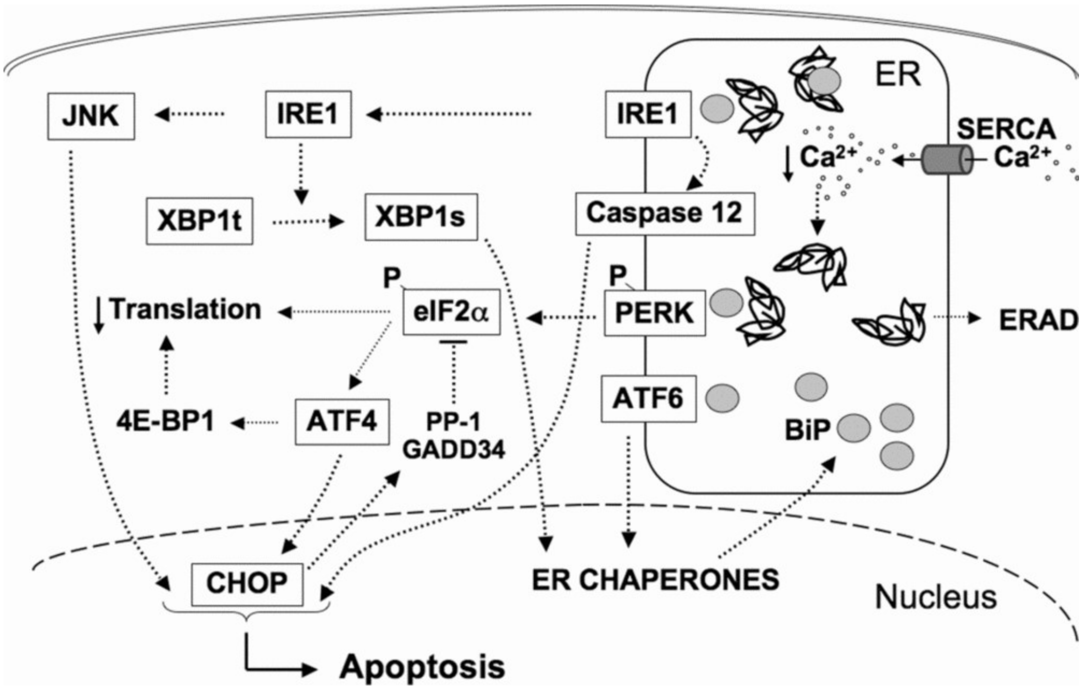

Figure 7.13: Schematic of the ER stress response in cells initiated by one of three sensor proteins. (Image taken from [267]) Inositol-requiring transmembrane kinase and endonuclease 1 (Ire1) is one of these sensor proteins which is dimerized and phosphorylated promoting splicing of X-box binding protein-1 (XBP1) mRNA [267]. XBP1 protein from spliced mRNA induced the expression of a molecular chaperone BIP (also known as glucose-regulated protein 78 (GRP78)) which, along with several other molecular chaperones, relive ER stress by refolding of the unfolded or malfolded proteins [268]. The second sensor protein, activating transcription factor 6 (ATF6), also induced the expression of molecular chaperones. The final sensor protein, protein kinase-like ER kinase (PERK), is activated by autophosphorylation which then phosphorylates the translation initiation factor eukaryotic translation-initiation factor 2α (elF2α) [269]. This causes a translational arrest of most proteins which leads to cell cycle arrest [270]. ATF4 escapes translational suppression and can translocate to the cell nucleus where it can active transcription of growth-arrest DNA damage gene 34 (GADD34) and CCAAT-enhancer-binding protein homologous protein (CHOP). GADD34 feeds back to inhibit PERK while CHOP induced cell death after severe ER stress.

There was a very significant increase ($p \leq 0.005$) in the ER area per cell after treatment for all cell lines except RD and MDA-MB-231. The U2OS and the U-87 MG cell lines showed the largest increase in total ER area per cell of (108% ± 3) and (155% ± 5) respectively compared to the control cells.

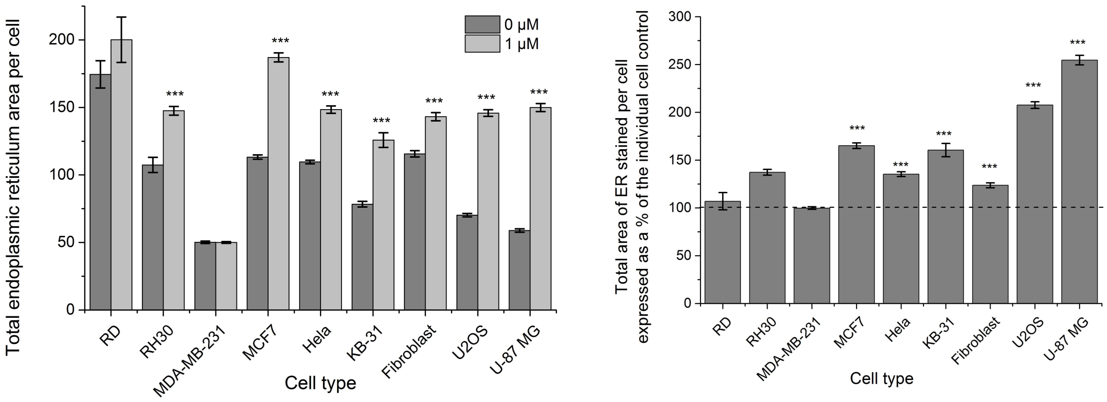

Figure 7.14: OphA can induce endoplasmic reticulum (ER) swelling. Results from independent experiments (n=2-3) showing the change in area of the ER per cell measured using an automated high throughput image acquisition and analysis system (IN Cell). The data is presented as mean ± SE of between 435 and 1915 cells per sample run in triplicate for each individual cell line expressed as A) the raw data and B) as a percentage of the untreated cells. Significance was tested using a two tailed t-test compared to the untreated cells for each cell line (*p ≤ 0.05, **p ≤ 0.01, ***p ≤ 0.005).

The ER stress response was probed once using immunoblotting and antibodies for BIP, PDI and CHOP, three proteins implicated in ER stress response (Fig 7.15A,B). For all cell lines, except MDA-MB-231 and KB-31, there was an increase in expression of either BIP or PDI or both BIP and PDI indicating that OphA might induce an ER survival stress response however repetition is required to confirm these results. There was no increase in expression of CHOP for any of the cell lines indicating that it is likely that the ER death response was not induced after 24 hours of 1 µM OphA treatment however again repetition is required to confirm these results.

7.3.5 OphA affected mitochondrial area, size and branching network

Mitochondria are known to be implicated in cell death, therefore we studied the effect of OphA on mitochondrial area, size and branching network. Similar to the ER, an IN Cell was used and the mitochondria were stained with TOM20. There was a very

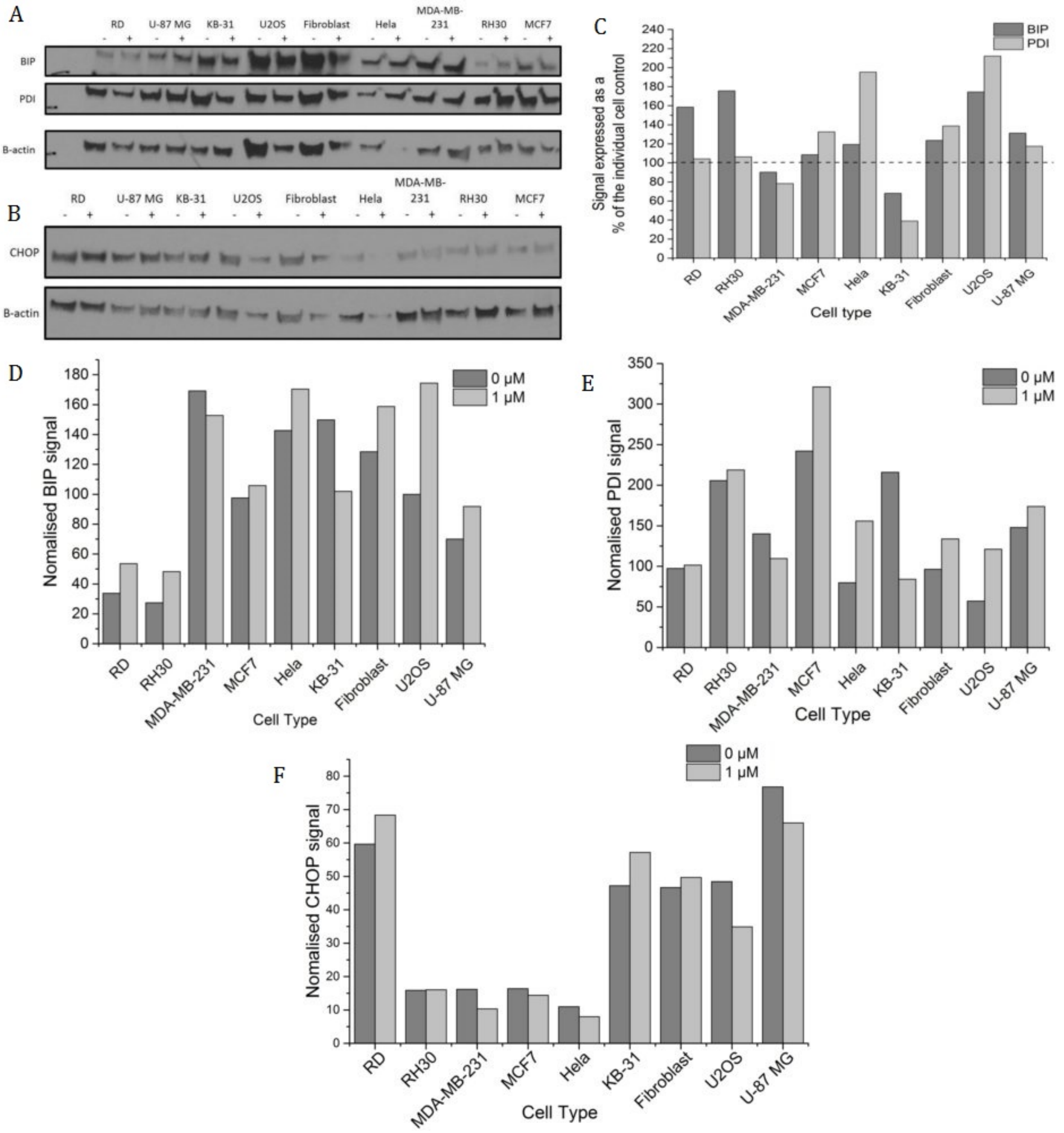

Figure 7.15: OphA induced a endoplasmic reticulum (ER) survival response. Western blots showing the expression of A) BIP, PDI and B) CHOP. C-E) Results from an single experiment showing the ratio of BIP and PDI to β-actin expression. Data is presented as C) a percentage of untreated cells for each individual cell line and D-E) normalised data. F) Results from an single experiment showing the ratio of CHOP to β-actin expression with data presented as the normalised data. (N.B This experiment was only performed once due to time constraints and therefore needs to be repeated to confirm the results.)

significant ($p \leq 0.005$) decrease of (13% ± 1), (8% ± 1), (17% ± 1) and (29% ± 1) in mitochondrial area per cell compared to the control for MDA-MB-231, MCF7, HeLa and

Fibroblast cells, respectively (Fig 7.16A,B). Conversely, there was a very significant ($p \leq 0.005$) increase in mitochondrial area per cell of (7% ± 2) and (45% ± 3) for U2OS and U-87 MG cells, respectively, compared to the control. There was no significant change in mitochondrial area per cell for RD, RH30 and KB-31 cells.

The change in mitochondrial morphology was evaluated by calculating the circularity, f_{circ}, of each mitochondrion

$$f_{circ} = \frac{P_m^2}{4\pi A_m} \tag{7.1}$$

where P_m is the perimeter of the mitochondrion and A_m is the area of the mitochondrion. A threshold on the circularity of 0.9 was applied and mitochondrion which were more circular were deemed small while mitochondrion which were less circular and more elongated were deemed long. In all cell lines tested, the mitochondria became shorter after treatment with OphA as shown by the increase in the proportion of the mitochondria which are short compared to the number which were long (Fig 7.16C,D,E). Lastly, there was a suggestion that there was an increase in the number of mitochondrial bifurcations after OphA treatment for MCF7, HeLa, KB-31, Fibroblast, U2OS and U-87 MG cells however improved resolution than that provided by the IN Cell is required to confirm this (Fig 7.16F).

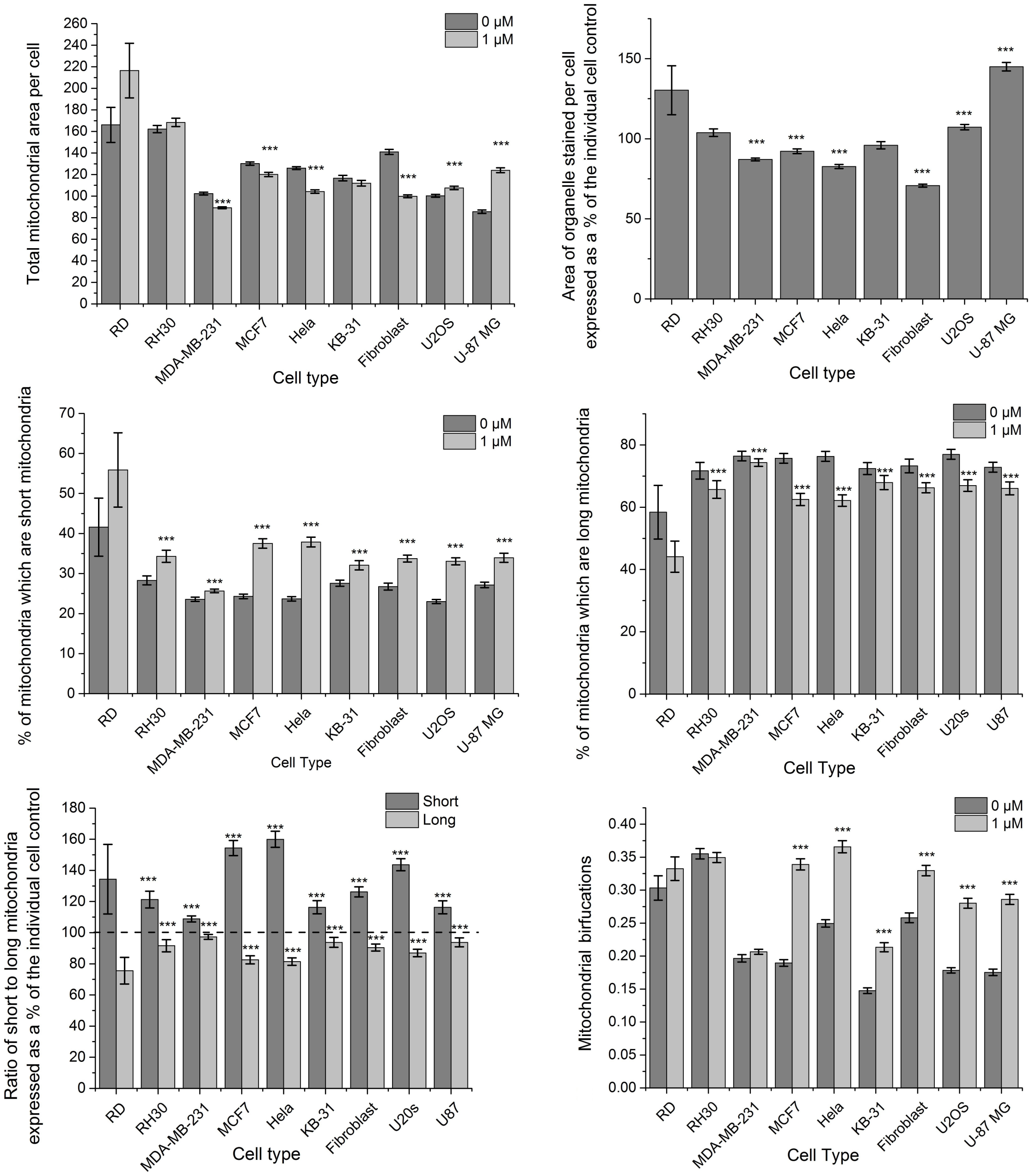

Figure 7.16: Effect of Ophiobolin A on mitochondria measured using an automated high throughput image acquisition and analysis system (IN Cell). Results from independent experiments (n=2-3) showing the change in area of the mitochondria per cell. Results from independent experiments (n=2-3) showing the % of C) short, D) long and E) ratio of short to long mitochondria. Short mitochondria are defined as having a circularity of ≥ 0.9 and long having a circularity of ≤ 0.9. F) Results from independent experiments (n=2-3) showing the change in the mitochondrial bifurcations after treatment with OphA. The data for all graphs is presented as mean ± SE of between 435 and 1915 cells per sample run in triplicate for each individual cell line expressed as either A,C,D,F) the raw data or B,E) as a percentage of the untreated cells.

Figure 7.16: (Cont.). Significance was tested using a two tailed t-test compared to the untreated cells for each cell line (*p $\leq$ 0.05, **p $\leq$ 0.01, ***p $\leq$ 0.005).

7.3.6 OphA causes mitochondrial membrane depolarization

In addition to the effect of OphA on mitochondrial morphology, mitochondrial function was also investigated. Active mitochondria were stained with TMRM while all the mitochondria were stained with Mitotracker® Green (Fig 7.17A). Immunofluorescence images of control RD cells show co-localisation of the Mitotracker® Green and the TMRM indicating that all the mitochondria had been stained and were active (Fig 7.17A). After one hour treatment with 1 µM OphA the TMRM fluorescence was similar to the control however after treatment with 10 µM OphA TMRM fluorescence had disappeared showing that the mitochondria had been deactivated (Fig 7.17A).

The fluorescence intensity of the TMRM is related to the mitochondrial membrane potential $\Delta\Psi_m$, therefore we used flow cytometry to quantify the change in $\Delta\Psi_m$ after one hour OphA treatment (Fig 7.17B,C). There was a significant increase ($p \leq 0.05$) of (40% ± 18) and (22% ±12) in $\Delta\Psi_m$ after 1 µM treatment in RH30 and U2OS cells, respectively, compared to the untreated cells indicating hyperpolarization. However, there was a significant ($p \leq 0.05$) decrease of at least (24% ± 10), in $\Delta\Psi_m$ after 10 µM OphA treatment for all cell lines except MDA-MB-231 and KB-31 cells indicating depolarisation of the mitochondrial membrane potential.

7.3.7 OphA induced reactive oxygen species production

Reactive oxygen species (ROS) can be used for cell signalling but excessive production induces damage to cell organelles. Therefore ROS production after one hour of OphA treatment using the fluorescent dye CM-H_2DCFDA was investigated. Immunofluores-

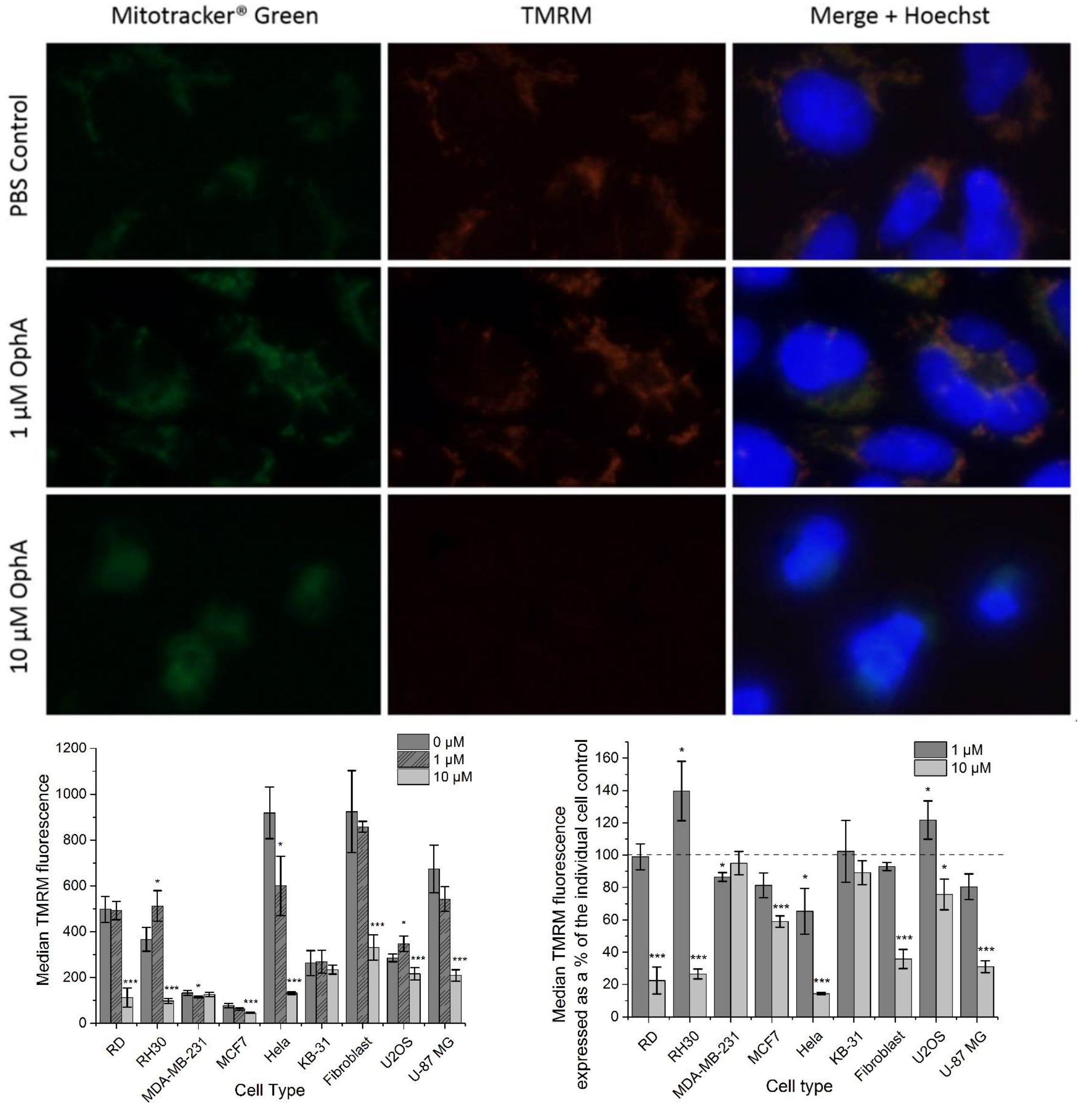

Figure 7.17: Effect of OphA on mitochondrial membrane potential ($\Delta\Psi_m$) measured using Tetramethylrhodamine (TMRM). A) Representative immunofluorescence images of RD cells treated for an hour with 1 µM and 10 µM OphA and dyed with Mitotracker® green, staining all the mitochondria, TMRM, staining the active mitochondria and Hoechst, staining the cell nucleus. Flow cytometry results for independent experiments (n=2-3) for each cell line showing the change in TMRM fluorescence as an indicator for $\Delta\Psi_m$ after one hour treatment with 1 µM and 10 µM OphA. Data is presented as mean ± SD of triplicate samples for each individual cell line expressed as B) raw data or C) as a percentage of the untreated cells. Significance was tested using a two tailed t-test compared to the untreated cells for each cell line (*p $\leq$ 0.05, **p $\leq$ 0.01, ***p $\leq$ 0.005).

cence images of control RD cells which were healthy and adherent to the bottom of the plate showed no CM-H_2DCFDA fluorescence while the cells which had rounded up showed high CM-H_2DCFDA fluorescence (Fig 7.18A). After treatment with 1 µM OphA the majority of the cells showed low CM-H_2DCFDA fluorescence while after treatment with 10 µM OphA cells appear rounded up and high CM-H_2DCFDA was observed. Quantification of the CM-H_2DCFDA was performed by flow cytometry and showed that the basal reactive oxygen species production varied between cell lines (Fig 7.18B). There was a significant ($p \leq 0.05$) decrease of (17% ± 7) in CM-H_2DCFDA fluorescence for U2OS cells treated with 10 µM OphA compared to the control cells (Fig 7.18C). The remaining cells all showed a significant increase in reactive oxygen species production at either 1 µM or 10 µM OphA treatment. Fibroblasts and U-87 MG cells showed the largest increase in ROS generation with an increase of (388% ± 31) and (420% ± 55) after one hour of 10 µM OphA treatment compared to the control cells. After 10 µM OphA treatment in RD, RH30 and KB-31 cells showed a decrease in CM-H_2DCFDA fluorescence which was due to the majority, at least 97%, of the cells being dead and the remaining cells having low CM-H_2DCFDA fluorescence.

7.3.8 OphA induced phosphatidylserine translocation to the outer membrane of RD, RH30 and MDA-MB-231 cells

Annexin V staining was used to probe whether cell death was induced by an apoptotic pathway. Annexin V binds to phosphatidylserine (PS) and PI stains the DNA of cells with a permeable membrane. In apoptosis, PS is translocated onto the outer membrane and thus cells which are early apoptotic show Annexin V positive and PI negative staining. Flow cytometry was used to quantify PS translocation to the outer membrane after 24 hours of OphA treatment by staining cells with APC-annexin V and PI. RD, RH30 and MDA-MB-231 cells treated with 10 µM OphA showed a very significant (p

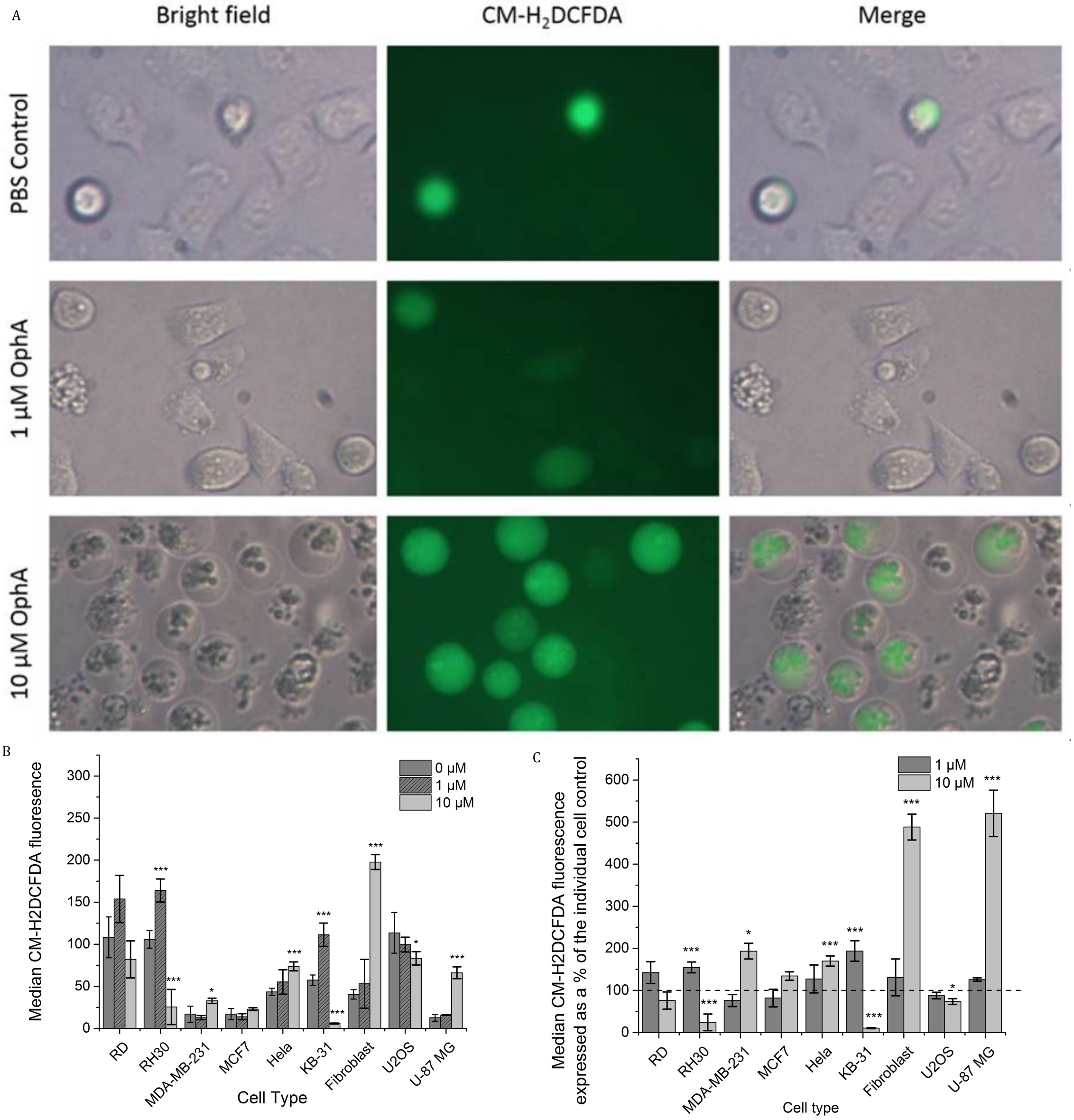

Figure 7.18: Effect of OphA on reactive oxygen species production measured using CM-H$_2$DCFDA. A) Representative bright field and immunofluorescence images of RD cells treated for an hour with 0 µM–10 µM OphA and dyed with CM-H$_2$DCFDA as an indicator of reactive oxygen species. Flow cytometry results for independent experiments (n=2-3) for each cell line showing the change in CM-H$_2$DCFDA fluorescence after one hour treatment with 1 µM and 10 µM OphA. Data is presented as mean ± SD of triplicate samples for each individual cell line expressed as B) the raw data and C) as a percentage of the untreated cells. Significance was tested using a two tailed t-test compared to the untreated cells for each cell line (*$p \leq 0.05$, **$p \leq 0.01$, ***$p \leq 0.005$).

≤ 0.005) increase in the percentage of apoptotic cells compared to the control cells of (75% ± 4), (71% ± 17) and (56% ≤ 4) respectively (Fig 7.19B). The remaining cell lines showed a much smaller but still significant increase in the percentage of apoptotic cells compared to the untreated cells.

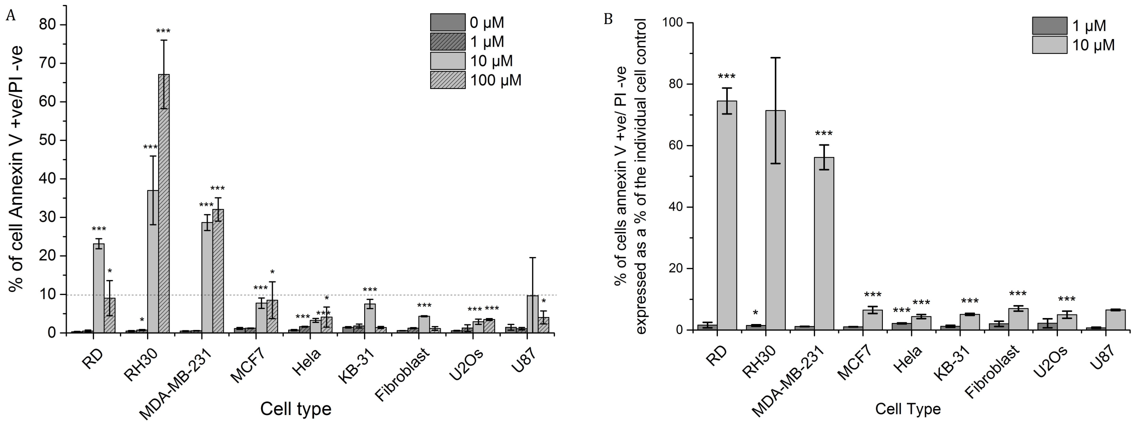

Figure 7.19: Effect of OphA on Annexin V staining measured using flow cytometry. Results from independent experiments (n=2-3) for each cell line showing the percentage of cells which are Annexin V positive but PI negative. Data is presented mean ± SD of triplicate samples for each individual cell line as A) the raw data and B) as a percentage of the untreated cells. Significance was tested using a two tailed t-test compared to the untreated cells for each cell line (*p ≤ 0.05, **p ≤ 0.01, ***p ≤ 0.005).

7.3.9 OphA causes PARP inactivation in RD and RH30 cells

Poly ADP ribose polymerase (PARP) is inactivated in apoptosis due to cleavage caused by the caspase signalling pathway. Therefore cleaved PARP expression levels after 24 hours of 1 µM OphA treatment were investigated using a western blot. Fibroblasts and U-87 MG cells showed high levels of cleaved PARP expression in both the control and 1 µM OphA treated cells (Fig 7.20A). RD and RH30 cells showed an extremely large increase in cleaved PARP expression after treatment with OphA (Fig 7.20B).

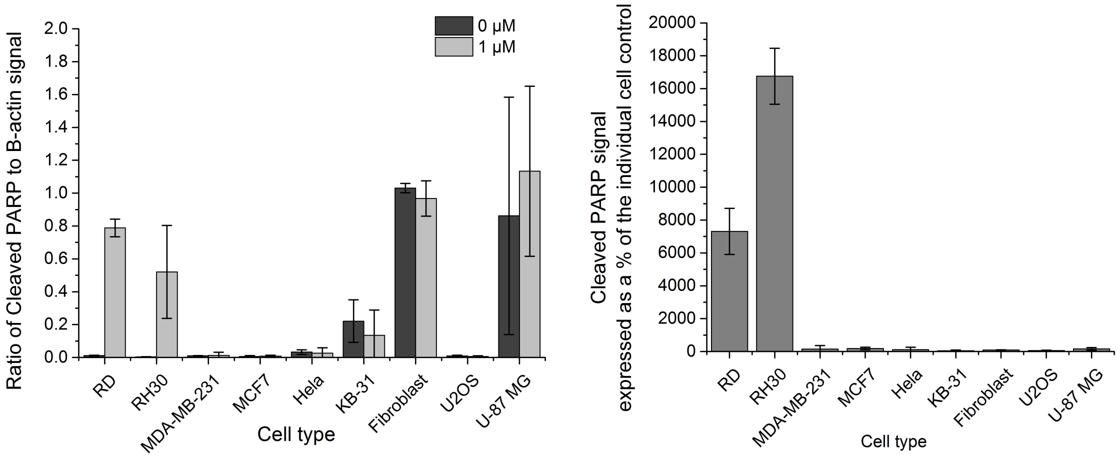

Figure 7.20: Effect on OphA on PARP cleavage assessed by western blot. Results from duplicate experiments showing the ratio of cleaved PARP expression to β-actin expression. Data is presented as A) mean ± SD of the data normalised to β-actin and B) as the mean ± SD of the percentage of untreated cells for each individual cell line.

7.3.10 OphA induced G2/M cell cycle arrest in U2OS cells and G0/G1 cell cycle arrest in HeLa cells

Cell cycle checkpoints are signaling pathways used by the cell to ensure that all events are successfully completed prior to proceeding to the next phase in the cell cycle (Fig 7.21) [271] . Cells can arrest at the cell cycle checkpoints to temporarily allow for: i) cellular damage to be repaired; ii) the dissipation of an exogenous cellular stress signal; or iii) ensuring the availability of essential growth factors, hormones or nutrients. Checkpoint signalling can also result in activation of pathways leading to programmed cell death.

The ability of OphA to affect the cell cycle was tested on all nine cell lines using flow cytometry. Cells were treated for 24 and 48 hours with OphA and the cell DNA was stained with PI after fixing in methanol. The intensity of the PI fluorescence was related to the amount of DNA in the cell and can be observed on typical cell cycle plots as shown in Fig 7.22A. The percentage of cells at each stage of the cell cycle, G_0/G_1, S and G_2/M, was quantified by fitting curves to the data using FCS express software [263].

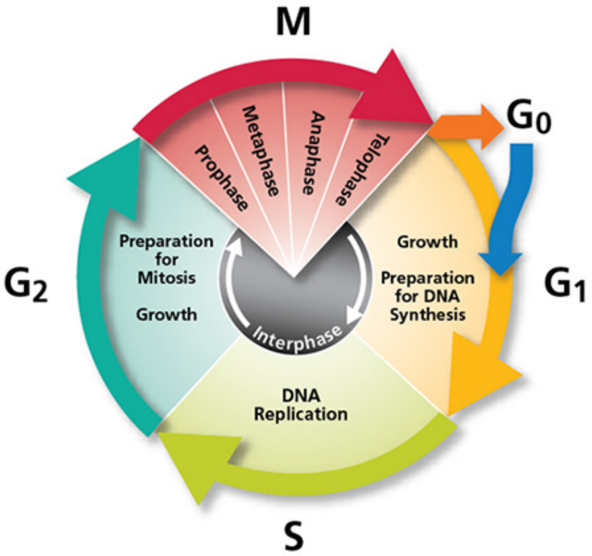

Figure 7.21: Schematic of the cell cycle. (Image taken from [272]) The cell cycle has two major phases: the phase between miotic events call interphase and the mitotic phase where the cell divides into two genetically identical daughter cells. Interphase has three distinct phases called the G_0/G_1, S and G_2 phases. During the first stage, G_0/G_1, cells monitor their environment and when the requisite signals are received the cell synthesises RNA and proteins to induce growth. The G_1 checkpoint ensures that everything is ready for DNA synthesis. Once the cell has committed to the cell cycle it enters S phase where it replicates its chromosomal DNA. The last phase G_2 cells continue growing to prepare for mitosis. The G_2 checkpoint ensures everything is ready for the cell to enter the mitosis phase.

For U2OS cells the percentage of cells in the G_2/M phase after 1 µM increased to (31.8% ± 5.7) after 24 hours treatment compared to (5.5% ± 2) for the untreated control and (12.1% ± 0.7) after 48 hours treatment compared to (6.0% ± 0.8) for the untreated control (Fig 7.22B,C). This indicates that OphA induced a significant G_2/M cell cycle arrest in U2OS cells as shown on Fig 7.22. For HeLa cells the percentage of cells in the G_0/G_1 phase after 1 µM OphA treatment increased to (77.4% ± 1.6) after 24 hours treatment compared to (68.9% ± 2.7) for the untreated control and (80.5% ± 1.8) after 48 hours treatment compared to (73.8% ± 1.8) for the untreated control (Fig 7.22B,C). This indicates that OphA induced a significant G_0/G_1 cell cycle arrest in HeLa cells. Fibroblasts showed no significant difference in the cell cycle after OphA treatment compared to the untreated control after 24 and 48 hours indicating that OphA did not affect the fibroblasts cell cycle (Fig 7.22B,C). For the remaining cell lines there was no clear arrest in any of the cell cycle phases however there are differences between the untreated and treated cells which could indicate either a slowing of the cell cycle or a temporary cell cycle arrest.

7.4 DISCUSSION

Cell death can be triggered by a range of intracellular stresses such as DNA damage, oxidative stress, cystolic Ca^{2+} overload and the accumulation of misfolded proteins [242]. The ability of OphA to induce cell death on eight cancer cell lines and one control fibroblast cell line was investigated. Furthermore, the effects of OphA on cell, nuclear, mitochondrial and ER morphology has been studied. A summary of the data for all nine cell lines tested is presented in Table 7.4.

OphA induced a potent cell death in all cell lines tested with LD_{50} values ranging from 0.7 µM to 4.5 µM. The LD_{50} values matched closely with data obtained from the National Cancer Institute (NCI) Natural Product Repository which showed the LD_{50} values of 0.5 µM and 4 µM for MDA-MB-231 and MCF7 respectively compared to 0.7 µM and 4 µM observed in this study [273].

Intracellular [Ca^{2+}] is strictly regulated in cells by a combination of passive diffusion of calcium into the cell and by active transport of calcium against a concentration gradient [274]. An increase in intracellular calcium levels can be a consequence of release from the ER stores, influx of extracellular calcium and/ or the release from other organelles such as the mitochondria [275]. A decrease in calcium concentration can be due to calcium being pumped out of the cell or by re-entering the calcium stores in the ER and mitochondria through Ca^{2+} transport systems. There was a delay of at least one hour in

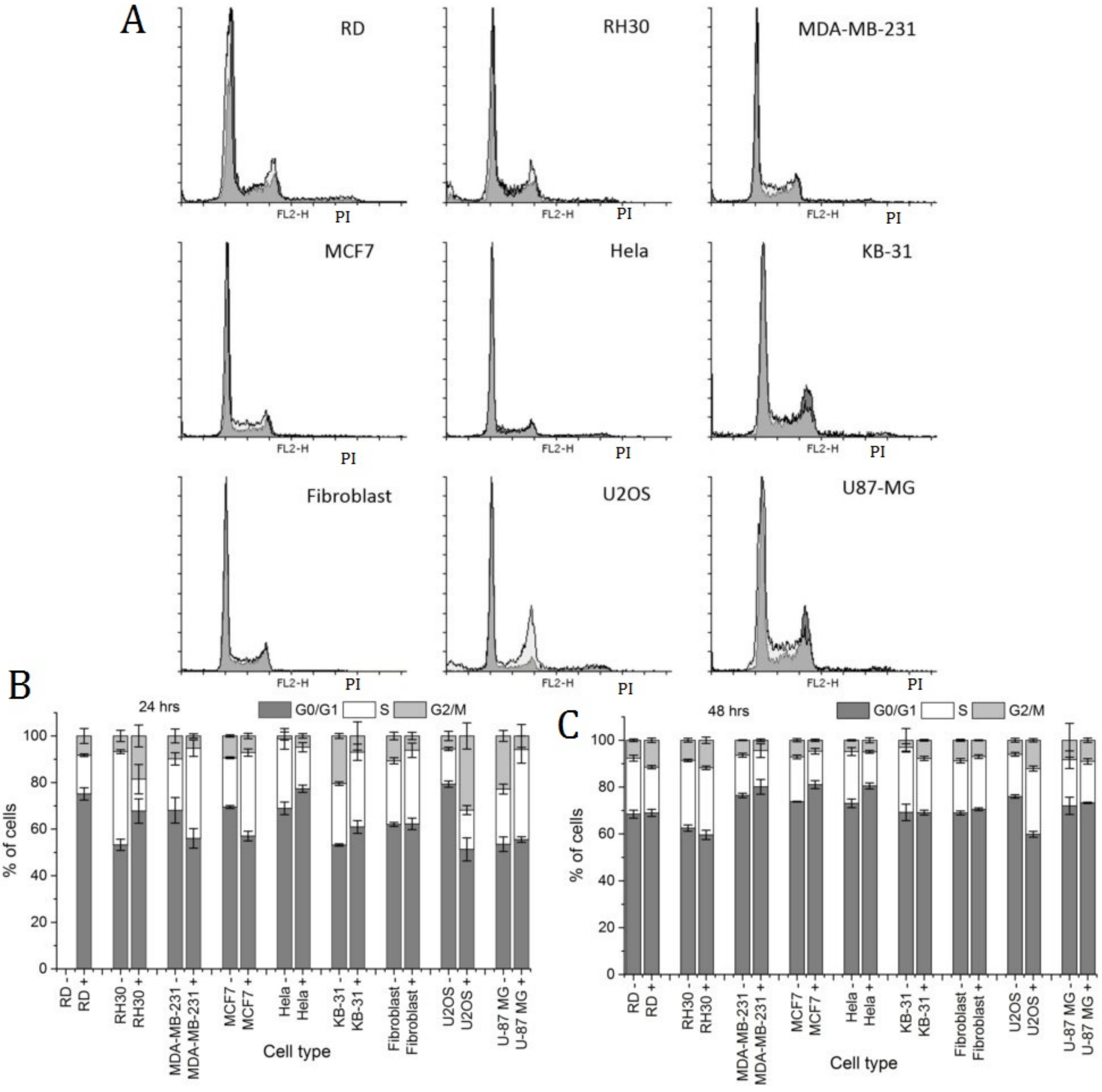

Figure 7.22: Effect on OphA on cell cycle assessed by flow cytometry after methanol fixation and PI staining. A) Representative flow cytometry traces after 24 hours of PBS treated (dark grey trace) and 1 µM OphA treated (light grey trace) showing the number of cells against their DNA content. Results from an independent experiment (n=2) showing the percentage of cells in G_0/G_1, M and G_2 phase of the cell cycle after B) 24 hour or C) 48 hour treatment with either PBS (-) or 1 µM OphA (+) treatment. Data is presented as mean ± SD of triplicate samples.

Table 7.4: Summary of the data showing the effect of OphA on the 9 cell lines tested. ('NS' no significant change from the untreated cells, significant change from the untreated cells with the following p values $*p \leq 0.05$, $**p \leq 0.01$, $***p \leq 0.005$).

Effect of OphA treatment on	**Treatment applied**	**RD**	**RH30**	**MDA-MB-231**	**MCF7**	**HeLa**	**KB-31**	**Fibroblast**	**U2OS**	**U-87 MG**
Cell size	**1 µM**	NS	NS	NS	NS	NS	NS	NS	NS	NS
Cell size	**10 µM**	*** Shrinkage	*** Shrinkage	*** Shrinkage	*** Shrinkage	*** Swelling	NS	** Swelling	*** Swelling	No change
Cell nucleus	**10 µM**	Karyorrhexis	Karyorrhexis Karyolysis	Karyorrhexis Karyolysis	Karyorrhexis Karyolysis	Karyorrhexis Karyolysis	Karyorrhexis Karyolysis Pynkosis	Pynkosis	Karyorrhexis Pynkosis	No destruction observed
ER area per cell	**1 µM**	NS	*** Swelling	NS	*** Swelling	*** Swelling	*** Swelling	*** Swelling	*** Swelling	*** Swelling
Mitochondria area per cell	**1 µM**	NS	NS	*** Shrinkage	*** Shrinkage	*** Shrinkage	NS	*** Shrinkage	*** Swelling	*** Swelling
Mitochondria number of short	**1 µM**	NS	***Increase in the number of short mitochondria (all except RD)							
Mitochondria number of long	**1 µM**	NS	*** Decrease in the number of long mitochondria (all except RD)							
Mitochondrial membrane potential	**1 µM**	NS	* Hyperpolarisation	*** Depolarisation	NS	NS	NS	NS	* Hyperpolarisation	NS
Mitochondrial membrane potential	**10 µM**	*** Depolarisation	*** Depolarisation	NS	*** Depolarisation	*** Depolarisation	*** Depolarisation	*** Depolarisation	*** Depolarisation	*** Depolarisation
Reactive oxygen species	**1 µM**	NS	*** Increase	NS	NS	NS	*** Increase	NS	NS	NS
Reactive oxygen species	**10 µM**	NS	*** Decrease	* Increase	NS	*** Increase	*** Decrease	*** Increase	* Decrease	*** Increase
Annexin V positive/ PI negative staining	**1 µM**	NS	* Increase	NS	NS	*** Increase	NS	NS	NS	NS
Annexin V positive/ PI negative staining	**10 µM**	*** Increase	*** Increase	*** Increase	*** Increase	*** Increase	*** Increase	*** Increase	*** Increase	NS
PARP Cleavage	**1 µM**	Increase	Increase	NS	NS	NS	NS	NS	NS	NS

calcium being released in the cytosol for all cell lines after OphA treatment compared to the control cell indicating that OphA affects calcium signalling. Furthermore some cell lines showed a huge increase in the amount of cystolic calcium release after six hours of treatment.

Historically it was believed that OphA induced cell death by inhibiting calmodulin [265]. However by obtaining LD_{50} values from National Cancer Institute (NCI) Natural Products Repository [273] for the NCI cell lines treated with OphA and comparing these to calmodulin mRNA expression levels for the same NCI cell lines from CBioPortal [276] it has been shown that there is no correlation between calmodulin mRNA expression levels and OphA toxicity (Fig 7.23). This suggests that, although OphA can inhibit calmodulin, it is not the only molecular target for the molecule.

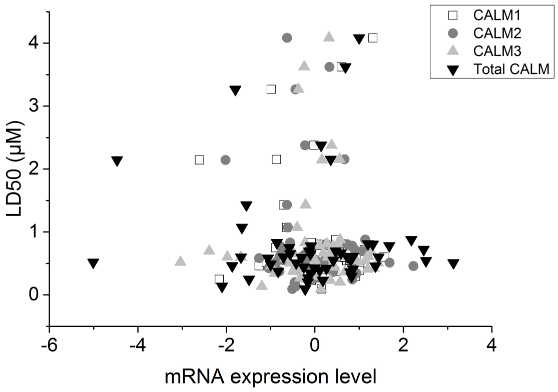

Figure 7.23: Ophiobolin A LD_{50} does not correlate with calmodulin mRNA expression levels. LD_{50} values were obtained from the NCI-60 DTP Human Tumor Cell Line Screen for Ophiobolin A (Sept 2014) [273] and plotted against the mRNA expression levels of the three calmodulin genes (CALM1, CALM2, CALM3 and total CALM) obtained from cBioPortal for the same NCI-60 cell lines [276].

Nuclear destruction was observed in all cell lines, except U-87 MG, after 24 hour OphA treatment indicating that DNA damage occurred during the process of cell death. RD cells which were pre-stained with Hoechst prior to 0 µM–100 µM OphA treatment did not show any nuclear destruction after two hours (data not shown). Therefore it is likely that the observed nuclear destruction is a secondary process caused by death signals within the cell.

Reactive oxygen species (ROS) can be produced by cells in response to stress and can cause damage to proteins, lipids and DNA. Excessive production of ROS results in cell death, for example ROS facilitates the release of cytochrome c from the mitochondria in apoptosis [277]. An increase in reactive oxygen species was observed in all cell lines, except U2OS, after one hour OphA treatment which indicated that oxidative stress is one of the early signals of cell death. U-87 MG and Fibroblast both show a very significant increase in the generation of reactive oxygen species. This was accompanied by a reduction in $\Delta\Psi_m$ indicating that the mitochondria are also affected early in the cell death pathway.

The majority of the ROS produced by the cell originates from the mitochondria [278] and therefore it is not surprising that there was an accumulation of ROS at the same time as the reduction in $\Delta\Psi_m$. A dissipation of the $\Delta\Psi_m$ can occur after MOMP through the uncoupling of the mitochondrial respiratory change or through the opening of the MPT pore [248]. MOMP is commonly associated with apoptosis with the release of toxic proteins into the cytosol. Opening of the MPT causes the mitochondria to become leaky to water and other small molecules which results in mitochondria swelling eventually leading to necrosis [279]. Therefore a sustained drop in $\Delta\Psi_m$ indicates that the cells are dying however it does not elucidate the mechanism of cell death. Bencsik *et al.* [43] also showed that OphA could cause a decrease in the mitochondrial membrane potential in boar spermatozoa.

The unfolded protein response (UPR) is a survival mechanism of the cell in response to

ER stress which occurs when there is an accumulation of unfolded or misfolded proteins in the lumen of the ER [280]. The three aims of the UPR are to halt protein translation, degrade misfolded proteins and to up regulate the production of molecular chaperones involved in protein folding. The expression levels of two molecular chaperones, BIP and PDI, were assessed by western blot. After 1 µM OphA treatment, all the cell lines, except MDA-MB-231 and KB-31, showed an increase in the expression of both BIP and PDI indicating that OphA induced the unfolded protein response in the remaining cell lines. MDA-MB-231 and KB-31 cells had high basal levels of BIP indicating that the cancer cells were already stressed before the addition of the drug which could explain the apparent reduction in the BIP levels with drug treatment. The ER stress response can be chronically activated in cancer cells and thus this can provide support for continuous proliferation and survival even under adverse microenvironments which can include chemotherapy [281].

If the survival mechanism of the UPR fails and the stress encountered is too excessive or too severe then the ER can enlist a death response. This causes the phosphorylation of PERK and eIF2α which activates the transcription of CHOP which induces a death response in mitochondria. OphA was not shown to increase the protein levels of CHOP in any of the cell lines tested and therefore while the ER is inducing a survival mechanism no death response was observed.

In addition to testing the effect of OphA on the ER its effect on the mitochondria was also studied. For all cell lines tested, except RD, there was an increase in the number of short mitochondria compared to long mitochondria indicating that the mitochondria are undergoing mitochondrial fission. Smaller mitochondria are easier for cells to degrade and therefore significant mitochondrial fission occurs when a cell has severely damaged mitochondria [282]. Additionally, mitochondrial fusion in inhibited when cells have a low $\Delta\Psi_m$ and in all cell lines tested, except KB-31, there was a decrease in $\Delta\Psi_m$ after one hour OphA treatment.

The type of cell death that occurs after a given treatment is determined by the mechanism of action of the drug, the dose administered and the genetic background of the treated cells [274]. Therefore, links between the mutations found each cell type have and the type of cell death have been analysed and possible suggestions presented.

The two rhabdomyosarcoma cell lines tested both showed that OphA induced an apoptotic like cell death through the characteristic features of apoptosis including the rounding up of the cell, cell shrinkage, chromatin condensation, nuclear fragmentation (karyohexis), PS exposure on the outer membrane and the cleavage of PARP. MDA-MB-231 cells showed similar features of apoptosis without the PARP cleavage. RD, RH30 and MDA-MB-231 cells all have mutated p53, the tumour suppressor protein. p53 is inactivated by mutation in approximately 50% of all cancers [283]. Wild type p53 has a range of diverse and global functions which are best characterised in cell cycle arrest, senescence and apoptosis in response to DNA damage [284]. Several small molecules, including CP-31398, PRIMA-1, ellipticine, WR-1065 and p53R3, have been shown to act on mutant p53 by restoring its confirmation to wild type and then the cells can undergo cell cycle arrest or apoptosis [285]. Furthermore, RD, RH30 and MDA-MB-231 cells all have low, $\leq 1.5\,\mu M$, LD_{50} values. Ellipticinium salts were shown on average to be more potent on mutant p53 cells than cells with wild type p53 from the NCI database [286]. Also an ellipticine derivative, 9-hydroxy ellipticine, has been shown to induce apoptosis in mutant p53 cells but not wild type p53 cells [287]. Therefore, OphA could be restoring wild type function to p53 in RD, RH30 and MDA-MB-231 cells allowing them to die via apoptosis and explains the lower magnitude of the LD_{50} values observed.

Although MCF7 cells are another breast cancer cell line the LD_{50} value was significantly higher magnitude than the MDA-MB-231 cells. OphA did not induce an apoptotic like cell death in MCF7 cells as there was very low PS exposure on the outer membrane and no cleavage of PARP. This could be because MCF7 cells have increased level of the anti-apopotic protein Bcl-2 and no expression of caspase 3 and therefore MCF7 cells are not able to enlist an apoptotic response [259]. Furthermore, 1 µM OphA induced a G_0/G_1 cell cycle arrest after 24 hours although this was not maintained after 48 hours, which suggests a temporary cell cycle arrest or a slowing of the cell cycle. Ophiobolin O has been shown to induce a G_0/G_1 in MCF7 cells for up to 48 hours [46]. OphA also induced a G_0/G_1 cell cycle arrest in HeLa cells which was accompanied by a large ER stress response. The ER stress response has been shown to induce cell cycle arrest due to the accumulation of misfolded proteins [270].

OphA induced a significant G_2/M cell cycle arrest in U2OS cells which have wild type p53. Benz *et al.* [288] showed that the induced expression of both p53 and p21 are required to sustain the G_2 checkpoint and induce G_2 arrest. Therefore, since U2OS cells have wild type p53 they have the possibility of entering G_2/M cell cycle arrest. Shen *et al.* [289] showed that both ionizing radiation and Nutlin can induce the expression of p53 and p21 in U2OS cells causing cell death. Furthermore, since U2OS cells have a single functional copy of P53 and overexpression of necdin they are able to evade apoptosis *in vivo*[261] and this could further explain the propensity to die by cell cycle arrest rather than apoptosis. Furthermore, U2OS cells showed no increase in ROS or Ca^{2+} with OphA treatment. Cisplatin has been previously shown to induce a concentration dependent increase in $[Ca^{2+}]$ in HeLa-S3 cells (a derivative of the parent HeLa cell line) but not in the U2OS cells [290]. They showed that the rise in $[Ca^{2+}]$ in the HeLa-S3 cells was due to the extracellular influx of calcium ions though the IP_3, receptor however there was no expression of the IP_3 receptor on the cell membrane of U2OS cells and therefore no increase in [Ca^{2+}] was observed. In this study HeLa cells showed an increase in the intracellular calcium concentration after both 1 and 10 µM OphA treatment compared to the control.

Fibroblasts underwent a necrotic like cell death through through the cellular swelling and pynkoic nucleus, and showed a relatively low LD_{50} value of 1.4 µM. Furthermore, both the PBS treated and the 1 µM OphA fibroblast cells had high levels of cleaved PARP and a large increase in ROS generation. OphA induced a parapotic like cell death in U-87 MG cells indicated by the significant cell, ER and mitochondrial swelling. Moreover, Hoescht staining showed that OphA did not induce chromatin condensation in U-87 MG cells; paraptosis does not cause chromatin condensation [291]. Furthermore, as Paraptosis is not initiated by the caspase cascade there is no cleavage of PARP [291] again observed by the cleaved PARP expression levels after OphA treatment. The only characteristic feature of paraptosis which was not observed was there was no significant vacuolisation after OphA treatment.

U-87 MG cells have a mutation in the phosphate and tensin homolog (PTEN) gene which has previously been shown to inhibit apoptosis. Additionally, Bury *et al.* [41] showed that OphA induced paraptosis in other glioma cell line which also have the PTEN mutation. Lee *et al* [176] compared the effect of 8 Gy radiation treatment U-87 MG cells and the PTEN proficient cell line LN18 and found that the radiation induced senescence in U-87 MG cells but apoptosis in LN18. Additionally the radiation induced the production of ROS in both cell lines however it was significantly greater in the U-87 MG cells. This is similar to the significantly large increase in ROS after OphA treatment for U-87 MG cells found in this study. An increase in PTEN expression has been shown to modulate the PI3K/AKT signalling to reduce ROS generation [292]. Therefore it is likely that the large increase in ROS in U-87 MG cells after 10 µM OphA treatment is due to the PTEN mutation.

7.5 CONCLUSIONS

OphA has been shown to induce cell death in all the cell lines tested. This was accompanied by changes in cell, nuclear, ER and mitochondrial morphology. Furthermore there was an increase in mitochondrial fission, a drop in mitochondrial membrane potential and a generation of reactive oxygen species after OphA treatment. Also OphA caused a delay in the release of calcium and an ER stress survival response but not an ER stress death response.

OphA induced an apoptotic like cell death in RD, RH30 and MBA-MB-231 cells. HeLa and U2OS cells underwent a G_0/G_1 and G_2/M cell cycle arrest respectively after OphA treatment. Fibroblast presented with a necrotic like cell death and U-87 MG cells underwent a paraptotic like cell death after OphA treatment. Since OphA has the potential to induce different types of cell death in the different cell lines it is possibly that it could be used to treat apoptosis resistant cells and therefore provide an effective chemotherapeutic. The results indicate that OphA is a promising novel chemotherapeutic and further work is required in vivo to determine its effectiveness in animals.

Chapter 8

Final discussion and conclusions

The aim of this thesis was to develop novel embolic particles for cancer therapy using a combination of nanoparticles and microparticles. The embolic particles were designed and synthesised to have a polystyrene core which could effectively block tumour vasculature; thereby limiting oxygen and nutrient delivery to the tumour and causing tumour necrosis. The utility of the embolic particles was enhanced by adding X-ray contrast, a radiosensitiser component and a high capacity for loading of a novel chemotherapeutic Ophiobolin A onto the surface. This created radiopaque embolic particles, radio-sensitising embolic particles and chemoembolization particles respectively.

The core of the embolic particle successfully incorporated with 5 nm to 8 nm tantalum oxide nanoparticles to provide X-ray contrast to the particle. This allows the particles to be visualised by X-ray and CT scans during the particle placement procedure and post-operatively. The contrast enhancement of the particles was linearly related to the level of tantalum doping and up to 9.4% tantalum doping was achieved. Furthermore calculations were performed to determine the contrast enhancement of the embolic particles and it was found that 75 particles doped with 9.4% tantalum oxide should provide the same contrast as 5 cm of bone. Therefore radiopaque embolic particles have been successfully synthesised.

The surface of the embolic particle was successfully coated with either rare earth doped TiO_2 nanoparticles or mesoporous SiO_2 nanoparticles. The rare earth doped TiO_2 nanoparticles were previously developed by Townley *et al.* [100, 101] to produce reactive oxygen species upon X-ray activation and therefore operate as a radiosensitiser. The rare earth doped TiO_2 nanoparticles were shown to produce reactive oxygen species upon both UV irradiation, as a proof of concept, and X-ray radiation. Furthermore the rare earth doped TiO_2 nanoparticles and the embolic particles coated with the rare earth doped TiO_2 nanoparticles inhibited cell proliferation compared to radiation treatment alone. This is the first time that an embolic particle combined with a radiosensitiser agent has been shown. Previously, embolic particles combined with a radioactive element have been developed to provide localised radiotherapy however this technique has many limitations regarding the radioactive element which requires careful handling. Therefore a radiosensitising embolic particle is much more useful as it is inert until activation.

Mesoporous SiO_2 nanoparticles can be loaded with chemotherapy drugs to allow for targeted delivery. By coating the embolic particles with the mesoporous SiO_2 nanoparticles and subsequently loading with a drug chemoembolization particles were prepared. These allow chemotherapy to be delivered directly at the tumour location therefore potentially reducing the toxic side effects of systemic treatment. The SiO_2 nanoparticles were loaded with Ophiobolin A a novel chemotherapeutic derived from a fungal secondary metabolite. Approximately 95% uptake of OphA into the pores of the SiO_2 nanoparticles was seen depending on the solvent selected for loading, and the subsequent controlled release was observed. Furthermore, release from the embolic particles coated with the SiO_2 nanoparticles and loaded with OphA caused an approximately 70% reduction in cell viability after 24 treatment indicating that the embolic particles were effective. The SiO_2 nanoparticles were also shown to limit the degradation of OphA therefore increasing its half life and ensuring that it is active for longer.

In addition to developing a drug delivery system for OphA the mechanism of cell death on eight cancer cell lines, one control cell line and one drug resistant cell line was also assessed. OphA had been shown to induce two different types of cell death, apoptosis [240] and paraptosis [41], on different cell lines. The effect of OphA on nuclear, ER and mitochondrial morphology and function was studied. Furthermore the generation of reactive oxygen and intracellular calcium concentration was investigated. Finally the ability of OphA to induce apoptosis and cell cycle arrest was studied. OphA was shown to cause changes in cell size, nuclear destruction, swelling of the ER and changes in the mitochondrial morphology. Furthermore there was an increase in mitochondrial fission, a drop in mitochondrial membrane potential and a generation of reactive oxygen species after OphA treatment. OphA also caused perturbations in the intracellular calcium concentration and an ER stress survival response but not an ER stress death response. Furthermore different types of cell death were observed in the the cell line and this seemed to be related to the mutations found in that particular cell line.

OphA was shown to be effective against a vinblastine resistant cell line to the same level as the parent cell line and therefore it was demonstrated that OphA could be effective at treating some types of drug resistant cells. OphA was also shown to be more toxic to the healthy control cell line than some of the cancer cell lines which demonstrates the need to encapsulate it for targeted delivery like the developed chemoembolization particles. Overall OphA has been shown to be an effective chemotherapeutic which could be useful for treating drug resistant cells and therefore further *in vivo* testing is required fully evaluate it before clinical use.

Future studies could include the creation of embolic particles which combine the three modalities studied; radiopaque, radio-sensitising and chemoembolization. It is not envisaged that there would be any technical difficulties in creating composite particles with a radiopaque core and either a doped TiO_2 or mesoporous SiO_2 shell as the tantalum is contained within the polystyrene during synthesis and therefore should not affect the sintering process. TiO_2 nanoparticles have also been shown to increase X-ray contrast but it is significantly less than can be obtained for the tantalum nanoparticles. For example, one study showed that $30\,\mathrm{mg\,mL^{-1}}$ of TiO_2 nanoparticles had a CT value of 50 HU [10] while at the same concentration the tantalum nanoparticles used developed in chapter 4 had a CT value of 800 HU [153]. Therefore the TiO_2 nanoparticles will increase the X-ray contrast of the embolic particles but the tantalum nanoparticles will have a more significant effect.

There are potential challenges involved in preparing composite doped TiO_2 and SiO_2 nanoparticle coated embolic particles. This is because the SiO_2 coated embolic particles required a much longer sintering time due to the lower magnitude thermal conductively of the SiO_2 nanoparticles than the TiO_2 nanoparticles and hence the longer time required for the heat to transfer through the SiO_2 nanoparticles and melt the surface of the polystyrene. Increasing the sintering time of the TiO_2 nanoparticles could cause the crystal phase of the TiO_2 to change and therefore reduce their effectiveness. Therefore, a combined radio-sensitising and chemoembolization particles would require synthesis optimisation to ensure than an effective particle was obtained. Combing radio-active embolic particles with chemotherapy drugs have been shown to have a synergistic effect on tumour area and survival times [68] and therefore creating a combined radio-sensitising and chemoembolization embolic particle could be a worthwhile endeavour.

Once the perfect embolic particle has been created *in vivo* testing is required to determine if the particles have potential for clinical translation. Moreover the plasma stability and ability to project a protein corona would need to be studied if the particles are to achieve clinical regulation. Also the long term stabily of the particles requires testing to ensure that the nanopartilces do not become unattached from the embolic particle and then transport elsewhere in the body.

The lenghtscales that the reactive oxygen species produced by the doped TiO_2 nanopartilces would need to be investigated to ensure that they were in close proximity to the cancerous tissue otherwise healthy surround vascualture could be damaged. The SiO_2 nanoparticles were shown to increase the stability of OphA and therefore kept it more potent for longer. It would be interesting to investigate if a similar nanopartilce drug delivery system could be useful for delivering other chemically unstable compounds. Additionally the bonding of the SiO_2 nanopartilces to the OphA could be investigated.

Further work is required to fully understand the mechanism of cell death caused by Ophiobolin A in cells. Based on the cell lines tested the mode of cell death appeared to fall into groups bases on the tissue of origin of the cells. A large scale study could be conducted to determine if this is true. Further protein expression experiments could be carried out to more fully understand the affect that OphA is having on the cells and if there is a difference in the cell lines. Moreover the tests presented in this thesis were only carried out at single timepoint and at a few concentrations which could have affected the results observed and more temporal testing could revel more information of the types of cell death. Furthermore *in vivo* testing could be carried out to determine if OphA is effective at killing a range of different cancer types especially apoptosis resistant cells.

In conclusion radiopaque embolic, radio-sensitising embolic and chemoembolization particles have been successfully designed and synthesised to provide X-ray contrast, act as a radiosensitiser and successfully deliver OphA directly at the tumour location. Furthermore the mechanisms of cell death of OphA have been further elucidated.

Appendix A

Appendix

A.1 Material source and justification

A table providing all the materials used within this thesis, the supplier and a justification for using them is provided below.

Material	Source	Reason for selection
2′,7′-dichlorodihydrofluorescein diacetate	Invitrogen	For staining cell reactive oxygen species
3-Mercaptopropyl trimethoxysilane	Sigma	For silica coating the TiO2 nanoparticles
3-trihydroxysilyl propyl methylphosphonate	Sigma	For preparation of SiO2 nanoparticles
Acetic acid	Sigma	For crystal violet solubilising solution
Acetonitrile	Fisher	For LC gradient
Alexa-Fluor secondary antibodies	Invitrogen	Secondary antibodies for fluorescent imaging
Ammonium hydroxide	Sigma	For preparation of polystyrene microparticles containing tantalum oxide nanoparticles and polystyrene-TiO2 embolic particles
Anhydrous isopranol	Sigma	For preparation of TiO2 nanoparticles
Antibodies for BIP, PDI and CHOP	Cell signal	For determining protein expression levels
Antibodies for cleaved PARP and B-actin	ABCam	For determining protein expression levels
APC-Annexin V	BioLegend	For staining cells undergoing early apoptosis
Azobisisobutyronitrile	Sigma	For preparation of polystyrene microparticles
Benzyl dimethylamine	Agar	For sectioning of polystyrene microparticles
Bicinchoninic acid assay	Pierce	For determining protein concentration
Binding buffer	BioLegend	Buffer for APC-Annexin V
Calnexin	Santa Cruz	For staining cell endoplasmic reticulum
Carbon taped SEM stub	Agar Scientific	For SEM imaging
CellMask orange	Life technologies	For staining microvesicle plasma membrane
Cetyl trimethylammonium bromide	Sigma	For preparation of SiO2 nanoparticles
Complete lysis-M kit	Roche Diagnostics	For preparing cell lysates
Coumarin	Sigma	Fluorescent dye for monitoring reactive oxygen species generation
Crystal violet	Sigma	For staining the cell nucleus
Cyclohexane	Sigma	For preparation of tantalum oxide nanoparticles
Cytochalasin D	Sigma	Inhibitor of actin polymerisation used to probe OphA mechanism of action
DAPI	Sigma	For staining cell nucleus
Dichloromethane	Sigma	For dying polystyrene microparticles, for loading of the SiO2 with OphA
Dodecenyl succinic anhydride	Agar	For sectioning of polystyrene microparticles
Dulbecco's Modified Eagle's Medium-high glucose	Sigma	For cell culture media
ELC	Biorad	Kit for revealing western blots
Epoxy resin	Agar	For sectioning of polystyrene microparticles
Erbium (III) nitrate pentahydrate	Sigma	For doping the TiO2 nanoparticles
Ethanol	Sigma	For preparation of tantalum oxide nanoparticles
Ethanol	Sigma/Fisher	For preparation of SiO2 nanoparticles, for loading of the SiO2 with OphA
Ethylene glycol dimethacrylate	Sigma	For preparation of polystyrene microparticles
Europium (III) nitrate hydrate	Sigma	For doping the TiO2 nanoparticles
Fetal calf serum	Sigma	For cell culture media
Fluo-4 AM	Invitrogen	For staining cell intracellular calcium concentration

Material	Source	Reason for selection
Fluorescein isothiocyanate	Sigma	For dying polystyrene microparticles
Gadolinium (III) nitrate hexahydrate	Sigma	For doping the TiO2 nanoparticles
Gafchromic EBT3 film	Vertec Scientific	Film for X-ray contrast experiments
Glutaraldehyde	Sigma	For fixing cells
Glycine	Sigma	For SDS-Page transfer buffer
Hoechst	Sigma	For staining cell DNA
Holey carbon coated copper TEM grids	Agar Scientific	For TEM imaging
Hydrochloric acid	Sigma	For preparation of SiO2 nanoparticles
Igepal C0-520	Sigma	For preparation of tantalum oxide nanoparticles
Isopropanol	Sigma	For dying polystyrene microparticles, for preparation of the TiO2 nanoparticles and polystyrene-TiO2 embolic particles
L-Glutamine	Sigma	For cell culture media
Methanol	Sigma	For preparation of polystyrene microparticles, polystyrene microparticles containing tantalum oxide nanoparticles, polystyrene-TiO2 embolic particles and SiO2 nanoparticles, For SDS-Page transfer buffer
Metharcyloxypropyl trimethoxysilane	Sigma	For preparation of polystyrene-TiO2 embolic particles
Methyl nadic anhydride	Agar	For sectioning of polystyrene microparticles
Mitotracker ® Green	Invitrogen	For staining cell mitochondria
Mycoplasma detection kit	Lonza	For testing if cell have mycoplasma
Nitric acid	Sigma	For preparation of polystyrene microparticles containing tantalum oxide nanoparticles
Oleic acid	Sigma	For preparation of polystyrene microparticles containing tantalum oxide nanoparticles
OPTIMEM	Gibco	Low serum media with no phenol red and low basal levels of microvesicles
P25	Degussa	Commercially available TiO2 nanoparticles used as control particles
Paraformaldehyde	Sigma	For fixing cells
Penicillin and Streptomycin	Sigma	Antibiotics in cell culture media
Poly vinyl alcohol	Sigma	For preparation of polystyrene microparticles
Poly(diallydimethylammonium chloride	Sigma	For preparation of polystyrene-TiO2 embolic particles
Polystyrene divinlybenzene	Duke scientific	Commercially available polystyrene particles
Potassium chloride	Sigma	For preparation of polystyrene-TiO2 embolic particles
Precise Tris-HEPES 8%-16% gels	Invitrogen	For SDS-Page
Propidium iodide	Sigma	For dying cells with a permeable membrane
Rare earth doped TiO2 nanoparticles	Johnson Matthey	TiO2 nanoparticles prepared by flame spray pyrolysis, a commercially viable option for producing nanoparticles
Resin holder	Gilder grids	For sectioning of polystyrene microparticles
Rhodamine B	Sigma	For dying polystyrene microparticles
Sodium dodecyl sulphate	Sigma	For crystal violet solubilising solution
Sodium hydroxide	Sigma	For preparation of tantalum oxide nanoparticles and SIO2 nanoparticles
Sodium silicate	Sigma	For silica coating the TiO2 nanoparticles
Styrene	Sigma	For preparation of polystyrene microparticles
Sucrose	Sigma	For creating sucrose density gradients
SYBR ® green	Life technologies	For staining microvesicle DNA

Material	Source	Reason for selection
Synthetic microvessel models	SynDaver	For demonstrating effective blocking of a vessel using the polystyrene microparticles
Terbium (III) nitrate pentahydrate	Sigma	For doping the TiO2 nanoparticles
Tetraethyl orthosilicate	Sigma	For preparation of SiO2 nanoparticles
Tetramethylrhodamine, methyl ester	Invitrogen	For staining cell active mitochondria
TiO2 (IV) isopropoxide	Sigma	For preparation of TiO2 nanoparticles
Toluene	Sigma	For preparation of polystyrene-TiO2 embolic particles, For loading of the SiO2 with OphA
TOM20	Santa Cruz	For staining cell mitochondria
Tris base	Sigma	For SDS-Page transfer buffer and for membrane blocking
Tris hydroxymethyl aminomethane	Sigma	Buffer for zeta potential measurements
TRIS-HEPES-SDS running buffer	Invitrogen	For SDS-Page
Trypan blue	Sigma	For staining dead cells
Trypsin-EDTA	Sigma	For detecting adherent cells from tissue culture flasks and plates
Tween 20	Sigma	For western blot membrane blocking
Tween 80	Sigma	For dying polystyrene microparticles

Bibliography

[1] R. Weinberg, *The Biology of Cancer.* Garland Science, 2013.

[2] D. Hanahan and R. A. Weinberg, "The hallmarks of cancer," *Cell*, vol. 100, no. 1, pp. 57–70, 2000.

[3] S. K. Parks, J. Chiche, and J. Pouyssegur, "Disrupting proton dynamics and energy metabolism for cancer therapy," *Nat Rev Cancer*, vol. 13, no. 9, pp. 611–623, Sep. 2013.

[4] V. Estrella, T. Chen, M. Lloyd, J. Wojtkowiak, H. H. Cornnell, A. Ibrahim-Hashim, K. Bailey, Y. Balagurunathan, J. M. Rothberg, B. F. Sloane, J. Johnson, R. A. Gatenby, and R. J. Gillies, "Acidity generated by the tumor microenvironment drives local invasion," *Cancer Res*, vol. 73, no. 5, pp. 1524–35, 2013.

[5] S. D. Steichen, M. Caldorera-Moore, and N. A. Peppas, "A review of current nanoparticle and targeting moieties for the delivery of cancer therapeutics," *European Journal of Pharmaceutical Sciences*, vol. 48, no. 3, pp. 416–427, Feb. 2013.

[6] T. Sun, Y. S. Zhang, B. Pang, D. C. Hyun, M. Yang, and Y. Xia, "Engineered nanoparticles for drug delivery in cancer therapy," *Angewandte Chemie International Edition*, vol. 53, no. 46, pp. 12 320–12 364, 2014.

[7] R. Baskar, K. A. Lee, R. Yeo, and K. W. Yeoh, "Cancer and radiation therapy: Current advances and future directions," *Int J Med Sci*, vol. 9, no. 3, pp. 193–9, 2012.

[8] A. Norlund, "Costs of radiotherapy," *Acta Oncol*, vol. 42, no. 5-6, pp. 411–5, 2003.

[9] D. Kwatra, A. Venugopal, and S. Anant, "Nanoparticles in radiation therapy: a summary of various approaches to enhance radiosensitization in cancer," *Translational Cancer Research*, vol. 2, no. 4, 2013.

[10] L. Smith, Z. Kuncic, K. Ostrikov, and S. Kumar, "Nanoparticles in cancer imaging and therapy," *Journal of Nanomaterials*, vol. 2012, p. 7, 2012.

[11] Macmillan. (2012) Intensity-modulated radiation therapy (IMRT) factsheet. [Online]. Available: http://www.nhs.uk/ipgmedia/National/Macmillan%20Cancer%20Support/assets/IMRTMCS5pages.pdf

[12] L. Veldeman, I. Madani, F. Hulstaert, G. De Meerleer, M. Mareel, and W. De Neve, "Evidence behind use of intensity-modulated radiotherapy: a systematic review of comparative clinical studies," *The Lancet Oncology*, vol. 9, no. 4, pp. 367–375, 2008.

[13] A. Dan, B. Edith, G. Alain, H.-M. Christine, L. Eric, M. Jean-Jacques, M. Harm, P. Richard, S. Pierre, L. Erik Van, V. Jack, and W. André, *The GEC ESTRO Handbook of Brachytherapy.* ESTRO, 2002.

[14] S. Nazir, T. Hussain, A. Ayub, U. Rashid, and A. J. MacRobert, "Nanomaterials in combating cancer: Therapeutic applications and developments," *Nanomedicine: Nanotechnology, Biology and Medicine*, vol. 10, no. 1, pp. 19–34, 2014.

[15] K. N. Morris, M. D. Weil, and R. Malzbender, "Radiochromic film dosimetry of contrast-enhanced radiotherapy (CERT)," *Physics in Medicine and Biology*, vol. 51, no. 22, p. 5915, 2006.

[16] E. Borowski, M. Bontemps-Gracz, and A. Piwkowska, "Strategies for overcoming ABC-transporters-mediated multidrug resistance (MDR) of tumor cells," *Acta Biochimica Polonica*, vol. 52, no. 3, pp. 609–627, 2005.

[17] Y. Wang, X. Zhu, Z. Yang, and X. Zhao, "Honokiol induces caspase-independent paraptosis via reactive oxygen species production that is accompanied by apoptosis in leukemia cells," *Biochemical and Biophysical Research Communications*, vol. 430, no. 3, pp. 876–882, 2013.

[18] N. A. Boon, N. R. Colledge, B. R. Walker, and J. A. A. Hunter, *Davidson's Principles and Practice of Medicine*, 20th ed. Churchill Livingstone, 2006.

[19] D. J. Newman and G. M. Cragg, "Natural products as sources of new drugs over the 30 years from 1981 to 2010," *J Nat Prod*, vol. 75, no. 3, pp. 311–35, 2012.

[20] D. A. Dias, S. Urban, and U. Roessner, "A historical overview of natural products in drug discovery," *Metabolites*, vol. 2, no. 2, pp. 303–36, 2012.

[21] T. Henkel, R. M. Brunne, H. Mucci, L. A.Muller, and F. Reichel, "Statistical investigation into the structural complementarity of natural products and synthetic compounds," *Angewandte Chemie International Edition*, vol. 38, no. 5, pp. 643–647, 1999.

[22] C. Basmadjian, Q. Zhao, A. Djehal, E. Bentouhami, C. G. Nebigil, R. A. Johnson, M. Serova, A. De Gramont, S. Faivre, E. Raymond, and L. G. Dacsaubry, "Cancer wars: Natural products strike back," *Frontiers in Chemistry*, vol. 2, no. 20, 2014.

[23] U. Hollstein, "Actinomycin. chemistry and mechanism of action," *Chemical Reviews*, vol. 74, no. 6, pp. 625–652, 1974.

[24] L.-A. Giddings and D. Newman, "Microbial natural products: molecular blueprints for antitumor drugs," *Journal of Industrial Microbiology & Biotechnology*, vol. 40, no. 11, pp. 1181–1210, 2013.

[25] C. Zubrod, "The national program for cancer chemotherapy," *JAMA*, vol. 222, no. 9, pp. 1161–1162, 1972.

[26] A. Stierle, G. Strobel, and D. Stierle, “Taxol and taxane production by taxomyces andreanae, an endophytic fungus of pacific yew,” *Science*, vol. 260, no. 5105, pp. 214–216, 1993.

[27] B. B. Mishra and V. K. Tiwari, “Natural products: An evolving role in future drug discovery,” *European Journal of Medicinal Chemistry*, vol. 46, no. 10, pp. 4769–4807, 2011.

[28] C. Ferlini, L. Cicchillitti, G. Raspaglio, S. Bartollino, S. Cimitan, C. Bertucci, S. Mozzetti, D. Gallo, M. Persico, C. Fattorusso, G. Campiani, and G. Scambia, “Paclitaxel directly binds to Bcl-2 and functionally mimics activity of Nur77,” *Cancer Research*, vol. 69, no. 17, pp. 6906–6914, 2009.

[29] G. M. Cragg and D. J. Newman, “Natural products: A continuing source of novel drug leads,” *Biochimica et Biophysica Acta (BBA) - General Subjects*, vol. 1830, no. 6, pp. 3670–3695, 2013.

[30] C. J. Nobel RL, Beer CT, “Vincaleukoblastine,” *Can Med Assoc J*, vol. 85, no. 10, pp. 610–1, 1961.

[31] R. H. Shoemaker, “The NCI60 human tumour cell line anticancer drug screen,” *Nat Rev Cancer*, vol. 6, no. 10, pp. 813–823, Oct. 2006.

[32] W. Gerwick and B. Moore, “Lessons from the past and charting the future of marine natural products drug discovery and chemical biology,” *Chemistry & Biology*, vol. 19, no. 1, pp. 85–98, 2012.

[33] M. Saleem, M. S. Ali, S. Hussain, A. Jabbar, M. Ashraf, and Y. S. Lee, “Marine natural products of fungal origin,” *Nat. Prod. Rep.*, vol. 24, pp. 1142–1152, 2007.

[34] A. Demain, “Valuable secondary metabolites from fungi,” in *Biosynthesis and Molecular Genetics of Fungal Secondary Metabolites*, ser. Fungal Biology, J.-F. Martn, C. Garca-Estrada, and S. Zeilinger, Eds. Springer New York, 2014, pp. 1–15.

[35] A. Evidente, A. Kornienko, A. Cimmino, A. Andolfi, F. Lefranc, V. Mathieu, and R. Kiss, “Fungal metabolites with anticancer activity,” *Nat. Prod. Rep.*, vol. 31, pp. 617–627, 2014.

[36] A. K. Chattopadhyay and K. R. Samaddar, “Effects of helminthosporium oryzae infection and ophiobolin on the cell membranes of host tissues,” *Physiological Plant Pathology*, vol. 8, no. 2, pp. 131–139, 1976.

[37] P. C. Leung, W. A. Taylor, J. H. Wang, and C. L. Tipton, “Ophiobolin-A - a natural product inhibitor of calmodulin,” *Journal of Biological Chemistry*, vol. 259, no. 5, pp. 2742–2747, 1984.

[38] T. K. Au, W. S. H. Chick, and P. C. Leung, “The biology of ophiobolins,” *Life Sciences*, vol. 67, no. 7, pp. 733–742, 2000.

[39] M. Bury, E. Novo-Uzal, A. Andolfi, S. Cimini, N. Wauthoz, P. Heffeter, B. Lallemand, F. Avolio, C. Delporte, A. Cimmino, J. Dubois, P. Van Antwerpen, M. C. Zonno, M. Vurro, Y. Poumay, W. Berger, A. Evidente, L. De Gara, R. Kiss, and V. Locato, “Ophiobolin A, a sesterterpenoid fungal phytotoxin, displays higher in vitro growth-inhibitory effects in mammalian than in plant cells and displays in vivo antitumor activity,” *Int J Oncol*, vol. 43, no. 2, pp. 575–85, 2013.

[40] I. J. de Vries-van Leeuwen, C. Kortekaas-Thijssen, J. A. Nzigou Mandouckou, S. Kas, A. Evidente, and A. H. de Boer, “Fusicoccin-A selectively induces apoptosis in tumor cells after interferon-alpha priming,” *Cancer Letters*, vol. 293, no. 2, pp. 198–206, 2010.

[41] M. Bury, A. Girault, V. Megalizzi, S. Spiegl-Kreinecker, V. Mathieu, W. Berger, A. Evidente, A. Kornienko, P. Gailly, C. Vandier, and R. Kiss, “Ophiobolin A induces paraptosis-like cell death in human glioblastoma cells by decreasing BKCa channel activity,” *Cell Death Dis*, vol. 4, p. e561, 2013.

[42] S. Sperandio, K. Poksay, I. de Belle, M. J. Lafuente, B. Liu, J. Nasir, and D. E. Bredesen, “Paraptosis: mediation by MAP kinases and inhibition by AIP-1 Alix,” *Cell Death Differ*, vol. 11, no. 10, pp. 1066–1075, Jun. 2004.

[43] O. Bencsik, T. Papp, M. Berta, A. Zana, P. Forgo, G. Dombi, M. Andersson, M. Salkinoja-Salonen, C. Vagvolgyi, and A. Szekeres, “Ophiobolin A from bipolaris oryzae perturbs motility and membrane integrities of porcine sperm and induces cell death on mammalian somatic cell lines,” *Toxins*, vol. 6, no. 9, pp. 2857–2871, 2014.

[44] D. Hoornstra, M. Andersson, R. Mikkola, and M. Salkinoja-Salonen, “A new method for in vitro detection of microbially produced mitochondrial toxins,” *Toxicology in Vitro*, vol. 17, no. 5 6, pp. 745–751, 2003.

[45] T. Yang, Z. Lu, L. Meng, S. Wei, K. Hong, W. Zhu, and C. Huang, “The novel agent ophiobolin O induces apoptosis and cell cycle arrest of MCF-7 cells through activation of MAPK signaling pathways,” *Bioorganic & Medicinal Chemistry Letters*, vol. 22, no. 1, pp. 579–585, 2012.

[46] C. Lv, W. Qin, T. Zhu, S. Wei, K. Hong, W. Zhu, R. Chen, and C. Huang, “Ophiobolin O isolated from aspergillus ustus induces G1 arrest of MCF-7 cells through interaction with AKT/GSK3/Cyclin D1 signaling,” *Marine Drugs*, vol. 13, no. 1, pp. 431–443, 2015.

[47] W. Sun, C. Lv, T. Zhu, X. Yang, S. Wei, J. Sun, K. Hong, W. Zhu, and C. Huang, “Ophiobolin-O reverses adriamycin resistance via cell cycle arrest and apoptosis sensitization in adriamycin-resistant human breast carcinoma (MCF-7/ADR) cells,” *Marine Drugs*, vol. 11, no. 11, pp. 4570–4584, Oct. 2013.

[48] D. Xue, Q. Wang, Z. Chen, L. Cai, L. Bao, Q. Qi, L. Liu, X. Wang, H. Jin, J. Wang, H. Wu, H. Liu, and Q. Chen, “3-Anhydro-6-hydroxy-ophiobolin A, a fungal sesterterpene from bipolaris oryzae induced autophagy and promoted the degradation of alpha-synuclein in PC12 cells,” *Bioorganic & Medicinal Chemistry Letters*, no. 0, pp. –, 2015.

[49] S. D. Abramowitz, G. M. Israel, S. M. McCarthy, J. S. Pollak, J. White, Robert I., and M. G. Tal, "Comparison of four embolic materials at uterine artery embolization by using postprocedural MR imaging enhancement," *Radiology*, vol. 250, no. 2, pp. 482–487, 2009.

[50] X. Liu, P. Wan Sia Heng, Q. Li, and L. W. Chan, "Novel polymeric microspheres containing norcantharidin for chemoembolization," *Journal of Controlled Release*, vol. 116, no. 1, pp. 35–41, 2006.

[51] K. Y. Tam, K. C.-F. Leung, and Y.-X. J. Wang, "Chemoembolization agents for cancer treatment," *European Journal of Pharmaceutical Sciences*, vol. 44, no. 12, pp. 1–10, 2011.

[52] R. J. Lewandowski, J.-F. Geschwind, E. Liapi, and R. Salem, "Transcatheter intraarterial therapies: Rationale and overview," *Radiology*, vol. 259, no. 3, pp. 641–657, 2011.

[53] C. S. Soo, V. P. Chuang, S. Wallace, C. Charnsangavej, and H. Carrasco, "Treatment of hepatic neoplasm through extrahepatic collaterals." *Radiology*, vol. 147, no. 1, pp. 45–49, 1983.

[54] S. Vaidya, K. R. Tozer, and J. Chen, "An overview of embolic agents," *Semin Intervent Radiol*, vol. 25, no. 3, pp. 204–15, 2008.

[55] M. Lubarsky, C. E. Ray, and B. Funaki, "Embolization agents-which one should be used when? part 1: large-vessel embolization," *Seminars in interventional radiology*, vol. 26, no. 4, pp. 352–7, 2009.

[56] C. S. J. van Hooy-Corstjens, K. Saralidze, M. L. W. Knetsch, P. J. Emans, M. W. de Haan, P. C. M. M. Magusin, B. Mezari, and L. H. Koole, "New intrinsically radiopaque hydrophilic microspheres for embolization: Synthesis and characterization," *Biomacromolecules*, vol. 9, no. 1, pp. 84–90, 2007.

[57] X.-J. Lu, Y. Zhang, D.-C. Cui, W.-J. Meng, L.-R. Du, H.-T. Guan, Z.-Z. Zheng, N.-Q. Fu, T.-S. Lv, L. Song, Y.-H. Zou, W.-L. Lu, and T.-Y. Fan, "Research of novel biocompatible radiopaque microcapsules for arterial embolization," *International Journal of Pharmaceutics*, vol. 452, no. 12, pp. 211–219, 2013.

[58] B. C. Thanoo, M. C. Sunny, and A. Jayakrisnnan, "Tantalum-loaded polyurethane microspheres for particulate embolization: preparation and properties," *Biomaterials*, vol. 12, no. 5, pp. 525–528, 1991.

[59] B. C. Thanoo and A. Jayakrishnan, "Barium sulphate-loaded p(HEMA) microspheres as artificial emboli: Preparation and properties," *Biomaterials*, vol. 11, no. 7, pp. 477–481, 1990.

[60] S. Dhand and R. Gupta, "Hepatic transcatheter arterial chemoembolization complicated by postembolization syndrome," *Semin Intervent Radiol*, vol. 28, no. 2, pp. 207–11, 2011.

[61] J. J. Bissler, J. Racadio, L. F. Donnelly, and N. D. Johnson, "Reduction of postembolization syndrome after ablation of renal angiomyolipoma," *American Journal of Kidney Diseases*, vol. 39, no. 5, pp. 966–971, 2002.

[62] B. Scientific, “Contour PVA embolization particles,” Jan. 2014. [Online]. Available: http://www.bostonscientific.com/en-EU/home.html

[63] Biocompatabiles, “Biocompatabiles products,” Jan. 2014. [Online]. Available: http://www.biocompatibles.com/

[64] M. Medical, “Embolics,” 2014. [Online]. Available: http://www.merit.com/products/default.aspx?code=embolization

[65] SIRTeX, “About SIR-Spheres microspheres,” Jan. 2014. [Online]. Available: http://www.sirtex.com/us/clinicians/about-sir-spheres-microspheres/

[66] M. a Varela, M. a Isabel Real, M. Burrel, A. Forner, M. Sala, M. Brunet, C. Ayuso, L. Castells, X. Montana, J. M. Llovet, and J. Bruix, “Chemoembolization of hepatocellular carcinoma with drug eluting beads: Efficacy and doxorubicin pharmacokinetics,” *Journal of Hepatology*, vol. 46, no. 3, pp. 474–481, 2007.

[67] K. Malagari, M. Pomoni, A. Kelekis, A. Pomoni, S. Dourakis, T. Spyridopoulos, H. Moschouris, E. Emmanouil, S. Rizos, and D. Kelekis, “Prospective randomized comparison of chemoembolization with doxorubicin-eluting beads and bland embolization with beadblock for hepatocellular carcinoma,” *CardioVascular and Interventional Radiology*, vol. 33, no. 3, pp. 541–551, 2010.

[68] N. H. Nicolay, D. P. Berry, and R. A. Sharma, “Liver metastases from colorectal cancer: radioembolization with systemic therapy,” *Nat Rev Clin Oncol*, vol. 6, no. 12, pp. 687–697, 2009.

[69] A. S. Kennedy, C. Nutting, D. Coldwell, J. Gaiser, and C. Drachenberg, “Pathologic response and microdosimetry of ^{90}Y microspheres in man: Review of four explanted whole livers,” *International Journal of Radiation Oncology*Biology*Physics*, vol. 60, no. 5, pp. 1552–1563, 2004.

[70] M. Kawashita, N. Matsui, Z. Li, and T. Miyazaki, “Novel synthesis of yttrium phosphate microspheres for radioembolization of cancer,” *IOP Conference Series: Materials Science and Engineering*, vol. 18, no. 19, 2011.

[71] M. Kawashita, R. Shineha, H.-M. Kim, T. Kokubo, Y. Inoue, N. Araki, Y. Nagata, M. Hiraoka, and Y. Sawada, “Preparation of ceramic microspheres for in situ radiotherapy of deep-seated cancer,” *Biomaterials*, vol. 24, no. 17, pp. 2955–2963, 2003.

[72] B. Sangro, J. I. Bilbao, J. Boan, A. Martinez-Cuesta, A. Benito, J. Rodriguez, A. Panizo, B. Gil, M. Inarrairaegui, I. Herrero, J. Quiroga, and J. Prieto, “Radioembolization using ^{90}Y-resin microspheres for patients with advanced hepatocellular carcinoma,” *International Journal of Radiation Oncology*Biology*Physics*, vol. 66, no. 3, pp. 792–800, 2006.

[73] M. Auffan, J. Rose, J.-Y. Bottero, G. V. Lowry, J.-P. Jolivet, and M. R. Wiesner, “Towards a definition of inorganic nanoparticles from an environmental, health and safety perspective,” *Nat Nano*, vol. 4, no. 10, pp. 634–641, Oct. 2009.

[74] K. H. Wilczewska, AZand Niemirowicz K FAU Markiewicz, H. Markiewicz KH FAU Car, and C. H, "Nanoparticles as drug delivery systems." *Pharmacol Rep*, no. 1734-1140 (Linking), pp. –, 2012.

[75] H. Shi, R. Magaye, V. Castranova, and J. Zhao, "Titanium dioxide nanoparticles: a review of current toxicological data," *Part Fibre Toxicol*, vol. 10, p. 15, 2013.

[76] N. Barkalina, C. Charalambous, C. Jones, and K. Coward, "Nanotechnology in reproductive medicine: Emerging applications of nanomaterials," *Nanomedicine: Nanotechnology, Biology and Medicine*, vol. 10, no. 5, pp. 921–938, Jul. 2014.

[77] H. Maeda, "The enhanced permeability and retention (EPR) effect in tumor vasculature: the key role of tumor-selective macromolecular drug targeting," *Advances in Enzyme Regulation*, vol. 41, no. 1, pp. 189–207, 2001.

[78] S. Kim, J. H. Kim, O. Jeon, I. C. Kwon, and K. Park, "Engineered polymers for advanced drug delivery," *Eur J Pharm Biopharm*, vol. 71, no. 3, pp. 420–30, 2009.

[79] R. Hidalgo-Alvarez, *Structure and Functional Properties of Colloidal Systems.* CRC Press, 2009.

[80] D. Peer, J. M. Karp, S. Hong, O. C. Farokhzad, R. Margalit, and R. Langer, "Nanocarriers as an emerging platform for cancer therapy," *Nat Nano*, vol. 2, no. 12, pp. 751–760, Dec. 2007.

[81] A. Baeza, M. Colilla, and Vallet-Regi, "Advances in mesoporous silica nanoparticles for targeted stimuli-responsive drug delivery," *Expert Opinion on Drug Delivery*, vol. 12, no. 2, pp. 319–337, 2015.

[82] H. Kobayashi, R. Watanabe, and P. L. Choyke, "Improving conventional enhanced permeability and retention (EPR) effects; what is the appropriate target?" *Theranostics*, vol. 4, no. 1, pp. 81–89, Aug. 2013.

[83] S. Jain, D. G. Hirst, and J. M. O'Sullivan, "Gold nanoparticles as novel agents for cancer therapy," *The British Journal of Radiology*, vol. 85, no. 1010, pp. 101–113, 2012.

[84] Y. X. J. Wang, "Superparamagnetic iron oxide based MRI contrast agents: Current status of clinical application," *Quant Imaging Med Surg*, vol. 1, no. 1, pp. 35–40, 2011.

[85] E. Stride and N. Saffari, "Microbubble ultrasound contrast agents: A review," *Proceedings of the Institution of Mechanical Engineers, Part H: Journal of Engineering in Medicine*, vol. 217, no. 6, pp. 429–447, 2003.

[86] J. Owen, Q. Pankhurst, and E. Stride, "Magnetic targeting and ultrasound mediated drug delivery: Benefits, limitations and combination," *International Journal of Hyperthermia*, vol. 28, no. 4, pp. 362–373, 2012.

[87] D. P. Cormode, P. C. Naha, and Z. A. Fayad, "Nanoparticle contrast agents for computed tomography: a focus on micelles," *Contrast Media & Molecular Imaging*, vol. 9, no. 1, pp. 37–52, 2014.

[88] D. P. Cormode, T. Skajaa, Z. A. Fayad, and W. J. Mulder, “Nanotechnology in medical imaging: Probe design and applications,” *Arteriosclerosis, Thrombosis, and Vascular Biology*, vol. 29, no. 7, pp. 992–1000, 2009.

[89] J. Key and J. F. Leary, “Nanoparticles for multimodal in vivo imaging in nanomedicine,” *Int J Nanomedicine*, vol. 9, pp. 711–26, 2014.

[90] J. F. Hainfeld, H. M. Smilowitz, M. J. O Connor, F. A. Dilmanian, and D. N. Slatkin, “Gold nanoparticle imaging and radiotherapy of brain tumors in mice,” *Nanomedicine*, vol. 8, no. 10, pp. 1601–1609, 2012.

[91] N. Lee, S. H. Choi, and T. Hyeon, “Nano-sized CT contrast agents,” *Advanced Materials*, vol. 25, no. 19, pp. 2641–2660, 2013.

[92] J. F. Hainfeld, D. N. Slatkin, and H. M. Smilowitz, “The use of gold nanoparticles to enhance radiotherapy in mice,” *Physics in Medicine and Biology*, vol. 49, no. 18, p. N309, 2004.

[93] Y. Zheng, D. J. Hunting, P. Ayotte, and L. Sanche, “Radiosensitization of DNA by gold nanoparticles irradiated with high-energy electrons,” *Radiat Res*, vol. 169, no. 1, pp. 19–27, 2008.

[94] E. Brun, L. Sanche, and C. Sicard-Roselli, “Parameters governing gold nanoparticle x-ray radiosensitization of DNA in solution,” *Colloids and Surfaces B: Biointerfaces*, vol. 72, no. 1, pp. 128–134, 2009.

[95] D. Y. Joh, L. Sun, M. Stangl, A. Al Zaki, S. Murty, P. P. Santoiemma, J. J. Davis, B. C. Baumann, M. Alonso-Basanta, D. Bhang, G. D. Kao, A. Tsourkas, and J. F. Dorsey, “Selective targeting of brain tumors with gold nanoparticle-induced radiosensitization,” *PLoS ONE*, vol. 8, no. 4, p. e62425, Apr. 2013.

[96] L. Bobyk, M. Edouard, P. Deman, M. Vautrin, K. Pernet-Gallay, J. Delaroche, and J, “Photoactivation of gold nanoparticles for glioma treatment,” *Nanomedicine: Nanotechnology, Biology and Medicine*, vol. 9, no. 7, pp. 1089–1097, 2013.

[97] L. Maggiorella, G. Barouch, C. Devaux, A. Pottier, E. Deutsch, J. Bourhis, E. Borghi, and L. Levy, “Nanoscale radiotherapy with hafnium oxide nanoparticles,” *Future Oncology*, vol. 8, no. 9, pp. 1167–1181, Sep. 2012.

[98] C. Mirjolet, A. Papa, G. Crehange, O. Raguin, C. Seignez, C. Paul, G. Truc, P. Maingon, and N. Millot, “The radiosensitization effect of titanate nanotubes as a new tool in radiation therapy for glioblastoma: A proof-of-concept,” *Radiotherapy and Oncology*, vol. 108, no. 1, pp. 136–142, 2013.

[99] R.-T. Mostafa, D. Elham, H. Hadi, S. Samaneh-Sadat, S. Vahid, and S. Sara, “TiO2 nanoparticle as a sensitizer drug in radiotherapy: in vitro study,” *Iranian Journal of cancer prevention*, vol. 6, 2013.

[100] H. E. Townley, E. Rapa, G. Wakefield, and P. J. Dobson, “Nanoparticle augmented radiation treatment decreases cancer cell proliferation,” *Nanomedicine: Nanotechnology, Biology and Medicine*, vol. 8, no. 4, pp. 526–536, 2012.

[101] H. E. Townley, J. Kim, and P. J. Dobson, “In vivo demonstration of enhanced radiotherapy using rare earth doped titania nanoparticles,” *Nanoscale*, 2012.

[102] M. E. Davis, Z. G. Chen, and D. M. Shin, “Nanoparticle therapeutics: an emerging treatment modality for cancer,” *Nat Rev Drug Discov*, vol. 7, no. 9, pp. 771–782, Sep. 2008.

[103] O. C. Farokhzad and R. Langer, “Impact of nanotechnology on drug delivery,” *ACS Nano*, vol. 3, no. 1, pp. 16–20, 2009.

[104] Wikipedia. (2015, Apr.) Zeta potentail. [Online]. Available: http://en.wikipedia.org/wiki/Zeta_potential

[105] T. Kafri, H. van Praag, F. H. Gage, and I. M. Verma, “Lentiviral vectors: Regulated gene expression,” *Molecular Therapy*, vol. 1, no. 6, pp. 516–521, 2000.

[106] D. W. Shen, C. Cardarelli, J. Hwang, M. Cornwell, N. Richert, S. Ishii, I. Pastan, and M. M. Gottesman, “Multiple drug-resistant human KB carcinoma cells independently selected for high-level resistance to colchicine, adriamycin, or vinblastine show changes in expression of specific proteins,” *J Biol Chem*, vol. 261, no. 17, pp. 7762–70, 1986.

[107] S. Wang, H. Yu, and J. K. Wickliffe, “Limitation of the MTT and XTT assays for measuring cell viability due to superoxide formation induced by nano-scale TiO2,” *TOXICOLOGY IN VITRO*, vol. 25, no. 8, pp. 2147–2151, DEC 2011.

[108] M. Lubarsky, C. Ray, and B. Funaki, “Embolization agents-which one should be used when? part 2: small-vessel embolization,” *Seminars in interventional radiology*, vol. 27, no. 1, pp. 99–104, 2010.

[109] C. P. Derdeyn, C. J. Moran, D. T. Cross, H. H. Dietrich, and R. G. Dacey, “Polyvinyl alcohol particle size and suspension characteristics.” *American Journal of Neuroradiology*, vol. 16, no. 6, pp. 1335–43, 1995. [Online]. Available: http://www.ajnr.org/content/16/6/1335.abstract

[110] C. P. Derdeyn, V. B. Graves, M. S. Salamat, and A. Rappe, “Collagen-coated acrylic microspheres for embolotherapy: *in vivo* and *in vitro* characteristics.” *American Journal of Neuroradiology*, vol. 18, no. 4, pp. 647–53, 1997. [Online]. Available: http://www.ajnr.org/content/18/4/647.abstract

[111] A. Laurent, R. Beaujeux, M. Wassef, D. Rfenacht, E. Boschetti, and J. J. Merland, “Trisacryl gelatin microspheres for therapeutic embolization, i: development and *in vitro* evaluation.” *American Journal of Neuroradiology*, vol. 17, no. 3, pp. 533–40, 1996. [Online]. Available: http://www.ajnr.org/content/17/3/533.abstract

[112] K. Saralidze, L. Koole, and M. Knetsch, “Polymeric microspheres for medical applications,” *Materials*, vol. 3, pp. 3537–3564, 2010.

[113] D. J. Chauvel-Lebret, P. Pellen-Mussi, P. Auroy, and M. Bonnaure-Mallet, “Evaluation of the in vitro biocompatibility of various elastomers,” *Biomaterials*, vol. 20, no. 3, pp. 291–299, 1999.

[114] W. Russell and R. Burch, *The Principles of Humane Experimental Technique.* Methuen, London, 1959.

[115] A. E. Infolink, “Three Rs-replacment,” April 2015. [Online]. Available: http://www.animalethics.org.au/three-rs/replacement

[116] H. Ihara, S. Kubota, A. Uchimura, Y. Sakai, T. Wakiya, M. M. Rahman, S. Nagaoka, and M. Takafuji, “A facile preparation method for self-assembled monolayers with silica particles on polystyrene-based microspheres,” *Materials Chemistry and Physics*, vol. 114, no. 1, pp. 1–5, 2009.

[117] A. Uchimura, S. Kubota, S. Yamada, T. Wakiya, M. Takafuji, T. Shirosaki, S. Nagaoka, and H. Ihara, “Facile and versatile method for preparing core-shell microspheres with controlled surface structures based on silica particles-monolayer,” *Materials Chemistry and Physics*, vol. 129, no. 3, pp. 871–880, 2011.

[118] P. Ajikumar and K. Devaky, “Egdma -cross-linked polystyrene resin: An efficient support for gel phase peptide synthesis,” *Journal of Chemical Sciences*, vol. 112, no. 4, pp. 465–474, 2000. [Online]. Available: http://dx.doi.org/10.1007/BF02704352

[119] S. Labs, “Synthetic human tissues and body parts- venous models,” 2004. [Online]. Available: http://syndaver.com/shop/syntissue/straight-vein-designer-new/

[120] M. Papetti and I. M. Herman, “Mechanisms of normal and tumor-derived angiogenesis,” *American Journal of Physiology - Cell Physiology*, vol. 282, no. 5, pp. C947–C970, 2002.

[121] M. R. Dreher, K. V. Sharma, D. L. Woods, G. Reddy, Y. Tang, W. F. Pritchard, O. A. Chiesa, J. W. Karanian, J. A. Esparza, D. Donahue, E. B. Levy, S. L. Willis, A. L. Lewis, and B. J. Wood, “Radiopaque drug-eluting beads for transcatheter embolotherapy: experimental study of drug penetration and coverage in swine,” *J Vasc Interv Radiol*, vol. 23, no. 2, pp. 257–64e4, 2012.

[122] L. A. Mucci, A. Powolny, E. Giovannucci, Z. Liao, S. A. Kenfield, R. Shen, M. J. Stampfer, and S. K. Clinton, “Prospective study of prostate tumor angiogenesis and cancer-specific mortality in the health professionals follow-up study,” *J Clin Oncol*, vol. 27, no. 33, pp. 5627–33, 2009.

[123] F. Tadayyon, M. Mellat, F. Alizadeh, M. Hadi, M. Khorrami, M. Yazdani, and R. H. Joozdani, “Prostate cancer: Relationship between vascular diameter, shape and density and gleason score in needle biopsy specimens,” *Adv Biomed Res*, vol. 2, p. 3, 2013.

[124] J. Laitakari, V. Nayha, and F. Stenback, “Size, shape, structure, and direction of angiogenesis in laryngeal tumour development,” *Journal of Clinical Pathology*, vol. 57, no. 4, pp. 394–401, 2004.

[125] J. S. Burrell, R. S. Bradley, S. Walker-Samuel, Y. Jamin, L. C. J. Baker, J. K. R. Boult, P. J. Withers, J. Halliday, J. C. Waterton, and S. P. Robinson, “MRI measurements of vessel calibre in tumour xenografts: Comparison with vascular corrosion casting,” *Microvascular Research*, vol. 84, no. 3, pp. 323–329, 2012.

[126] Y. S. Chang, E. di Tomaso, D. M. McDonald, R. Jones, R. K. Jain, and L. L. Munn, "Mosaic blood vessels in tumors: Frequency of cancer cells in contact with flowing blood," *Proceedings of the National Academy of Sciences*, vol. 97, no. 26, pp. 14 608–14 613, 2000.

[127] H. Hashizume, P. Baluk, S. Morikawa, J. W. McLean, G. Thurston, S. Roberge, R. K. Jain, and D. M. McDonald, "Openings between defective endothelial cells explain tumor vessel leakiness," *American Journal of Pathology*, vol. 156, no. 4, pp. 1363–1380, 2000.

[128] H. Harada, X. Xie, S. Itasaka, L. Zeng, Y. Zhu, A. Morinibu, K. Shinomiya, and M. Hiraoka, "Diameter of tumor blood vessels is a good parameter to estimate HIF-1-active regions in solid tumors," *Biochemical and Biophysical Research Communications*, vol. 373, no. 4, pp. 533–538, 2008.

[129] J. R. Less, T. C. Skalak, E. M. Sevick, and R. K. Jain, "Microvascular architecture in a mammary carcinoma: branching patterns and vessel dimensions," *Cancer Res*, vol. 51, no. 1, pp. 265–73, 1991.

[130] S. A. Skinner, P. J. Tutton, and P. E. O'Brien, "Microvascular architecture of experimental colon tumors in the rat," *Cancer Res*, vol. 50, no. 8, pp. 2411–7, 1990.

[131] S. D. Packard, J. B. Mandeville, T. Ichikawa, K. Ikeda, K. Terada, S. Niloff, E. A. Chiocca, B. R. Rosen, and J. J. Marota, "Functional response of tumor vasculature to PaCO2: determination of total and microvascular blood volume by MRI," *Neoplasia*, vol. 5, no. 4, pp. 330–8, 2003.

[132] C. D. Frickm, A. Rudin, and R. H. Wiley, "Reactivity ratios for divinylbenzene and ethylene glycol dimethacrylate copolymerizations with styrene and methyl methacrylate," *Journal of Macromolecular Science: Part A - Chemistry*, vol. 16, no. 7, pp. 1275–1282, 1981.

[133] T. L. U. Nguyen, S. Y. Tey, M. H. Pourgholami, D. L. Morris, T. P. Davis, C. Barner-Kowollik, and M. H. Stenzel, "Synthesis of semi-biodegradable crosslinked microspheres for the delivery of 1,25 dihydroxyvitamin d3 for the treatment of hepatocellular carcinoma," *European Polymer Journal*, vol. 43, no. 5, pp. 1754–1767, 2007.

[134] U. O. Hafeli and G. J. Pauer, "In vitro and in vivo toxicity of magnetic microspheres," *Journal of Magnetism and Magnetic Materials*, vol. 194, no. 13, pp. 76–82, 1999.

[135] P. Menei, A. Croue, V. Daniel, A. Pouplardbarthelaix, and J. P. Benoit, "Fate and biocompatibility of 3 types of microspheres implanted into the brain," *Journal of Biomedical Materials Research*, vol. 28, no. 9, pp. 1079–1085, 1994.

[136] J. Hubbell, "Photon mass attenuation and energy-absorption coefficients," *The International Journal of Applied Radiation and Isotopes*, vol. 33, no. 11, pp. 1269–1290, 1982.

[137] S.-B. Yu and A. D. Watson, “Metal-based X-ray contrast media,” *Chemical Reviews*, vol. 99, no. 9, pp. 2353–2378, 1999.

[138] M. A. Hahn, A. K. Singh, P. Sharma, S. C. Brown, and B. M. Moudgil, “Nanoparticles as contrast agents for in-vivo bioimaging: current status and future perspectives,” *Anal Bioanal Chem*, vol. 399, no. 1, pp. 3–27, 2011.

[139] J. Black, “Biologic performance of tantalum,” *Clinical Materials*, vol. 16, no. 3, pp. 167–173, 1994.

[140] B. F. Mullan, M. T. Madsen, L. Messerle, V. Kolesnichenko, and J. Kruger, “X-ray attenuation coefficients of high-atomic-number, hexanuclear transition metal cluster compounds: A new paradigm for radiographic contrast agents,” *Academic Radiology*, vol. 7, no. 4, pp. 254–259, 2000.

[141] A. Dumont and A. Martelli, “X-ray opacification of hepatic lymph nodes following intravenous injection of tantalum dust.” *Lymphology*, vol. 2, no. 3, p. 91, 1969.

[142] J. A. Nadel, W. G. Wolfe, and P. D. Graf, “Powdered tantalum as a medium for bronchography in canine and human lungs,” *Investigative radiology*, vol. 3, no. 4, pp. 229–237, 1968.

[143] J. Nadel, W. Wolfe, P. Graf, J. Youker, N. Zamel, J. Austin, W. Hinchcliffe, R. Greenspan, and R. Wright, “Powdered tantalum: a new contrast medium for roentgenographic examination of human airways,” *New England Journal of Medicine*, vol. 283, no. 6, pp. 281–286, 1970.

[144] J. Nadel, G. Cabezas, and J. Austin, “In vivo roentgenographic examination of parasympathetic innervation of small airways: use of powdered tantalum and a fine focal spot x-ray tube,” *Investigative radiology*, vol. 6, no. 1, pp. 9–17, 1971.

[145] J. S. K. Laitakari and A. E. Kortekangas1, “Radiography of the maxillary sinus mucosal surface with tantalum,” *Acta Oto-laryngologica*, vol. 95, no. 5-6, pp. 454–459, 1983.

[146] C. Tegtmeyer, N. Smith, A. El-Mahdi, G. Fitz-Hugh, and W. Constable, “The value of tantalum powder as a contrast medium in laryngography,” *Canad J Otolaryngol*, vol. 4, no. 1, pp. 81–85, 1975.

[147] N. Zamel, J. H. M. Austin, P. D. Graf, H. H. Dedo, M. D. Jones, and J. A. Nadel, “Powdered tantalum as a medium for human laryngography,” *Radiology*, vol. 94, no. 3, pp. 547–553, 1970.

[148] R. G. Vieth, G. T. Tindall, and G. L. Odom, “The use of tantalum dust as an adjunct in the postoperative management of subdural hematomas,” *Journal of Neurosurgery*, vol. 24, no. 2, pp. 514–519, 1966.

[149] R. E. Colborn, J. P. J. Bonitatibus, A. S. Torres, M. E. Marino, M. D. Butts, A. Kulkarni, B. C. Bales, and B. A. Hay, “Nanoparticle contrast agents for diagnostic imaging,” Dec. 18 2009, WO Patent App. PCT/EP2009/067,468.

[150] P. J. Bonitatibus Jr., A. S. Torres, G. D. Goddard, P. F. FitzGerald, and A. M. Kulkarni, “Synthesis, characterization, and computed tomography imaging of a tantalum oxide nanoparticle imaging agent,” *Chem. Commun.*, vol. 46, pp. 8956–8958, 2010.

[151] A. S. Torres, P. J. Bonitatibus Jr, R. E. Colborn, G. D. Goddard, P. F. FitzGerald, B. D. Lee, and M. E. Marino, “Biological performance of a size-fractionated core-shell tantalum oxide nanoparticle x-ray contrast agent,” *Investigative Radiology*, vol. 47, no. 10, pp. 578–587, 2012.

[152] P. J. Bonitatibus, A. S. Torres, B. Kandapallil, B. D. Lee, G. D. Goddard, R. E. Colborn, and M. E. Marino, “Preclinical assessment of a zwitterionic tantalum oxide nanoparticle x-ray contrast agent,” *ACS Nano*, vol. 6, no. 8, pp. 6650–6658, 2012.

[153] M. H. Oh, N. Lee, H. Kim, S. P. Park, Y. Piao, J. Lee, S. W. Jun, W. K. Moon, S. H. Choi, and T. Hyeon, “Large-scale synthesis of bioinert tantalum oxide nanoparticles for x-ray computed tomography imaging and bimodal image-guided sentinel lymph node mapping,” *J. Am. Chem. Soc.*, vol. 133, no. 14, pp. 5508–5515, Mar. 2011.

[154] N. Lee, H. R. Cho, M. H. Oh, S. H. Lee, K. Kim, B. H. Kim, K. Shin, T.-Y. Ahn, J. W. Choi, Y.-W. Kim, S. H. Choi, and T. Hyeon, “Multifunctional Fe3O4/TaOx core/shell nanoparticles for simultaneous magnetic resonance imaging and x-ray computed tomography,” *Journal of the American Chemical Society*, vol. 134, no. 25, pp. 10 309–10 312, 2012.

[155] J. Puig, C. E. Hoppe, L. A. Fasce, C. J. Prez, Y. Pieiro-Redondo, M. Baobre-Lpez, M. A. Lpez-Quintela, J. Rivas, and R. J. J. Williams, “Superparamagnetic nanocomposites based on the dispersion of oleic acid-stabilized magnetite nanoparticles in a diglycidylether of bisphenol a-based epoxy matrix: Magnetic hyperthermia and shape memory,” *The Journal of Physical Chemistry C*, vol. 116, no. 24, pp. 13 421–13 428, 2012.

[156] L. Zhang, R. He, and H.-C. Gu, “Oleic acid coating on the monodisperse magnetite nanoparticles,” *Applied Surface Science*, vol. 253, no. 5, pp. 2611–2617, 2006.

[157] M. Bloemen, W. Brullot, T. Luong, N. Geukens, A. Gils, and T. Verbiest, “Improved functionalization of oleic acid-coated iron oxide nanoparticles for biomedical applications,” *Journal of Nanoparticle Research*, vol. 14, no. 9, pp. 1–10, 2012.

[158] V. B. Barbeta, R. F. Jardim, P. K. Kiyohara, F. B. Effenberger, and L. M. Rossi, “Magnetic properties of fe_3o_4 nanoparticles coated with oleic and dodecanoic acids,” *Journal of Applied Physics*, vol. 107, no. 7, p. 073913, 2010.

[159] P. Majewski and P. Krysinski, “Synthesis, surface modifications, and size-sorting of mixed nickel, zinc ferrite colloidal magnetic nanoparticles,” *Chemistry A European Journal*, vol. 14, no. 26, pp. 7961–7968, 2008.

[160] J. H. Hubbell and S. M. Seltzer. (1996) Tables of x-ray mass attenuation coefficients and mass energy-absorption coefficients from 1 keV to 20 MeV for elements Z = 1 to 92 and 48 Additional substances of dosimetric interest. NIST. [Online]. Available: http://www.nist.gov/pml/data/xraycoef/index.cfm

[161] G. Poludniowski, G. Landry, F. DeBlois, P. M. Evans, and F. Verhaegen, "Spekcalc : a program to calculate photon spectra from tungsten anode x-ray tubes," *Physics in Medicine and Biology*, vol. 54, no. 19, p. N433, 2009.

[162] BioCompatables, "How many beads are there per vial of DC bead®," 2014. [Online]. Available: http://www.btg-im.com/products/uk-322/dcbead-3/debdox-dc-bead

[163] F. Bensadoun, N. Kchit, C. Billotte, F. Trochu, and E. Ruiz, "A comparative study of dispersion techniques for nanocomposite made with nanoclays and an unsaturated polyester resin," *Journal of Nanomaterials*, p. 12, 2011.

[164] H.-X. Xu, X.-Y. Yin, M.-D. Lu, G.-J. Liu, and Z.-F. Xu, "Estimation of liver tumor volume using a three-dimensional ultrasound volumetric system," *Ultrasound in Medicine & Biology*, vol. 29, no. 6, pp. 839–846, 2003.

[165] S. M. Limited, "SIR-spheres® microspheres- training program," March 2015. [Online]. Available: http://foxfireglobal.sirtex.com/sites/foxfireglobal.sirtex.com/files/user/trn-us-05_for_us.pdf

[166] M. Babaei and M. Ganjalikhani, "The potential effectiveness of nanoparticles as radio sensitizers for radiotherapy," *BioImpacts : BI*, vol. 4, no. 1, pp. 15–20, Nov. 2013.

[167] I. Miladi, C. Alric, S. Dufort, P. Mowat, A. Dutour, C. Mandon, G. Laurent, E. BrÃ¤uer-Krisch, N. Herath, J.-L. Coll, M. Dutreix, F. Lux, R. Bazzi, C. Billotey, M. Janier, P. Perriat, G. Le Duc, S. Roux, and O. Tillement, "The in vivo radiosensitizing effect of gold nanoparticles based MRI contrast agents," *Small*, vol. 10, no. 6, pp. 1116–1124, 2014.

[168] R. Nath, P. Bongiorni, P. I. Rossi, and S. Rockwell, "Enhanced IUdR radiosensitization by 241am photons relative to 226ra and 125i photons at 0.72 Gy/hr," *International Journal of Radiation Oncology*Biology*Physics*, vol. 18, no. 6, pp. 1377–1385, 1990.

[169] Q. Zheng, H. Yang, J. Wei, J.-l. Tong, and Y.-q. Shu, "The role and mechanisms of nanoparticles to enhance radiosensitivity in hepatocellular cell," *Biomedicine & Pharmacotherapy*, vol. 67, no. 7, pp. 569–575, Sep. 2013.

[170] T. Lopez, E. Ortiz, M. Alvarez, J. Navarrete, J. A. Odriozola, F. Martinez-Ortega, E. A. Paez-Mozo, P. Escobar, K. A. Espinoza, and I. A. Rivero, "Study of the stabilization of zinc phthalocyanine in sol-gel TiO2 for photodynamic therapy applications," *Nanomedicine-Nanotechnology Biology and Medicine*, vol. 6, no. 6, pp. 777–785, 2010.

[171] S. J. Xu, J. Q. Shen, S. Chen, M. H. Zhang, and T. Shen, "Active oxygen species (1o2, o2*-) generation in the system of TiO2 colloid sensitized by hypocrellin b," *Journal of Photochemistry and Photobiology B-Biology*, vol. 67, no. 1, pp. 64–70, 2002.

[172] Y. Kubota, T. Shuin, C. Kawasaki, M. Hosaka, H. Kitamura, R. Cai, H. Sakai, K. Hashimoto, and A. Fujishima, "Photokilling of T-24 human bladder cancer cells with titanium dioxide," *Br J Cancer*, vol. 70, no. 6, pp. 1107–1111, Dec. 1994.

[173] N. Lagopati, P. Kitsiou, A. Kontos, P. Venieratos, E. Kotsopoulou, A. Kontos, D. Dionysiou, S. Pispas, E. Tsilibary, and P. Falaras, "Photo-induced treatment of breast epithelial cancer cells using nanostructured titanium dioxide solution," *Journal of Photochemistry and Photobiology A: Chemistry*, vol. 214, no. 23, pp. 215–223, 2010.

[174] R. Cai, Y. Kubota, T. Shuin, H. Sakai, K. Hashimoto, and A. Fujishima, "Induction of cytotoxicity by photoexcited TiO2 particles," *Cancer Research*, vol. 52, no. 8, pp. 2346–2348, 1992.

[175] I. Roy, T. Y. Ohulchanskyy, H. E. Pudavar, E. J. Bergey, A. R. Oseroff, J. Morgan, T. J. Dougherty, and P. N. Prasad, "Ceramic-based nanoparticles entrapping water-insoluble photosensitizing anticancer drugs: A novel drug-carrier system for photodynamic therapy," *Journal of the American Chemical Society*, vol. 125, no. 26, pp. 7860–7865, 2003.

[176] Y. Lee and E. D. Baron, "Photodynamic therapy: current evidence and applications in dermatology," *Seminars in cutaneous medicine and surgery*, vol. 30, no. 4, pp. 199–209, 2011.

[177] W. Chen and J. Zhang, "Using nanoparticles to enable simultaneous radiation and photodynamic therapies for cancer treatment," *Journal of Nanoscience and Nanotechnology*, vol. 6, no. 4, pp. 1159–1166, 2006.

[178] M. Meinhardt, R. Krebs, A. Anders, U. Heinrich, and H. Tronnier, "Effect of ultraviolet adaptation on the ultraviolet absorption spectra of human skin in vivo," *Photodermatology, Photoimmunology & Photomedicine*, vol. 24, no. 2, pp. 76–82, 2008.

[179] S. Klein, M. L. Dell'Arciprete, M. Wegmann, L. V. Distel, W. Neuhuber, M. C. Gonzalez, and C. Kryschi, "Oxidized silicon nanoparticles for radiosensitization of cancer and tissue cells," *Biochemical and Biophysical Research Communications*, vol. 434, no. 2, pp. 217–222, 2013.

[180] S. Radice, P. Kern, H. Dietsch, S. Mischler, and J. Michler, "Methods for functionalization of microsized polystyrene beads with titania nanoparticles for cathodic electrophoretic deposition," *Journal of Colloid and Interface Science*, vol. 318, no. 2, pp. 264–270, 2008.

[181] M. E. Fabiyi and R. L. Skelton, "Photocatalytic mineralisation of methylene blue using buoyant TiO2-coated polystyrene beads," *Journal of Photochemistry and Photobiology A: Chemistry*, vol. 132, no. 12, pp. 121–128, 2000.

[182] Nanoshel. (2015, 01) Degussa, titanium oxide nanopowder (tio2, degussa, rutile:anatase/ 85:15, 99+http://www.nanoshel.com/product/degussa-p25-tio2/

[183] B. Thiébaut, "Final analysis: Flame spray pyrolysis: A unique facility for the production of nanopowders," *Platinum Metals Review*, vol. 55, no. 2, pp. 149–151, 2011.

[184] K.-i. Ishibashi, A. Fujishima, T. Watanabe, and K. Hashimoto, "Detection of active oxidative species in TiO2 photocatalysis using the fluorescence technique," *Electrochemistry Communications*, vol. 2, no. 3, pp. 207–210, 2000.

[185] J. S. McManus, P. D. Cunningham, L. B. Regan, P. W. Dunne, J. S. McManus, P. D. Cunningham, L. B. Regan, and P. W. Dunne, "The synthesis of organo-soluble anatase nanocrystals from amorphous titania," *Chemical Communications*, vol. 48, no. 60, pp. 7453–7455, 2012.

[186] Y. He, A. Tilocca, O. Dulub, A. Selloni, and U. Diebold, "Local ordering and electronic signatures of submonolayer water on anatase TiO2 (101)," *Nature materials*, vol. 8, no. 7, pp. 585–589, 2009.

[187] A. Sclafani* and J. M. Herrmann, "Comparison of the photoelectronic and photocatalytic activities of various anatase and rutile forms of titania in pure liquid organic phases and in aqueous solutions," *J. Phys. Chem.,*, vol. 100, no. 32, pp. 13 655–13 661, 1996.

[188] Z. L. Xu, Q. J. Yang, C. Xie, W. J. Yan, Y. G. Du, Z. M. Gao, and J. H. Zhang, "Structure, luminescence properties and photocatalytic activity of europium doped-TiO2 nanoparticles," *Journal of Materials Science*, vol. 40, no. 6, 2005.

[189] Y. Zhang, H. Zhang, Y. Xu, and Y. Wang, "Europium doped nanocrystalline titanium dioxide: preparation, phase transformation and photocatalytic properties," *Journal of Materials Chemistry*, vol. 13, no. 9, pp. 2261–2265, 2003.

[190] I. F. Robey, B. K. Baggett, N. D. Kirkpatrick, D. J. Roe, J. Dosescu, B. F. Sloane, A. I. Hashim, D. L. Morse, N. Raghunand, R. A. Gatenby, and R. J. Gillies, "Bicarbonate increases tumor pH and inhibits spontaneous metastases," *Cancer Research*, vol. 69, no. 6, pp. 2260–2268, 2009.

[191] T. A. Egerton, "The influence of surface alumina and silica on the photocatalytic degradation of organic pollutants," *Catalysts*, vol. 3, no. 1, pp. 338–362, 2013. [Online]. Available: http://www.mdpi.com/2073-4344/3/1/338

[192] M. Gilles, E. Brun, and C. Sicard-Roselli, "Gold nanoparticles functionalization notably decreases radiosensitization through hydroxyl radical production under ionizing radiation," *Colloids and Surfaces B: Biointerfaces*, vol. 123, no. 0, pp. 770–777, 2014.

[193] R. R. Zhang, C. L. Wu, L. L. Tong, B. Tang, and Q. H. Xu, "Multifunctional core-shell nanoparticles as highly efficient imaging and photosensitizing agents," *Langmuir*, vol. 25, no. 17, pp. 10 153–10 158, 2009.

[194] S. W. Shin, “The current practice of transarterial chemoembolization for the treatment of hepatocellular carcinoma,” *Korean Journal of Radiology*, vol. 10, no. 5, pp. 425–434, 2009.

[195] Z. Li, J. C. Barnes, A. Bosoy, J. F. Stoddart, and J. I. Zink, “Mesoporous silica nanoparticles in biomedical applications,” *Chemical Society Reviews*, vol. 41, no. 7, pp. 2590–2605, 2012.

[196] I. I. Slowing, B. G. Trewyn, S. Giri, and V. S. Y. Lin, “Mesoporous silica nanoparticles for drug delivery and biosensing applications,” *Advanced Functional Materials*, vol. 17, no. 8, pp. 1225–1236, 2007.

[197] I. I. Slowing, J. L. Vivero-Escoto, C.-W. Wu, and V. S. Y. Lin, “Mesoporous silica nanoparticles as controlled release drug delivery and gene transfection carriers,” *Advanced Drug Delivery Reviews*, vol. 60, no. 11, pp. 1278–1288, 2008.

[198] D. Niu, Z. Ma, Y. Li, and J. Shi, “Synthesis of core-shell structured dual-mesoporous silica spheres with tunable pore size and controllable shell thickness,” *Journal of the American Chemical Society*, vol. 132, no. 43, pp. 15 144–15 147, 2010.

[199] C. Argyo, V. Weiss, C. Bruchle, and T. Bein, “Multifunctional mesoporous silica nanoparticles as a universal platform for drug delivery,” *Chemistry of Materials*, 2013.

[200] H. Meng, M. Xue, T. Xia, Y.-L. Zhao, F. Tamanoi, J. F. Stoddart, J. I. Zink, and A. E. Nel, “Autonomous in vitro anticancer drug release from mesoporous silica nanoparticles by pH-sensitive nanovalves,” *Journal of the American Chemical Society*, vol. 132, no. 36, pp. 12 690–12 697, 2010.

[201] S. R. Abulateefeh, S. G. Spain, K. J. Thurecht, J. W. Aylott, W. C. Chan, M. C. Garnett, and C. Alexander, “Enhanced uptake of nanoparticle drug carriers via a thermoresponsive shell enhances cytotoxicity in a cancer cell line,” *Biomater. Sci.*, vol. 1, pp. 434–442, 2013.

[202] M.-W. Chang, M. Edirisinghe, and E. Stride, “Ultrasound mediated release from stimuli-responsive core-shell capsules,” *J. Mater. Chem. B*, vol. 1, pp. 3962–3971, 2013.

[203] X. Wan, G. Zhang, and S. Liu, “pH-disintegrable polyelectrolyte multilayer-coated mesoporous silica nanoparticles exhibiting triggered co-release of cisplatin and model drug molecules,” *Macromolecular Rapid Communications*, vol. 32, no. 14, pp. 1082–1089, 2012.

[204] N. Raghunand, X. He, R. van Sluis, B. Mahoney, B. Baggett, C. W. Taylor, G. Paine-Murrieta, D. Roe, Z. M. Bhujwalla, and R. J. Gillies, “Enhancement of chemotherapy by manipulation of tumour pH,” *British Journal of Cancer*, vol. 80, no. 7, pp. 1005–1011, 1999.

[205] X. Huang, N. P. Young, and H. E. Townley, “Characterisation and comparison of mesoporous silica particles for optimised drug delivery,” *Nanomaterials and Nanotechnology*, in press.

[206] A. Chan, "The application of nanomaterials for the delivery of natural antimicrobials in engineered systems," Ph.D. dissertation, University of Oxford, 2013.

[207] C. Hom, J. Lu, M. Liong, H. Luo, Z. Li, J. I. Zink, and F. Tamanoi, "Mesoporous silica nanoparticles facilitate delivery of siRNA to shutdown signaling pathways in mammalian cells," *Small*, vol. 6, no. 11, pp. 1185–1190, 2010.

[208] U. of Strathclyde. (2015, Mar.) Sorbent sythesis and application. [Online]. Available: http://info.chem.strath.ac.uk/people/academic/lorraine_gibson/research/sorbents

[209] C.-M. J. Hu and L. Zhang, "Nanoparticle-based combination therapy toward overcoming drug resistance in cancer," *Biochemical Pharmacology*, vol. 83, no. 8, pp. 1104–1111, 2012.

[210] K. Patel and I. Tannock, "The influence of P-glycoprotein expression and its inhibitors on the distribution of doxorubicin in breast tumors," *BMC Cancer*, vol. 9, no. 1, p. 356, 2009.

[211] X. Dong and R. J. Mumper, "Nanomedicinal strategies to treat multidrug-resistant tumors: current progress," *Nanomedicine (Lond)*, vol. 5, no. 4, pp. 597–615, 2010.

[212] R. Simpson and S. Mathivanan, "Extracellular microvesicles: the need for internationally recognised nomenclature and stringent purification criteria," *J Proteomics Bioinform*, vol. 5, 2012.

[213] G. Raposo and W. Stoorvogel, "Extracellular vesicles: Exosomes, microvesicles, and friends," *The Journal of Cell Biology*, vol. 200, no. 4, pp. 373–383, 2013.

[214] A. Azmi, B. Bao, and F. Sarkar, "Exosomes in cancer development, metastasis, and drug resistance: a comprehensive review," *Cancer and Metastasis Reviews*, vol. 32, no. 3-4, pp. 623–642, 2013.

[215] S. Mathivanan and R. J. Simpson, "ExoCarta: A compendium of exosomal proteins and RNA," *PROTEOMICS*, vol. 9, no. 21, pp. 4997–5000, 2009.

[216] J. Akers, D. Gonda, R. Kim, B. Carter, and C. Chen, "Biogenesis of extracellular vesicles (EV): exosomes, microvesicles, retrovirus-like vesicles, and apoptotic bodies," *Journal of Neuro-Oncology*, vol. 113, no. 1, pp. 1–11, 2013.

[217] V. Muralidharan-Chari, J. W. Clancy, A. Sedgwick, and C. D'Souza-Schorey, "Microvesicles: mediators of extracellular communication during cancer progression," *Journal of Cell Science*, vol. 123, no. 10, pp. 1603–1611, 2010.

[218] S. Elmore, "Apoptosis: A review of programmed cell death," *Toxicologic Pathology*, vol. 35, no. 4, pp. 495–516, 2007.

[219] A. materails. (2015, Feb.) Silica - silicon dioxide (SiO2). [Online]. Available: http://www.azom.com/properties.aspx?ArticleID=1114

[220] ——. (2015, Feb.) Titanium dioxide - titania (TiO2). [Online]. Available: http://www.azom.com/properties.aspx?ArticleID=1179

[221] H. Hata, S. Saeki, T. Kimura, Y. Sugahara, and K. Kuroda, “Adsorption of taxol into ordered mesoporous silicas with various pore diameters,” *Chemistry of Materials*, vol. 11, no. 4, pp. 1110–1119, 1999.

[222] R. Zhang, T. Cherdhirankorn, K. Graf, K. Koynov, and R. Berger, “Swelling of cross-linked polystyrene beads in toluene,” *Microelectronic Engineering*, vol. 85, no. 56, pp. 1261–1264, 2008.

[223] Q. He and J. Shi, “Mesoporous silica nanoparticle based nano drug delivery systems: synthesis, controlled drug release and delivery, pharmacokinetics and biocompatibility,” *Journal of Materials Chemistry*, vol. 21, no. 16, pp. 5845–5855, 2011.

[224] S. Karve, M. E. Werner, R. Sukumar, N. D. Cummings, J. A. Copp, E. C. Wang, C. Li, M. Sethi, R. C. Chen, M. E. Pacold, and A. Z. Wang, “Revival of the abandoned therapeutic wortmannin by nanoparticle drug delivery,” *Proceedings of the National Academy of Sciences*, vol. 109, no. 21, pp. 8230–8235, 2012.

[225] J. E. B. Fox and D. R. Phillips, “Inhibition of actin polymerization in blood platelets by cytochalasins,” *Nature*, vol. 292, no. 5824, pp. 650–652, 1981.

[226] J. F. Casella, M. D. Flanagan, and S. Lin, “Cytochalasin D inhibits actin polymerization and induces depolymerization of actin filaments formed during platelet shape change,” *Nature*, vol. 293, no. 5830, pp. 302–305, 1981.

[227] C. Krakstad and M. Chekenya, “Survival signalling and apoptosis resistance in glioblastomas: opportunities for targeted therapeutics,” *Molecular Cancer*, vol. 9, no. 1, p. 135, 2010.

[228] G. Zhu, Y. Zheng, L. Zhang, Y. Shi, W. Li, Z. Liu, B. Peng, J. Yin, W. Liu, and X. He, “Coxsackievirus A16 infection triggers apoptosis in RD cells by inducing ER stress,” *Biochemical and Biophysical Research Communications*, vol. 441, no. 4, pp. 856–861, 2013.

[229] W. Shi, X. Li, X. Hou, H. Peng, Q. Jiang, M. Shi, Y. Ji, X. Liu, and J. Liu, “Differential apoptosis gene expressions of rhabdomyosarcoma cells in response to enterovirus 71 infection,” *BMC Infectious Diseases*, vol. 12, no. 1, p. 327, 2012.

[230] K. Shedden, X. T. Xie, P. Chandaroy, Y. T. Chang, and G. R. Rosania, “Expulsion of small molecules in vesicles shed by cancer cells: Association with gene expression and chemosensitivity profiles,” *Cancer Research*, vol. 63, no. 15, pp. 4331–4337, 2003.

[231] E. L. Gregoraszczuk and S. Stoklosowa, “The effect of microtubule and microfilament-disrupting drugs on prolactin-stimulated progesterone synthesis and secretion by cultured porcine theca cells,” *Acta Histochemica*, vol. 99, no. 2, pp. 207–215, 1997.

[232] M. Schliwa, “Action of cytochalasin D on cytoskeletal networks,” *The Journal of Cell Biology*, vol. 92, no. 1, pp. 79–91, 1982.

[233] M. L. Coleman, E. A. Sahai, M. Yeo, M. Bosch, A. Dewar, and M. F. Olson, "Membrane blebbing during apoptosis results from caspase-mediated activation of ROCK I," *Nature Cell Biology*, vol. 3, no. 4, pp. 339–345, 2001.

[234] Y. Yano, J. I. Kambayashi, E. Shiba, M. Sakon, E. Oiki, K. Fukuda, T. Kawasaki, and T. Mori, "The role of protein phosphorylation and cytoskeletal reorganization in microparticle formation from the platelet plasma membrane." *Biochemical Journal*, vol. 299, pp. 303–308, 1994.

[235] C. I. Timar, Á. M. Lőrincz, R. Csépányi-Kömi, A. Vályi-Nagy, G. Nagy, E. I. Buzás, Z. Iványi, Á. Kittel, D. W. Powell, K. R. McLeish, and E. Ligeti, "Antibacterial effect of microvesicles released from human neutrophilic granulocytes," *Blood*, vol. 121, no. 3, pp. 510–518, 2013.

[236] L. Balaj, R. Lessard, L. Dai, Y.-J. Cho, S. L. Pomeroy, X. O. Breakefield, and J. Skog, "Tumour microvesicles contain retrotransposon elements and amplified oncogene sequences," *Nature Communications*, vol. 2, p. 180, 2011.

[237] M. Guescini, S. Genedani, V. Stocchi, and L. Agnati, "Astrocytes and glioblastoma cells release exosomes carrying mtDNA," *Journal of Neural Transmission*, vol. 117, no. 1, pp. 1–4, 2010.

[238] A. Bergsmedh, A. Szeles, M. Henriksson, A. Bratt, M. J. Folkman, A.-L. Spetz, and L. Holmgren, "Horizontal transfer of oncogenes by uptake of apoptotic bodies," *Proceedings of the National Academy of Sciences*, vol. 98, no. 11, pp. 6407–6411, 2001.

[239] A. Waldenstrom, N. Gennebock, U. Hellman, and G. Ronquist, "Cardiomyocyte microvesicles contain DNA/RNA and convey biological messages to target cells," *PloS one*, vol. 7, no. 4, p. e34653, 2012.

[240] R. Morrison, C. Gardiner, A. Evidente, R. Kiss, and H. Townley, "Incorporation of Ophiobolin A into novel chemoembolization particles for cancer cell treatment," *Pharmaceutical Research*, pp. 1–14, 2014.

[241] J. Krysiak and R. Breinbauer, "Activity-based protein profiling for natural product target discovery," in *Activity-Based Protein Profiling*, ser. Topics in Current Chemistry, S. A. Sieber, Ed. Springer Berlin Heidelberg, 2012, vol. 324, pp. 43–84.

[242] L. Galluzzi, I. Vitale, J. M. Abrams, E. S. Alnemri, E. H. Baehrecke, M. V. Blagosklonny, T. M. Dawson, V. L. Dawson, W. S. El-Deiry, S. Fulda, E. Gottlieb, D. R. Green, M. O. Hengartner, O. Kepp, R. A. Knight, S. Kumar, S. A. Lipton, X. Lu, F. Madeo, W. Malorni, P. Mehlen, G. Nunez, M. E. Peter, M. Piacentini, D. C. Rubinsztein, Y. Shi, H. U. Simon, P. Vandenabeele, E. White, J. Yuan, B. Zhivotovsky, G. Melino, and G. Kroemer, "Molecular definitions of cell death subroutines: recommendations of the nomenclature committee on cell death 2012," *Cell Death Differ*, vol. 19, no. 1, pp. 107–120, 2012.

[243] G. Kroemer and B. Levine, "Autophagic cell death: the story of a misnomer," *Nat Rev Mol Cell Biol*, vol. 9, no. 12, pp. 1004–1010, Dec. 2008.

[244] G. Kroemer, L. Galluzzi, P. Vandenabeele, J. Abrams, E. S. Alnemri, E. H. Baehrecke, M. V. Blagosklonny, W. S. El-Deiry, P. Golstein, D. R. Green, M. Hengartner, R. A. Knight, S. Kumar, S. A. Lipton, W. Malorni, G. NuÃ±ez, M. E. Peter, J. Tschopp, J. Yuan, M. Piacentini, B. Zhivotovsky, and G. Melino, "Classification of cell death: recommendations of the nomenclature committee on cell death 2009," *Cell death and differentiation*, vol. 16, no. 1, pp. 3–11, 2009.

[245] N. N. Danial and S. J. Korsmeyer, "Cell death: Critical control points," *Cell*, vol. 116, no. 2, pp. 205–219, 2004.

[246] A. Ashkenazi, "Directing cancer cells to self-destruct with pro-apoptotic receptor agonists," *Nat Rev Drug Discov*, vol. 7, no. 12, pp. 1001–1012, Dec. 2008.

[247] J. S. Fridman and S. W. Lowe, "Control of apoptosis by p53," *Oncogene*, vol. 22, no. 56, pp. 9030–9040, 0000.

[248] D. R. Green and G. Kroemer, "The pathophysiology of mitochondrial cell death," *Science*, vol. 305, no. 5684, pp. 626–629, 2004.

[249] S. W. G. Tait and D. R. Green, "Mitochondria and cell death: outer membrane permeabilization and beyond," *Nat Rev Mol Cell Biol*, vol. 11, no. 9, pp. 621–632, Sep. 2010.

[250] S. Fulda and K.-M. Debatin, "Extrinsic versus intrinsic apoptosis pathways in anticancer chemotherapy," *Oncogene*, vol. 25, no. 34, pp. 4798–4811, 0000.

[251] H. Walczak and P. H. Krammer, "The CD95 (APO-1/Fas) and the TRAIL (APO-2L) apoptosis systems," *Experimental Cell Research*, vol. 256, no. 1, pp. 58–66, 2000.

[252] D. Glick, S. Barth, and K. F. Macleod, "Autophagy: cellular and molecular mechanisms," *J Pathol*, vol. 221, no. 1, pp. 3–12, 2010.

[253] A. Vaseva, N. Marchenko, K. Ji, S. Tsirka, S. Holzmann, and U. Moll, "p53 opens the mitochondrial permeability transition pore to trigger necrosis," *Cell*, vol. 149, no. 7, pp. 1536–1548, 2012.

[254] C. D. Bortner and J. A. Cidlowski, "Ion channels and apoptosis in cancer," *Philosophical Transactions of the Royal Society of London B: Biological Sciences*, vol. 369, no. 1638, 2014.

[255] P. Mroz, A. Yaroslavsky, G. B. Kharkwal, and M. R. Hamblin, "Cell death pathways in photodynamic therapy of cancer," *Cancers*, vol. 3, no. 2, pp. 2516–2539, 2011.

[256] L. Galluzzi, O. Kepp, S. Krautwald, G. Kroemer, and A. Linkermann, "Molecular mechanisms of regulated necrosis," *Seminars in Cell & Developmental Biology*, vol. 35, no. 0, pp. 24–32, 2014.

[257] ATTC. (2014) ATCC cell lines by gene mutation. [Online]. Available: http://www.atcc.org

[258] A. R. P. Hinson, R. Jones, L. E. S. Crose, B. C. Belyea, F. G. Barr, and C. M. Linardic, “Human rhabdomyosarcoma cell lines for rhabdomyosarcoma research: Utility and pitfalls,” *Front Oncol*, vol. 3, 2013.

[259] D. L. Morse, H. Gray, C. M. Payne, and R. J. Gillies, “Docetaxel induces cell death through mitotic catastrophe in human breast cancer cells,” *Molecular Cancer Therapeutics*, vol. 4, no. 10, pp. 1495–1504, 2005.

[260] J. J. M. Landry, P. T. Pyl, T. Rausch, T. Zichner, M. M. Tekkedil, A. M. Stutz, A. Jauch, R. S. Aiyar, G. Pau, N. Delhomme, J. Gagneur, J. O. Korbel, W. Huber, and L. M. Steinmetz, “The genomic and transcriptomic landscape of a HeLa cell line,” *G3: Genes—Genomes—Genetics*, vol. 3, no. 8, pp. 1213–1224, 2013.

[261] P. Akan, A. Alexeyenko, P. Costea, L. Hedberg, B. Solnestam, S. Lundin, J. Hallman, E. Lundberg, M. Uhlen, and J. Lundeberg, “Comprehensive analysis of the genome transcriptome and proteome landscapes of three tumor cell lines,” *Genome Medicine*, vol. 4, no. 11, p. 86, 2012.

[262] I. M. Probes. (2015, Feb.) Acetoxymethyl (AM) and acetate esters. [Online]. Available: http://tools.lifetechnologies.com/content/sfs/manuals/g002.pdf

[263] D. Software. (2015, Mar.) Multicycle av cell cycle data display explained. [Online]. Available: http://www.denovosoftware.com/Download/FCSExpressMultiCycleAVExplained.pdf

[264] G. Majno and I. Joris, “Apoptosis, oncosis, and necrosis. an overview of cell death,” *Am J Pathol*, vol. 146, no. 1, pp. 3–15, 1995.

[265] P. C. Leung, W. A. Taylor, J. H. Wang, and C. L. Tipton, “Role of calmodulin inhibition in the mode of action of Ophiobolin A,” *Plant Physiology*, vol. 77, no. 2, pp. 303–308, 1985.

[266] R. Bravo, V. Parra, D. Gatica, A. E. Rodriguez, N. Torrealba, F. Paredes, Z. V. Wang, A. Zorzano, J. A. Hill, E. Jaimovich, A. F. G. Quest, and S. Lavandero, “Endoplasmic reticulum and the unfolded protein response: Dynamics and metabolic integration,” *Int Rev Cell Mol Biol*, vol. 301, pp. 215–90, 2013.

[267] M. Cnop, M. Igoillo-Esteve, D. A. Cunha, L. Ladriere, and D. L. Eizirik, “An update on lipotoxic endoplasmic reticulum stress in pancreatic beta-cells,” *Biochem Soc Trans*, vol. 36, no. Pt 5, pp. 909–15, 2008.

[268] J. H. Lee and Y. S. Yang, “Effect of HCl concentration and reaction time on the change in the crystalline state of TiO2 prepared from aqueous TiCl4 solution by precipitation,” *Journal of the European Ceramic Society*, vol. 25, no. 16, pp. 3573–3578, 2005.

[269] H. P. Harding, Y. Zhang, and D. Ron, “Protein translation and folding are coupled by an endoplasmic-reticulum-resident kinase,” *Nature*, vol. 397, no. 6716, pp. 271–274, Jan. 1999.

[270] J. W. Brewer, “PERK mediates cell-cycle exit during the mammalian unfolded,” *PNAS*, vol. 97, no. 23, pp. 12 625–30, 2000.

[271] J. Pietenpol and Z. Stewart, “Cell cycle checkpoint signaling: Cell cycle arrest versus apoptosis,” *Toxicology*, vol. 181182, no. 0, pp. 475–481, 2002.

[272] B. BD. (2015, Mar.) Cell cycle and cell proliferation: An overview. [Online]. Available: http://www.bdbiosciences.com/us/applications/research/apoptosis/m/1277312/analysis?cc=US

[273] N.-. D. H. T. C. L. Screen, “LC50 mean graph for compound 114340,” Sept 2014. [Online]. Available: http://dtp.nci.nih.gov/dtpstandard/servlet/dwindex?searchtype=NSC&chemnameboolean=and&outputformat=html&searchlist=+114340&Submit=Submit

[274] B. D. Florea A-M, “Cisplatin as an anti-tumor drug: Cellular mechanisms of activity, drug resistance and induced side effects,” *Cancers (Basel)*, vol. 3, no. 1, pp. 1351–71, 2011.

[275] M. A. Gronski, J. M. Kinchen, I. J. Juncadella, N. C. Franc, and K. S. Ravichandran, “An essential role for calcium flux in phagocytes for apoptotic cell engulfment and the anti-inflammatory response,” *Cell Death Differ*, vol. 16, no. 10, pp. 1323–31, 2009.

[276] W. C. Reinhold, M. Sunshine, H. Liu, S. Varma, K. W. Kohn, J. Morris, J. Doroshow, and Y. Pommier, “Cellminer: A web-based suite of genomic and pharmacologic tools to explore transcript and drug patterns in the NCI-60 cell line set,” *Cancer Research*, vol. 72, no. 14, pp. 3499–3511, 2012.

[277] A. Atlante, P. Calissano, A. Bobba, A. Azzariti, E. Marra, and S. Passarella, “Cytochrome c is released from mitochondria in a reactive oxygen species (ROS)-dependent fashion and can operate as a ROS scavenger and as a respiratory substrate in cerebellar neurons undergoing excitotoxic death,” *Journal of Biological Chemistry*, vol. 275, no. 47, pp. 37 159–37 166, 2000.

[278] P. Murphy, “How mitochondria produce reactive oxygen species,” *Biochem J*, vol. 417, no. Pt 1, pp. 1–13, 2009.

[279] S. M. Behar, C. J. Martin, M. G. Booty, T. Nishimura, X. Zhao, H.-X. Gan, M. Divangahi, and H. G. Remold, “Apoptosis is an innate defense function of macrophages against mycobacterium tuberculosis,” *Mucosal Immunol*, vol. 4, no. 3, pp. 279–287, May 2011.

[280] H. Liu, S. Zhao, Y. Zhang, J. Wu, H. Peng, J. Fan, and J. Liao, “Reactive oxygen species-mediated endoplasmic reticulum stress and mitochondrial dysfunction contribute to polydatin-induced apoptosis in human nasopharyngeal carcinoma CNE cells,” *Journal of Cellular Biochemistry*, vol. 112, no. 12, pp. 3695–3703, 2011.

[281] A. H. Schonthal, “Targeting endoplasmic reticulum stress for cancer therapy,” *Front Biosci (Schol Ed)*, vol. 4, pp. 412–31, 2012.

[282] L. M. Westrate, J. A. Drocco, K. R. Martin, W. S. Hlavacek, and J. P. MacKeigan, “Mitochondrial morphological features are associated with fission and fusion events,” *PLoS ONE*, vol. 9, no. 4, p. e95265, 2014.

[283] B. Vogelstein, D. Lane, and A. J. Levine, “Surfing the p53 network,” *Nature*, vol. 408, no. 6810, pp. 307–310, Nov. 2000.

[284] K. K. Hoe, C. S. Verma, and D. P. Lane, “Drugging the p53 pathway: understanding the route to clinical efficacy,” *Nat Rev Drug Discov*, vol. 13, no. 3, pp. 217–236, Mar. 2014.

[285] Z. Wang and Y. Sun, “Targeting p53 for novel anticancer therapy,” *Translational Oncology*, vol. 3, no. 1, pp. 1–12, 2010.

[286] L. M. Shi, T. G. Myers, Y. Fan, P. M. Oâ€™Connor, K. D. Paull, S. H. Friend, and J. N. Weinstein, “Mining the national cancer institute anticancer drug discovery database: Cluster analysis of ellipticine analogs with p53-inverse and central nervous system-selective patterns of activity,” *Molecular Pharmacology*, vol. 53, no. 2, pp. 241–251, 1998.

[287] E. Sugikawa, T. Hosoi, N. Yazaki, M. Gamanuma, N. Nakanishi, and M. Ohashi, “Mutant p53 mediated induction of cell cycle arrest and apoptosis at G1 phase by 9-hydroxyellipticine,” *Anticancer Res*, vol. 19, no. 4b, pp. 3099–108, 1999.

[288] F. Bunz, A. Dutriaux, C. Lengauer, T. Waldman, S. Zhou, J. P. Brown, J. M. Sedivy, K. W. Kinzler, and B. Vogelstein, “Requirement for p53 and p21 to sustain G2 arrest after DNA damage,” *Science*, vol. 282, no. 5393, pp. 1497–1501, 1998.

[289] H. Shen and C. G. Maki, “p53 and p21(Waf1) are recruited to distinct PML-containing nuclear foci in irradiated and Nutlin-3a-treated U2OS cells,” *J Cell Biochem*, vol. 111, no. 5, pp. 1280–90, 2010.

[290] F. Splettstoesser, A.-M. Florea, and D. Busselberg, “IP3 receptor antagonist, 2APB, attenuates cisplatin induced Ca2+-influx in HeLa-S3 cells and prevents activation of calpain and induction of apoptosis,” *British Journal of Pharmacology*, vol. 151, no. 8, pp. 1176–1186, 2007.

[291] T. Wei, Q. Kang, B. Ma, S. Gao, X. Li, and Y. Liu, “Activation of autophagy and paraptosis in retinal ganglion cells after retinal ischemia and reperfusion injury in rats,” *Exp Ther Med.*, 2015.

[292] Kitagishi and Matsuda, “Redox regulation of tumor suppressor PTEN in cancer and aging (review),” *International Journal of Molecular Medicine*, vol. 31, no. 3, pp. 511–515, 2013.